RSETHZ 340.311

DISS. ETH NO. 30376

NONLINEAR AND METAMATERIALS-BASED SOLUTIONS FOR ELASTIC WAVE AND ENERGY GUIDING

A thesis submitted to attain the degree of

DOCTOR OF SCIENCES
(Dr. sc. ETH Zurich)

presented by

BAO ZHAO

MSc. in Microelectronics and Solid State Electronics, University of Chinese Academy of Sciences

born on *16.01.1993*

accepted on the recommendation of
Prof. Dr. Eleni Chatzi (examiner)
Dr. Andrea Colombi (co-examiner)
Prof. Dr. Raffaele Ardito (co-examiner)
Prof. Dr. Stephanos Theodossiades (co-examiner)
Dr. Bart Van Damme (co-examiner)

2024

Acknowledgments

I would like to express my sincere gratitude to the following:

- My supervisors Dr. Andrea Colombi and Prof. Eleni Chatzi. Thank you for being navigators for my PhD journey. Without your creative ideas, all-around support, and constructive feedback, I could not get into the field of wave propagation. Let alone go through the past three and a half years towards independence in academia!
- My co-supervisors Dr. Bart Van Damme and Dr. Andrea Berganimi. I would like to extend my gratitude to you for the fruitful collaborations, the enthusiasm expressed toward these projects, and the valuable comments.
- My co-examiners Prof. Raffaele Ardito, Prof. Stephanos Theodossiades, and Dr. Bart Van Damme. For your informative feedback and constructive comments, which helped me to enhance this thesis.
- My collaborators Dr. Jacopo Maria De Ponti, Dr. Xingbo Pu, Prof. Guobiao Hu, Prof. Junrui Liang, and Prof. Wei-Hsin Liao. Your insightful perspectives and passion for research inspired me a lot! Especially I would like to thank Prof. Guobiao Hu for hosting my research visit!
- I gratefully acknowledge the ETH Research Grant (ETH-02 20-1), the H2020 FET-proactive project METAVEH (952039), and the SNSF R'Equip grant (206021_205418) for the funding supporting these research projects and a fantastic lab in the HIF building where I will definitely miss a lot!
- All the colleagues in the Chair of Structural Mechanics and Monitoring. Thank you for making this journey a memorable experience. In particular, thanks to the former meta-group members Henrik, Giulia, and Aida. Your companion and supportive help in research and out through the pandemic time means a lot to me! My days in the HIT and HIL offices with you will always be a precious memory.
- My friends in Zurich. Thank you for all the experiences we shared: the hiking to the mountains, the trips to the woods, and dinners with self-made Chinese food and hotpots!

I wish to thank my parents who raised me. Without your unwavering support for every choice I made, I could not make it so far from a small mountain city. There are no words that can describe my gratefulness to you! Finally to my wife, Jingchun, the beacon of light on this challenging journey and my beloved partner in the longest project called life.

Contents

Abstract

The recent thrusts in wave propagation and semiconductors since the late 20^{th} century have gradually shifted the design paradigm of civil and mechanical structures from trial-and-error iterations into target-oriented applications. Through integration of wave manipulation mechanisms, the elastic or mechanical energy can be guided, reflected, redirected, or localized with predefined paths, thus enabling diverse functionalities for the original structures. From the mechanical perspective, these functions could be exploited for vibration mitigation or attenuation under certain frequency ranges, so-called as bandgaps. From the electrical perspective, they can also be utilized for signal sensing and energy harvesting when the elastic wave is focused or amplified at desired positions or frequencies. To introduce such novel wave manipulation mechanisms into the conventional elastic systems, the concepts of metamaterials and nonlinear dynamics are discussed and studied in this thesis. In particular, we capitalize on local resonance effects and the nonlinear effect induced via use of auxiliary structures as local resonators.

These artificially altered mechanical systems are further combined with electromechanical coupling materials and interface circuits for the purposes of energy harvesting and/or dynamics control, expanding their functionalities and utility with semiconductors and programmable logic. By putting forth a framework that extends beyond linear dynamics and electromechanical coupling, the studied mechanical systems in this thesis produce solutions for engineered structures which exhibit resilience to mechanical vibrations and yield sustainable mechanisms for vibration-powered applications, e.g., for Internet of Things (IoT) devices. This thesis presents a set of novel mechanical systems for various applications, including vibration mitigation, energy harvesting, and dynamics control i.e., covering use cases from attenuation of low-frequency vibrations to the harvesting of localized elastic energy, and further towards the utilization of the harvested energy in mechanical dynamics control.

The first part of this work proposes a graded locally resonant metamaterial for broadband and high-capability piezoelectric energy harvesting, which preserves its original mechanical bandgap for vibration attenuation. Its design, comprising gradual increase of length of local resonant beams on a host beam as wave carrier, enables the gradual change of mechanical impedance for the dual functions of frequency separation and wave amplification. These two mechanical characteristics enable broadband and high-capability piezoelectric energy harvesting. Theoretical lumped parameter models, full scale numerical models, and experimental realizations with piezoelectric interface circuits have been realized to validate the proposed metamaterial-based energy harvesting solution. The outcomes of

this work reveal the capacity for milliwatt-level DC output power with a frequency range that spans from 50 Hz to 150 Hz, paving the way for powering of IoT devices with metamaterials under low-frequency vibrations.

A typical application for such harvested energy from mechanical vibration is for use with IoT devices. In addition, the electromechanical coupling in mechanical systems offers a bidirectional energy conversion channel, opening up a direct energy conversion path from the mechanical domain to the electrical domain and vice versa. Based on this idea, the second part of the thesis shifts to applications in the domain of control for nonlinear mechanical oscillators, using the harvested energy. In forced and periodic nonlinear dynamical systems, if hysteresis is present, multiple stable states or fixed points exist, serving as attractors; this leads in generation of different orbits comprising dramatically different displacement amplitudes. The high-energy orbits are preferred for energy harvesting due to their high amplitudes. Motivated by this observation, this work proposes a circuit solution to reverse boost the electrical energy, thus forming an anti-phase piezoelectric actuating force applied on the oscillator concerning its velocity. Using a multiple time scale analysis, the orbit jump mechanism from low-to-high orbit is revealed, which is effectuated via an unstable spiral and a saddle-node bifurcation. The theoretical results have been validated experimentally in monostable and bistable nonlinear energy harvesting systems, which offer a compact circuit solution to guide the energy in the coupled electromechanical system.

The final part of this thesis is dedicated to an extension of the nonlinear dynamic mechanisms which were initially studied at the resonator level, to the level of multiple nonlinear local resonators. The outcome is a nonlinear metamaterial, which is able to control and mitigate elastic wave propagation in a broadband fashion. The geometric design of local resonators employs an inertia amplification mechanism, which introduces nonlinear damping forces as reaction forces applied on the substrate beam system. By introducing a numerical harmonic balance method with Alternating Frequency Time and numerical continuation techniques, the nonlinear frequency response of a finite nonlinear metamaterial beam can be solved and verified. The obtained theoretical and experimental results suggest that the bandgap has been broadened as a result of the nonlinear damping effect. In addition, nonlinear modal coupling is also revealed for higher modal frequency dissipation, which not only works for harmonic excitation but also effectively demonstrates the shock wave attenuation through low-to-high frequency energy transfer and dissipation. This work not only expands the utility of locally resonant metamaterials to a broader frequency range, but further delivers methods to estimate the nonlinear frequency response of nonlinear metamaterials, which poses a current challenge for commercially available simulation software and broadly adopted time domain integration methods.

This thesis contributes to the quest for multifunctional mechanical systems in elastic wave and energy control, covering a broad range of studies and applications from the mitigation of vibrations via metamaterials to energy harvesting and dynamics control with electromechanical coupling designs.

Zusammenfassung

Die jüngsten Fortschritte in der Wellenausbreitung und Halbleitertechnologie seit dem späten 20. Jahrhundert haben das Designparadigma von zivilen und mechanischen Strukturen schrittweise von iterativen Versuch-und-Irrtum-Methoden hin zu zielorientierten Anwendungen verschoben. Durch die Integration von Wellenmanipulationsmechanismen kann die elastische oder mechanische Energie entlang vordefinierter Pfade geleitet, reflektiert, umgelenkt oder lokalisiert werden, was den ursprünglichen Strukturen vielfältige Funktionalitäten verleiht. Aus mechanischer Sicht könnten diese Funktionen zur Minderung oder Dämpfung von Vibrationen in bestimmten Frequenzbereichen, den sogenannten Bandlücken, genutzt werden. Aus elektrischer Sicht können sie auch zur Signalaufzeichnung und Energierückgewinnung verwendet werden, wenn die elastische Welle an gewünschten Positionen oder Frequenzen fokussiert oder verstärkt wird. Um solche neuartigen Wellenmanipulationsmechanismen in konventionelle elastische Systeme einzuführen, werden in dieser Arbeit die Konzepte von Metamaterialien und nichtlinearen Dynamiken untersucht und diskutiert. Insbesondere nutzen wir lokale Resonanzeffekte und den nichtlinearen Effekt, der durch den Einsatz von Hilfsstrukturen als lokale Resonatoren induziert wird.

Diese künstlich veränderten mechanischen Systeme werden weiter mit elektromechanischen Kopplungsmaterialien und Schnittstellenschaltungen kombiniert, um Energie zu gewinnen und/oder die Dynamik zu steuern, wodurch ihre Funktionalitäten und Einsatzmöglichkeiten mit Halbleitern und programmierbarer Logik erweitert werden. Durch die Einführung eines Rahmens, der über lineare Dynamik und elektromechanische Kopplung hinausgeht, bieten die in dieser Arbeit untersuchten mechanischen Systeme Lösungen für konstruierte Strukturen, die eine Widerstandsfähigkeit gegen mechanische Vibrationen aufweisen und nachhaltige Mechanismen für vibrationsbetriebene Anwendungen ermöglichen, z.B. für Geräte des Internets der Dinge (IoT). Diese Arbeit stellt eine Reihe neuartiger mechanischer Systeme für verschiedene Anwendungen vor, darunter Schwingungsdämpfung, Energierückgewinnung und Dynamiksteuerung, d.h. sie deckt Anwendungsfälle von der Dämpfung niederfrequenter Vibrationen über die Rückgewinnung lokalisierter elastischer Energie bis hin zur Nutzung der gewonnenen Energie zur Steuerung der mechanischen Dynamik ab.

Der erste Teil dieser Arbeit schlägt ein abgestuftes lokal resonantes Metamaterial für breitbandige und hochleistungsfähige piezoelektrische Energierückgewinnung vor, das seine ursprüngliche mechanische Bandlücke zur Schwingungsdämpfung bewahrt. Sein Design, das eine allmähliche Verlängerung der lokal resonanten Strahlen auf einem Trägerstrahl als

Wellenträger umfasst, ermöglicht die allmähliche Änderung der mechanischen Impedanz für die dualen Funktionen der Frequenztrennung und Wellenverstärkung. Diese beiden mechanischen Eigenschaften ermöglichen eine breitbandige und hochleistungsfähige piezoelektrische Energierückgewinnung. Theoretische Modelle mit gebündelten Parametern, numerische Modelle im großen Maßstab und experimentelle Realisierungen mit piezoelektrischen Schnittstellenschaltungen wurden durchgeführt, um die vorgeschlagene Metamaterial-basierte Energierückgewinnungslösung zu validieren. Die Ergebnisse dieser Arbeit zeigen die Fähigkeit zur Erzeugung einer Gleichstromleistung im Milliwatt-Bereich mit einem Frequenzbereich von 50 Hz bis 150 Hz und ebnen den Weg zur Stromversorgung von IoT-Geräten mit Metamaterialien unter niederfrequenten Vibrationen.

Eine typische Anwendung für solche aus mechanischen Vibrationen gewonnene Energie ist die Nutzung in IoT-Geräten. Darüber hinaus bietet die elektromechanische Kopplung in mechanischen Systemen einen bidirektionalen Energieumwandlungskanal, der einen direkten Energieumwandlungspfad vom mechanischen in den elektrischen Bereich und umgekehrt eröffnet. Basierend auf dieser Idee wechselt der zweite Teil der Arbeit zu Anwendungen im Bereich der Steuerung von nichtlinearen mechanischen Oszillatoren unter Nutzung der gewonnenen Energie. In erzwungenen und periodischen nichtlinearen dynamischen Systemen, wenn Hysterese vorhanden ist, existieren mehrere stabile Zustände oder feste Punkte, die als Attraktoren dienen; dies führt zur Erzeugung verschiedener Bahnen, die deutlich unterschiedliche Verschiebungsamplituden aufweisen. Die Hochenergie-Bahnen werden aufgrund ihrer hohen Amplituden für die Energierückgewinnung bevorzugt. Motiviert durch diese Beobachtung schlägt diese Arbeit eine Schaltungslösung vor, um die elektrische Energie rückwärts zu verstärken und so eine Piezoaktorkraft gegenphasig zur Geschwindigkeit des Oszillators anzuwenden. Mittels einer Mehrfachzeit-Skalenanalyse wird der Mechanismus des Bahnsprungs von einer niedrigen zu einer hohen Bahn aufgedeckt, der durch eine instabile Spirale und eine Sattel-Knoten-Bifurkation zustande kommt. Die theoretischen Ergebnisse wurden experimentell in monostabilen und bistabilen nichtlinearen Energierückgewinnungssystemen validiert, die eine kompakte Schaltungslösung bieten, um die Energie im gekoppelten elektromechanischen System zu leiten.

Der letzte Teil dieser Arbeit widmet sich einer Erweiterung der nichtlinearen dynamischen Mechanismen, die zunächst auf der Ebene des Resonators untersucht wurden, auf die Ebene mehrerer nichtlinearer lokaler Resonatoren. Das Ergebnis ist ein nichtlineares Metamaterial, das in der Lage ist, die elastische Wellenausbreitung in einem breiten Frequenzbereich zu steuern und zu dämpfen. Das geometrische Design der lokalen Resonatoren nutzt einen Trägheitsverstärkungsmechanismus, der nichtlineare Dämpfungskräfte als Reaktionskräfte auf das Trägerstrahlsystem einführt. Durch die Einführung einer numerischen harmonischen Bilanzmethode mit alternierender Frequenzzeit und numerischen Fortsetzungstechniken kann die nichtlineare Frequenzantwort eines endlichen nichtlinearen Metamaterialstrahls gelöst und verifiziert werden. Die erhaltenen theoretischen und experimentellen Ergebnisse legen nahe, dass die Bandlücke aufgrund des nichtlinearen Dämpfungseffekts erweitert wurde. Darüber hinaus wird auch eine nichtlineare Modenkopplung für die Dissipation höherer Modalfrequenzen aufgedeckt, die nicht nur für harmonische Erregung, sondern auch für die Dämpfung von Stoßwellen durch Energieübertragung und -dissipation von niedrigen zu hohen Frequenzen wirksam ist. Diese

Arbeit erweitert nicht nur den Einsatz von lokal resonanten Metamaterialien auf ein breiteres Frequenzspektrum, sondern liefert auch Methoden zur Schätzung der nichtlinearen Frequenzantwort von nichtlinearen Metamaterialien, was eine aktuelle Herausforderung für kommerziell verfügbare Simulationssoftware und weit verbreitete zeitbereichsbasierte Integrationsmethoden darstellt.

Diese Arbeit trägt zur Suche nach multifunktionalen mechanischen Systemen in der elastischen Wellen- und Energiekontrolle bei und deckt ein breites Spektrum an Studien und Anwendungen ab, von der Dämpfung von Vibrationen durch Metamaterialien bis hin zur Energierückgewinnung und Dynamiksteuerung mit elektromechanischen Kopplungsdesigns.

Chapter 1

Introduction

1.1 Motivation and Problem Statement

Waves, movements of particles governed by energy flows, are present in every corner of our daily lives, though they often go unnoticed. Sound waves allow us to hear words, radio waves enable us to navigate maps, and elastic waves transmit vibrations. Among these waveforms, this thesis focuses on **elastic waves** propagating in solids [1] and studies the underlying mechanical systems to guide wave propagation and energy flow within these systems.

While this thesis relies on concepts from electromagnetism, piezoelectricity, and power electronics, the primary focus is on mechanical systems serving as host structures for the entire coupled system. Common applications of these systems involve, for example, **guided wave** testing. A wave generation technique used from non-destructive evaluation for structural health monitoring of civil, aerospace, naval, and mechanical structures [2, 3]. Guided waves are typically generated by arrays of piezoelectric actuators, reflected by defects and damages, and detected with piezoelectric sensors for damage detection and localization. This electrical-to-mechanical energy conversion intermediated by elastic waves also happens in energy harvesting systems, where the elastic waves are **focused**, **trapped**, and **converted** into electricity through electromechanical coupling transducers like electromagnetic or piezoelectric materials.

In these examples, waves serve functional purposes. However, there also exist extreme cases in which large wave amplitudes lead to destructive, detrimental, or disturbing consequences for mankind. Common examples include seismic waves from the potential release in crustal materials and airplane noises from the combination of rotational engines. Besides human-related disturbances,, large wave amplitudes also raise fatigue issues, cracks, and strength failures for structures. The spectrum of these examples covers the wave propagation spanning from low-frequency (Hz) to high-frequency (MHz) and highlights the importance of wave control and attenuation in mechanical systems. Conventional vibration attenuation methods have been proposed to address this issue. Common methods include dynamic vibration absorbers, which protect the host structure with auxiliary os-

cillators targeting the detrimental frequency; nonlinear dampers, which dissipate kinetic energy using energy-absorbing materials; and energy harvesters, which convert mechanical energy into electricity, thus providing electrically induced damping and stiffness for vibration control. However, these customary approaches have several practical *limitations*, including a narrow frequency range for vibration control and low efficiency in energy conversion, which motivates the search for new technologies.

During the process of vibration control, mechanical energy is either confined or reflected by auxiliary structures or absorbed by damping materials or coupling transducers. Of particular interest for this thesis is the case of energy harvesting, where the originally detrimental wave energy is transformed into useful electricity, simultaneously leading to the vibration control of the host structures. General energy harvesters consist of vibration sources, coupling materials, and interface circuits. For piezoelectric energy harvesting, the best-known interface circuits include the resistive shunting circuit and the standard energy harvesting circuit (full-bridge rectifier). They both convert the alternating mechanical vibrations into electricity, however, one in AC (alternating current) form and another in DC (direct current) form. When considering the applications of vibration-powered IoT devices, the harvested power should bear a DC form for power supplies of microcontrollers and wireless sensor nodes. Thus, recent years have witnessed the growth of this domain with the thrust of power electronics; more and more interface circuits applied the switching-mode power conversion rather than simple shunting or analog circuits to increase the energy harvesting capability and bandwidth. Such as the self-power SSHI (synchronized switching harvesting on inductor) and SECE (synchronized electrical charge extraction) circuits, which eliminate the phase difference induced by the inner capacitance from the piezoelectric transducers. However, these interface circuits for energy harvesting and vibration control also lead to challenges in structural dynamics, to name a few: the electromechanical dynamics and its effect on wave propagation and the system-level integration for vibration-powered IoT devices.

Recent advances in mechanics and electronics have introduced a new realm of **electromechanical systems**, which have garnered attention for their remarkable ability to guide wave paths and convert mechanical energy for sensing and powering IoT devices. Unlike conventional vibration absorbers, their underlying mechanical systems rely on so-called bandgaps to efficiently cancel or reflect the propagation waves under certain frequency ranges. Depending on different physical mechanisms, mechanical systems with bandgaps are often referred to as metamaterials and can be classified into photonic crystals [4] and locally resonant metamaterials [5], as detailed in Section 1.2.1. They initially gained momentum in electromagnetism [6–8], to sprawl only later to the acoustic [5, 9] and elastic domains [10, 11].

Despite the staggering perspectives of photonic crystals and metamaterials, only the pure mechanical systems are not sufficient to reach the level of maturity for applications of vibration control and energy conversion, where they are facing a number of *challenges*. In power electronics, energy sources are typically stable and independent of load conditions. However, practical applications of mechanical systems for power conversion are challenged by wave propagation, where the equivalent energy sources depend on the input and configuration of the mechanical system. Additionally, the coupling effect induced

by transducers and circuits generates reaction forces on the host mechanical systems, further complicating wave propagation. This poses a challenging requirement for electromechanical systems, as metamaterials, characterized by bandgaps and circuits with easy tunablilities, offer electrically controlled properties, thus motivating the quest for integration, such as those relying on the combination of the two. Among the numerous electromechanical designs proposed in the literature, **multifunctional metamaterials** have recently drawn the interest of the research community for their signal processing and energy harvesting capabilities, in addition to their established uses in wave control applications [12]. However, research in this direction is still in its infancy, and much has yet to be discovered about their dynamic and electrical performance.

It is precisely this gap and the limitations of standard metamaterials and power electronics designs that inspire the current work. This thesis presents novel methods and systems based on conventional wave manipulation systems for innovative technologies such as energy harvesting and dynamics control. The first part of this thesis aims to integrate the piezoelectric energy harvesting interface circuits into graded metamaterials for broadband and high-capability energy harvesting. By utilizing the harvested energy, the study transitions toward novel solutions for dynamics control in nonlinear oscillating systems, which are common in many structural engineering applications (e.g., wings and blades vibrations under heavy wind load), and ultimately focuses on theoretical methods and experimental applications of nonlinear dynamics induced by geometric deformation and interface circuits to guide wave and energy in multifunctional mechanical systems.

1.2 Theoretical Background and Methods

This section provides an overview of the physical framework and key theoretical concepts adopted in this thesis, providing an overview of the thesis structure and main topics covered.

1.2.1 Elastic Wave Propagation

Elastic waves propagate in solids depending on the properties and geometry of the media, which can be tailored using auxiliary structures. Wave propagation can be altered in these artificially fabricated metamaterials. The following subsections describe wave propagation in host elastic systems and their corresponding mechanical metamaterials, which consist of host elastic substrates and local resonators.

Elastic waves in structural components

Structural components are fundamental to wave propagation and engineering applications. The common structures include rods, beams, plates, and shells. Given the applications discussed in the following chapters, this section focuses on the principles of wave propagation in plates and beams.

Consider a homogeneous, isotropic, elastic thin plate with thickness $2h$ in y direction as shown in Figure 1.1 (a). Given the infinite lateral extension in x direction, we can adopt

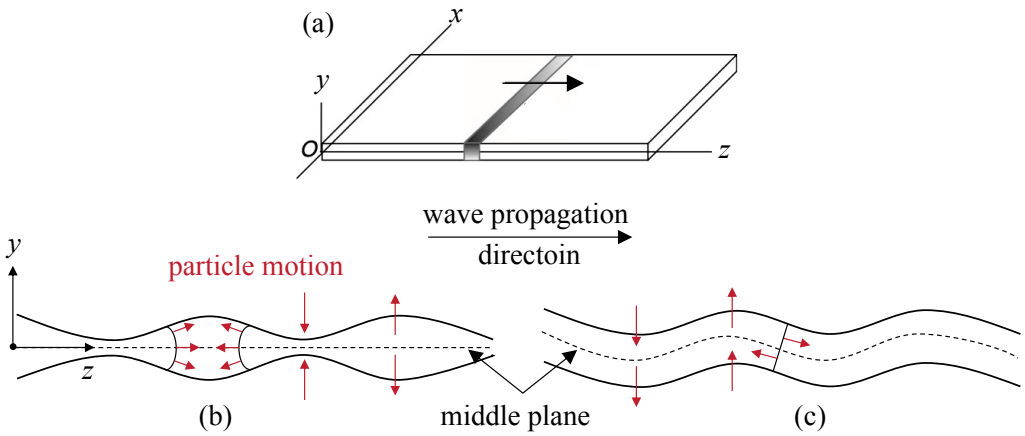

Figure 1.1: Sketch of a thin plate; Symmetric (a) and antisymmetric (b) Lamb wave modes.

plane strain assumption in z direction. The strain in xy plane is defined as $u = u(x, y, t)$, $v = v(x, y, t)$. When considering wave propagation in the z direction, there exist two main classes of waves according to their particle motions: (1) shear horizontal waves, where the particle motion is parallel to the middle plane of the plate; (2) Lamb wave, which consists of parallel and perpendicular particle motions with respect to the middle plane of the plate. This section focuses on Lamb wave propagation, particularly the asymmetric zero mode of Lamb wave propagation in plates and beams. The equation of motion of the plate in the x and y direction can be given as:

$$\begin{aligned} \frac{\partial \sigma_{xx}}{\partial x} + \frac{\partial \sigma_{xy}}{\partial y} &= \rho \frac{\partial^2 u}{\partial t^2} \\ \frac{\partial \sigma_{xy}}{\partial x} + \frac{\partial \sigma_{yy}}{\partial y} &= \rho \frac{\partial^2 v}{\partial t^2} \end{aligned} \tag{1.1}$$

with Hooke's law given as:

$$\begin{aligned} \sigma_{xx} &= \lambda \left(\frac{\partial u}{\partial x} + \frac{\partial v}{\partial y} \right) + 2\mu \frac{\partial u}{\partial x} \\ \sigma_{yy} &= \lambda \left(\frac{\partial u}{\partial x} + \frac{\partial v}{\partial y} \right) + 2\mu \frac{\partial v}{\partial y} \\ \sigma_{xy} &= \mu \left(\frac{\partial u}{\partial y} + \frac{\partial v}{\partial x} \right) \end{aligned} \tag{1.2}$$

By substituting Eq. 1.2 into Eq. 1.1, the following relationship reads:

$$\begin{aligned} \lambda \left(\frac{\partial^2 u}{\partial x^2} + \frac{\partial^2 v}{\partial x \partial y} \right) + 2\mu \frac{\partial^2 u}{\partial x^2} + \mu \left(\frac{\partial^2 u}{\partial y^2} + \frac{\partial^2 v}{\partial x \partial y} \right) &= \rho \frac{\partial^2 u}{\partial t^2} \\ \mu \left(\frac{\partial^2 v}{\partial x^2} + \frac{\partial^2 u}{\partial x \partial y} \right) + \lambda \left(\frac{\partial^2 v}{\partial y^2} + \frac{\partial^2 u}{\partial x \partial y} \right) + 2\mu \frac{\partial^2 v}{\partial y^2} &= \rho \frac{\partial^2 v}{\partial t^2} \end{aligned} \tag{1.3}$$

where the Lame coefficient λ relates to the Young's modulus E, the shear modulus G, and the Poisson's ratio ν as:

$$\mu = G = \frac{E}{2(1+\nu)}, \quad \lambda = \frac{2G\nu}{1-2\nu}, \quad \frac{\lambda}{\mu} = \frac{2\nu}{1-2\nu}. \tag{1.4}$$

By the plain strain assumption and the Helmholtz decomposition, the displacement will have the form:

$$u = \frac{\partial \varphi}{\partial x} + \frac{\partial \psi_z}{\partial y}, \quad v = \frac{\partial \varphi}{\partial y} - \frac{\partial \psi_z}{\partial x} \tag{1.5}$$

where the potential φ and ψ_z satisfy the 2D wave equations:

$$\begin{aligned} \frac{\partial^2 \varphi}{\partial x^2} + \frac{\partial^2 \varphi}{\partial y^2} &= \frac{1}{c_1^2}\frac{\partial^2 \varphi}{\partial t^2} \\ \frac{\partial^2 \psi_z}{\partial x^2} + \frac{\partial^2 \psi_z}{\partial y^2} &= \frac{1}{c_2^2}\frac{\partial^2 \psi_z}{\partial t^2}. \end{aligned} \tag{1.6}$$

By assuming the harmonic solution and considering the top and bottom of the plate as traction-free boundaries, the wave propagation of a plain strain thin plate can be solved. These solutions of Lamb wave propagation can be separated into symmetric modes and asymmetric modes as shown in Figure 1.1 (b) and (c). Their dispersion relationship can be expressed as [13]:

$$\frac{\tan(\alpha h)}{\tan(\beta h)} = -\left[\frac{4\alpha\beta k^2}{(k^2-\beta^2)^2},\right]^{\pm 1} \tag{1.7}$$

where:

$$\alpha^2 = \frac{\omega^2}{v_p^2} - k^2, \quad \beta^2 = \frac{\omega^2}{v_s^2} - k^2. \tag{1.8}$$

The positive exponent in Eq. 1.7 denotes symmetric modes, also named S modes. The red arrows in Figure 1.1 (b) show the particle motion is symmetric with respect to the plate middle plane and, therefore, induces compression and extension of the plate. On the contrary, Figure 1.1 (c) indicates the asymmetric modes where the particles are asymmetric with the middle plane. The asymmetric mode is also shortened as A Lamb mode, which thus undergoes pure bending due to the lack of symmetry with respect to the middle plane.

In order to validate the dispersion relationships of the symmetric and asymmetric modes given in Eq. 1.7, here we demonstrate the wave propagation of zero-order Lamb waves: the S0 and A0 modes. In the low frequency range, these modes are also referred as extensional mode and flexural mode, which contain most of the elastic energy compared with higher order Lamb modes. By simulating the Lame wave propagation within an 1 m long thin plate via COMSOL Multiphysics, the wave field and dispersion relationships of the S0 and A0 modes are shown in Figure 1.2. With a small cross-section area and thickness, this plate fits the assumption of plain strain, and the numerical results match the theoretical relationship in Eq. 1.8. It can be seen that the S0 mode is nondispersive at

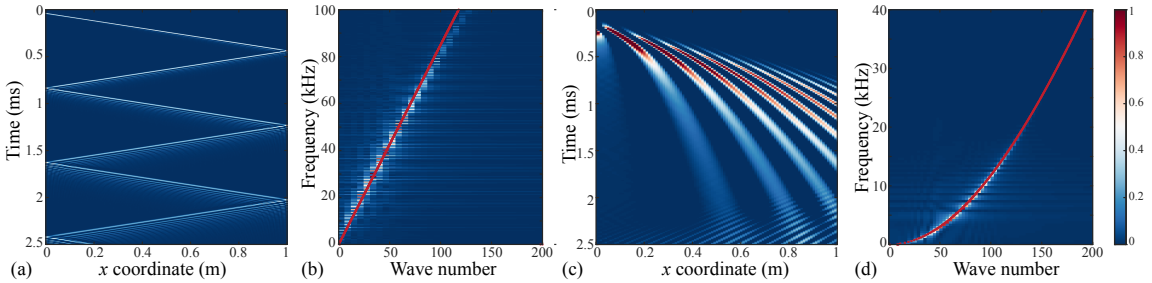

Figure 1.2: Symmetric and asymmetric Lamb wave modes S0 and A0 in a thin plate. The red dispersion lines represent the dispersion calculated with theoretical Lame wave dispersion relationship in Eq. 1.8. (a) and (b): Wave propagation and dispersion relationship of S0 mode (with free boundary conditions); (c) and (d): Wave propagation and dispersion relationship of A0 mode (with low reflection boundary conditions).

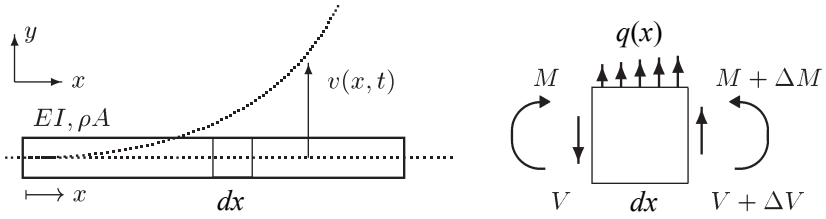

Figure 1.3: Beam undergoes transverse motion and its infinitesimal element with loads.

low frequency while the A0 mode is dispersive, which indicates the dependency of phase velocity on frequency and leads to the dispersive nature of asymmetric modes in plates.

Similar to flexural waves propagating in thin plates, we further discuss the flexural wave in beams as the host substrates for mechanical metamaterials. By adopting the Euler-Bernoulli theory of beam, namely, the cross-section of the beam remains perpendicular to the middle plane of the beam during the bending process. Thus, the relationship of the bending movement M and the curvature reads:

$$\partial^2 y/\partial x^2 = -M/EI, \tag{1.9}$$

where y coordinates to the middle plane. With reference to Figure 1.3, the equation of motion in y direction can be given as:

$$\frac{\partial V}{\partial x} + q = \rho A \frac{\partial^2 y}{\partial t^2}, \tag{1.10}$$

where A is the cross section area and ρ is the density per unit volume. By neglecting the rotational inertia, the movement balance follows $V = \partial M/\partial x$. Combining this relationship with the equation of motion and the relationship of deformation curvature, the governing equation of the transverse motion of a beam can be given as:

$$\frac{\partial^2}{\partial x^2}\left(EI\frac{\partial^2 y}{\partial x^2}\right) + \rho A \frac{\partial^2 y}{\partial t^2} = q(x,t). \tag{1.11}$$

Under the absence of external load and homogeneity of the beam, the Euler-Bernoulli equation of the beam reduces to:

$$EI\frac{\partial^4 y}{\partial x^4} + \rho A\frac{\partial^2 y}{\partial t^2} = 0. \tag{1.12}$$

Consider an infinite beam governed by this equation, and we can assume the propagation of harmonic wave by:

$$y = A\mathrm{e}^{i(kx-\omega t)}, \tag{1.13}$$

And substituting Eq. 1.13 into the Euler-Bernoulli beam equation, the dispersion of flexural wave reads:

$$\omega = k^2\sqrt{\frac{EI}{\rho A}}. \tag{1.14}$$

It can be seen that the dispersion of the flexural wave in Euler-Bernoulli beams is also dispersive. The positive and negative wave numbers k in Eq. 1.14 correspond to the right and left going wave, and the imaginary wave number corresponds to the spatially evanescent wave. It should be noted that the Euler-Bernoulli beam equation only works for low-frequency flexural wave propagation since it neglects the rotational inertia and shear effects.

Elastic waves in mechanical metamaterials

Adding auxiliary structures, such as local resonators, to the underlying host substrate can modify the dispersion relationship of elastic waves. This introduces the concept of metamaterials, which feature a periodic pattern similar to crystals. The smallest element in this periodic arrangement is called a unit cell. An artificially fabricated metamaterial can be considered a spatially repeatable matrix consisting of unit cells [14]. This spatial arrangement, known as a crystal lattice, enables the band characteristics from solid-state physics and is essential to wave propagation in metamaterials. The periodicity of metamaterials is characterized by translational and rotational symmetries.

This thesis primarily discusses wave propagation in beam- and plate-based locally resonant metamaterials, with their unit cells and typical configurations shown in Figure 1.4. Due to the translational symmetry in the periodic arrangement, their periodicities are described by basis vectors $\boldsymbol{a_1}$ and $\boldsymbol{a_2}$ as [15]:

$$\mathbf{r_{n_1,n_2}} = n_1\boldsymbol{a_1} + n_2\boldsymbol{a_2}, \tag{1.15}$$

where n_1 and n_2 are integers expanded in the xy plane as shown in Figure 1.4 (b). In the simpler case of beam-based metamaterials, the unit cells repeat in only one direction, as shown in Figure 1.4 (a).

The mechanism of locally resonant metamaterials depends on the local resonance of auxiliary resonators, which can enable control of low-frequency elastic wave propagation. The

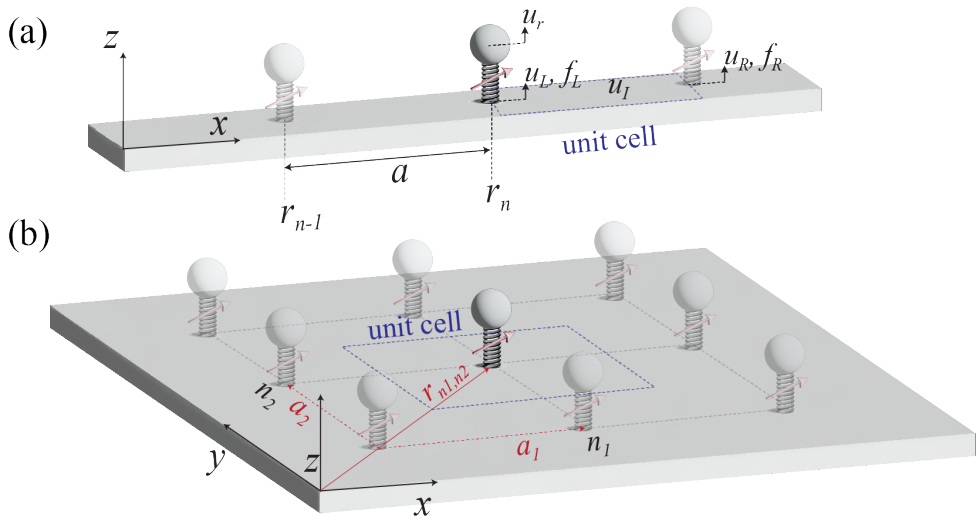

Figure 1.4: Schematics of mechanical metamaterials. (a) Metamaterial beam; (b) Metamaterial plate.

equation of motion for these local resonators can be given as follows:

$$m_r\ddot{x} + c_r\dot{x} + k_r x = f, \tag{1.16}$$

which stands for a linear local resonator with mass m_r, damping c_r, stiffness k_r, and the external force f. For elastic wave propagation in Euler-Bernoulli beams or Kirchhoff plates, a linear differential operator $\boldsymbol{L}$ is introduced to describe the wave propagation:

$$\boldsymbol{L} = \frac{\partial^4}{\partial x^4}, \quad \boldsymbol{L} = \left(\frac{\partial^2}{\partial x^2} + \frac{\partial^2}{\partial y^2}\right)^2. \tag{1.17}$$

The governing equation of beams and plates reads:

$$D_0\boldsymbol{L}u + \rho_0\frac{\partial^2 u}{\partial t^2} = f, \tag{1.18}$$

where $D_0 = EI$ and f is the external load. Assuming a local resonator (n_1, n_2) couples with the substrate structure at the coordinate: $\boldsymbol{x_{n1,n2}} = \boldsymbol{x_c} + \boldsymbol{r_{n1,n2}}$, then the governing equation of a unit cell can be given as:

$$\begin{cases} D_0\boldsymbol{L}u + \rho_0\partial^2 u/\partial t^2 = f\left(\mathbf{x}_{\mathbf{n_1},\mathbf{n_2}}, t\right) \\ m_r\ddot{u}_r + c_r\dot{u}_r + k_r u_r = f_r(t) \\ f_r(t) = \boldsymbol{L_f}u\left(\mathbf{x}_{\mathbf{n_1},\mathbf{n_2}}, t\right) \\ f\left(\mathbf{x}_{\mathbf{n_1},\mathbf{n_2}}, t\right) = \mathbf{P}f_r(t) \end{cases} \tag{1.19}$$

where $\boldsymbol{L_f}$ is the differential operator for boundary forces, P is the transformation matrix for the applied force $f\left(\mathbf{x}_{\mathbf{n_1},\mathbf{n_2}}, t\right)$.

Bloch's theorem originally stemmed from quantum physics for solutions of Schrödinger equation with a periodic potential [14], which was later introduced to elastic wave prop-

agation with periodic configurations. The theorem utilizes the plane wave to represent the wave propagation elastic solids with periodicity [14, 16]. Take an example of the metamaterial beam as shown in Figure 1.4 (a). The undamped differential equation of a unit cell can be discretized into:

$$\tilde{\mathbf{M}}\ddot{\mathbf{u}} + \tilde{\mathbf{K}}\tilde{\mathbf{u}} = \tilde{\mathbf{f}}, \tag{1.20}$$

where $\tilde{\mathbf{M}}$, $\tilde{\mathbf{K}}$, and $\tilde{\mathbf{f}}$ are the mass, stiffness, and force matrices. $\mathbf{u}$ is the coordinate vector. Let $\tilde{\mathbf{u}} = \left[\mathbf{u}_{\mathrm{L}}^{\mathrm{T}}, \mathbf{u}_{\mathrm{I}}^{\mathrm{T}}, \mathbf{u}_{\mathrm{R}}^{\mathrm{T}}, \mathbf{u}_{\mathrm{r}}^{\mathrm{T}}\right]^{\mathrm{T}}$, $\tilde{\mathbf{f}} = \left[\mathbf{f}_{\mathrm{L}}^{\mathrm{T}}, \mathbf{0}, \mathbf{f}_{\mathrm{R}}^{\mathrm{T}}, \mathbf{0}\right]^{\mathrm{T}}$, and the subscripts $\boldsymbol{L}$, $\boldsymbol{I}$, $\boldsymbol{R}$ represent the coordinates at left, inner, and right side of the unit cell. When applying Bloch's theorem, the boundary conditions of a unit cell can be given as:

$$\mathbf{u}_{\mathrm{R}} = e^{-i\kappa a}\mathbf{u}_{\mathrm{L}}, \quad \mathbf{f}_{\mathrm{R}} = -e^{-i\kappa a}\mathbf{f}_{\mathrm{L}}, \tag{1.21}$$

where the wave number $k \in [0, 2\pi]$. If we redefine $\mathbf{u} = \left[\mathbf{u}_{\mathrm{L}}^{\mathrm{T}}, \mathbf{u}_{\mathrm{I}}^{\mathrm{T}}, \mathbf{u}_{\mathrm{r}}^{\mathrm{T}}\right]^{\mathrm{T}}$, $\mathbf{f} = \left[\mathbf{f}_{\mathrm{L}}^{\mathrm{T}}, \mathbf{0}, \mathbf{0}\right]^{\mathrm{T}}$, the boundary conditions can be rewritten as:

$$\tilde{\mathbf{u}} = \mathbf{R}\mathbf{u}, \tag{1.22}$$

where

$$\mathbf{R} = \begin{bmatrix} \mathbf{I} & \mathbf{0} & \mathbf{0} \\ \mathbf{0} & \mathbf{I} & \mathbf{0} \\ e^{-i\kappa a}\mathbf{I} & \mathbf{0} & \mathbf{0} \\ \mathbf{0} & \mathbf{0} & \mathbf{I} \end{bmatrix}. \tag{1.23}$$

In addition, the relationship holds:

$$\mathbf{R}^{\mathrm{H}}\tilde{\mathbf{f}} = \mathbf{0}, \tag{1.24}$$

where H stands for conjugate transpose. And $\mathbf{R}^{\mathrm{H}}\mathbf{R} = \mathbf{I}$ holds due to:

$$\tilde{\mathbf{u}}^{2j+1} = \left(\tilde{\mathbf{u}}\tilde{\mathbf{u}}^{\mathrm{T}}\right)^{j}\tilde{\mathbf{u}} = \left(\mathbf{R}\mathbf{u}\mathbf{u}^{\mathrm{T}}\mathbf{R}^{\mathrm{H}}\right)^{j}\mathbf{R}\mathbf{u} = \mathbf{R}\left(\mathbf{u}\mathbf{u}^{\mathrm{T}}\right)^{j}\mathbf{u} = \mathbf{R}\mathbf{u}^{2j+1}. \tag{1.25}$$

Therefore the coordinate in Eq. 1.20 can be replaced with $\mathbf{u}$:

$$\overline{\mathbf{M}}\ddot{\mathbf{u}} + \overline{\mathbf{K}}\mathbf{u} = \mathbf{0}, \tag{1.26}$$

where $\overline{\mathbf{M}} = \mathbf{R}^{\mathrm{H}}\tilde{\mathbf{M}}\mathbf{R}$, $\overline{\mathbf{K}} = \mathbf{R}^{\mathrm{H}}\tilde{\mathbf{K}}\mathbf{R}$.

By this finite element discretization, Eq. 1.26 can be formulated as an eigenvalue problem in matrix form [17]:

$$|\overline{\mathbf{K}} - \omega^2\overline{\mathbf{M}}| = 0, \tag{1.27}$$

where ω represents the frequency of the wave propagation. The solution to this eigenvalue problem is the so-called band structure or dispersion relationship of a periodic lattice. This representation of the frequency-wavenumber relationship of the traveling wave in the considered periodic medium enables passbands, which allow the freely propagating waves, and bandgaps or stop bands, where forbidden the wave propagation within these frequency ranges [18]. Within bandgaps, the eigenvalue solution of Eq. 1.27 leads to imaginary wave numbers which give the evanescent waves, whose amplitude decays exponentially in the

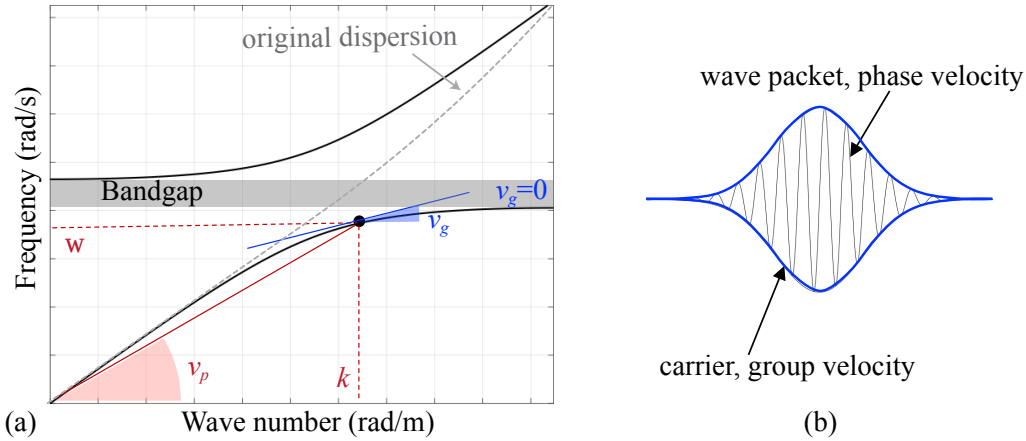

Figure 1.5: (a) Dispersion relationship of a metamaterial beam; (b) Wave packet.

spacial domain [19].

The dispersion relationship of the original Euler-Bernoulli beam is indicated with the gray dash line in Figure 1.5 (a). It can be seen that with local resonators, a frequency range exists without real solutions for wave numbers. This grey region is referred to as a bandgap of a locally resonant metamaterial. Considering their dispersive nature, it is essential to introduce the concepts of phase and group velocity, which can be promptly derived from the dispersion relation. A wave packet consisting of multiple harmonic waves is shown in Figure 1.5(b), where the traveling speed of the individual wave is defined as phase velocity v_p while the traveling speed of the group of these waves is defined as group velocity v_g [19] for the one-dimensional case as:

$$v_p = \frac{\omega}{k}, \quad v_g = \frac{d\omega}{dk}. \tag{1.28}$$

The geometrical interpretation of these velocities is expressed in Figure 1.5 (a). For a frequency-wavenumber pair fixed in the dispersion curve, the phase velocity is the slope of the secant line in red that passes through this point from the dispersion curve to the origin. The group velocity is given for a fixed pair wavenumber-frequency in the dispersion curve as the slope of the tangent line in blue at this point (i.e., of the $\omega(k)$ curve). In a non-dispersive medium, all sinusoidal waves travel with equal speed, and so does their envelope; thus, $v_p = v_g$. On the other hand, in a dispersive system, if each propagating sinusoidal wave moves with a characteristic speed depending on its frequency, then it will result in the wave packet moving with a velocity different from that of the group velocity. Since the group velocity is related to the energy transport of the wave packet, an obvious solution is to look for the case of zero-group velocity waves, which are related to the boundaries of the Brillouin zone [20]. They result from the interference between two identical waves propagating in opposite directions, which forms the typical application of elastic metamaterials for vibration attenuation.

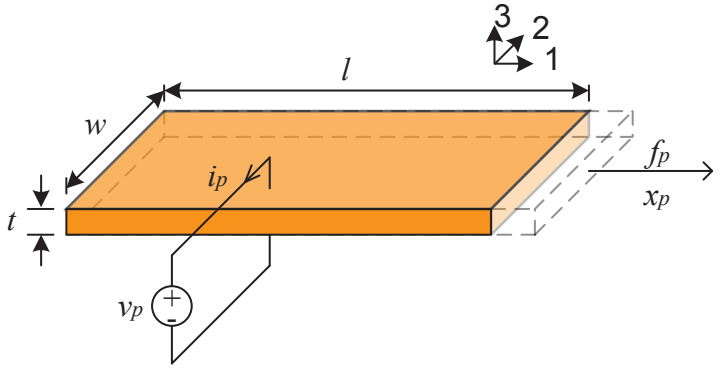

Figure 1.6: Schematic of a piezoelectric patch.

1.2.2 Electromechanical Coupled Piezoelectric Systems

Piezoelectric materials are used in this thesis to guide elastic wave and energy flow in the underlying mechanical systems. These materials, combined with mechanical systems, form electromechanically coupled systems that can achieve multifunctions such as energy harvesting and vibration actuation. This section focuses on the theoretical background of piezoelectric energy harvesting and impedance modeling through piezoelectric interface circuits, particularly those employing synchronized bias-flip techniques [21–23].

Device model of piezoelectric transducers

Piezoelectric materials have direct and inverse piezoelectric effects. Thus they can be used as energy harvesters or vibration actuators to damp or excite vibrations, respectively. In order to analyze the dynamical performance of piezoelectric materials under an electrical field, we can refer to the characteristic equation of piezoelectric materials with the IEEE Standard on Piezoelectricity [24]. Assuming linear deformation, the characteristic equation reads:

$$\begin{bmatrix} T_p \\ D_i \end{bmatrix} = \begin{bmatrix} c_{pq}^E & -e_{kp} \\ e_{iq} & \varepsilon_{ik}^S \end{bmatrix} \begin{bmatrix} S_q \\ E_k \end{bmatrix} \tag{1.29}$$

where T, S, D, and E are stress, strain, electrical displacement, and electrical field; c is the elastic stiffness coefficient; ε is the dielectric constant; e is the piezoelectric constant; the lower labels represent tensor notions of the material; the upper labels indicate the relevant material parameters under a certain applied field. Due to the reciprocity of the characteristic equation, the electromechanical coupling response can be calculated using known material properties and applied stress or electrical field.

Figure 1.6 represents an ideal piezoelectric device. If a mechanical load is applied along 1 direction on the cross section, there will be an electrical signal generated along 3 direction. Assume the length of piezoelectric material is much larger than the scattering wavelength, and the stress, strain, and electrical displacement are evenly distributed along the material. The relationships of these physical parameters can be given as:

$$f_p = twT_1, \quad x_p = lS_1, \quad v_p = -tE_3, \quad q_p = wlD_3 \tag{1.30}$$

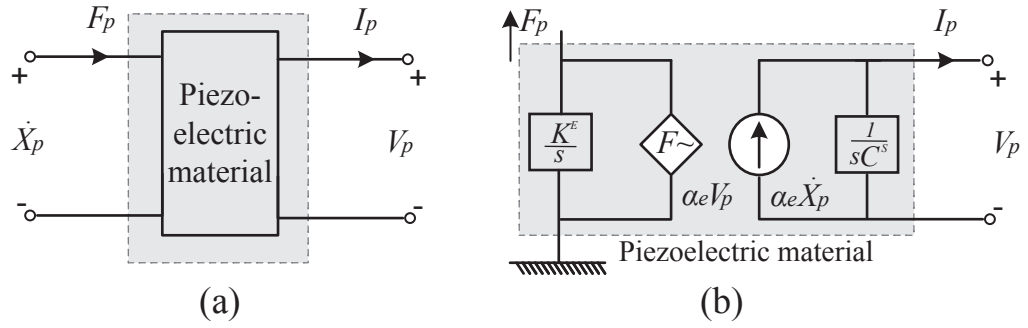

Figure 1.7: The two-port network of a piezoelectric transducer.

where f_p and x_p are the applied force and displacement along 1 direction; v_p and q_p are the generated voltage and charge along 3 direction due to the direct piezoelectric effect. Through these relationships, the macroscopic piezoelectric equation can be derived from the case:

$$\begin{bmatrix} f_p \\ q_p \end{bmatrix} = \begin{bmatrix} \frac{tw}{l} c_{11}^E & we_{31} \\ we_{31} & -\frac{wl}{t}\varepsilon_{33}^S \end{bmatrix} \begin{bmatrix} x_p \\ v_p \end{bmatrix} \tag{1.31}$$

In order to introduce dynamical responses, we can replace the charge q_p and displacement x_p with their derivatives as:

$$i_p = \frac{dq_p}{dt}, \quad \dot{x}_p = \frac{dx_p}{dt}, \tag{1.32}$$

where i_p and $\dot{x}_p$ are the current and velocity. By Laplace transform, the piezoelectric equation can be represented in Laplace domain as:

$$\begin{bmatrix} F_p \\ I_p \end{bmatrix} = \begin{bmatrix} K^E/s & \alpha_e \\ \alpha_e & -sC^s \end{bmatrix} \begin{bmatrix} X_p \\ V_p \end{bmatrix} \tag{1.33}$$

where F_p, I_p, X_p, and V_p are the amplitudes of these parameters. K^E, c^E, and α_e are the short circuit stiffness, clamped capacitance, and electromechanical coupling factor of the piezoelectric material.

As shown in Figure 1.7 (a), we can employ a two-port network to describe the dynamical performance of piezoelectric materials due to the bidirectional energy conversion ability between mechanical energy and electricity [25, 21]. Two-port networks can assemble the systems with their partial external parameters without considering the details in the coupling "black box", which transforms the system into easier representations and extracts the system as external parameters. A piezoelectric energy harvesting (PEH)system can be represented by four variables, which include two cross-variables (velocity and voltage) and two through variables (force and current).

Figure 1.7 (b) illustrates Eq. 1.33 with the input and output of the piezoelectric transducer. The left side stands for the external force F_p, which equals the internal forces from the mechanical domain and electrically induced forces. The right side indicates the output current I_p, which equals the current flowing through the mechanical impedance and the clamped capacitance. This two-port network forms the basis of an electromechanical coupling system, allowing the equivalent impedance of an arbitrary circuit to be

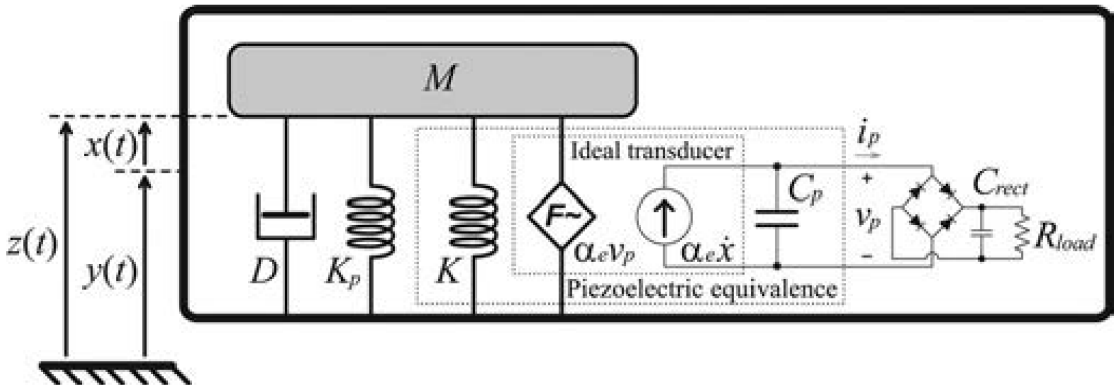

Figure 1.8: Equivalent model of a PEH system [21].

transformed to either side of the network. This enables the study of electrically induced dynamics by transforming electrical impedance into the mechanical domain or exploring bandwidth and power performance by transforming mechanical components into the electrical domain. From an energy perspective, this two-port network also shows the possibility of bidirectional energy flows in this electromechanical coupled system, which features the direct piezoelectric effect for energy harvesting and the inverse piezoelectric effect for vibration actuating.

Equivalent circuit of PEH systems

The previously mentioned two-port network forms the energy conversion model for piezoelectric materials. This section further introduces practical interface circuits to form an equivalent model of a PEH system [21]. A typical PEH system comprises a piezoelectric cantilever beam and an interface circuit, as shown in Figure 1.8. Under base excitation, the mechanical part of the system can be considered a single degree of freedom (SDOF) oscillator around the frequency of its first bending mode. M, D, K, and K_p are the equivalent mass, damping, mechanical stiffness, and short circuit stiffness of the piezoelectric cantilever. C_p, v_p, i_p, and α_e are the clamped capacitance, piezoelectric voltage, piezoelectric current, and the electromechanical coupling factor of the piezoelectric transducer. $\ddot{y}(t)$ is the sinusoidal base excitation acceleration. $x(t)$ is the relative displacement of the energy harvester versus the base. For the power supply of DC loads, the standard method is to utilize a full bridge rectifier to regulate the AC input. As shown in Figure 1.8, the standard energy harvesting (SEH) circuit is connected with a storage capacitor to regulate the input voltage, store the harvested energy, and power the load represented with R_{load}. The governing equation of this SDOF energy harvester can be given as [21]:

$$\begin{cases} M\ddot{x}(t) + D\dot{x}(t) + (K + K_p)\, x(t) + \alpha_e v_p(t) = -M\ddot{y}(t), \\ i_p(t) = \alpha_e \dot{x}(t) - C_p \dot{v}_p(t), \end{cases} \tag{1.34}$$

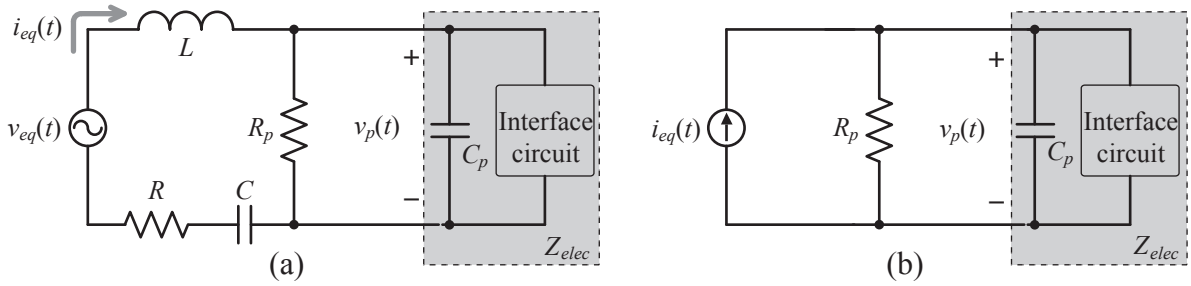

Figure 1.9: Equivalent circuit of PEH system. (a) Strongly coupled model. (b) Weakly coupled model.

where the electromechanical relationships read:

$$\begin{aligned} v_{\mathrm{eq}}(t) &= -\frac{M}{\alpha_e}\ddot{y}(t), \\ i_{\mathrm{eq}}(t) &= \alpha_e \dot{x}(t), \\ L &= \frac{M}{\alpha_e^2}, \\ R &= \frac{D}{\alpha_e^2}, \\ C &= \frac{\alpha_e^2}{K + K_p}, \end{aligned} \tag{1.35}$$

by combining these equations:

$$\begin{aligned} v_{eq}(t) &= L\frac{di_{eq}(t)}{dt} + Ri_{eq}(t) + \frac{1}{C}\int_0^t i_{eq}(t)dt + v_p(t), \\ i_{eq}(t) &= i_p(t) + C_p\dot{v}_p(t). \end{aligned} \tag{1.36}$$

The governing equations of a PEH system in the electrical domain are shown in Eq. 1.36, and its equivalent circuit model is illustrated in Figure 1.9. Here, v_{eq}, R, L, and C represent the equivalent sinusoidal voltage source of the base excitation, equivalent resistance for the damping of the cantilever, and equivalent reactance for the stiffness and mass of the cantilever, respectively. The piezoelectric interface circuit combined with the clamped capacitance C_p are equivalent to the electrical impedance Z_{elec}. Therefore, for different interface circuits, the equivalent impedance Z_{elec} is different, which inspires the application of impedance matching methods to evaluate the power and bandwidth performance of the PEH system. In addition, a leakage resistance R_p is introduced to describe the charge leakage of the clamped capacitor and correct the dielectric loss of a PEH system.

Compared with the fully coupled model in Figure 1.9 (a), the weakly coupled model in Figure 1.9 (b) describes the situation where the electromechanical coupling factor is relatively small, and the electrically induced damping and stiffness can be neglected [21]. Thus, the vibration amplitude of the harvester would not be influenced by interface circuits. We can use a single current source proportional to the velocity amplitude as the

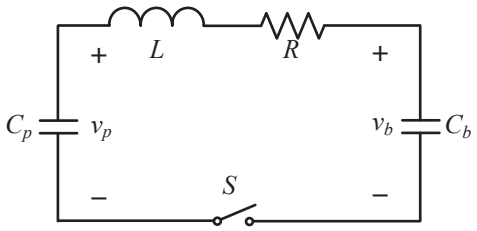

Figure 1.10: RLC resonance circuit.

mechanical energy source. For a PEH system, there are generally two experimental types of excitation methods: (1) Excitation with constant acceleration and (2) Excitation with constant displacement [26]. Under constant displacement, the amplitudes of displacement and velocity remain the same due to the feedback control of the shaker. Thus, the weakly coupled model is more suitable. However, the coupling effect matters significantly for real applications and dynamics tuning with interface circuits. We will adopt the fully coupled model for analyses in the following parts of this thesis.

Synchronized voltage flip circuits

Synchronized voltage flip circuits utilize the LC resonance to flip the piezoelectric voltage v_p at the current crossing zero point [27, 28]. Compared to conventional SEH circuits, this technology regulates the piezoelectric voltage and synchronizes it with the piezoelectric current to increase energy harvesting efficiency. It can be seen in Figure 1.10, the bias capacitor C_b offers a bias voltage v_b for the bias-flip action carried by clamped capacitor C_p and inductor L. R stands for the parasitic resistance of the inductor, and the switch S controls the LC resonance. Assuming a large capacitance of C_b compared with C_p, v_b can be regarded as constant during the bias-flip process. Through Kirchhoff's KVL law, the second-order ordinary equation of this bias-flip circuit reads:

$$v_p(t) = V_b + rC_p\dot{v}_p(t) + LC_p\ddot{v}_p(t). \tag{1.37}$$

Based on the principle of bias-flip actions, the initial conditions of this ordinary equation are set to be maximum v_p with zero inductor current:

$$\begin{aligned} v_p(t)|_{t=0} &= V_0, \\ C_p\dot{v}_p(t)|_{t=0} &= 0. \end{aligned} \tag{1.38}$$

with underdamped conditions, the piezoelectric voltage response of this second-order circuit can be solved as:

$$v_p(t) = V_0 \cos\left(\frac{\pi}{\tau}t\right) e^{-\xi\pi/\sqrt{1-\xi^2}} + V_b, \tag{1.39}$$

where

$$\begin{aligned} \xi &= \frac{R}{2}\sqrt{\frac{C_p}{L}}, \\ \tau &= \pi\sqrt{LC_P}, \end{aligned} \tag{1.40}$$

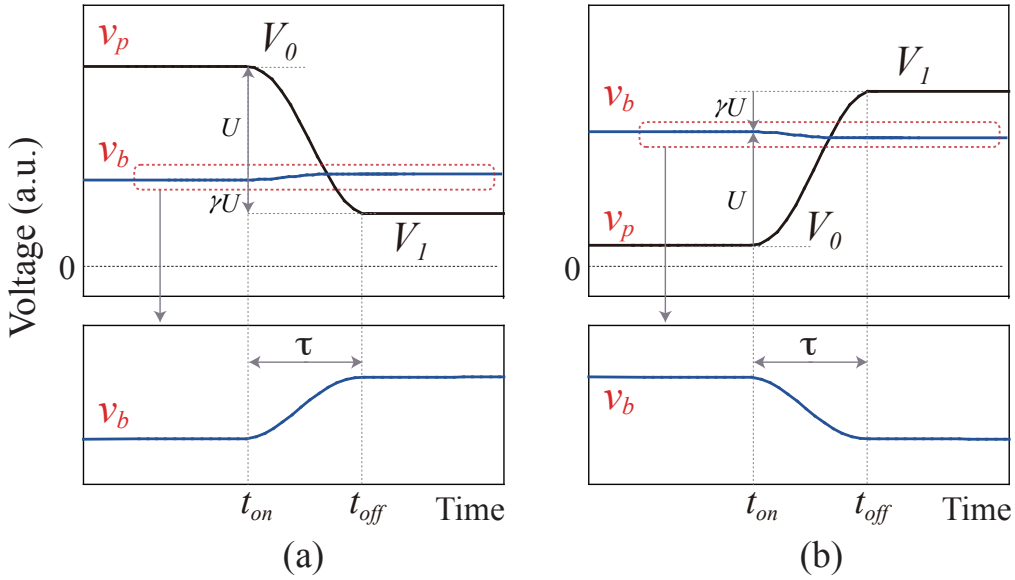

Figure 1.11: Voltage waveform of bias-flip. (a) Passive bias-flip action; (b) Active bias-flip action.

represent the damping ratio and half cycle of this second-order oscillating system, respectively.

The waveforms of piezoelectric voltage during the bias-flip actions are shown in Figure 1.11, where γ represents the flip factor defined by the ratio between the difference of piezoelectric voltage V_1 after the bias-flip and the difference of piezoelectric voltage V_0 before the bias-flip, both with respect to the bias voltage V_b. To achieve the maximum bias-flip result, the bias-flip should end at half the LC resonance period, meaning the switch is conducted for time τ, and the voltage after the bias-flip can be represented as:

$$V_1 = -V_0 e^{-\xi\pi/\sqrt{1-\xi^2}} + V_b, \tag{1.41}$$

where the flip factor is defined as:

$$\gamma \triangleq \frac{V_1 - V_b}{V_0 - V_b} = -e^{-\xi\pi/\sqrt{1-\xi^2}}. \tag{1.42}$$

It can be seen that the damping ratio ξ greatly influences the flip factor, which means the loss in the conducting path matters significantly for bias-flip-based circuits. To achieve better bias-flip actions, inductors with small parasitic losses are recommended.

In bias-flip actions, there exist passive and active bias-flips according to the inward or outward energy flow with respect to the bias capacitor C_b [29], as indicated in Figure 1.11 (a) and (b). Take an example of energy input in C_b; this part of the energy can be represented by charge movement as:

$$\Delta E_b = \Delta Q V_b = C_p(1-\gamma)UV_b. \tag{1.43}$$

It can be seen that the energy income for C_b is determined by the sign of UV_b, which means

the energy can flow from C_p through the inductor to bias capacitor C_b and vice versa. Positive ΔE_b indicates passive bias-flip and energy flow for energy harvesting; negative ΔE_b indicates active bias-flip and reverse energy flow for energy injection or vibration actuation [30] to boost the energy harvesting efficiency by increase the displacement amplitude.

In addition to the harvested energy, there also exists dissipated energy due to the bias flip. This part of energy loss is given as:

$$E_{d,flip} = \frac{1}{2} C_p U^2 \left(1 - \gamma^2\right), \tag{1.44}$$

where the flip factor γ influences the loss. By increasing the flip factor, the dissipated energy can be reduced. During the bias-flip action, the net energy change of the clamped capacitor reads:

$$\Delta E_{C_p} = \frac{1}{2} C_p \left(V_0^2 - V_1^2\right). \tag{1.45}$$

By quantifying different energy flows, the energy harvesting efficiency and equivalent impedance of different circuit typologies can be calculated, which serve as essential methods for analyses of the interface circuits of PEH systems.

Based on the principle of the bias-flip actions, we further discuss the synchronized electrical charge extraction (SECE) [28] circuit as an example. Compared with conventional synchronized switching harvesting on inductor (SSHI) [27] circuit, SECE has the advantage of simplified topology and load independence. Therefore, there's no need for impedance matching to offer a stable power output.

The circuit topology of SECE is shown in Figure 1.12, which includes a full-bridge rectifier and a buck-boost converter from a power electronics perspective. It remains open circuit during the majority of the vibration cycle, and takes actions during the current crossing zero points which are refereed as synchronized instants. At each synchronized instant, the integral of the piezoelectric current i_{eq} is reset to zero due to the charge extraction, whose voltage flip action at the current failing down edge is shown in Figure 1.12. SECE works on DCM (discontinuous conducting mode) while it differs from the conventional PWM (pulse width modulation) controlled buck-boost converter in restricting mechanical local displacement maximums or velocity minimums [31].

The operation of SECE during the positive current half-cycle can be separated into three phases [22]: Open Circuit Phase, Extraction Phase, and Freewheeling Phase, as shown from Figure 1.12 (a) to (c).

Open Circuit Phase: Figure 1.12 (a) shows the conduction path during the open circuit phase in red. The duration of this phase is approximately half of the vibration period. Switch S and diode D are in the off-state. Therefore, the SECE circuit does not take any action during this phase. v_p is the integration of the current i_{eq} starting from an initial voltage of zero, as highlighted in red in Figure 1.12 (d) and (e).

Extraction Phase: When the displacement of the piezoelectric beam reaches its maximum value, switch S is turned on for slightly more than a quarter of the $L_i C_p$ oscillation period,

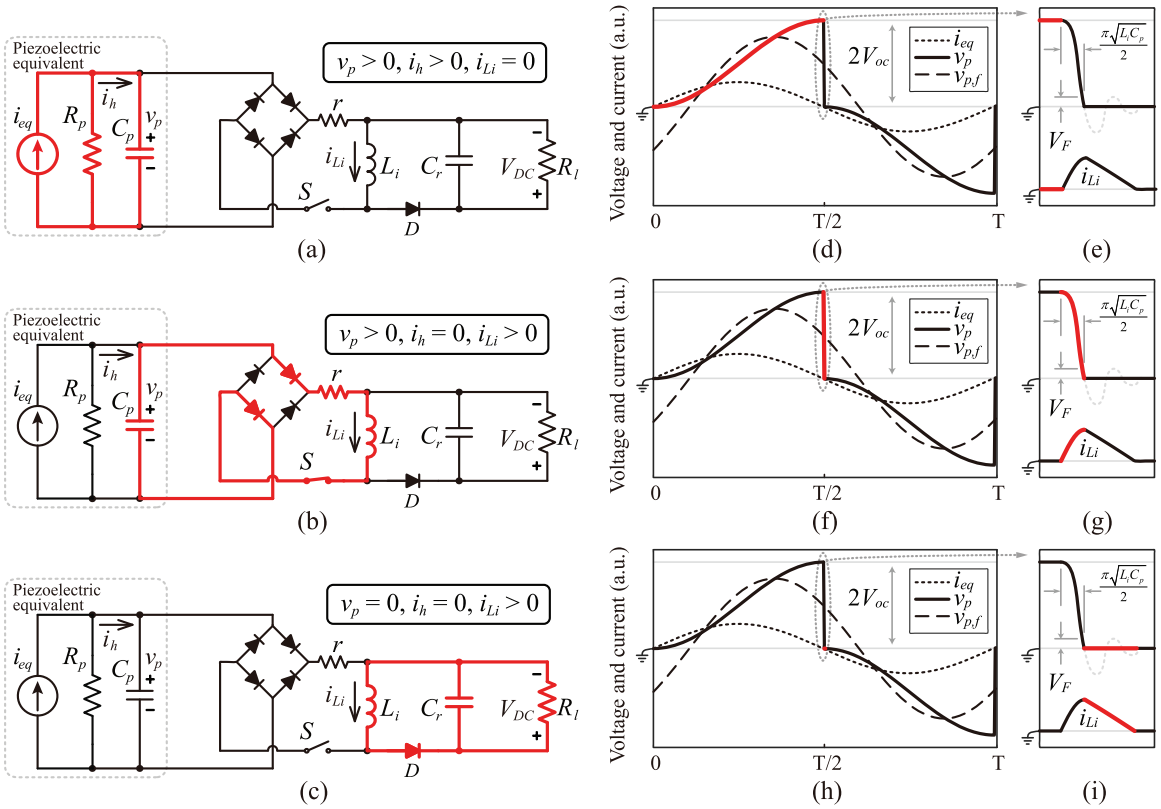

Figure 1.12: The circuit topology of (a)-(c) and characteristic waveforms (d)-(i) of a vibration cycle of SECE [22].

thus activating the switching phase. The conduction path during the extraction phase is highlighted in red in Figure 1.12 (b). During this phase, C_p and L_i form an LC circuit, through which the energy stored in C_p is rapidly transferred to L_i. Since the voltage v_p is proportional to the charge stored in C_p, v_p immediately drops to zero a quarter period after the L_iC_p cycle, as shown by the red curve in Figure 1.12 (f) and (g). Strictly speaking, after a quarter period of the L_iC_p oscillation, v_p drops to twice the forward conduction voltage of the diode. The conduction interval of S is designed to be slightly longer than a quarter period to ensure that C_p is completely discharged. When v_p reaches zero, the rectifier automatically stops extracting the charge. After this conduction period, most of the energy stored in C_p is transferred to L_i, while the remaining energy is dissipated at resistor r, equivalent to the equivalent series resistance (ESR) of the switch branch.

Freewheeling Phase: After the switching phase, switch S is opened, and the energy accumulated in L_i is transferred to the filter capacitor C_r through the continuation diode D. C_r is designed to be much larger than C_p to provide a DC output voltage for the load resistor R_1. The conduction path during this phase is highlighted in red in Figure 1.12 (c). Since the conduction paths are not connected to the piezoelectric source, they do not affect the piezoelectric elements. In other words, the source and load are decoupled through the intermediate inductor L_i. This decoupling function is very similar to the Buck-Boost DC-DC converter in power electronics, with the difference being that SECE converts AC to DC here. Since the piezoelectric patches do not participate in this phase,

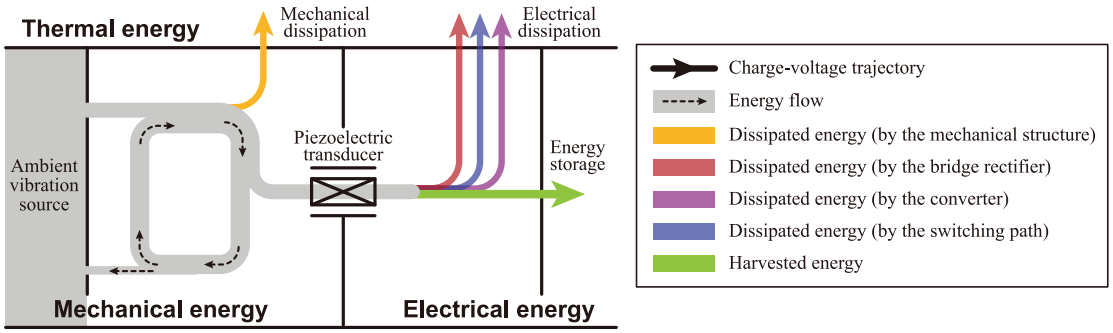

Figure 1.13: Detailed energy flow chart in SECE [22].

it has no effect on the piezoelectric voltage v_p. The corresponding waveforms are shown in Figure 1.12 (h) and (i). The continuation diode D stops conducting until the current i_{Li} drops to zero, as shown in Figure 1.12 (i).

In the other half of the vibration cycle, that is, when $i_{eq} < 0$, the operation can also be divided into three phases, which are the opposite of those in the positive current half-cycle. As shown in Figure 1.12, from the distribution diagram of the piezoelectric voltage v_p, we can find that it has the same sign as the current source i_{eq} throughout the vibration cycle; hence, the power extracted from the mechanical source is always positive. Given the decoupling relationship between the source and the load, the waveform of v_p does not change under different load conditions, thus giving SECE the load-independent feature.

The general energy flow of a PEH system based on SECE is shown in Figure 1.13. Mechanical energy enters the PEH system from the surrounding vibration source and cycles between kinetic and potential energy within the mechanical resonance [32], as shown by the grey loop. In the case of resonance, no energy returns from the resonator back to the energy source, while in non-resonant conditions, the energy of the incoming reactive component (equivalent mass or stiffness) returns to the energy source. During the vibration process, some mechanical energy is dissipated (converted into thermal energy) due to mechanical damping, as shown by the orange branch in Figure 1.13. The piezoelectric transducer converts some of the mechanical energy into electrical energy. In SECE, since no energy returns from the electrical part to the mechanical part, the converted energy is merely extracted from the mechanical part. The extracted energy usually has two destinations. A part of it is converted into usable electrical energy that can be stored, called the harvested electrical energy. The harvested energy is represented by the green arrow. During power regulation, the rest of the extracted energy is dissipated, that is, converted into heat. This dissipation is caused by three reasons: the non-zero forward voltage drop V_F in the bridge rectifier, whose corresponding energy branch is represented by the red arrow in the figure; the parasitic ESR r in the L_iC_p cycle, whose corresponding energy branch is indicated by the blue arrow; the non-zero V_D in the converter's continuation path, whose corresponding energy branch is represented by the purple arrow.

Through a detailed description of the energy flow, we can have a more comprehensive understanding of the issue of the extracted energy not being equal to the harvested energy. The total extraction is usually related to the loss factor, which evaluates the damping effect [21]. However, increasing the extracted energy does not guarantee better harvesting

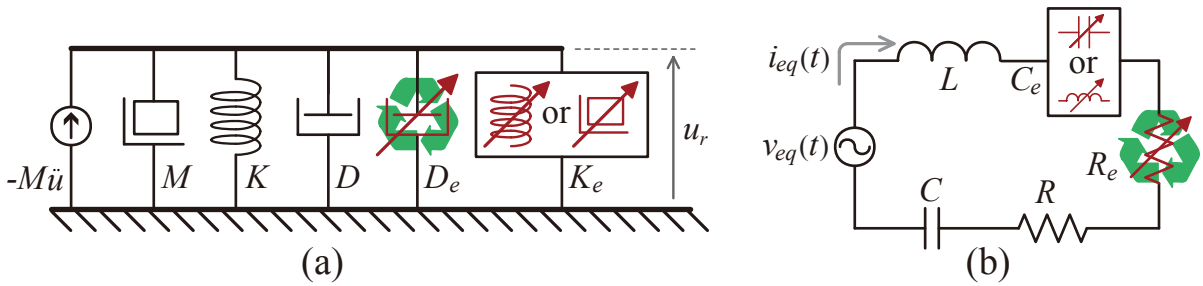

Figure 1.14: A Electromechanical coupled resonator. (a) The mechanical schematic; (b) The electrical schematic.

performance. The design should be carried out by taking the harvested energy or power as the optimization objective.

1.2.3 Multifunctional Metamaterials

Based on the principles of the locally resonant metamaterials and piezoelectric interface circuits discussed above, we can combine the two areas for multifunctional metamaterials to guide the elastic wave and energy in these electromechanical systems. Given the flexibility and tunability of interface circuits, programmable electrically induced impedance can be achieved by tuning the load, phase, and other circuit parameters. Additionally, piezoelectric transducers can convert electrical resistance and reactance into mechanical damping and stiffness. This capability allows for the utilization of elastic energy from wave propagation or the alteration of wave propagation through electrically induced components.

For a mechanical resonator with a general piezoelectric interface circuit, its governing equation in the Laplace domain can be obtained with reference to Eq. 1.16 and Eq. 1.34 as:

$$\begin{cases} s^2 M U_r + s D U_r + K U_r + \alpha_e V_p = F, \\ I_p = s\alpha_e U_r - s C_p V_p. \end{cases} \tag{1.46}$$

Substitute the second line in Eq. 1.46 into the first line, it reads:

$$F = \left(Z_m + \alpha_e^2 Z_e\right) s U_r, \quad Z_e = \frac{1}{s C_p + I_p / V_p}, \tag{1.47}$$

where Z_m and Z_e are the impedance from the mechanical resonator and the piezoelectric interface circuit. Their detailed expressions are given as:

$$\begin{cases} Z_m(\omega) = D + j(\omega M - K/\omega), \\ Z_e(\omega) = D_e - jK_e/\omega = 1/(sC_p + I_p/V_p). \end{cases} \tag{1.48}$$

It can be seen that the equivalent impedance Z_e is the parallel impedance of the clamped capacitor C_p and the interface circuit. If we first neglect the leakage resistance R_p in Figure 1.9, and assume harmonic solution for the wave propagation, the real and imaginary parts of Z_e will give rise to the electrically induced damping D_e and stiffness K_e in Figure 1.14

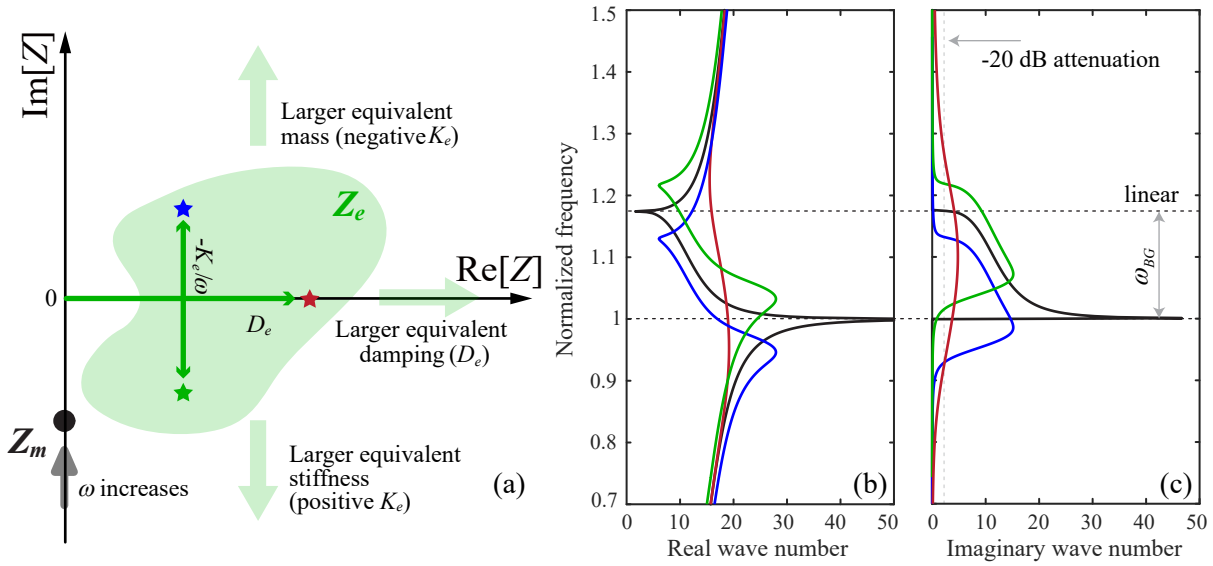

Figure 1.15: Multifunctional metamaterials enabled by piezoelectric interface circuits. (a) A plane of general equivalent impedance from the mechanical resonator and the interface circuit; (b) The dispersion curves considering the electrically induced damping and stiffness.

(a), the relationship reads [33]:

$$D_e = \alpha_e^2 \,\mathrm{Re}[Z_e], \quad K_e = -\alpha_e^2 \omega \,\mathrm{Im}[Z_e]. \tag{1.49}$$

As shown in Figure 1.14, the interface circuits introduce additional damping and stiffness to the original mechanical resonator. Therefore, the updated governing equation of an electromechanical coupled resonator is:

$$M\ddot{u}_r + (D + D_e)\,\dot{u}_r + (K + K_e)\,u_r = -M\ddot{u}. \tag{1.50}$$

By combining the equations of a metamaterial beam, the governing equation of a multifunctional metamaterial beam can be obtained as:

$$\begin{cases} D_0 \boldsymbol{L} u + \rho_0 \partial^2 u/\partial t^2 = -\rho_0 \ddot{u}_b + \sum_{j=1}^{S} f_j \delta\left(x - x_j\right), \\ M\left(\ddot{u}_{rj} + \ddot{u} + \ddot{u}_b\right) = -\left(K + K_e\right) u_{rj} - \left(D + D_e\right) \dot{u}_{rj} = f_j, \end{cases} \tag{1.51}$$

where S stands for the total number of local resonators attached to the host beam at position x_j. And $\ddot{u}_b$ is the external acceleration. For low-frequency elastic wave propagation, the lattice constant a in Figure 1.4 (a) is sufficiently smaller than the wavelength of the elastic wave. Thus, the wave profile between two adjacent unit cells can be approximated by a smooth function by neglecting the near-field scattering around the local resonators. Thus, we can utilize the averaging technique from the homogenization method [34] and transform the concentrated reaction force of the local resonator with the Dirac function δ into a uniformly distributed force f_j applied evenly along the unit cell. The simplified

equations read:

$$\begin{cases} D_0 \boldsymbol{L} u + \rho_0 \partial^2 u / \partial t^2 = -\rho_0 \ddot{u}_b - f_j, \\ M\left(\ddot{u}_{rj} + \ddot{u} + \ddot{u}_b\right) = -\left(K + K_e\right) u_{rj} - \left(D + D_e\right) \dot{u}_{rj} = a f_j, \end{cases} \tag{1.52}$$

By applying the fundamental harmonic wave propagation as $u = Ue^{\mathrm{i}(\omega t - kx)}$ and neglecting the external force, the dispersion relationship of a multifunctional metamaterial beam reads:

$$k(\omega) = \left[\left(\rho_0 + \frac{K + K_e + \mathrm{i}(D + D_e)\omega}{a\left(\omega_r^2 - \omega^2 + \mathrm{i}(D + D_e)\omega / M\right)} \right) \frac{\omega^2}{D_0} \right]^{\frac{1}{4}}, \tag{1.53}$$

where ω_r represents the resonant frequency of the local resonator. By introducing the piezoelectric interface circuits, the original mechanical metamaterials can enable multiple functions:

- **Wave attenuation**: As shown with the black dispersion curves in Figure 1.15 (b) and (c), the wave propagation will be attenuated within the frequency bandgap induced by local resonators.
- **Bandgap shifting**: As shown with blue and green stars in Figure 1.15 (a) and their corresponding blue and green dispersion curves in Figure 1.15 (b) and (c), the bandgap of the metamaterial beam can be shifted downwards and upwards through electrically induced negative K_e or positive K_e, thus leading to the resonant frequency shifting of local resonators for broader bandgap ranges.
- **Bandgap broadening**: As shown with red star in Figure 1.15 (a) and the dispersion curves in Figure 1.15 (b) and (c), the bandgap of the metamaterial beam can be broadened by the additional electrically induced damping D_e, which indicates the energy conversion from elastic energy into electricity and thus leads to the damping effect for the metamaterial beam.
- **Energy harvesting**: Based on the electrically induced damping D_e, the absorbed energy by the piezoelectric interface circuits can be regulated into useful power for the power supply of microcontrollers, sensors, and IoT devices.

It should be noted that the tunability of the piezoelectric interface circuits severely depends on the electromechanical coupling factor α_e. If the coupling effect is weak, the attainable range of electrically induced components is relatively limited, impeding the effects on wave propagation and energy conversion.

The previous discussion on multifunctional metamaterials with piezoelectric interface circuits mainly focuses on elastic wave propagation through the dispersion analysis. To demonstrate the applications listed, here we further discuss the energy harvesting function of multifunctional metamaterials with piezoelectric interface circuits. Compared to the conventional energy harvesters based on simple structures like cantilever beams, the metamaterials own the advantage of wave manipulation abilities, thus enabling the possibilities to guide, redirect, or focus the elastic wave in the desired position under certain frequency ranges. Thus, the topic of piezoelectric energy harvesting with mechanical

structures utilizing metamaterial concepts has gained enormous attention during the last decade [35–38]. Take the example of a metamaterial beam with piezoelectric cantilever beams for energy harvesting [39]; the piezoelectric output voltage and harvested power depend on the displacement amplitudes of the local resonators. Therefore, here we briefly mention the method of separation of variables, also called mode superpositioning, to solve the governing equation Eq. 1.51. The transverse displacement of the host beam can be approximated as:

$$u(x,t) = \sum_{i=1}^{N} \eta_i(t)\phi_i(x), \tag{1.54}$$

where N is the number of modes considered. η and ϕ represent the modal coordinate and the mode shape. By substituting this ansatz of solution into Eq. 1.51 and apply orthogonality relationships with respect to mode shapes, the relative displacement amplitude of jth local resonator can be expressed as:

$$U_{rj} = \frac{\omega^2 U_b + \omega^2 \sum_{n=1}^{N} H_n \phi_n(x_j)}{(1 + K_e/K)\,\omega_r^2 + \mathrm{i}2\,(1 + D_e/D)\,\zeta_r \omega_r \omega - \omega^2}, \tag{1.55}$$

where U_b and H_n represent the amplitude of the harmonic excitation and the nth modal amplitude, respectively. Recall the electromechanical analogy in Eq. 1.35, the equivalent current of jth piezoelectric energy harvester reads:

$$I_{eq,j} = \alpha_e \omega U_{rj}. \tag{1.56}$$

With reference to the equivalent circuit illustrated in Figure 1.14(b), the total harvested power from the local resonators can be formulated as:

$$P_h = \sum_{j=1}^{S} \eta_{h,j} \frac{I_{eq,j}^2}{2} R_{e,j}, \tag{1.57}$$

where $\eta_{h,j}$ is the efficiency of a particular piezoelectric interface circuit considering the energy loss from leakage resistance, diode conduction, and MOSFET (Metal Oxide Semiconductor Field Effect Transistor) switching.

An example of a metamaterial beam for piezoelectric energy harvesting is shown in Figure 1.16, the blue line represents the tip transmissibility of the metamaterial beam with local resonators as piezoelectric energy harvesters. Due to the presence of the local resonators, a frequency bandgap star exists that ranges from 54 Hz to 92 Hz. By adding the SECE interface circuits discussed in Figure 1.12, the total harvested power is shown with the green curve. It can be seen that at the beginning of the bandgap, the resonance of the local resonators not only leads to the bandgap for vibration attenuation, but the total harvested power also increases around this resonant frequency. It should be noted that there are other power peaks that correspond to the modal frequencies due to the boundary condition of the metamaterial beam. By introducing piezoelectric material and interface circuit, the otherwise reflected mechanical energy is harvested as a power supply for further electrical devices while maintaining the original function for wave attenuation. The multifunctions

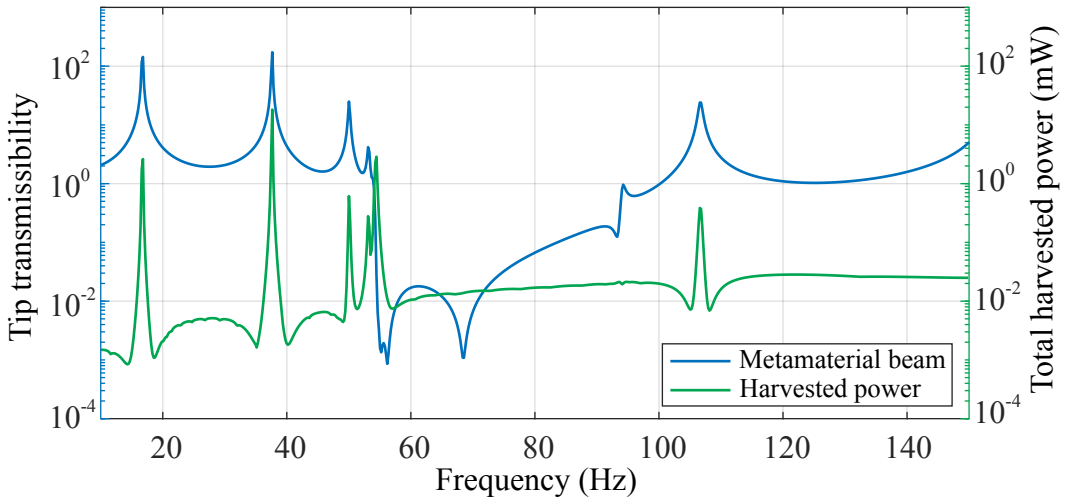

Figure 1.16: A case study of a metamaterial beam for piezoelectric energy harvesting, which shows the tip transmissibility and total harvested power.

enabled by piezoelectric coupling have provoked much research in this direction to utilize mechanical energy [40]. However, limited by the same resonant frequency of the local resonators, the bandwidth of the power performance is narrow. In order to broaden the energy harvesting bandwidth, we have proposed a graded metamaterial design, which will be discussed in detail in Chapter 2.

1.3 State of the Art and Open Challenges

The design paradigm of mechanical structures has shifted from trial-and-error iterations to demand-guided and goal-oriented designs that capitalize on mechanics, electronics, and computations principles. By tailoring the mechanical response of elastic systems, it is possible to instill beneficial traits such as resilience to vibrations and impacts. With the recent thrust of semiconductors and IoT devices, the definition of mechanical metamaterials extends beyond conventional wave propagation concepts, which are restricted to bandgap ranges. New concepts, such as electromechanical and nonlinear coupling effects, have emerged to fulfill the demands for multifunctional systems. These allow for tunable wave attenuation and guiding, energy harvesting and signal sensing, and active control and actuation interacting with vibrations and elastic wave propagation.

This section provides an overview of recent breakthroughs in elastic wave control and energy conversion achieved through electromechanical coupling or nonlinearities for multifunctional mechanical systems. The discussion follows the overarching structure of the thesis outlined in Section 1.5 with a focus on mechanical metamaterials: the two main classes of mechanical systems, passive and active systems, are reviewed separately for their novel functions involving wave attenuation and guiding, energy harvesting and signal sensing, and active control and actuation.

1.3.1 Mechanical Systems for Wave Attenuation and Guiding

Since 2000, **locally resonant metamaterials** [5] have emerged as a promising field for manipulating acoustic and elastic waves. Different from the concept of photonic crystals [8, 41], locally resonant metamaterials depend on the anti-phase vibration of local resonators within the bandgap range rather than the Bragg scattering mechanism depends on the ratio of the lattice constant and the propagation wavelength. Thus, the sub-wavelength or the low-frequency bandgap can be enabled by tuning local resonators. Specifically, the low-frequency ranges include kilo-hertz to ten-hertz level vibrations of structural components, hertz-level vibrations of architected buildings and bridges, or even sub-hertz level seismic waves from earthquakes.

Research in this area conventionally applies mainly mechanical or architected structures, such as tuned mass dampers [42], base-isolation resonators [43], and seismic barriers Meseguer et al. [44]. These local resonators are typically unable to change after installation, which limit the flexibility considering wave propagation outside the designed frequency range of the bandgap. Unlike conventional approaches, novel locally resonant metamaterials have recently employed mechanisms such as multiphysics coupling, nonlinear dynamics, wave trapping and conversion, and topological features to manipulate wave attenuation or waveguides.

Concerning the elastic wave propagation in structural components, two main aspects of the research are being pursued: wave attenuation and waveguiding. Here, we briefly discuss the recent thrusts in these two aspects, focusing on flexural wave propagation.

Wave attenuation in structural mechanics involves mitigating traveling waves or standing waves in structural components. Conventional methods include tuned mass dampers [42], nonlinear vibration absorbers [49], electromechanical shunting [50], and multiple dynamical vibration absorbers [51]. With the progress of locally resonant metamaterials, wave mitigation has shifted from single frequency or narrow band into bandgap or broadband mitigation. The early research in this direction covers simple theoretical models, i.e., the lumped parameter model of diatomic lattice chain [52], to continuum elastic systems as metamaterials, i.e., beams and plates with identical local resonators [40].

Following the track towards broadband and flexibility of metamaterials, recent endeavors, as shown in Figure 1.17, have applied coupling effects such as electromechanical coupling or nonlinear dynamics in the locally resonant metamaterial. Two main mechanisms are applied for electromechanical coupling effects: piezoelectric coupling and electromagnetic coupling. Compared with electromagnetic coupling, piezoelectric coupling has the advantage of high power density and ease of integration. Thus, piezoelectric coupled metamaterials have gained much attention since the last decade [40, 45, 53, 54]. Among these, Sugino et al. [55, 45, 46] have contributed a series of research work on the piezoelectric coupled locally resonant metamaterials. As shown in Figure 1.17 (a), Sugino et al. [45] have replaced the local resonator with a piezoelectric coupled circuit, so-called synthetic impedance circuit, to create an equivalent impedance/transfer function in the electrical domain, which reflects the effect of a single degree of freedom oscillator in the mechanical domain. By programming the analog circuit, different equivalent "local resonators" can be achieved in an electrical manner, which releases the potential of electromechanical

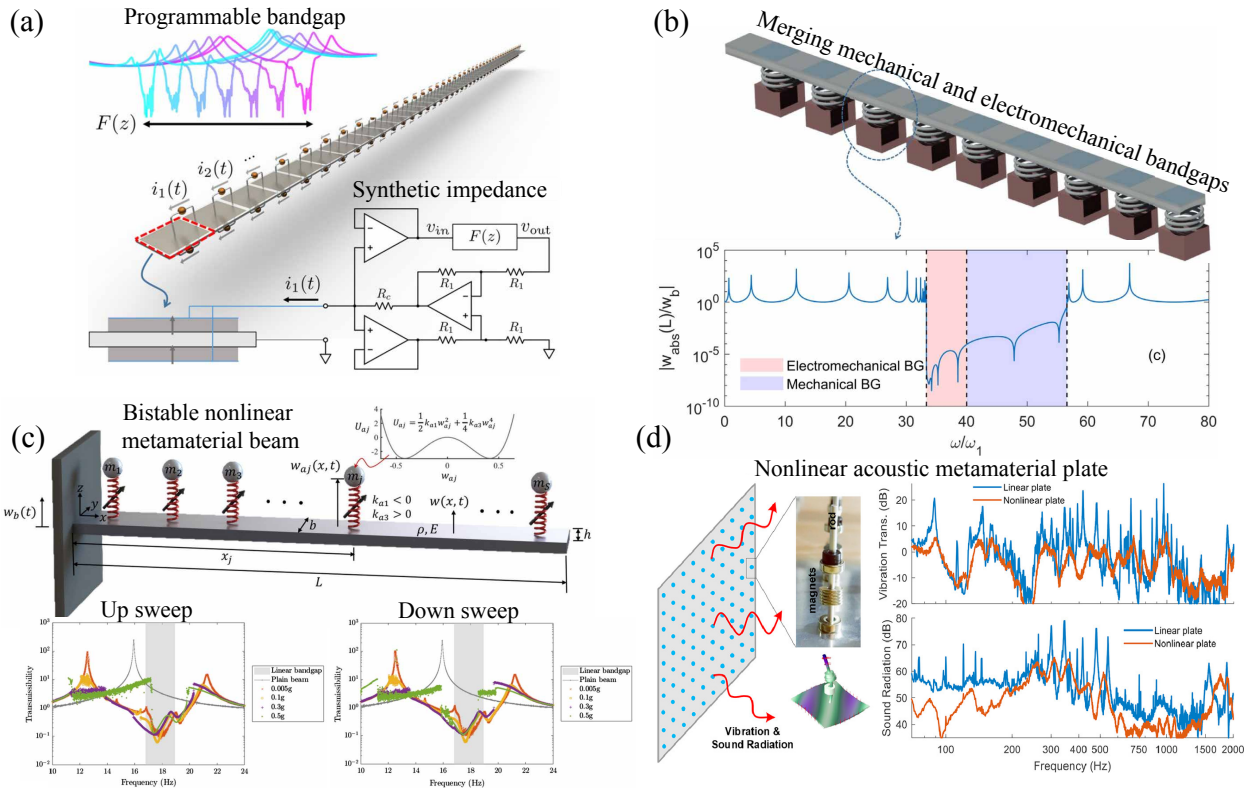

Figure 1.17: Metamaterials for wave attenuation. (a) Programmable bandgap by synthetic impedance circuit (Adapted from Ref. [45]); (b) Merging bandgaps from mechanical and electrical domains (Adapted from Ref. [46]); (c) Nonlinear metamaterial by bistable local resonators (Adapted from Ref. [47]); (d) Nonlinear metamaterial plate for elastic and acoustic wave attenuation (Adapted from Ref. [48]).

coupling in wave attenuation and waveguides. Different bandgap ranges can be realized by tuning the electrically induced mass or stiffness, as discussed in Section 1.2.3.

Based on this work, Sugino et al. [46] combine this idea with the original locally resonant metamaterial beam [55]. Conventionally, multiple local resonant bandgaps are often realized by different groups of resonators with different resonant frequencies [56] or the same local resonators but with multiple degrees of freedom [57]. Instead of complex designs of local resonators, electromechanical coupling offers a convenient and tunable method for broadening the original mechanical bandgap. As shown in Figure 1.17 (b), by tuning the electrically induced bandgap, a merging effect of the electrically induced bandgap and the original mechanical bandgap can be achieved, which significantly broadens the overall bandgap range from elastic wave attenuation. And due to the tunability of the coupling circuits, the electrically induced bandgap also preserves its ability for shifting as shown in Figure 1.17 (a), which further offers more flexibility for the frequency range of propagating wave outside the original design bandgap range.

Similarly to electromechanical coupling, nonlinearity can also enable novel wave control mechanisms. The study of nonlinear dynamics dates back to the early 19th century when Poincaré first studied the three-body problem in celestial dynamical systems [58], which inspired the work of Duffing and Van der Pol for their contribution to nonlinear structural dynamics with the well known Duffing equation [59] and Van der Pol equation [60]. For

the single resonator level, there exists extensive research on how the nonlinearities can interact with the structural dynamics, i.e., the coupling with mode shapes. Unlike linear dynamical systems, nonlinear dynamical systems essentially couple multiple coordinates of the system under different excitation levels, leading to the so-called harmonic generations and chaotic motions for energy transfer and exchange [61]. These characteristics are particularly useful for wave attenuation and are recently introduced into locally resonant metamaterials [62, 47, 48, 63, 64].

As shown in Figure 1.17 (a), Xia et al. [47] proposed a nonlinear bistable metamaterial beam for broadband wave attenuation. This paper introduces the cubic nonlinearity by a magnet-repulsive force, which enables nonlinear reaction forces to be applied to the host cantilever beam. Under relatively high input excitation, the bistable bifurcation of local resonators causes multiple branches of bandgaps, which broaden the bandgap with the stiffening effect of local resonators. It should be noted that the nonlinearity phenomena are usually amplitude-dependent, which means the motion of the traveling wave in the host system and the vibration of the local resonators also rely on the input amplitudes. For example, higher harmonic waves may exist except for the fundamental frequency of the traveling wave in the dynamical system, which forms the typical periodic waveform for nonlinear periodic motions. Further increase of the input amplitude could also lead to chaotic motions of nonlinear local resonators, as shown in Figure 1.17 (b), where multiple frequency components are mixed, and limit cycles can not be distinguished anymore. As suggested by Fang et al. [48], the chaotic motion of local resonators leads to the so-called chaotic bandgap for local resonant metamaterials beyond the attainable ranges induced by hysteresis range of the nonlinear local resonators. The application of nonlinearities in metamaterials spans from static [65] to dynamical systems [66] and differs in forms such as nonlinear stiffness [47], nonlinear damping [67], vibro-impact [68], and contact dynamics [69], which open novel opportunities for nonlinear metamaterials to reach the wave attenuation ranges beyond the conventional linear limits.

Wave guiding as the second application of metamaterials features multiple wave manipulation functions such as negative refraction, focusing, trapping, steering, and lensing [70]. Adding auxiliary local resonators can alter the effective medium along the wave propagation direction, stimulating wave guides to change directions. Figure 1.18 lists a few typical waveguide metamaterials. Colombi et al. [71] proposed a geophysical scale study of the graded metamaterial indicated in Figure 1.18 (a). It can be seen that by gradual change of the rod length, different resonant frequencies can form a gradual change of impedance to trap the incoming waveguide from the left side and convert the surface wave into a bulk wave from the right side. Compared with the classical local resonant metamaterials with identical local resonators, the graded design offers a broader bandgap due to the gradual change of resonant frequency, which is known as the rainbow trapping effect originated from electromagnetism [72] and further in acoustics [73]. With the graded design, different frequency components can be trapped and localized at different positions of the local resonators, which behaves like a mechanical filter both in frequency and spatial domain. Drawing by this founding, further investigations have raised in Rayleigh and Love wave guiding [74, 37, 75] and energy harvesting [38, 76, 54].

Different from the graded design mentioned above, Figure 1.18 (b) and (c) feature an-

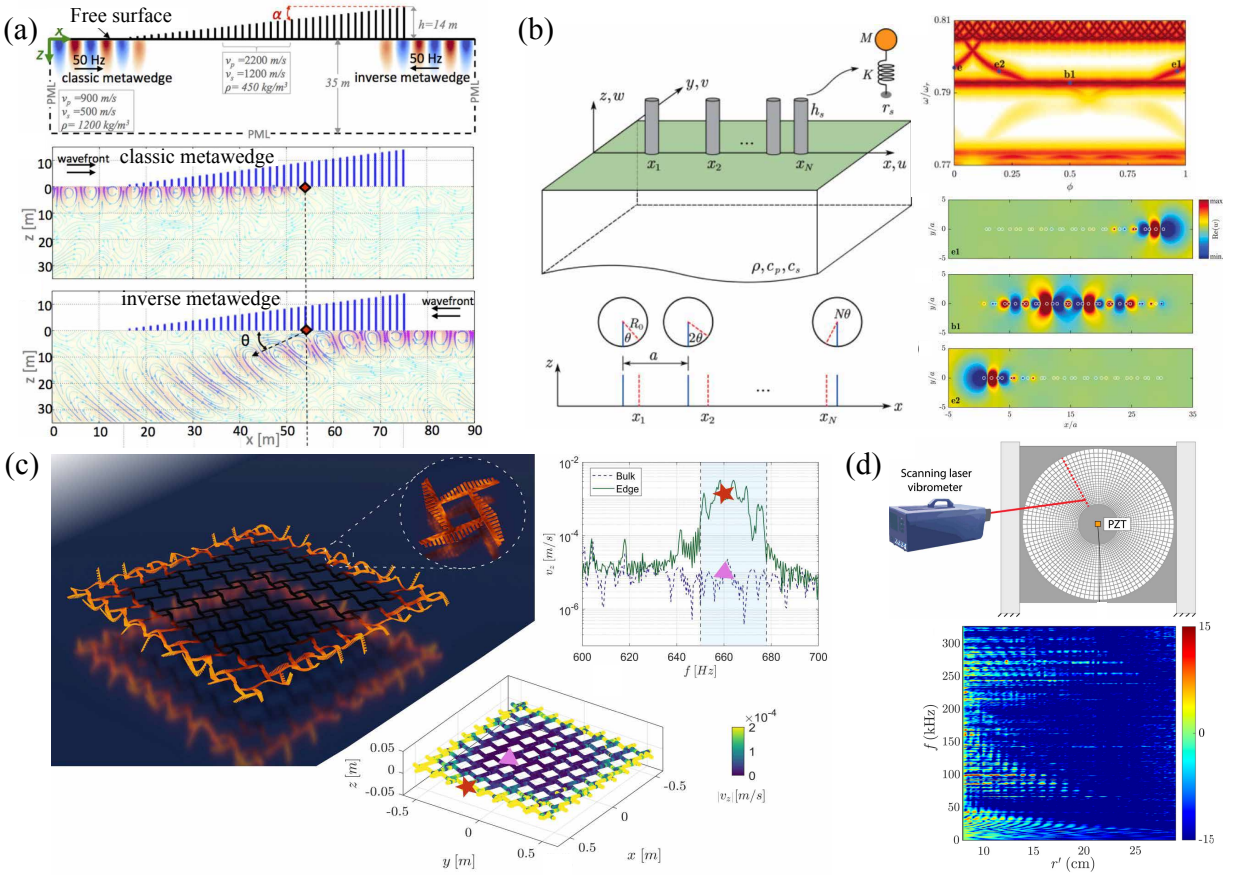

Figure 1.18: Metamaterials for waveguiding. Graded metamaterial for wave trapping and conversion (Adapted from Ref. [71]); (b) Topological edge states for wave focusing (Adapted from Ref. [77]); (c) Topological edge waves with a graded design (Adapted from Ref. [78]); (d) Conformal graded metamaterial for wave guides (Adapted from Ref. [79]).

other class of method for waveguides in locally resonant metamaterials, which involves the topological invariant of these systems. Compared with the periodic arrangement of photonic-like lattices, the quasi-periodic lattice has gained enormous attention with the findings in quasicrystals [80]. By manipulating the symmetry in space, quasiperiodic structures enable the topological effects such as quantum spin Hall effect and quantum valley Hall effect, which extend the periodic arrangements with the so-called defect-immune topological interface modes [77, 78].

Figure 1.18 (b) shows a typical configuration of a quasiperiodic topological metamaterial, where the position of the local resonators no longer follows a fixed lattice constant but with a quasiperiodic pattern [77], where the periodic arrangement can be regarded as a particular case of a trivial quasiperiodic arrangement. The interest of this topic lies in the rich spectral properties, such as edge states, which can be regarded as low dimensional projections from the higher dimensions described by the quasiperiodicity and their invariance determined associated with the nontrivial bandgaps. In Figure 1.18 (b), Pu et al. [77] studied Rayleigh-like edge modes spanning the nontrivial gaps of a finite cluster of resonators. By tuning the quasiperiodic phase, they have shown that these edge modes can be used for wave pumping by transferring the elastic energy from one boundary to

the opposite.

In Figure 1.18 (b), the symmetry breaking happens with spin-orbit interactions, which leads to the quantum spin Hall effect. In Figure 1.18 (c), De Ponti et al. [78] leveraged the quantum valley Hall effect with the breaking of space inversion symmetry, which permits easier applications of wave controls. This study utilizes a tetrarchical lattice with a graded design, which possesses tunable topological states with graded arrays of masses within each unit cell. By doing so, they realized different topological edge waves with different frequency inputs, which can precisely direct the elastic wave and energy to the desired position of the structure, which could be a potential candidate for vibration isolation, energy harvesting, and lossless signal transport for sensing applications.

The aforementioned mechanical systems for wave attenuation or wave guides rely on the periodic or quasiperiodic arrangements of unit cells, where the bandgaps are formed, leading to the opening of dispersion curves and non-intersecting dispersion surfaces. However, periodic-like arrangements are not necessary conditions to forbid wave propagation. Recent studies suggest that it is possible to have non-intersecting dispersion surfaces that are not separated by a bandgap [79]. Thus, attenuation is also possible in the absence of a bandgap. In Figure 1.18 (d), Dorn and Kochmann [79] realized a conformal mapped graded metamaterial with a non-periodic design. By the scaled conformal mapping, a nonperiodic arrangement can also support non-intersecting dispersion surfaces where wave propagation is forbidden. According to the adiabatic theorem, high-frequency waves cannot propagate along trajectories with significant changes in unit cell size [81]. This idea inspires the design with grading and thus leads to the forbidden region in the spatial-frequency plot in Figure 1.18 (d), where no wave propagation can exist around the outer range of the transformed graded metamaterial where the unit size is relatively large. Except for this example of non-periodic metamaterial for wave guiding, there also exist other studies, such as aperiodic [82] and disordered [83] metamaterials for more novel mechanisms on elastic waveguiding.

Research gap and open challenges

The extensive research over the past decade on wave attenuation and wave guiding via mechanical systems, especially mechanical metamaterials, demonstrate the remarkable progress made in this direction. However, some open questions and challenges also need to be tackled. Given the broad frequency range of ambient vibration, designing a mechanical system that can be tuned with external control or by itself to fit the frequency range still remains a prominent challenge. Considering the existing solution of electromechanical coupling or nonlinear designs, the coupling effect or nonlinear effect within the mechanical system should be boosted for more effective wave attenuation and waveguiding. Furthermore, novel theoretical methods and numerical tools should be developed, given these coupling or nonlinear dynamics problems are often difficult or time-consuming for commercial software and existing numerical tools. Last but not least, to control and manipulate elastic waves for low-frequency, the devices need to be scaled but with limited size from practical perspectives when considering the local resonant or Bragg scattering mechanisms. Thus, novel mechanisms, such as non-periodic or effective media designs, besides conventional ones, should be investigated for structural and mechanical applica-

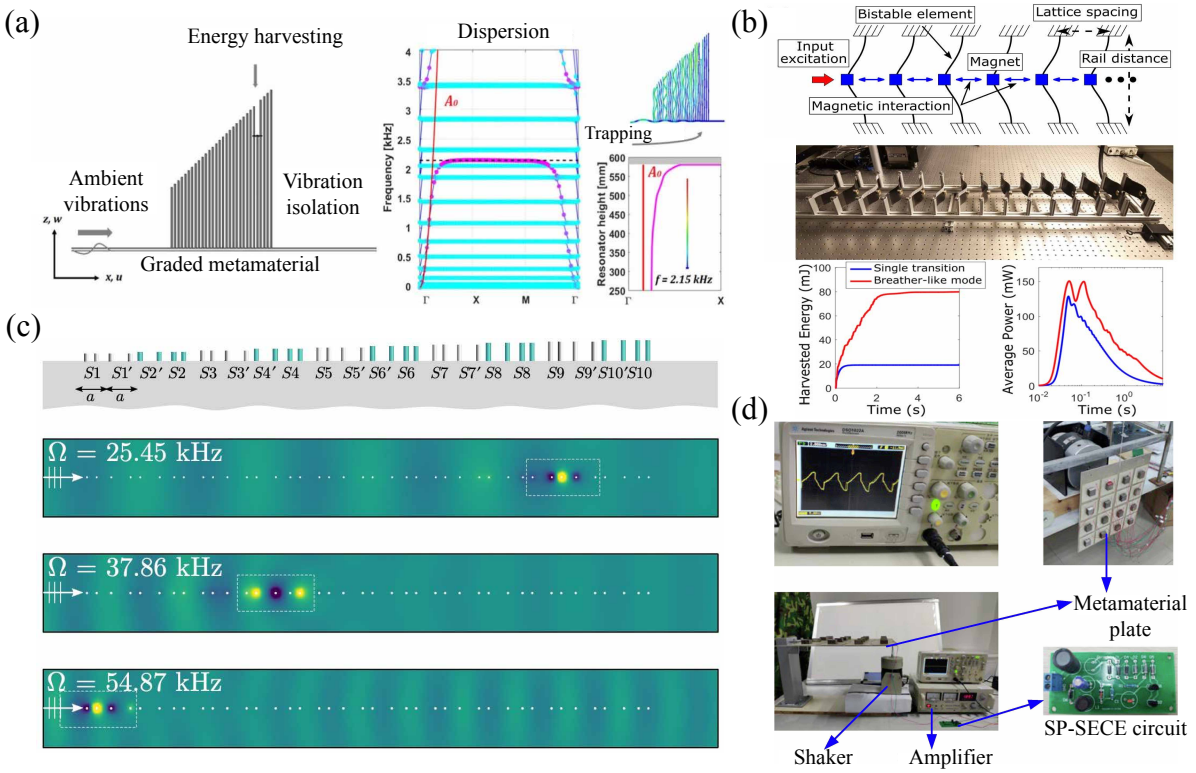

Figure 1.19: Metamaterials for energy harvesting. (a) Graded metamaterial for energy harvesting (Adapted from Ref. [85]); (b) Nonlinear bistable lattice (Adapted from Ref. [86]); (c) Topological graded metamaterial (Adapted from Ref. [87]); (d) Piezoelectric metamaterial plate (Adapted from Ref. [53]).

tions.

1.3.2 Mechanical Systems for Energy Harvesting and Sensing

Mechanical systems under loads, such as harmonic, broadband, and random excitation, can present dynamical responses. By means of electromechanical and electromagnetic coupling materials, the mechanical energy can be further utilized for energy harvesting to power wireless sensor nodes or signal sensing to collect vibrational or environmental data, which makes use of renewable energy sources and saves the need for conventional chemical batteries. Owing to their outstanding abilities to manipulate elastic waves and guide mechanical energy, mechanical metamaterials have been applied in these domains since the last decade [40]. In order to adapt to this new trend, there have been developments in the relative fields such as electrical interface circuits [23], dynamics methods to increase mechanical energy density and bandwidth [84], and novel mechanisms to convert vibrations and waves into digital signals. To demonstrate the application of mechanical systems in energy conversion, two areas are predominantly leveraged: energy harvesting and signal sensing.

Energy harvesting has a long history that dates back to the last century when electromagnetism enabled the invention of the generator, which unleashed the potential energy

with hydroelectric power generation. Different from electromagnetic power generation, the application of piezoelectric materials for energy harvesting began in the later 90s last century [88] with the development of semiconductors and power electronics. However, the piezoelectric energy harvesting devices remained in low-degree-of-freedom mechanical systems in early 2000, which employed mechanical systems such as cantilever beams [21] and nonlinear bistable beams [89]. Since the last decade, the application of metamaterials for energy harvesting has gained significant attention due to the wave-manipulating abilities of metamaterials beyond conventional mechanical systems. As shown in Figure 1.19 (a), De Ponti et al. [38] have introduced the graded metamaterial, which was originally used for broadband wave attenuation into piezoelectric energy harvesting considering the rainbow energy trapping ability, which slows down the group velocity of the traveling flexural wave and enables longer interaction time with the local resonators to harvest more mechanical energy. Compared to the early studies to utilize the identical local resonators [40], the graded design makes full use of all local resonators by trapping the wave energy at different frequencies. In contrast, for the prior case, only the first few resonators can be used for energy harvesting since the wave is forbidden to travel inside the metamaterial.

Based on a similar idea, this separation of frequency concept is further expanded into topological metamaterials as shown in Figure 1.19 (c), Chaplain et al. [87] combined the quasiperiodic metamaterial discussed in Figure 1.18 (b) with the graded design and achieved topological rainbow trapping effect, which supports multiple, simultaneous, topologically protected edge states. Therefore, the multiple edge modes can be used to localize elastic energy at the position of a particular local resonator separated by different frequency ranges, which enables higher energy density for more harvested power, given the stronger localization effect.

These studies indicate that the two main research targets for piezoelectric energy harvesting are (1) Higher harvested power and (2) Broader bandwidth. For the graded metamaterials, the multiple resonant frequencies and slow wave mechanism lead to broad bandwidth and higher harvested power. While the application of topological edge modes further increases the harvested power [87]. Alternatively, we can also turn to nonlinear dynamics, which also gain favor in energy harvesting, considering the hysteresis characteristic of some nonlinearities, such as the bistability and multi-stabilities induced by magnetic forces [90].

As shown in Figure 1.19 (b), Hwang and Arrieta [86] demonstrated a nonlinear bistable lattice for input-independent piezoelectric energy harvesting. The bistable lattice is achieved by buckled beams with magnets attached to transfer the mechanical energy and introduce nonlinearities. Given the cascaded potential wells with different unit cells, a quasi-static or dynamic load on one side of the structure will lead to a soliton wave [61] transmission to the other side. Thus, the mechanical energy can be harvested with the piezoelectric transducers attached to the buckled beams. To further increase the harvested power, they deliberately induced defects for a particular nonlinear oscillator, raising the breather mode localized around the defect position and significantly boosting the harvested power. Compared with conventional nonlinear energy harvesting solutions, this study employed a nonlinear lattice chain to extend the possibilities of novel wave propagation and control mechanisms, which is not limited to the hysteresis range of a single degree of freedom

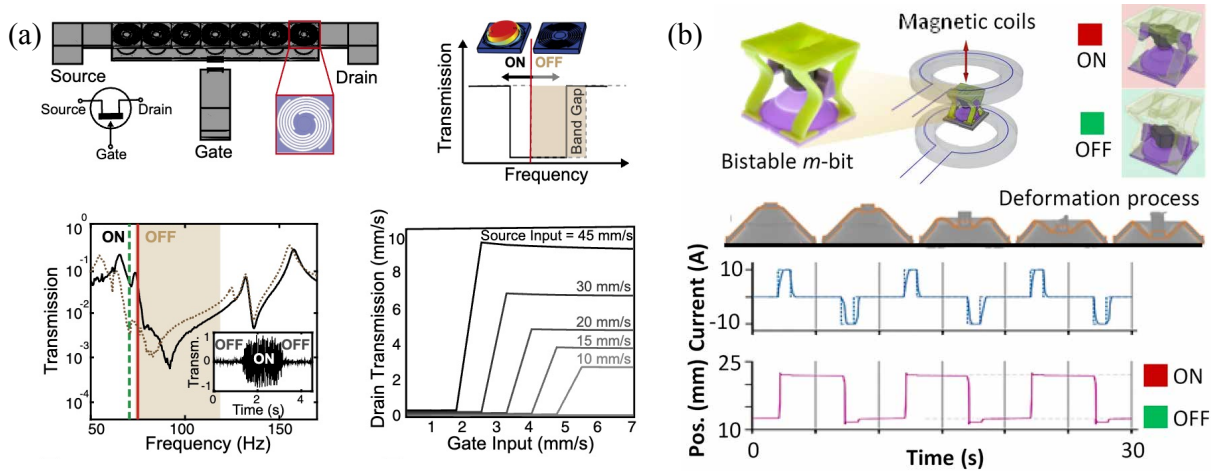

Figure 1.20: Metamaterials for signal sensing. (a) Bistable beam for switching (Adapted from Ref. [92]); (b) Bistable metamaterial for binary memory (Adapted from Ref. [93]).

nonlinear harvester. Further studies from the same group also reveal the frequency conversion mechanism with solitons [91] in a similar setup, in which both low-to-high and high-to-low frequency interactions have been observed. This frequency-independent characteristic of the nonlinear lattice chain significantly broadens the bandwidth for energy harvesting, demonstrating the advantage of nonlinear phenomena in piezoelectric energy harvesting.

The aforementioned studies of mechanical systems for energy harvesting mainly focus on mechanical design and wave manipulation to increase the bandwidth or energy density of mechanical harvesters. However, the mechanical vibrations have an AC (alternating current) form, while different from the DC (direct current) form power supply for an electrical load such as a microcontroller. This neglect of power conversion is actually an essential challenge for energy harvesting with mechanical systems like metamaterials discussed in this thesis. Consider a case when the piezoelectric voltage is around 1 V. It seems the power calculation can be easily delivered by the square of the voltage amplitude over the load resistance. However, when the simplest AC-DC circuit, a full bridge rectifier, is applied for power conversion, this voltage turns out to be insufficient to overcome the forward voltage drop of the two Schottky diodes, thus leading to zero harvested power in practical scenarios. This gap between wave dynamics and power electronics should be addressed by considering both domains together in an application-oriented manner. An early effort in this direction is shown in Figure 1.19 (d), Chen et al. [53] utilized the SECE circuit reviewed in Section 1.2.2 to convert the mechanical vibration into DC voltage. In this study, the harvested power is derived and measured considering the electrically induced damping and stiffness, thus leading to the absorption of the elastic energy into electricity. Further studies in this direction also features the graded metamaterial combined with piezoelectric interface circuits for milliwatt DC harvested power [54], which will be discussed in detail in Section 2.

Signal sensing, in principle, is also an energy conversion process like energy harvesting. However, the difference lies in the information accompanied by the energy flow in the sensing system. For mechanical systems, different forms of signals exist according

to the motion of the system, including static deformation and vibrations (wave propagation). Conventional methods [94] of measuring signals from mechanical systems include strain gauges, optical fibers, accelerometers, and laser Doppler vibrometers. With the recent progress in wave propagation and dynamics, novel mechanisms appear as potential supplements for these conventional signal measuring and processing techniques.

Through the analogy of a MOSFET, Bilal et al. [92] proposed a bistable metamaterial beam as an elastic MOSFET in Figure 1.20 (a). The essential idea behind this is to utilize an external magnetic field to shift the bandgap range of the metamaterial beam by shifting the resonance frequency of the nonlinear local resonators with additional stiffness. Once the bandgap is shifted, some portion of the originally non-propagating frequency will be propagating frequency, which supports the wave traveling from the "Source" to the "Drain" side. Thus, an elastic MOSFET is formed and can be controlled with an external voltage applied to the coils. This analogy with mechanical systems enables elastic wave sensing in the simplest situation, where the on and off represent the propagation and non-propagation waves like an electrically controlled switch. The tunability enabled by nonlinearities offers rich dynamical responses that can be used for sensing. As shown in Figure 1.20 (b), Chen et al. [93] demonstrated a bistable plate that consists of multiple bistable elements with snap-through bistabilities [65]. The two stable states of a nonlinear unit form a digital bit with on and off states described in Figure 1.20 (a). The authors designed an array of these mechanical elements, which forms a 2-D programmable plate, of which each unit is fully elastic and can be reversibly cycled until the system is reprogrammed. Thus, a mechanical bit-map can be achieved and programmed like a hard disk to record the applied deformation upon the loading surface.

The above two examples mainly focus on signal sensing with mechanical systems but with an electrical analogy. Mechanical systems for sensing also exist, but they focus on circuit and system designs. Gao et al. [95] proposed a self-sensing bidirectional energy conversion circuit, which not only can harvest the mechanical energy but can sense the vibration displacement by multiple short-term inductor-capacitor charge transfers during a vibration cycle. This study indicates the potential to combine multifunctions in a single electromechanical coupling system and power itself through the mechanical energy flows into the system, which shields light on multifunctional mechanical systems' design and realization.

Research gap and open challenges

The literature reviewed for energy harvesting and signal sensing in mechanical systems covers both the conversion of mechanical energy into electrical power or signals. Thus, they can be regarded as the same energy conversion process but with different purposes. Regardless of the purpose, the essential consideration is to view the system as a whole, accounting for the coupling effects from both domains. This has raised an important challenge: Most research focuses on one side of the story, which may lead to infeasible designs from an application perspective. The advantages of mechanical metamaterials or nonlinear dynamics should be integrated into energy harvesting or signal sensing functions, which requires novel modeling methods and co-designs of both domains. Furthermore, with the trend of the Internet of Things, there are more opportunities to utilize wave

manipulations or nonlinearities to achieve multifunctionality. This includes considering the rich dynamics inherent in these mechanical systems, which may inspire not only passive functions like wave attenuation, energy harvesting, and sensing but also active functions for actuating and active controls towards smarter and more intelligent systems.

1.3.3 Mechanical Systems for Active Control and Actuation

The application of mechanical systems not only lies in passive functions such as wave manipulation and energy harvesting or sensing but also in active manners. For passive mechanical systems, wave propagation follows the rules of causality and reciprocity, which limit the effective operating bandwidth of these devices. Furthermore, mechanical or electrical damping strongly influences the efficiency of passive systems, particularly resonator-based metamaterials.

To mitigate these limits, the active mechanical systems have been extensively studied over the last decade, allowing the breaking of causality, passivity, and reciprocity [96, 97]. The active mechanical systems include non-passivity, nonlinearity, and time dependence, generally realized by coupling with piezoelectric materials, electromagnetic materials, and electrical circuits and motors. Take an example in Figure 1.21 (a), Wang et al. [98] proposed a spatiotemporal modulated by an external magnetic field with a linear elastic beam based on magnetically tunable resonators. By additional modulated stiffness through external magnetic reaction forces, multiple harmonics and asymmetric dispersion curves can be generated with respect to the spatial domain, yielding non-reciprocal wave transmission as shown in Figure 1.21 (a).

Besides spatiotemporal modulation, activity can also be introduced as gain and loss into the mechanical system. For example, external circuit actuation can enable asymmetric deformations along the two sides of a sensing position, which introduces shear stress. In Figure 1.21 (b), Chen et al. demonstrated [99] the so-called odd elasticity through this active control, allowing for unidirectional amplification and attenuation of wave propagation through the metamaterial beam.

The scope of active mechanical systems also includes the applications of nonlinear structures. As shown in the previous literature, nonlinear oscillators have broader bandwidth advantage when the system presents the hysteresis. However, this effect also leads to a problem when considering the bifurcation, which includes the solution with lower displacement amplitudes unfavorable for energy harvesting. Thus, active control is required to maintain the high amplitude orbit. Figure 1.21 (c) shows a classical active control method proposed by Yu et al. [100]. By shifting the linear stiffness of the nonlinear harvester, i.e., through buckling intensity or magnetic coupling force, the range of the hysteresis is shifted to a higher frequency, making the original state at low amplitude orbit unstable and forcing it to jump up to the high energy orbit. After shifting back to the original stiffness, the oscillator can operate at high amplitude orbits, leading to more harvested power. It can be seen that through active control, the stability of the mechanical system can be tuned at different bifurcation levels. By cascading these bifurcated nonlinear oscillators, nonreciprocal wave transmission can also be realized [101].

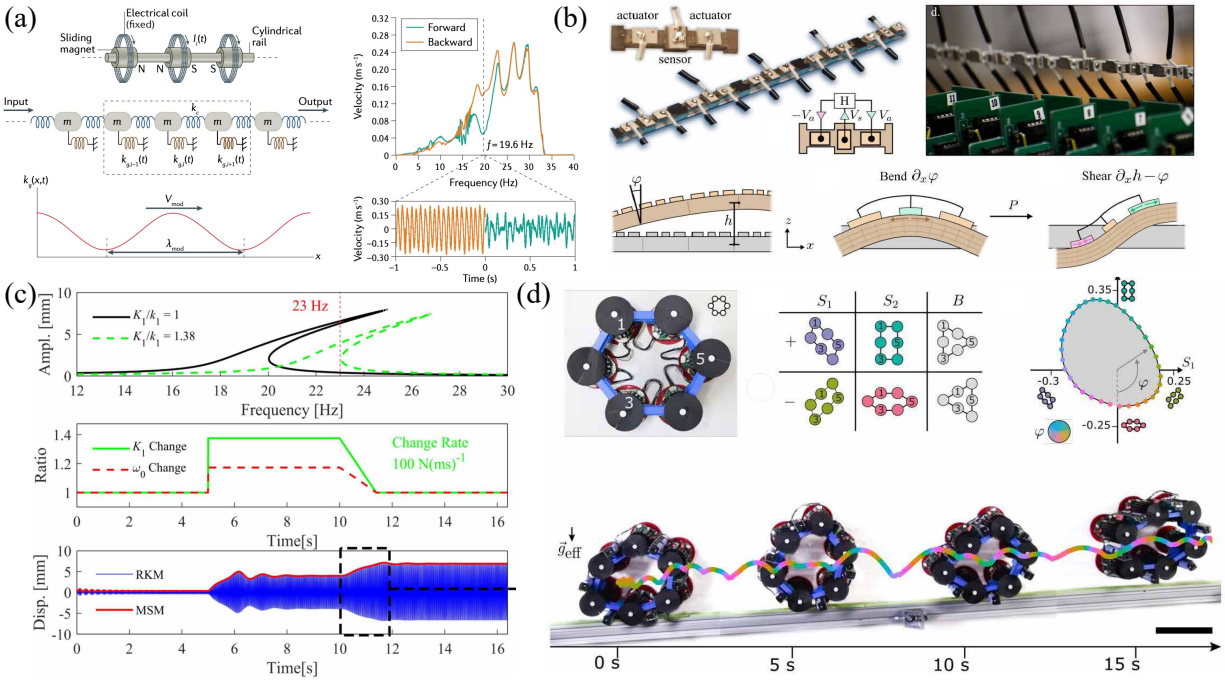

Figure 1.21: Metamaterials for active control and actuation. (a) Nonreciprocal wave through time modulated stiffness (Adapted from Ref. [98]); (b) Active metamaterials with odd elasticity (Adapted from Ref. [99]); (c) Orbit jumps for nonlinear oscillators (Adapted from Ref. [100]); (d) Nonlinear work generating limit cycles power locomotion (Adapted from Ref. [102]).

By combining odd elasticity and nonlinear dynamics mentioned in Figure 1.21 (b) and (c), Brandenbourger et al. [102] created a nonlinear robot driven by a unit cell with the mechanism of odd elasticity, where interaction forces between basic constituents are not constrained to be the gradient of a potential. Hence, by taking the system along a cycle, work is generated. By stability analysis, the nonlinear coupling forces between unit cells of the robot lead to work-generating limit cycles that allow it to roll autonomously with its deformation. This demonstrates how active mechanical systems and stabilities can create self-constrained motion beyond the conventional mechanism for actuating and driving.

Research gap and open challenges

All of the above works reveal the potential of active mechanical systems in controlling wave propagation and structural dynamics, serving as counterparts to the passive systems discussed previously. This research track, which seeks to combine wave dynamics with active coupling methods, is still in its infancy. On the one hand, the potential of the underlying mechanisms originating from optics, electromagnetism, and quantum mechanics is not fully revealed in elastic wave propagation and dynamics. Properly guiding the energy flows in these active systems could lead to self-powered, self-sensed, and self-controlled autonomous structures and systems. On the other hand, existing active mechanical systems heavily depend on external devices like digital signal processors, amplifiers, and data acquisition devices, which impede their practical application. Thus, integrating power electronics with mechanical structures should be explored, significantly

boosting the compactness and functionalities of these systems. This integration is a step towards the ultimate goal of autonomous systems that leverage elastic waves for energy harvesting, vibration damping, or dynamics control.

1.4 Thesis Objectives

This dissertation aims to further expand the theoretical methods and practical applications of mechanical systems, especially mechanical metamaterials, with electromechanical coupling designs and nonlinear dynamics to tackle the open challenges anticipated in Section 1.1 and further detailed in Section 1.3. To this end, this work proposes multifunctional mechanical systems to guide elastic wave propagation and the energy flows within the underlying systems. The term "guide" refers to functions such as attenuating waves, focusing, harvesting, dissipating, or utilizing the energy flows carried by wave propagation. Within this framework, the multifunctions of interest are those realized by electromechanical coupling mechanisms and nonlinearities with low-frequency vibrations. These aspects are further elaborated in the three detailed objectives of this thesis:

- Deep fusion of power electronics-based interface circuits with structural dynamics-based mechanical systems for multiple functions.
- Dynamics modeling for electromechanical coupling systems. This includes illustrating electrically induced dynamics and their effects through energy conversion processes within the systems.
- Expanding the application of nonlinearities to waveguiding effects, developing theoretical methods and practical systems for novel waveguiding mechanisms.

A previously developed AC-DC piezoelectric interface circuit is integrated into a graded metamaterial to leverage frequency separation and slow wave effects for broadband and high-capability energy harvesting, while retaining its original wave attenuation function, to fulfill the first objective. This approach simultaneously realizes wave control and energy flow to the electrical domain.

In line with the second goal, electromechanical dynamics are studied in a cubic nonlinear oscillator system. The mechanisms to control nonlinear stabilities with circuits are revealed through the dynamics modeling of interface circuits and the oscillator using the multiple time scales method. This objective involves reversely boosting the harvested energy back to the mechanical systems for dynamics control, offering a self-contained strategy to control energy flow and dynamics in mechanical systems.

The last objective extends the second objective into a continuum nonlinear metamaterial system; the amplitude-dependent bandgap and modal dissipation abilities are studied using an advanced numerical harmonic balance method in the frequency domain. This objective explores how nonlinearities within the systems enable novel energy dissipation and transfer mechanisms beyond their linear counterparts.

1.5 Thesis Outline

The thesis is structured in five chapters containing journal papers produced by the author during the doctoral studies and combined in a comprehensive flow.

In line with the first objective, **Chapter 2** presents a comprehensive analysis and realization of a graded metamaterial-based piezoelectric energy harvesting system. This system combines a graded metamaterial targeting lower frequency vibrations with a self-powered version of the SECE circuit based on power electronics discussed in 4.2. This work takes advantage of graded metamaterials with broad bandwidth and slow wave phenomena, integrating them with an advanced piezoelectric AC-DC interface circuit for improved energy harvesting performance. The proposed system is modeled using a lumped parameter model and numerical simulations to calculate the theoretical harvested power. The wave field amplification and dispersion relationship are verified both theoretically and experimentally. Alongside the original wave attenuation function within the bandgap range, this work extends the energy harvesting range and capability through mechanical and electrical designs, achieving a milliwatt DC power output for the first time. This chapter serves as the initial step in the deep fusion of power electronics and wave dynamics to control wave propagation and energy flow in a mechanical metamaterial system, laying the foundation for further in-depth modeling and control of electromechanical dynamics. This work is published in *Energy Conversion and Management* [54].

Drawing from the second objective, the attention in **Chapter 3** shifts toward circuit solutions for dynamics control in nonlinear energy harvesting systems, complementing **Chapter 2** and focuses on vibration control with the harvested energy. This chapter studies the cubic nonlinearity induced by dipole magnets due to its hysteresis characteristic for broader bandwidth in monostable, bistable, and multistable systems. Operations in high-energy orbits with larger displacement amplitudes are preferred for higher harvested power. A circuit solution with a switched-mode piezoelectric interface circuit is proposed to carry out orbit jumps from low-energy orbits to high-energy orbits. The electrical part is based on the cutting-edge switched-mode bidirectional energy conversion circuit (BECC) proposed by the author in [30], enabling time-sharing dual functions of energy harvesting and vibration excitation. The mechanical part features a monostable/bistable energy harvester as a single-degree-of-freedom nonlinear oscillator. Through impedance analysis of the equivalent circuit and the multiple time scales method, the electromechanical dynamical response in the time domain is revealed in both autonomous and nonautonomous cases. In particular, the influence of negative and positive electrically induced damping is analyzed in this nonlinear system for dynamics control of orbit jumps. Finally, experiments are performed to validate the full-hysteresis-range orbit jumps with the nonlinear energy harvester, resulting in a nine-fold increase in harvested power. The proposed solution refrains from using extra mechanical or electrical energy sources for orbit jumps, leading to the first self-contained solution for simultaneous energy harvesting and orbit jumps in nonlinear piezoelectric energy harvesting. This work enhances the practical utility of nonlinear energy harvesting technologies toward engineering applications and is published in *Mechanical Systems and Signal Processing* [103].

Delving into the investigation of multiple nonlinear oscillators, **Chapter 4** presents a

nonlinear damped metamaterial that combines a linear host cantilever beam with periodically distributed inertia amplifiers as nonlinear local resonators. The nonlinearity studied in this chapter features the geometric nonlinearity induced by the geometry of the inertia amplifiers, causing an amplitude-dependent nonlinear damping effect. Through the implementation of both modal superposition and numerical harmonic balance methods with alternating frequency time and numerical continuation techniques, a numerical method in the frequency domain is established for the analyses of finite nonlinear metamaterial systems. For the particular nonlinear damped metamaterial studied, the results show that the bandgap of the nonlinear metamaterial is both amplitude-dependent and broadened. Furthermore, the nonlinear interaction between the local resonators and the mode shapes of the host beam is discussed, leading to efficient modal frequency dissipation. The theoretical results are validated experimentally. By embedding the nonlinear damping effect into locally resonant metamaterials, wideband and shock wave attenuation are achieved, opening new possibilities for versatile metamaterials with novel nonlinear wave propagation and control mechanisms. This work is published in *Mechanical Systems and Signal Processing* [67].

In **Chapter 5**, a summary of the main findings and contributions of this dissertation is provided, followed by outlooks and perspectives on future developments of this research.

Chapter 2

Graded Metamaterial for Piezoelectric Energy Harvesting

Paper Details

The following chapter was published on October 01, 2022, as:
"**Zhao, B.**, Thomsen, H.R., De Ponti, J.M., Riva, E., Van Damme, B., Bergamini, A., Chatzi, E. and Colombi, A., 2022. A graded metamaterial for broadband and high-capability piezoelectric energy harvesting. *Energy Conversion and Management*, 269, p.116056."
DOI: https://doi.org/10.1016/j.enconman.2022.116056 - Under a Creative Commons license.
This is a post-print version of the article, which differs from the published version only in terms of layout, formatting, and minor amendments that have been implemented in the text to adapt the original paper to the format of the thesis and improve readability.

Author and Co-authors Contributions

The author of this thesis contributed to the physical realization and theoretical explanation of the graded metamaterial for broadband and high-capability piezoelectric energy harvesting in Section 2.1. The mechanical design of the graded metamaterial was initially conceived by Dr. J.M. De Ponti and Dr. A. Colombi and fine-tuned with the author of this thesis for low-frequency vibrations. In addition, he conceived the theoretical and numerical analyses in Section 2.2 and 2.3, based on an electromechanical lumped parameter model and the full-scale 3D COMSOL model. For experimental realizations in Section 2.4, the author of the thesis integrated the metamaterial with self-design interface circuits, he also gained help from Dr. H.R. Thomsen on the laser vibrometer system and from Dr. E. Riva, Dr. B. Bergamini, Dr. B. Van Damme on the experimental setup. Prof. Dr. E. N. Chatzi and Dr. A. Colombi initiated the project and provided overall supervision and guidance.

Key Findings

- Broadband and high capability design targets are achieved under low frequencies.
- The DC power output of the proposed design is evaluated with an integrated model.
- Spatial frequency separation and slow waves in the design are analyzed in detail.
- A near-milliwatt DC power output is realized with metamaterials for the first time.

General comments and link to the next chapter

This study fulfills the first objective of the thesis (see Section 1.4) by integrating the power electronics-based circuit with the locally resonant metamaterials for multiple functions: energy harvesting ($50 \sim 150$ Hz) and vibration attenuation ($50 \sim 300$ Hz). This study realized milliwatt DC power output from the proposed graded metamaterial-based energy harvesting system.
Moreover, this chapter offers a bridge between traditional passive and linear mechanical systems to active and nonlinear mechanical or metamaterial-based systems, as in the case of Chapters 3 and 4.

Abstract

This work proposes a graded metamaterial-based energy harvester integrating the piezoelectric energy harvesting function targeting low-frequency ambient vibrations (¡100 Hz). The harvester combines a graded metamaterial with beam-like resonators, piezoelectric patches, and a self-powered interface circuit for broadband and high-capability energy harvesting. Firstly, an integrated lumped parameter model is derived from both the mechanical and the electrical sides to determine the power performance of the proposed design. Secondly, thorough numerical simulations are carried out to optimise both the grading profile and wave field amplification, as well as to highlight the effects of spatial-frequency separation and the slow-wave phenomenon on energy harvesting performance and efficiency. Finally, experiments with realistic vibration sources validate the theoretical and numerical results from the mechanical and electrical sides. Particularly, the harvested power of the proposed design yields a five-fold increase with respect to conventional harvesting solutions based on single cantilever harvesters. Our results reveal that by bridging the advantages of graded metamaterials with the design targets of piezoelectric energy harvesting, the proposed design shows significant potential for realizing self-powered Internet of Things devices.

2.1 Introduction

Energy harvesting has received considerable attention over the last two decades mainly in the context of transitioning toward the Internet of Things (IoT) architectures with milliwatt-level sensor nodes [25]. The exploration of renewable energy sources not only relates to academic advances, but embraces significant social and economic values [104–106]. Since vibration energy harvesting (VEH) leverages one of the most ubiquitous and accessible energy sources, this research field has tremendous potential to replace conventional, limited-life, chemical batteries for energy-efficient IoT devices. Among different energy transduction methods [107], piezoelectric transduction is commonly used owing to its high power density and ease of integration in the design of compact energy harvesters. Through the so-called direct and reverse piezoelectric effect [108], an external force applied on piezoelectric materials can be converted into an electrical voltage across the material's electrodes and vice versa. As the block diagram shown in Figure 2.1, a piezoelectric energy harvesting (PEH) system can commonly be attained by attaching piezoelectric transducers on a mechanical transformer under the excitation of an ambient vibration source. The generated AC (alternating current) voltage can then be regulated with a power conditioning interface circuit into a DC (direct current) voltage [25]. Irrespective of the specific mechanical design, transducer, and interface circuit chosen, the two primary design targets for PEH systems are:

1. *The high-capability target*: to increase the harvested power at resonance;
2. *The broadband target*: to increase the off-resonance harvested power, i.e., to broaden the harvesting bandwidth.

Many studies have investigated these two targets for PEH systems from the mechanical and the electrical standpoints. To achieve the high-capability target (1), mechanical solu-

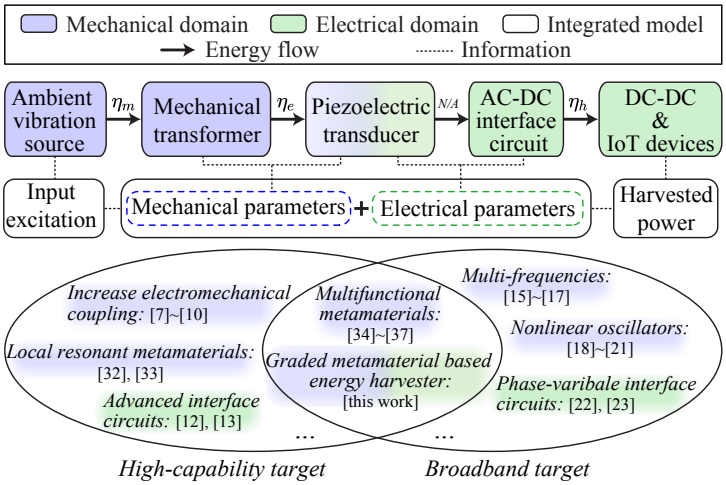

Figure 2.1: Block diagram of a piezoelectric energy harvesting (PEH) IoT system with its integrated model and design targets.

tions include an increase in the number of active materials, or a decrease of the equivalent mechanical stiffness [109–112]. All mechanical solutions yield an increased electromechanical coupling coefficient, which results in a stronger energy harvesting capability [113]. Without altering the mechanical structure, advanced interface circuits [23, 114] can also enhance the energy harvesting capability thanks to the increased impedance matching ability from the electrical side [115]. For fulfilling the broadband design target, most research efforts stem from the mechanical engineering community with a variety of available options, namely combinations of multiple vibrators with different resonant frequencies [116–118] and introduction of nonlinear dynamics in the vibrator [119–122]. Nevertheless, in strong coupling systems, the interface circuits can also contribute to the broadband target by additional electrically induced stiffness with phase-variable (PV) interface circuits [123, 84]. It is important to note that both mechanical and electrical designs play a synergistic role in the two design targets of PEH systems. The mechanical and electrical design integration is quickly becoming quintessential as piezoelectric harvesters are increasingly incorporated into metamaterial-based structures for enhanced energy harvesting [40, 124, 125].

Engineered materials can be mainly categorized into Bragg scattering phononic crystals [126] and locally resonant metamaterials [5]. When aiming to harvest mechanical energy from low frequencies to fit the scenarios of IoT devices, the relatively long wavelength of low-frequency ambient vibrations renders the use of Bragg scattering structures inefficient. It is well known that locally resonant metamaterials can surpass the size limitation of Bragg scattering systems, and generate sub-wavelength bandgaps leveraging local resonance mechanisms [127]. Sugino et al. [55, 128] pointed out that the utility in using locally resonant metamaterials to enhance energy harvesting lies in their unique properties to slow down the propagation of elastic waves and focus the mechanical energy into the local resonators within or close to the frequency range of a bandgap. Therefore, the high-capability target of PEH can be naturally addressed using metamaterials. Li et al. [129] proposed a piezoelectric cantilever-based metamaterial for simultaneous vibration isolation and energy harvesting. Chen et al. [35] also realized the same dual-function with

a membrane-type metamaterial and further increased the output power with double-layer resonators.

Despite the high-capability PEH by locally resonant metamaterials, the harvested power is noticeable only close to the bandgap frequency [40], hence in a relatively narrow band. Therefore, research efforts have also investigated multifunctional metamaterials for tackling the broadband target [40]. Hwang and Arrieta [86] adopted nonlinear resonators and realized an input-independent metamaterial to broaden the energy harvesting bandwidth. Without resorting to nonlinear dynamics, De Ponti et al. [38, 76, 130] explored the rainbow trapping phenomena [72, 131, 36] and realized graded metamaterials with simple and inherent broadband design. It can be seen that the research on enhanced energy harvesting with metamaterials mainly stems from the mechanical side. In contrast, the efforts from the electrical side for PEH with metamaterials are quite deficient. As shown in Figure 2.1, considerations regarding AC-DC interface circuits and IoT devices are essential parts of holistically vibration-powered IoT devices. It still remains an open question how to transfer the advantages of metamaterials mentioned above into electromechanically integrated PEH systems and address the power consumption of IoT devices under low-frequency vibrations.

Building on the recent published graded metamaterials by De Ponti et al. [38, 76, 130], we re-engineer and optimize a graded metamaterial-based energy harvester. For conciseness, this is referred to as "graded-harvester" hereafter. Different from previous results focusing on wave propagation under relatively high frequency ranges (>1 kHz) with absorbing boundary conditions, the proposed graded-harvester employs a clamped-free boundary condition to fit the practical PEH scenarios, which is capable to reach low frequencies and amplify the wave field, thus rendering operation under typical ambient vibration feasible (<100 Hz). Compared to the commonly used resistors as loads for PEH with metamaterials, the electrical part of the graded-harvester utilizes a self-powered interface circuit able to rectify the power produced by piezoelectric patches and provide a usable DC power supply for IoT devices. By combining the graded metamaterial and the AC-DC interface circuit through an integrated lumped model, the energy harvesting performance of the graded-harvester can be determined for the first time. The two design targets of PEH are thoroughly discussed with theoretical, numerical, and experimental analyses.

Section 2.1 introduces the technological background and the proposed design. Section 2.2 proposes an integrated model to calculate the harvested power and demonstrates the broadband energy harvesting ability of the design. Section 2.3 further discusses the wave propagation in the graded metamaterial for the high-capability energy harvesting target. Finally, Section 2.4 shows experimental results for validating the design.

2.2 Theoretical Analysis

In order to investigate the performance of energy harvesting systems, research efforts have been dedicated to theoretical [21] and numerical methods [38] to determine the harvested power and the bandwidth. Unlike the wave propagation at high frequencies typical of acoustic metamaterials satisfying the assumptions of traveling waves in a long

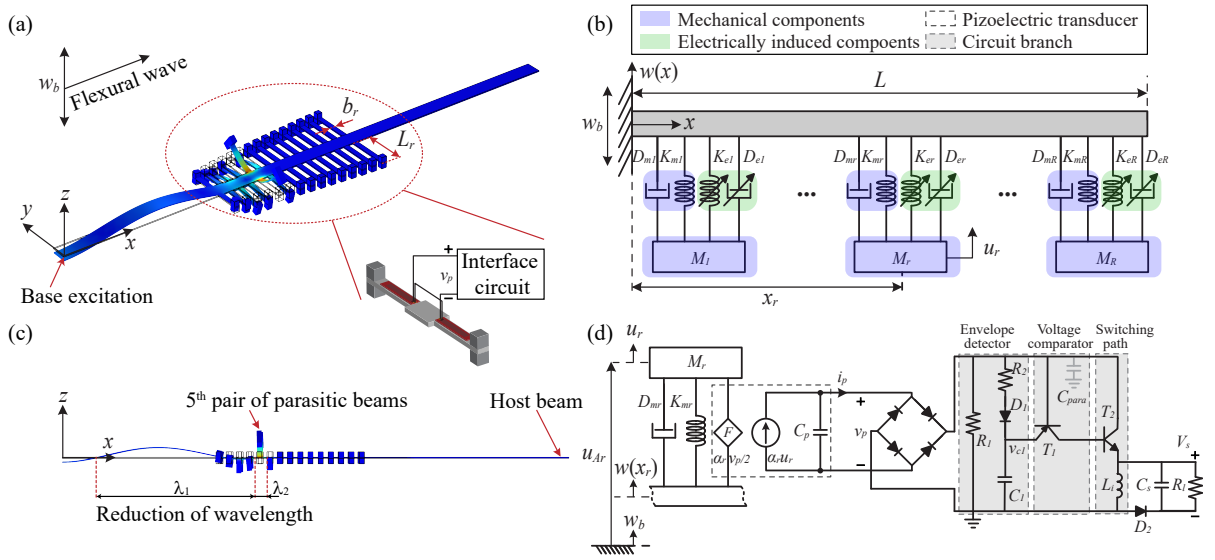

Figure 2.2: Illustrations of the graded metamaterial-based energy harvester and its theoretical model. (a) shows the flexural wave propagating in the graded metamaterial under base excitation in the z direction. The enlarged view shows the configuration of piezoelectric parasitic beams. (b) shows the model schematic corresponding to (a). (c) illustrates the xz cross-section of the structure depicted in (a). (d) displays the detailed equivalent parameter model of each piezoelectric parasitic beam.

structure when compared to the wavelength [127], a quasi-standing wave dominates the dynamic response of the finite structure under low-frequency vibrations [55]. From the electrical side, without the assumption of pure resistive loads for energy harvesting [38], the equivalent impedance of the AC-DC interface circuit should be considered [21]. In addition, the nonlinear coupling of interface circuits with mechanical structures [132] often renders the numerical simulation difficult due to the intensive computation and memory requirements. For these reasons, a simplified integrated model combining mechanical and electrical lumped parameters is developed in this paper. The flow chart of the integrated model used in this section is shown in Figure 2.1. The limited complexity of such a model, enables us to evaluate the energy harvesting performance of the graded-harvester with the chosen interface circuit.

2.2.1 Graded Metamaterial and Circuit Topology

We base our design on previous work by De Ponti et al. [76, 38], which exploited a graded metamaterial and slow waves to enhance the harvested power. Figure 2.2 (a) shows the proposed design, which consists of a host cantilever beam and an array of parasitic beams with tip masses. The host beam of length L, width b, bending stiffness EI, and mass per length m is excited by base excitation $w_b(t)$ in z direction to generate a flexural wave traveling along the x direction. R pairs of parasitic beams of length L_r and width b_r are symmetrically distributed at positions x_r along the host beam to minimize the torsional motion of the host beam. Identical tip masses and piezoelectric patches are attached to each pair of parasitic beams.

The graded design is achieved by gently increasing the length of each pair of parasitic

beams. As shown in Figure 2.2 (a) and (c), a wave generated by a sinusoidal base excitation undergoes a significant reduction of the wavelength along the host beam. At the location of the 5^{th} pair whose resonant frequency matches the excitation frequency, the traveling wave generated by this example vanishes with wave length and group velocity reductions. On the one hand, the low speed extends the interaction time between the parasitic beams with the traveling wave inside the graded array. On the other hand, it locally boosts the vibration amplitude to fulfill the high-capability energy harvesting target. At the same time, when compared against the non-graded metamaterial-based energy harvesters [55], the effective energy harvesting bandwidth can also be increased due to the spatial frequency separation, quintessential in rainbow devices [72, 36]. By combining the contributions of different pairs of parasitic beams located at increasing distances, the broadband ability can also be achieved.

In order to transform the mechanical energy confined inside the metamaterial into electricity, piezoelectric patches are mounted on the parasitic beams. Conventionally, the bulk of research on metamaterial energy harvesting is restricted to the use of resistors as loads of the piezoelectric patches to measure an AC output power [76, 37]. However, this choice is not well suited to the DC power supply demand of IoT devices. Several studies have explored AC-DC interface circuits in PEH systems for this purpose. The Standard Energy Harvesting (SEH) circuit is the most commonly used, which only utilizes a bridge rectifier. In order to boost the energy harvesting capability, more advanced interface circuits [28, 133, 27] have utilized LC resonance for regulating the phase difference between piezoelectric voltage and current.In this paper, the Self-Powered Synchronized Electrical Charge Extraction (SP-SECE) [114] is chosen as the interface circuit since it does not need any external driving signal for the switches and it is load-independent. As will be demonstrated later, we can partially decouple the nonlinear behavior of the electromechanical PEH system induced by the chosen interface circuit, which depends on different load and input amplitude conditions.

Figure 2.2 (d) shows the circuit topology of SP-SECE. The electrical part of the piezoelectric transducer can be regarded as a clamped capacitor C_p for each pair of piezoelectric patches in series and a parallel current source i_{eq} whose value is proportional to the parasitic beam's tip velocity $\dot{u}_r$. By neglecting the leakage resistance, the voltage across the piezoelectric transducer can be represented by v_p. With the electromechanical force-voltage coupling coefficient α_r, the reaction force $2F = \alpha_r v_p$ from the piezoelectric patch is evenly distributed at each parasitic resonator. Besides a full bridge rectifier, the SP-SECE circuit also features a buck-boost converter. Nevertheless, unlike the approach adopted for conventional buck-boost converters in power electronics [134], which follow the Pulse Width Modulation (PWM) controlled method, the switching cycle of SP-SECE follows the mechanical vibration cycles at the current and velocity crossing zero point for self-powered synchronized switching actions. The switching actions are generated by three branches in Figure 2.2 (d): the first is an envelope detector consisting of a discharge resistor R_1, D_1, and C_1; the second is a voltage comparator by an off-the-shelf PNP transistor T_1, and the third is a switching path formed by a NPN transistor T_2 and an inductor L_i.

In this paper, the two piezoelectric patches of each pair of parasitic beams are connected

in series with the interface circuit so it can easily overcome the voltage threshold induced by the bridge rectifier and the switching path under low-amplitude vibrations. In order to evaluate the energy harvesting performance of the graded-harvester, an integrated model is built in the following section from the mechanical and electrical sides.

2.2.2 Equivalent Lumped Parameters

With reference to the flow chart of the integrated model in Figure 2.1, a modal analysis method is implemented in order to derive the lumped parameters of the proposed design from the mechanical side, as shown in the schematic in Figure 2.2 (b). The schematic consists of a host cantilever beam and periodically distributed parasitic resonators corresponding to the host beam and parasitic beams in Figure 2.2 (a), respectively. Two identical parasitic beams of each pair are attached to the same position of the host beam, generating a joint resonance effect. In order to derive the lumped parameters of the resonators considering the additional stiffness introduced by piezoelectric patches, each parasitic beam can be represented as a partially covered piezoelectric cantilever beam with tip mass under a Single Degree Of Freedom (SDOF) system assumption [135], where the first flexural vibration mode is taken into account.

The SDOF model of a parasitic resonator for a piezoelectric parasitic beam in Figure 2.2 (b) can be represented with the PEH model in Figure 2.2 (d). Under given base excitation w_b on the clamped side of the host beam, the relative transverse displacement at x_r of the host beam can be regarded as $w(x_r)$. The absolute displacement of the SDOF parasitic resonator at x_r is $u_{Ar}(t) = w_b(t) + w(x_r, t) + u_r(t)$, as shown in Figure 2.2 (d). Therefore, a parasitic beam with piezoelectric patches can be represented with a SDOF energy harvester under base excitation with acceleration $\ddot{w}_{abs} = \ddot{w}_b + \ddot{w}$. The equivalent mass M_r, stiffness K_{mr}, damping coefficient D_{mr}, and the equivalent force-voltage coupling coefficient α_r can be formulated as:

$$\begin{aligned} M_r &= \frac{1}{\psi_r^2(L_r)}; \quad K_{mr} = \frac{\omega_r^2}{\psi_r^2(L_r)}; \\ D_{mr} &= \frac{2\zeta_r\omega_r}{\psi_r^2(L_r)}; \quad \alpha_r = \frac{\beta_r}{\psi_r(L_r)} \end{aligned} \tag{2.1}$$

where ψ_r is the first order mode shape of the beam section without piezoelectric layer [135] in the r^{th} pair of parasitic beams. ζ_r, β_r and ω_r describe the damping ratio, the coupling related factor and the first order resonance frequency of the r^{th} beams, respectively.

The first-order resonance frequency ω_r can be determined by solving the characteristic equation of the r^{th} pair of parasitic beams. Along with the boundary conditions, the mode shape ψ_r and the coupling related factor β_r are computed. It should be noted that the derived lumped parameters are effective only at the beam's tip. The reaction force at the root of the beam derived from the lumped parameters is slightly different from that derived from the analytical model [135]. However, by properly choosing a relatively large tip mass, these parameters are still valid for calculating the reaction force at the root of the beam [39].

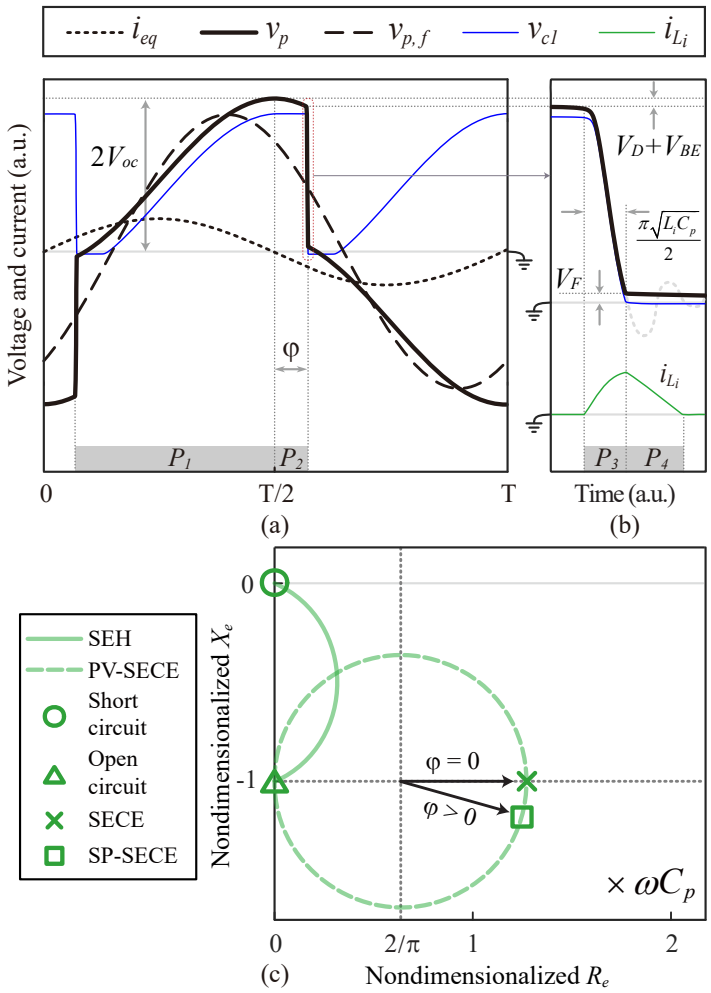

Figure 2.3: The waveform and equivalent impedance of SP-SECE interface circuit. (a) Operation waveform of SE-SECE. (b) L_i-C_p resonance switching phase and the freewheeling phase. (c) Nondimensionalized equivalent impedance of SEH, PV-SECE, SECE and SECE.

Additionally, we include the electrical side considering the lumped parameters of the interface circuit as shown in Figure 2.1. We employ a general impedance analysis method [21] to determine the lumped parameters, which relies on the computation of the first order electrically induced damping and stiffness coefficients: D_e and K_e. Figure 2.3 (a) shows the waveform of the SP-SECE interface circuit, including its piezoelectric voltage v_p, current waveform i_{eq}, and the voltage v_{cl} of C_1 (also the emitter voltage of T_1). In Figure 2.3, $\varphi \in [0, \pi/2]$ describes the positive switching phase lag and V_{oc} is the nominal open-circuit voltage depending on the relative displacement amplitude of a parasitic resonator. The operation of SP-SECE consists of four phases from P_1 to P_4 as shown in Figure 2.3 (a) and (b):

1. P_1: an open circuit phase between the end of the last switching phase P_3 and the current crossing zero point;

2. P_2: a switching delay phase, denoted by phase lag φ, due to the conduction of the switching path;

3. P_3: a switching phase to transfer the charge from C_p to L_i;
4. P_4: a freewheeling phase to transfer the energy in L_i into the storage capacitor C_s through the freewheeling diode D_2.

Based on these four steps, the equivalent impedance Z_e of SP-SECE interface circuit can be derived with impedance analysis (detailed in Appendix 2.A). The electrically induced damping D_{er} and stiffness K_{er} of each parasitic resonator in the r^{th} pair can be derived based on the electromechanical analogy in this coupling system, namely:

$$D_{er} = \alpha_r^2 R_e/2, \quad K_{er} = -\alpha_r^2 \omega X_e/2. \tag{2.2}$$

When the system operates at frequency ω, the real part R_e and the imaginary part X_e of Z_e form functions of φ, whose relationship is illustrated in the two-dimensional impedance plane depicted in Figure 2.3 (b). The figure shows the equivalent impedance of SECE (special case of PV-SECE [123] when $\varphi = 0$) and SP-SECE (special case of PV-SECE when $\varphi > 0$). Compared with SEH, the real part R_e of SECE or SP-SECE is larger, which means it has a stronger impedance matching ability to achieve a higher power output. By assuming $V_{oc} > 10(V_D + V_{BE})$, the difference of R_e between SP-SECE and SECE is less than 5%. Therefore, we can approximate the equivalent impedance of SP-SECE by that of SECE and remove the dependency on input amplitude under the relatively large V_{oc} condition. Consequently, different from the SEH case, the D_{er} and K_{er} of SP-SECE are independent of the load and input amplitude conditions, which decouple the system with invariant electrically induced components for the proposed metamaterial for energy harvesting.

2.2.3 Integrated Model

As shown in Figure 2.1, by combining the lumped parameters determined mechanically and electrically, each piezoelectric parasitic beam can be represented by a SDOF parasitic resonator with the SP-SECE interface circuit. Therefore, the governing equation for each parasitic resonator can be formulated as:

$$M_r \ddot{u}_r(t) + D_r \dot{u}_r(t) + K_r u_r(t) = -M_r \left(\frac{\partial^2 w(x_r, t)}{\partial t^2} + \ddot{w}_b(t) \right), \tag{2.3}$$

where $K_r = K_{mr} + K_{er}$ and $D_r = D_{mr} + D_{er}$ contain the combined effect of the mechanical and electrical induced stiffness and damping, respectively. As stated previously, the electrically induced components are determined by the chosen interface circuit. For SP-SECE, D_{er} is positive, which means it absorbs mechanical energy and converts it into electricity. In order to evaluate the energy harvesting performance of the proposed design, the displacement amplitude U_r of the r^{th} pair parasitic resonators shall be determined.

By adding the reaction forces of each pair of parasitic resonators onto the host beam, the

governing equation of the host beam can be expressed as:

$$\begin{aligned} &EI\frac{\partial^4 w}{\partial x^4} + m\frac{\partial^2 w}{\partial t^2} = -m\ddot{w}_b(t) + \\ &2\sum_{r=1}^{R} K_r u_r(t)\delta\left(x - x_r\right) + 2\sum_{r=1}^{R} D_r \dot{u}_r(t)\delta\left(x - x_r\right), \end{aligned} \tag{2.4}$$

where δ represents the Dirac function. The integrated model of the graded-harvester is then represented by Eq. 2.3 and Eq. 2.4.

U_r can be solved by modal analysis method with the electrically induced components from the SP-SECE interface circuit (detailed in Appendix 2.A). Furthermore, the magnitude of the piezoelectric current of the r^{th} pair of parasitic resonators in series can be expressed as [21]:

$$I_{eqr} = \alpha_r \omega U_r. \tag{2.5}$$

Taking into account the rectifier loss, switching loss, and freewheeling loss [22] of the SP-SECE interface circuit under the relatively large V_{oc} assumption, the harvested power for each pair of parasitic resonators can be formulated as:

$$P_r = \frac{I_{eqr}^2 E_h}{2\Delta E} R_e = \eta_h \frac{I_{eqr}^2}{2} R_e, \tag{2.6}$$

where ΔE and E_h represent the total extracted energy and the harvested energy in one cycle. The ratio between ΔE and E_h is denoted as the harvesting efficiency η_h:

$$\eta_h = \frac{E_h}{\Delta E} = \frac{|\gamma|\,\tilde{V}_s}{\tilde{V}_s + \tilde{V}_D}\left(1 - \tilde{V}_F\right), \tag{2.7}$$

where γ, $\tilde{V}_s$, $\tilde{V}_D$, and $\tilde{V}_F$ describe the flipping factor of the SP-SECE interface circuit, the V_{oc} normalized V_s, V_D and V_F, respectively. Consequently, the harvested power is a percentage of the extracted power. All the parameters in Eq. 2.6 are constant under the specific base excitation condition, except the harvesting efficiency η_h. Strictly speaking, the harvested power also changes with the load condition, which influences $\tilde{V}_s$. However, this dependency can be significantly weakened after the conduction of the freewheeling diode D_2 [22].

As a case study, the theoretical harvested power, computed using the integrated model described above, for different pairs of parasitic beams is plotted as a gray line in Figure 2.6 with the parameters from Table 2.1. For the harvested power in single resonant energy harvesters [21], the bandwidth usually refers to the -3 dB bandwidth. For the graded-harvester, there is no standard criterion to define the harvested power bandwidth. However, it can be seen that inside the graded area, there are multiple harvested power peaks corresponding to the resonance frequencies of different pairs of parasitic beams in the range from 60 Hz to 160 Hz. Therefore, the broadband energy harvesting ability of the graded-harvester is guaranteed.

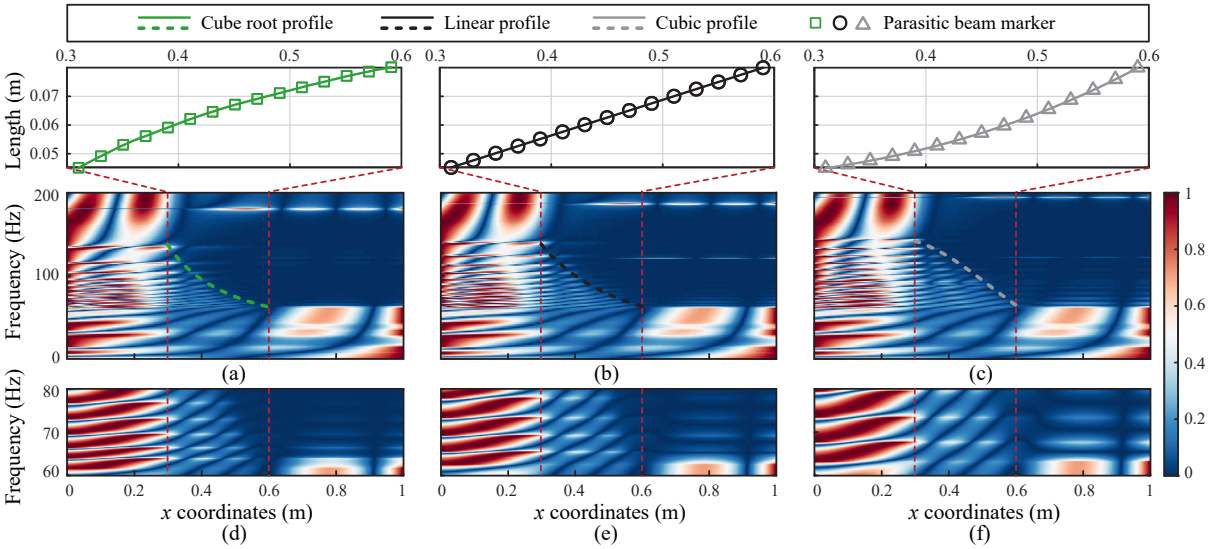

Figure 2.4: The different grading profiles and their numerical spatial-frequency analysis normalized at each frequency. (a) Cubic root profile. (b) Linear profile. (c) Cubic profile. (d), (e), and (f) show the 60-80 Hz enlarged view of (a), (b), and (c), respectively.

2.3 Numerical Analysis

The grading design of the metamaterial not only broadens the energy harvesting bandwidth. It also affects the dispersion relationship and the wave field propagation, which further influences the energy harvesting ability of the designed graded-harvester. This section investigates wave propagation within the graded metamaterial using numerical simulations (FEM) and demonstrates the broadband and high-capability energy harvesting characteristic of the graded-harvester.

2.3.1 Grading Profile

In order to evaluate the harvesting ability in the bandgap range, it is necessary to investigate the role of different grading profiles. As shown in Figure 2.4, the spatial-frequency analyses of three grading profiles for the parasitic beams are simulated in the frequency domain with COMSOL Multiphysics. The lengths of different pairs of parasitic beams distributed at the same positions on the host beam follow the cube-root profile, linear profile, and cubic profile, respectively. The three different grading profiles can be expressed as a function of the positions of different parasitic beams:

$$L_r = ax_r^p + b, \tag{2.8}$$

where $p = 1/3, 1, 3$ represents the cube-root, linear, and cubic profiles, respectively. By fixing the length of parasitic beam pair L_1 and L_{15}, parameter a and b can be determined. As shown in Figure 2.4, the cubic-root, linear, and cubic profiles exhibit the same bandgap ranges but different spatial-frequency separation curves[1] where the wave prop-

[1]It should be noted that the grading discussed here concerns the lengths rather than the resonance frequencies of parasitic beams determined by Eq. 2.1. Therefore the final spatial-frequency separation curves

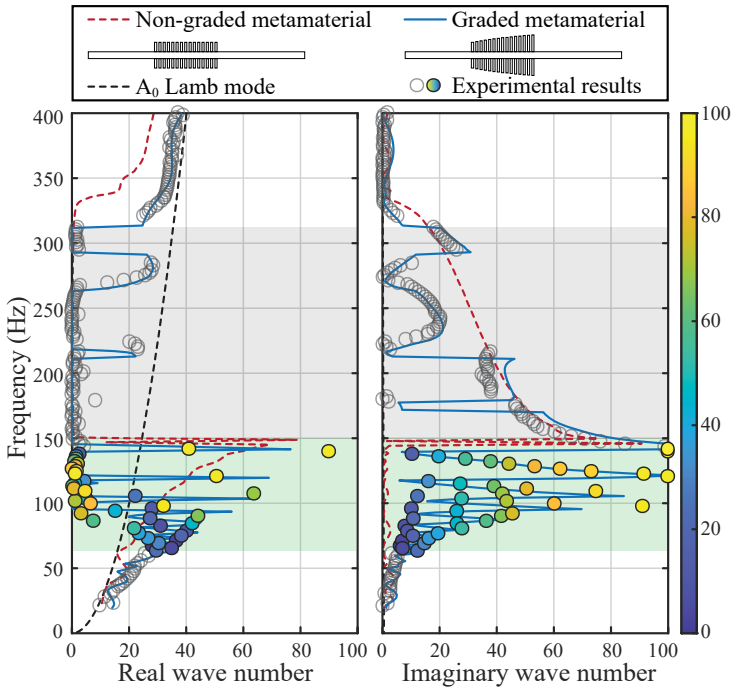

Figure 2.5: The dispersion relationship of the graded-harvester. The curves represent the numerical dispersion relationships of the A_0 Lamb mode (black dashed lines) of the host beam, the non-graded (red dashed lines) metamaterial, and the graded (blue lines) metamaterial, respectively. For experimental wave numbers of the graded metamaterial, the wave that propagates outside the grading frequency range is indicated by gray circles; the wave that propagates within the grading frequency range is indicated by color circles. In the grading frequency range, the real and imaginary parts of each complex wave number are labeled with the same color scale with respect to the amplitude of the imaginary wave number.

agation vanishes, as indicated with the green dashed line, black dashed line, and gray dashed line, respectively. Compared with the linear or cubic profiles as shown in Figure 2.4 (e) and (f), the cubic-root one shown in Figure 2.4 (d) enables more localized modes at the beginning of the bandgap range due to the increased number of longer parasitic beams [37]. This creates a stronger bandgap and suggests a higher energy density, ideal for boosting energy harvesting, and it is thus chosen for the proposed design.

2.3.2 Numerical Results

The dispersion relationship provides a general and fundamental description of the wave propagation characteristics of linear metamaterials. It leads to a better understanding of how the propagating wave could enable higher energy harvesting ability spanning the grading frequency range [36]. Based, therefore, on the cubic-root grading profile, we discuss wave propagation in the graded metamaterial by dispersion analysis. Due to the out-of-plane base excitation, traveling flexural waves (A_0) in the host beam are dominant versus longitudinal and torsional waves, or higher-order Lamb waves. Limited by the length of the host beam, the commonly used two-dimensional Fourier transform (2D-FFT)

indicated with dashed lines in Figure 2.4 (a), (b), and (c) do not have the same shapes corresponding to their grading profile functions.

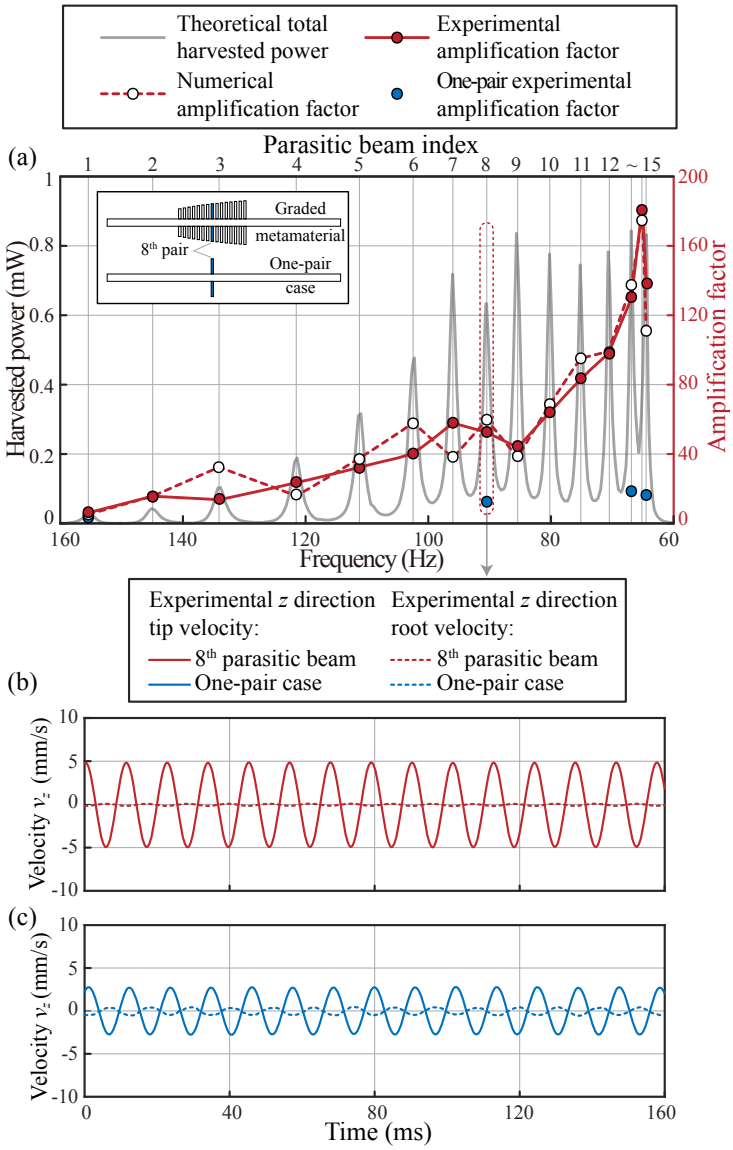

Figure 2.6: The harvested power and amplification factor of the graded-harvester. (a) shows the harvested power and amplification factor of the graded-harvester, the frequency axis is plotted in a descending order, according to the grading frequency distribution. (b) shows the experimental velocity of the 8^{th} parasitic beam. (c) shows the experimental velocity of the one-pair case corresponding to the 8^{th} parasitic beam.

[136] can not give a high-resolution dispersion relationship at low-frequency vibrations. As an alternative, we further herein adopt the Inhomogeneous Wave Correlation (IWC) method [137], which allows for accurate characterization of the dispersion relationship over short measurement distances. The wave number is calculated by the maximized correlation between a theoretical inhomogeneous running wave and the spatial response from measurements or simulations.

Figure 2.5 shows the numerical dispersion curves of the A_0 Lamb mode, a non-graded metamaterial, and the graded metamaterial from frequency domain analysis with COMSOL Multiphysics. Compared to the graded metamaterial, the non-graded metamaterial

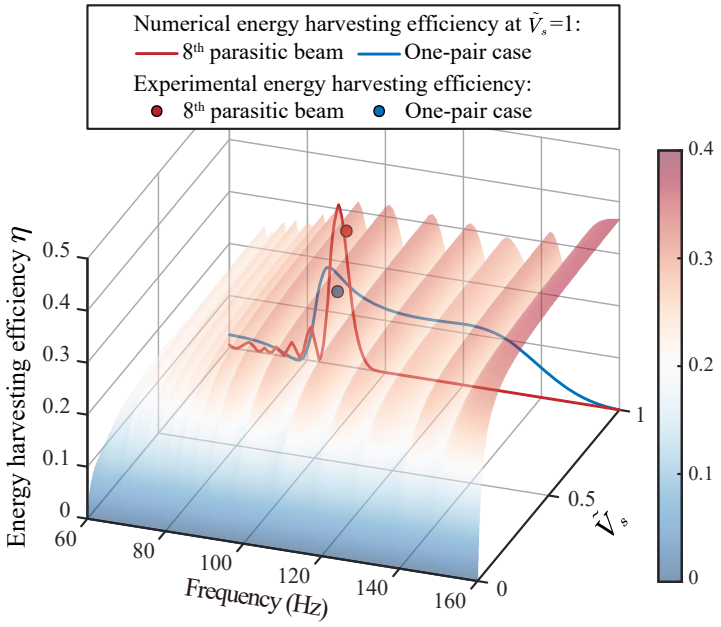

Figure 2.7: The energy harvesting efficiency η of the graded-harvester. The semitransparent surface represents the envelope of energy harvesting efficiencies from different parasitic beams of the graded-harvester.

simulated here represents the commonly used periodic design [55] with the same parasitic beam length equal to L_1. The different structures are excited with a constant acceleration field. The numerical dispersion curves are computed via the IWC method, using the simulated frequency-domain velocity responses spaced at 1mm intervals across the host beam. For the dispersion curves of the graded metamaterial, shown in blue lines, the wave propagates as a A_0 Lamb mode with no dissipation outside the bandgap range. Inside the bandgap range indicated by the gray shadow (starts from the resonant frequency of the 1^{st} pair of parasitic beams at 154 Hz to 317 Hz), most of the real wave numbers are zero, which means there is no wave propagation in this frequency range. Furthermore, the positive imaginary wave numbers indicate the exponential decay of traveling waves due to the local resonant effect [138].

Besides the bandgap creation described above, the graded design introduces an additional gap, which is indicated via a green shadow (the grading frequency range from the resonant frequency of the 15^{th} pair of parasitic beams at 66 Hz to 154 Hz). For the real wave numbers, the non-vanishing values become larger as the frequency increases. Rather than propagating through the metamaterial as in the non-graded case, the waves slow down at the positions of local resonators with group velocity and wavelength reduction. This slow-wave phenomenon can also be seen from the imaginary wave numbers. The imaginary wave numbers are more prominent in the graded range than in the non-graded case, which also explains the exponential decay of wave propagation with the graded design. The slow waves enable longer interaction with the local resonators, which leads to the amplification of the wave fields.

We introduce the amplification factor of the wave field in local resonators as a metric of the energy transfer capability from the metamaterials to local resonators. We firstly

define the relative velocity of a local resonator as the velocity difference between its tip and root positions of a parasitic beam: $\dot{u}'_r = \dot{u}_r - \dot{w}(x_r)$. Then the amplification factor can be expressed as the ratio of the relative velocity amplitude of a local resonator to the velocity amplitude at its root position on the host beam: $\dot{U}'_r/\dot{W}(x_r)$. Figure 2.6 (a) shows the simulated amplification factors of each pair of parasitic beams at their resonance frequencies using COMSOL time domain simulations. It is observed that the amplification factor of the graded metamaterial increases with the length of the parasitic beams, except for a drop at the 15^{th} parasitic beam due to the wave leakage at the beginning of the bandgap and the lack of additional resonators. The trend of the amplification curve follows that of the harvested power curve in the graded frequency range. This amplification of the wave field shows the potential to harvest mechanical energy with the graded metamaterial efficiently.

With the wave field amplification by the graded metamaterial, we further calculate the energy harvesting efficiency of the graded-harvester. From the perspective of energy flow [23, 139] shown in Figure 2.1, the energy transformation process of the graded-harvester contains three steps:

1. The mechanical energy inside the graded metamaterial is efficiently transferred to local resonators as mechanical transformers. The efficiency of this step is defined as η_m;
2. The mechanical energy in local resonators is converted into the electrical extracted energy with piezoelectric transducers. The efficiency of this step is defined as η_e;
3. By considering the piezoelectric transducer and the interface circuit as a whole, the electrical extracted energy is further converted into the net energy harvesting energy in the storage considering different losses. The efficiency of this step is η_h in Eq. 2.7.

In order to determine the total energy harvesting efficiency $\eta = \eta_m\eta_e\eta_h$, we firstly simulate η_m of each pair of parasitic beams. From energy conservation, the work done by the external load is finally consumed by the damping effect of the graded-harvester. We use an isotropic mechanical damping coefficient 0.001 for the graded metamaterial and the electrically induced damping D_{er} for each pair of parasitic beams. Therefore, η_m can be simulated by the ratio between the dissipation energy of each pair of parasitic beams and the total dissipation energy of the graded-harvester. Then, the transferred mechanical energy is converted into electrical energy with the efficiency $\eta_e = D_{er}/D_r$. By considering the electrical losses in the interface circuit, the total numerical energy harvesting efficiency η is shown in Figure 2.7. The efficiency of the 8^{th} parasitic beam at $\tilde{V}_s = 1$ reaches the peak value at its resonance frequency, after which the efficiency drops to zero due to the spatial frequency separation mentioned above. Compared to the one-pair case indicated with the blue line, the η of the 8^{th} parasitic beam increased 160% due to the wave field amplification by the graded metamaterial. This kind of relay of different parasitic beams forms the envelope surface of the total efficiency η, which maintains a high level in the grading frequency range and serves the high-capability energy harvesting target.

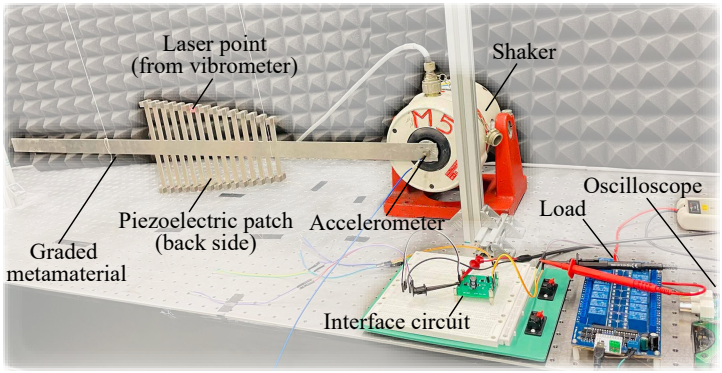

Figure 2.8: Experimental setup.

Table 2.1: Parameters in Experiment

Graded Metamaterial based Energy Harvester			
Host Beam			
Size	1000×30×2 (mm^3)	Material	Aluminum
Parasitic Beam			
Size	L_r×10×2 (mm^3)	Material	Aluminum
$L_r = 21.6\sqrt[3]{x_r} - 101.3$ (mm),		$x_r = 310 : 20 : 590$ (mm)	
Tip Mass			
Size	10×10×10 (mm^3)	Material	Steel
Piezoelectric Patch			
Size	40×7×0.8 (mm^3)	Material	PZT
d_{31}	-60 pC/N	C_p	19.6 nF
Interface Circuit			
Diodes	SS14 ($V_D = 0.5$ V)	L_i	10 mH
MOSFETs	XN4601 ($V_{BE} = 0.5$ V)	C_s	4.7 μF
Rectifier	MB6S ($V_F = 1$ V)	γ	-0.63

2.4 Experiment

Finally, both the broadband and high-capability energy harvesting of the designed graded-harvester are validated experimentally. From the mechanical side, the broadband energy harvesting induced by the graded metamaterial design is investigated via transmissibility and spatial-frequency analysis. Additionally, the high-capability energy harvesting is demonstrated by means of the experimental dispersion relationship and the amplification factor. From the electrical side, the practical energy harvesting performance of the graded-harvester is evaluated by comparison to a beam with only one pair of parasitic beams fixed to the host beam.

2.4.1 Setup

Figure 2.8 shows the experimental setup. The graded metamaterial was fabricated out of one aluminum plate by water-jet cutting. Two identical tip masses and one piezoelectric patch are attached to each parasitic beam. The graded metamaterial is then hung

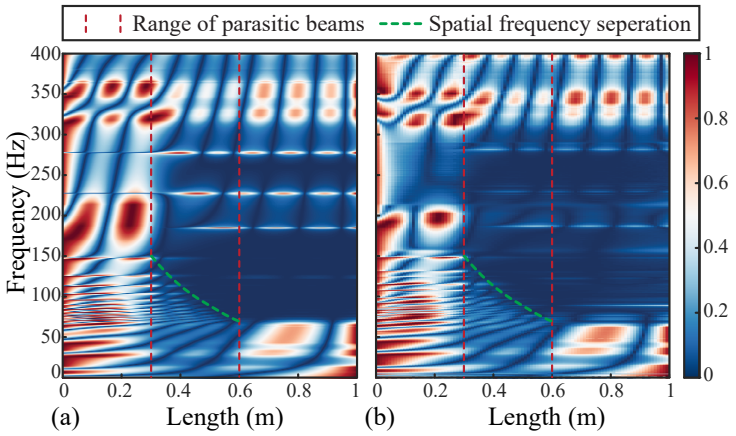

Figure 2.9: Comparison of spatial-frequency analyses. (a) and (b) show the numerical and experimental spatial-frequency analyses of the graded metamaterial. The spatial-frequency separation is shown with the green dashed line. The graded area is indicated with two vertical red dashed lines.

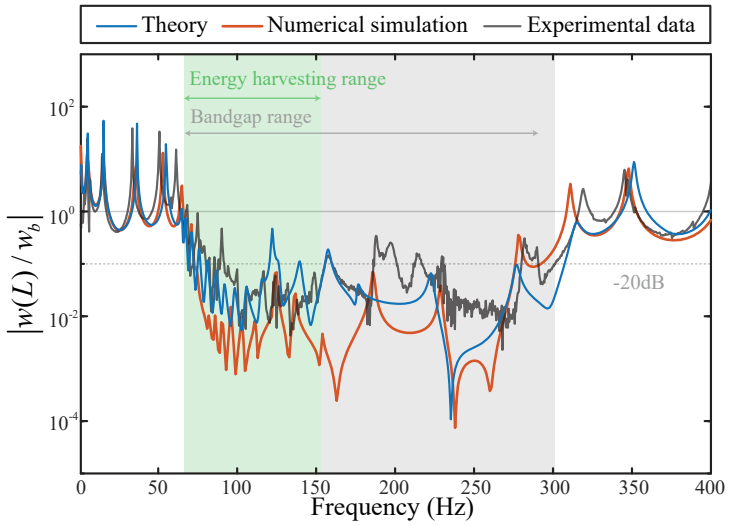

Figure 2.10: Comparison of transmissibilities. The three curves show the theoretical, numerical, and experimental tip transmissibility, respectively.

vertically by two ropes to maintain stability. One end of the graded metamaterial with shorter parasitic beams is clamped to a shaker (LDS V406) for base excitation resulting in a clamped-free boundary condition. The two piezoelectric patches of one pair of parasitic beams are connected in series. Because the base excitation is symmetric, the antisymmetric modes of the pair of parasitic beams are not excited [130]. This means each pair is free from out-of-phase vibration and charge cancellation. Therefore, it is feasible to configure two piezoelectric patches of one pair of parasitic beams in series. The piezoelectric voltage is connected to the SP-SECE interface circuit for energy harvesting. The parameters of the graded-harvester are shown in Tab. 2.1. These mechanical and electrical parameters were chosen to realize the energy harvesting function of the graded-harvester, considering mainly off-the-shelf, easily customizable (printed circuit board), and inexpensive components. The shaker is triggered simultaneously with a Polytec 3D scanning laser Doppler vibrometer (SLDV), which records the 3D velocity field at the center-axial points on the

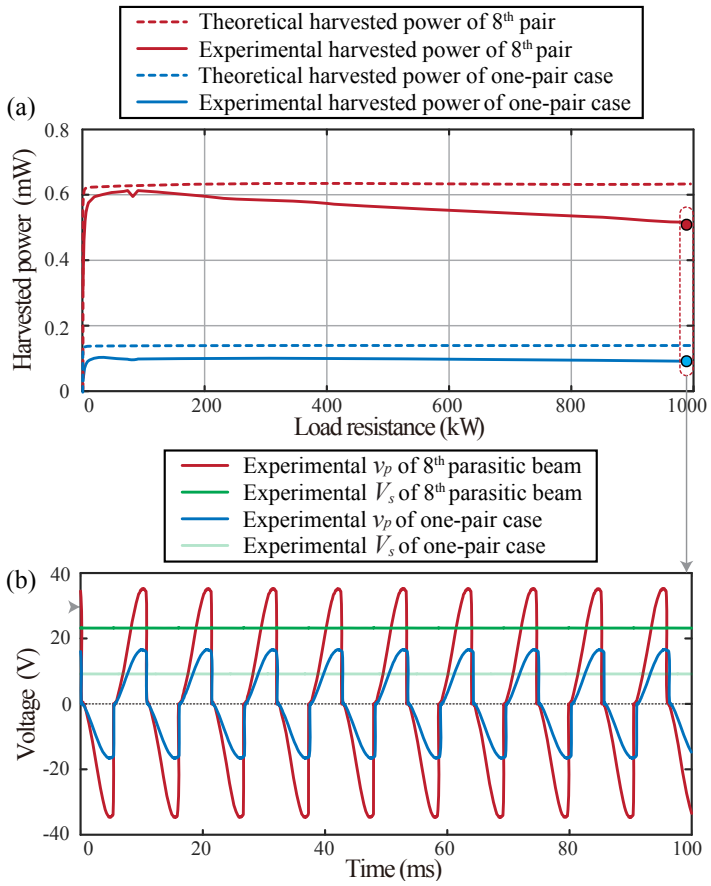

Figure 2.11: The harvested power of the 8^{th} pair parasitic beams and its corresponding one-pair case under 0.1N harmonic based excitation at their own resonance frequencies. (a) shows the theoretical and experimental harvested power of 8^{th} pair parasitic beams and its one-pair case. (b) shows the piezoelectric voltage v_p and the storage voltage V_s under 1MΩ load condition.

host beam with 5 mm spacing and the tip points of parasitic beams in the time domain through repeated acquisitions.

2.4.2 Experimental Results

Figure 2.9 (a) and (b) show the spatial-frequency separation of the graded metamaterial from numerical simulation and experimental data. The numerical simulation setup is identical to the procedure discussed in Section 2.3. In the experiment, the beam was excited with a broadband white noise signal. The experimental spatial-frequency was obtained from the Fourier transformed time-domain velocity responses of the center-axial points on the host beam. The bandgap range of the experimental data shows good agreement with the numerical simulation. Inside the graded bandgap area, the velocity amplitude and the wavelength decrease in agreement with Figure 2.9 (a), until it vanishes as shown with the green dashed lines in correspondence with the positions of the local parasitic beams. As stated before, this spatial-frequency separation enables the broadband energy harvesting target. From the bandgap perspective, Figure 2.10 shows the tip transmissibility under open circuit condition of the graded metamaterial. The results displayed are from the

theoretical model derived from Section 2.2, the numerical simulation corresponding to Section 2.3 with piezoelectric patches attached, and the experimental data. The isotropic damping coefficient used for the mechanical structure in the theoretical model and simulation is 0.001. Compared to the non-graded metamaterial, no closed form equation exists that governs the bandgap range of graded metamaterials. Therefore, -20 dB is regarded as the threshold below which the transmissibility is considered to reflect the bandgap [37]. It can be seen that the three transmissibility curves mutually agree, which validates the theoretical model proposed in Section 2.2. The difference of the numerical and theoretical curves versus the experimental curve is mainly due to the plastic cover of the piezoelectric patches, which differs from the homogeneous piezoelectric material property used in theoretical analysis and simulations.

Additionally, the experimental dispersion relationship of the graded metamaterial is indicated with gray and color circles in Figure 2.5. The experimental wave numbers were obtained by the IWC method with the Fourier transformed time-domain velocity responses of the center-axial points on the host beam under a 30-350 Hz broadband sweep. They indicate good agreement with the numerical dispersion curves. Inside the grading frequency range, the real and imaginary parts of an experimental wave number at each frequency are shown with the same color. These non-zero wave numbers further lead to the experimental amplification factor of the graded metamaterial in Figure 2.6 (a). The experimental amplification factors displayed in Figure 2.6 (a) were calculated by the definition in Section 2.3 with the experimental time-domain velocity responses under harmonic base excitation at the resonance frequencies of different parasitic beams. Compared with the one-pair cases of parasitic beam pairs L_1, L_8, L_{13}, and L_{15} shown as blue dots, the amplification factors of the graded metamaterial are larger, indicating more efficient energy transformation from the host beam to the local resonators under the same input conditions. Figure 2.6 (b) and (c) show an example of the tip velocity responses from the 8^{th} pair of parasitic beams and its one-pair case under their resonant frequencies. It can be seen that not only the amplitude $\dot{U}_8$ is larger than its one-pair case. The amplification ratio also outperforms its corresponding one-pair case.

Figure 2.11 illustrates a practical example of the harvested power from the graded metamaterial with the theoretical harvested power curves. Under 0.1 N harmonic input base excitation at the resonance frequency of the 8^{th} pair of parasitic beams and its corresponding one-pair case, the experimental harvested power was measured with the output voltage under different loads switched by an electromagnetic relay. It can be seen that all four harvested power curves quickly reach a stable output after a certain load threshold to conduct the bridge rectifier and the freewheeling diode, which shows the load-independent characteristic of the SP-SECE interface circuit. The theoretical harvested power curves indicated with dashed lines agree with the experimental harvested power curves. The difference is mainly due to the loss of the envelope detector. The drop of the experimental power curve of the 8^{th} pair of parasitic beams under large load resistance is induced by the parameter loss of the storage capacitor C_s under high voltages. Compared with the one-pair case, the maximum harvested power is enhanced by 489%. The experimental energy harvesting efficiency is defined as the ratio of the harvested power from the parasitic

Table 2.2: Comparison with Existing Works

Reference	Transducer	Size	Frequency	Power	Load
Li et al., 2017 [129]	PVDF	$35 \times 35 \times 1$ mm^3	170 Hz	0.5μW	1000 kΩ
Chen et al., 2019 [35]	PVDF	$45 \times 45 \times 2$ mm^3	348 Hz	1.25μW	200 kΩ
Hwang and Arrieta, 2018 [86]	PVDF	$225 \times 64 \times 0.25$ mm^3	Input independent	32μW	100 kΩ
De Ponti et al., 2020 [76]	PZT	$(250 \sim 650) \times 5 \times 5$ mm^3	$2000 \sim 5000$ Hz	70μW @ 2050 Hz	6.8 kΩ
This work	PZT	$L_r \times 10 \times 2$ mm^3	$60 \sim 160$ Hz	600μW @ 91 Hz	Load independent

beams to the base excitation RMS power:

$$\eta_{exp} = \frac{P_r}{\frac{1}{T}\int_T f_{in}(t)\,\dot{w}_b(t)\,\mathrm{d}t}, \tag{2.9}$$

where f_{in} and $\dot{w}_b$ represent the harmonic input force and the base velocity. The experimental efficiencies for the 8^{th} pair of parasitic beams and its one-pair case are 26% and 14%, respectively, which shows the high-capability energy harvesting of the proposed design. They also agree with the numerical results shown in Figure 2.7. Broadband energy harvesting can also be naturally realized by varying the different harvesting parasitic beam pairs. Figure 2.11 (b) shows the experimental waveform of the piezoelectric voltage v_p and the storage voltage V_s under 1 MΩ load of the 8^{th} pair of parasitic beams and its one-pair case. It can be seen that the piezoelectric voltage of the 8^{th} pair parasitic beams is higher due to the wave field amplification from the graded metamaterial, and the storage voltage is also higher.

2.5 Discussion

Locally resonant metamaterials fit the scenario of utilizing low-frequency vibrations for self-powered IoT devices. With reference to statistic studies [140], we discuss the PEH performance of the proposed graded-harvester with respect to existing metamaterial-based PEH harvesters as benchmark models. The PEH performance of these harvesters are summarized in Table 2.2, where the chosen transducer type (polyvinylidene difluoride (PVDF) or lead zirconate titanate (PZT)), resonator size, operating frequency, harvested power, and load condition of each harvester are listed in detail. Despite different power performances, all solutions listed provide higher efficiency when compared to conventional energy harvesters because they leverage the local resonant effect. As shown in the table, conventional locally resonant metamaterials (Li et al. [129] and Chen et al. [35]) can achieve low-frequency PEH, however, their energy harvesting bandwidth is relatively narrow. By exploiting the nonlinear dynamics or graded designs, the operating frequency[2]

[2]For multifunction metamaterials, there is no standard definition of the energy harvesting bandwidth. Therefore we use the operating frequency range as a replacement.

can be broadened with multifunction metamaterials, as presented by Hwang and Arrieta [86] and De Ponti et al. [76]. Building on these pioneering solutions, the graded-harvester presented here not only achieves near-milliwatt power output to accommodate the power demand of low-power consumption IoT devices, but also broadens the operating frequency for low-frequency PEH. Furthermore, its load independence characteristic provides stable output power from heavy to light load conditions. This allows tackling different operational conditions of IoT devices [141]. Given the simplicity, the robust underlying physics, the inherently broadband and high-capability designs, the proposed graded-harvester has great potential to power sensors or microcontrollers and realize self-powered IoT devices.

2.6 Conclusion

Based on the idea of graded metamaterials, this paper proposes a graded metamaterial-based energy harvester for broadband and high-capability piezoelectric energy harvesting focusing on ambient vibrations (<100 Hz). The broadband energy harvesting target has been inherently satisfied by the spatial-frequency separation of the graded metamaterial design with an efficient grading profile. Furthermore, the high capability energy harvesting target has been investigated by dispersion analysis of low-frequency wave propagation to reveal the slow wave phenomena and the wave field amplification mechanism of the graded metamaterial. By combining the two advantages of the graded metamaterial with the two main goals for piezoelectric energy harvesting, the power performance and the energy harvesting efficiency of the graded-harvester are thoroughly discussed with theoretical, numerical, and experimental analyses. Finally, experiments were carried out to validate the performance of the graded-harvester. It is shown that coupling of the graded metamaterial with the self-powered interface circuit results in a five-fold increase of the harvested power with respect to the conventional harvesting solution commonly adopted in IoT devices. Therefore our proposed design opens up new potential for self-sustainable IoT devices.

Acknowledgments

The authors acknowledge support from ETH Research Grant (ETH-02 20-1) and H2020 FET-proactive project METAVEH under the grant agreement 952039.

2.A Appendix

2.A.1 Equivalent Impedance of the SP-SECE Interface Circuit

In phase P_3 as shown in Figure 2.3, the L_i-C_p resonance should be introduced at the i_{eq} crossing zero point by conducting the switching path with T_2. Nevertheless, the cascaded connection of T_1 and T_2 renders the conduction of T_2 dependent on the conduction of T_1 to enable a nonzero base current. In order to conduct T_1, its base voltage (the bridge-rectified piezoelectric voltage with forward voltage drop V_F) should be lower than its emitter voltage V_{c1} by $V_D + V_{BE}$ (the sum of the forward voltage drop of D_1 and the

base-emitter voltage of T_1). In other words, v_p should also have the same voltage drop to conduct T_1. Therefore, the phase delay φ between the switching instant and current zero-crossing instant is calculated as:

$$\varphi = \arccos\left(1 - \frac{V_D + V_{BE}}{V_{oc}}\right), \tag{2.10}$$

Assuming that each bias-flip action takes much less time than a vibration cycle, the piezoelectric voltage v_p can be formulated by the following piece-wise equation:

$$v_p(t) = V_{oc}\times \begin{cases} \cos\varphi - \cos(\omega t), & \varphi \leq \omega t < \pi + \varphi; \\ -\cos\varphi - \cos(\omega t), & \pi + \varphi \leq \omega t < 2\pi + \varphi. \end{cases} \tag{2.11}$$

Through a Fourier analysis, the fundamental harmonic of v_p can be derived based on the piecewise expressions in (2.11). The fundamental component of v_p is denoted as $v_{p,f}$ [21]. Based on harmonic analysis, the dynamics of SP-SECE can be formulated in terms of equivalent impedance, which is obtained in the frequency domain as follows:

$$Z_e = \frac{1}{\omega C_p}\left[\frac{2}{\pi}\left(1 + \cos 2\varphi - j\sin 2\varphi\right) - j\right]. \tag{2.12}$$

2.A.2 Displacement Amplitude of the Parasitic Resonators

In order to solve the governing equations representing the graded-harvester, the solution of the host beam deflection is obtained with the separation of variables as $w(x,t) = \sum_{n=1}^{N} \phi_n(x)\eta_n(t)$, where ϕ_n and η_n represent the mode shape and modal coordinate of the n^{th} mode, respectively. By substituting this latter into Eq. 2.4, applying the orthogonality relationships for ϕ_m, and assuming harmonic excitation and solutions [55], the relative displacement amplitude of r^{th} pair of parasitic resonators can be expressed as:

$$U_r = \frac{\omega^2 W_b + \omega^2 \sum_{n=1}^{N} H_n \phi_n(x_r)}{\left(1 + K_{er}/k_{mr}\right)\omega_r^2 + j2\left(1 + D_{er}/D_{mr}\right)\zeta_r\omega_r\omega - \omega^2}, \tag{2.13}$$

where W_b and H_n represent the amplitude of the harmonic base excitation and the n^{th} mode modal amplitude, respectively.

Then, by plugging Eq. 2.13 into the modal form of Eq. 2.4, the governing equation can be simplified as:

$$\left(\omega_m^2 - \omega^2\right)\frac{H_m}{mL} - \omega^2 \sum_{n=1}^{N}\sum_{r=1}^{R} \hat{M}_r C_r \phi_m(x_r)\,\phi_n(x_r)\,H_n = Q_m \tag{2.14}$$

where $\hat{M}_r = 2M_r/(mL)$ is the normalized equivalent mass of r^{th} pair of parasitic res-

onators. The coefficient C_r and the modal force item Q_m can be expressed as:

$$\begin{aligned} C_r &= 1 + \frac{\omega^2}{\left(1 + K_{er}/k_{mr}\right)\omega_r^2 + j2\left(1 + D_{er}/D_{mr}\right)\zeta_r\omega_r\omega - \omega^2}, \\ Q_m &= W_b\omega^2\left(\sum_{r=1}^{R}\hat{M}_r C_r\phi_m\left(x_r\right) + \frac{1}{L}\int_0^L \phi_m(x)dx\right). \end{aligned} \tag{2.15}$$

By writing Eq. 2.14 into matrix form and accounting for the contributions of all N modes together, the modal amplitude H_n can be solved by matrix inversion. Finally, by substituting H_n back into Eq. 2.13, U_r can be solved.

Chapter 3

Circuit Solution for Controlling Nonlinear Dynamics

Paper Details

The following chapter was published on October 01, 2023, as:
"**Zhao, B.**, Wang, J., Hu, G., Colombi, A., Liao, W.H. and Liang, J., 2023. Time-sharing Orbit Jump and Energy Harvesting in Nonlinear Piezoelectric Energy Harvesters Using a Synchronous Switch Circuit. *Mechanical Systems and Signal Processing*, 200, p.110601"
DOI: https://doi.org/10.1016/j.ymssp.2023.110601 - Under a Creative Commons license.
This is a post-print version of the article, which differs from the published version only in terms of layout, formatting, and minor amendments that have been implemented in the text to adapt the original paper to the format of the thesis and improve readability.

Author and Co-authors Contributions

The author of this thesis proposed the conceptualization of the circuit solution for orbit jump in nonlinear piezoelectric energy harvesting systems. He also took charge of the theoretical analyses by electrical impedance modeling and the nonlinear time-domain simulations by multiple time scales method. Dr. J. Wang and Prof. Dr. G. Hu contributed to the experiments. Prof. Dr. W.H. Liao, Prof. Dr. J. Liang, and Dr. A. Colombi provided overall supervision and guidance.

Key Findings

- A self-contained solution for time-sharing orbit jump and energy harvesting in nonlinear piezoelectric energy harvesting by using a switched-mode circuit.
- Vibration energy is harvested and accumulated for later vibration exciting, such that to achieve vibration in the high-energy orbit.

- Phase evolution by multi-scale method, which reveals the mechanism of orbit jump, is theoretically studied.
- The harvested power yields a nine-fold increase after attaining the high-energy orbit compared with that in the low-energy orbit.

General comments and link to the next chapter

This chapter introduces the reader to the realm of nonlinear dynamics and active control to fulfill the second objective of this thesis (see Section 1.4). It initiates the investigation of the electromechanical dynamics of nonlinear piezoelectric harvester and proposes a circuit solution of **energy harvesting** and **vibration actuating** for self-contained orbit jumps. In addition, the preliminary results herein unveil the promising potential of nonlinear oscillators in dynamics control, hence laying the foundations for further in-depth research on nonlinear metamaterials to follow in Chapter 4.

Abstract

Nonlinearity has enabled energy harvesting to advance towards higher power output and broader bandwidth in monostable, bistable, and multistable systems. However, operating in the preferable high-energy orbit (HEO) rather than the low-energy orbit (LEO) for making such advancement has restricted their applications. Based on a monostable nonlinear system, this paper proposes a self-contained solution for time-sharing orbit jump and energy harvesting. The joint dynamics of an electromechanical assembly consisting of a nonlinear energy harvester and a switched-mode piezoelectric interface circuit for high-capability energy harvesting is studied. The proposed solution is carried out by utilizing a cutting-edge switched-mode bidirectional energy conversion circuit (BECC), which enables time-sharing dual functions of energy harvesting and vibration exciting. A theoretical model is established based on impedance analysis and multiple time scales method to analyze the stability, frequency response, and phase evolution of the autonomous and nonautonomous nonlinear energy harvesting systems. In particular, the detailed dynamics for the orbit jumps with the vibration exciting mode of BECC are studied. Experiments are performed to validate the full-hysteresis-range orbit jumps with the monostable nonlinear energy harvester. The harvested power after orbit jumps yields a nine-fold increase, compensating for the energy consumption under vibration exciting mode quickly. The proposed solution also refrains the system from extra mechanical or electrical energy sources for orbit jumps, which leads to the first self-contained solution for simultaneous energy harvesting and orbit jump in nonlinear piezoelectric energy harvesting. This work enhances the practical utility of nonlinear energy harvesting technologies toward engineering applications.

3.1 Introduction

Energy harvesting has been widely investigated over the last two decades as a potential solution for powering wireless sensor nodes in Internet of Things (IoT) applications. It enables the system to collect and convert energy, which opens up opportunities for self-sustaining systems [142]. According to application scenarios, different technologies may target solar energy, thermal energy, or vibration energy [143]. Among them, vibration energy harvesting draws massive attention due to its easy accessibility in the ambient environment. The most investigated electromechanical transduction mechanisms include the piezoelectric, electromagnetic, and electrostatic ones [144].

This paper focuses on piezoelectric energy harvesting (PEH) as a result of its high power density and compatibility in small-scale systems. Previous efforts have been made to improve power output and broaden the bandwidth of energy harvesters [145].

For one thing, mechanically, multi-resonance [54] and frequency-self-tuning [146] structures were developed to create a resonance condition for broadening the effective energy harvesting bandwidth. However, their power density and overall capability are inferior, compared with the nonlinear mechanical design [147]. To form a nonlinear energy harvester, attractive or repulsive forces, asymmetric geometry, and post-buckling configuration are usually utilized [148]. The caused nonlinearity expands the working bandwidth and may increase the power output, owing to the hardening or softening effects. Never-

theless, at the same time, the consequent hysteresis creates multiple root branches where the high-energy orbit (HEO) and the low-energy orbit (LEO) coincide [149]. For the objective of energy harvesting, the oscillation on HEO with a much higher power output is preferable. The studies of orbit jump in the energy harvesting field started by Erturk et al. [26], Sebald et al. [150], and Masuda et al. [151] in the early 2010s by methods of external impacts by hands, high voltage excitation with piezoelectric actuators, and negative resistance, respectively. Since then, different methods have been proposed for this target. The majority of the orbit jump methods utilize the system parameter tuning or perturbation strategies to force or perturb the oscillator out of its original LEO and seek the path to the HEO in the phase space, including negative impedance [152, 153], load perturbation [154], stiffness modulation [155], buckle level modulation [156, 157]. Meanwhile, other methods enable extra energy injected into the oscillator, which also facilitates the orbit jumps, including energy transfer by projectile impact [158], piezoelectric voltage excitation [159], magnetic plucking with bistable energy harvesters [160], attractor selection [161], sliding mode control methods [162, 163], and excitation tuning [100]. These methods were analytically and experimentally demonstrated, but these solutions are still tough to be implemented outside the laboratory since most of them rely on extra devices or energy sources to adjust their states. In addition, the energy or control cost of tuning the parameter may outweigh the overall outcome. In general, there are two common issues for carrying out these existing methods.

- An extra energy source, which is capable of intensive mechanical drive output, is required.
- An intensive energy injection, if introduced at an improper phase, may induce much negative work and reduces the actuating efficiency.

Therefore, more controllable, self-contained, and efficient energy injection methods for orbit jumps are still in demand to practically enhance the nonlinear energy harvester performance and implement the energy harvester in the field.

For another, electrically, many piezoelectric interface circuits are proposed. The linear AC energy harvesting circuit of a pure resistive load has reactive power under some phase ranges [21]. To better improve the power factor, more advanced nonlinear AC-DC circuits, required by most electronic devices, were developed. The standard energy harvesting circuit utilizes the rectifier and smoothing capacitor to output a DC voltage to the load [164]. Afterward, different charge manipulation approaches were employed to increase the power output further. The parallel or series synchronized switch harvesting on inductor (SSHI) circuits flips the piezoelectric voltage at displacement extreme over an inductor. They enlarge the harvested power by several folds [27, 165]. The synchronized electric charge extraction (SECE) circuit enhances the power output and has a load-independent feature [166]. Combining the SSHI and SECE concepts created the double synchronized switch harvesting circuit, which allows control of the extraction process and increase of voltage [167]. The synchronized triple bias-flip (S3BF) circuit [168] is proposed to reduce the switching loss and increase the voltage level by introducing three successive voltage bias-flips during each voltage-flip process. Based on this circuit, Zhao et al. [23, 30] proposed the bidirectional energy conversion circuit (BECC) by removing

the bridge rectifier. The BECC enables the dual functions of energy harvesting and vibration exciting by using the same circuit in a time-sharing manner. Compared with the applications in linear energy harvesting systems, some recent works have investigated these interface circuits with nonlinear energy harvesters to explore the joint dynamics [169–171]. Their results showed that the circuit might further extend the systems' bandwidth and increase the power output [145]. But how to ensure a vibration in the HEO in the inherent hysteresis range has not been addressed. As for the S3BF circuit, its interaction with a nonlinear energy harvester is not well-studied yet.

Although many efforts have been taken to enhance the power output and broaden the bandwidth of energy harvesters, general modeling methods covering both mechanical dynamics and electrically induced dynamics are quite deficient. Besides, present orbit jumps heavily rely on extra intensive mechanical or electrical energy sources, which is not realistic in practical applications. This work uses an impedance model and multiple time scales method to investigate the joint dynamics of a monostable energy harvester connected with the BECC circuit. Based on the dual functions of this circuit, this research proposes an efficient vibration exciting strategy for orbit jumps to enhance the harvested power and bandwidth for nonlinear energy harvester.

This paper is organized as follows. Following the introduction, the integration of the monostable energy harvester and BECC is presented in Section 3.2. The equivalent impedance model and electrically induced parameters are defined. In Section 3.3, the dynamics of the integrated system are investigated. Firstly, the stability analysis of an autonomous case is studied to reveal the effects of different operation modes on the dynamics of the nonlinear harvester. Next, the nonautonomous systems' frequency response and state-space phase evolution are performed with a multiple time scales method. The detailed steps for orbit jump from low-energy orbits to high-energy orbits are analyzed. Section 3.4 presents the experimental results for orbit jumps of the nonlinear energy harvesting system with BECC. An energy evaluation is conducted to quantify the overall energy consumption during orbit jumps. Section 3.5 discusses the extension of this orbit jump solution further to a bistable energy harvesting system. Finally, the conclusions are drawn in Section 3.6.

3.2 System Overview

3.2.1 Nonlinear PEH System using BECC

As Figure 3.1 shows, a nonlinear piezoelectric energy harvester is considered. The nonlinearity is introduced by the repelling force of two opposite magnets. A monostable oscillator is achieved by tuning the distance between magnets. The BECC interface circuit, to be explained in the Subsection 3.2.2, is connected with the piezoelectric energy harvester. The equations of motion for the integrated system can be represented as [21]:

$$\begin{cases} M\ddot{x} + C\dot{x} + Kx - K_1 x + K_2 x^3 + \alpha_e v_p = B_f \cos(\omega t) \\ \alpha_e \dot{x} - C_p \dot{v}_p - i_p = 0 \end{cases} \tag{3.1}$$

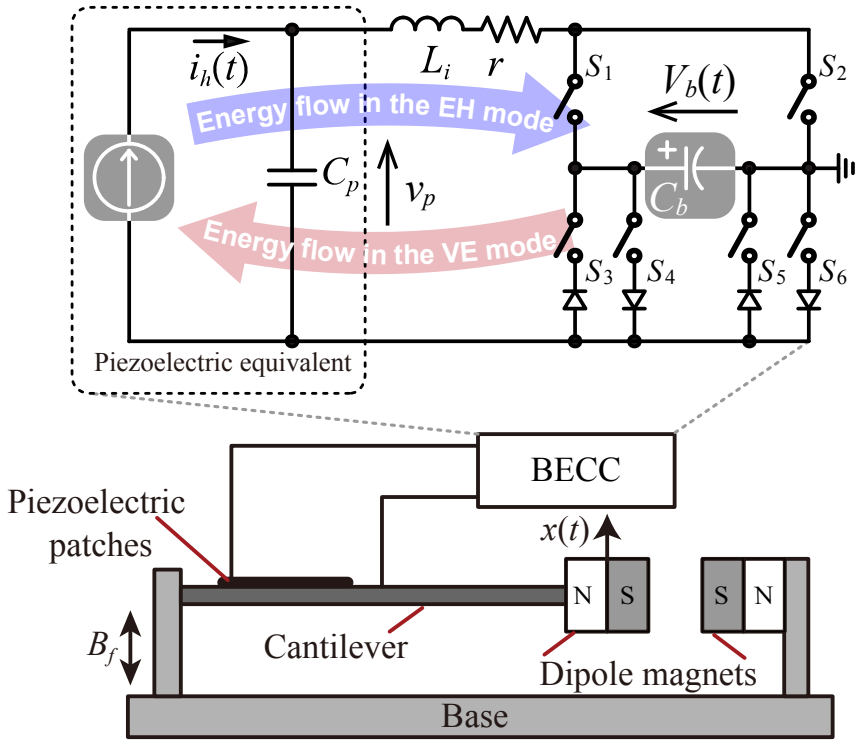

Figure 3.1: System overview of a nonlinear piezoelectric energy harvester with the bidirectional energy conversion circuit (BECC).

where M, C, and K are equivalent mass, damping, and stiffness of the cantilever beam, while K_1 and K_2 denote the coefficients of the nonlinear stiffness caused by magnets, respectively. α_e is the force-voltage factor in the electromechanical coupling. The shaker delivers a harmonic base excitation with an amplitude B_f and frequency ω. C_p is the clamped capacitance of the piezoelectric patch. The displacement of the equivalent mass is denoted by x, and v_p denotes the voltage of the piezoelectric element. i_p represents the current flowing through the interface circuit. In the circuit, C_b bears dual functions of voltage bias-flip and energy storage. An inductor L with an equivalent series resistance (ESR) r facilitates the charge manipulation together with the diode and MOSFET network. System parameters are summarized in Table 3.1.

3.2.2 System Characterization

To quantify the electrically induced dynamics by BECC, we first formulate Z_e the electrical equivalent impedance of the C_p and BECC combination. The current flowing through the C_p and BECC combination is indicated as follows:

$$i_h(t) = \alpha_e \dot{x}(t), \tag{3.2}$$

where i_h is a periodic current with the possibility of higher-order harmonics due to the presence of cubic nonlinearity in (3.1). For a linear energy harvester, i_h only contains the fundamental harmonic, and voltage flips occur at current crossing zero points (displace-

ment extremes). While cubic nonlinear energy harvesters span from periodic to chaotic oscillations, these high-order harmonics and chaotic oscillations may induce multiple voltage flips in one fundamental oscillation cycle. To prevent these behaviors, we employ a switch resting time after each voltage flip and assume weak nonlinearity in the system for periodic solutions. Therefore voltage v_p could still have a first-order resonant period, which can be formulated with a piecewise equation as follows:

$$v_p(t) = \begin{cases} \dfrac{1}{C_p}\displaystyle\int_0^t i_h(t)\mathrm{d}t - V_M, & 0 \le t < \dfrac{\pi}{\omega}; \\ V_M - \dfrac{1}{C_p}\displaystyle\int_{\frac{\pi}{\omega}}^t i_h(t)\mathrm{d}t, & \dfrac{\pi}{\omega} \le t < \dfrac{2\pi}{\omega}, \end{cases} \tag{3.3}$$

where V_M is the final voltage after the M^{th} bias-flip actions in each synchronized instant [30]. It can be expressed as a function of the bias voltage V_b and the open-circuit voltage V_{oc} according to the equations for energy harvesting modes and vibration exciting modes of BECC [30]. With the definition of the open-circuit voltage as the voltage accumulation on the clamped capacitor C_p during a quarter of a vibration cycle, V_{oc} reads:

$$V_{oc} = \frac{1}{2C_p}\int_0^{\frac{\pi}{\omega}} i_h(t)\mathrm{d}t. \tag{3.4}$$

In (3.3), $V_M < 0$ corresponds to energy harvesting modes, and $V_M > 0$ corresponds to vibration exciting modes. Different M number indicates the bias-flip action times. In this paper, we choose $M = 3$ and realize the S3BF energy harvesting mode and S3BF vibration exciting mode of BECC. These two modes are simply referred to as the energy harvesting (EH) mode and the vibration exciting (VE) mode of BECC. Figure 3.2 (a) and (c) show the voltage and current waveform under the EH and VE modes of BECC. The switching sequence which controls different MOSFETs in Figure 3.1 is referenced in [30]. The enlarged view in Figure 3.2 (b) and (d) illustrate the intermediate voltages at a falling edge and a rising edge, which are influenced by the flipping factor $\gamma \in (-1, 0)$ [30]. Under EH mode, the piezoelectric voltage v_p is in-phase with the oscillator velocity $\dot{x}$ (also with piezoelectric current i_h), which indicates the energy flow from the mechanical structure into the interface circuit. In contrast, the out-of-phase condition happens under VE mode. It should be noted that v_p is a piecewise and continuous function with respect to the oscillator velocity $\dot{x}$. The piezoelectric coupling force $\alpha_e v_p$ is also a piecewise and continuous force, which does not have a high degree of smoothness. However, here we employ the first-order assumption to avoid the tedious expansion and focus on weak nonlinear monostable systems. A complete solution that addresses higher-order harmonics induced by circuits will be discussed in future work.

By studying the magnitude and phase relation between the fundamental harmonic of v_p and i_h, we can formulate the equivalent impedance of the clamped capacitor C_p and

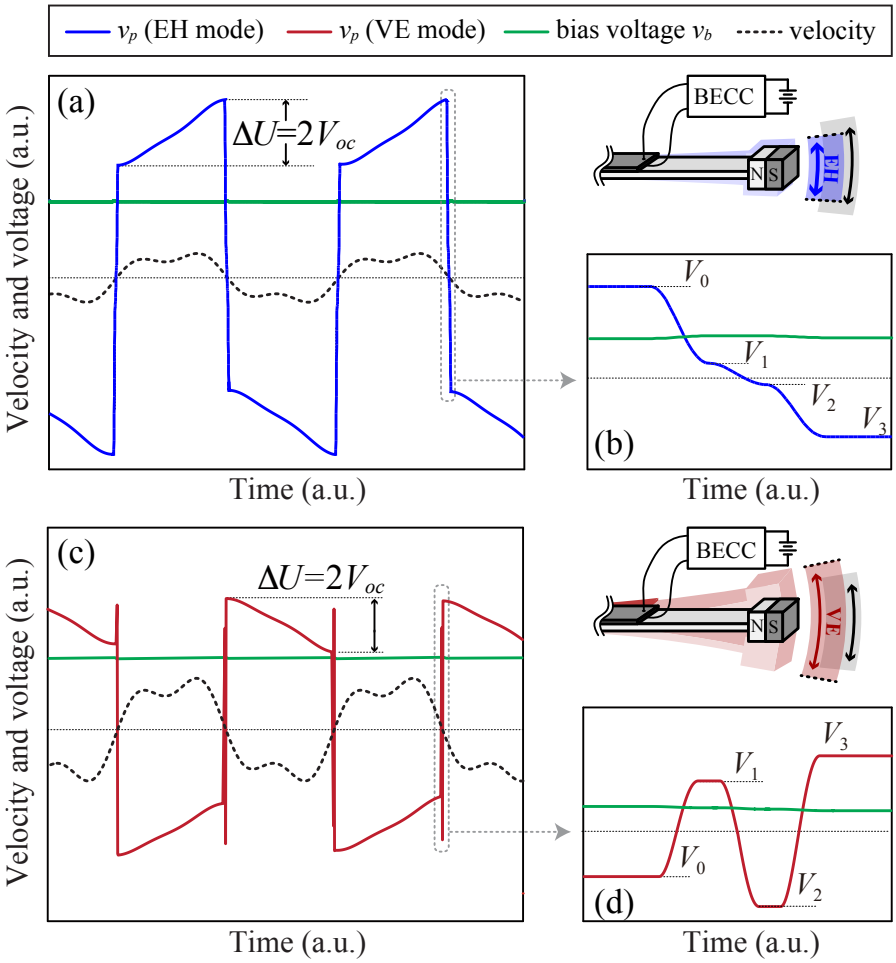

Figure 3.2: The waveform in different operation modes of BECC. (a) Energy harvesting (EH) mode; (b) The enlarged view of a falling edge showing the bias-flip actions; (c) Vibration exciting (VE) mode; (d) The enlarged view of a rising edge showing the bias-flip actions.

BECC combination in the frequency domain [172] as follows:

$$Z_e(j\omega) = \frac{V_{p,f}(j\omega)}{I_h(j\omega)} = \frac{1}{\omega C_p}\left[\frac{4}{\pi}\left(1-\tilde{V}_M\right)-j\right], \tag{3.5}$$

where $V_{p,f}$ is the magnitude of the fundamental harmonic of v_p. $\tilde{V}_M$ is the V_{oc} normalized final voltage after flipping. According to the electromechanical analogy, the electrical impedance can be represented by mechanical parameters as follows [21]:

$$\begin{aligned} C_e &= \alpha_e^2\,\mathrm{Re}\{Z_e\} \\ K_e &= -\omega\alpha_e^2\,\mathrm{Im}\{Z_e\}, \end{aligned} \tag{3.6}$$

where C_e and K_e are the electrically induced damping and stiffness. K_e is a constant value since the imaginary part of Z_e is constant, which represents the added stiffness from C_p. On the other hand, the tuning range of C_e depends on the load condition of BECC determined by the intermediate voltages [23]. The electrically induced damping range for

EH mode is given as follows:

$$\left\{ C_e \in \mathbb{R}^+ \left| \frac{4\alpha_e^2(1-\gamma)}{\omega\pi C_p} \leq C_e \leq \frac{4\alpha_e^2(3-3\gamma)}{\omega\pi C_p(1+\gamma)} \right. \right\}. \tag{3.7}$$

It can be seen that under the fundamental harmonic assumption, the dependence of C_e on the oscillator velocity is canceled. In EH mode, C_e is positive, which indicates that the nonlinear oscillator is damped for energy harvesting purposes. The stored energy in the bias/storage capacitor can be used for vibration-exciting propose. Therefore, with the maximum bias voltage $v_{b,max} = 2V_{oc}(1-\gamma)/(1+\gamma)$ [23], the range of C_e under VE mode reads:

$$\left\{ C_e \in \mathbb{R}^- \left| \frac{-4\alpha_e^2(3\gamma^4 - 5\gamma^3 + 8\gamma^2 - 7\gamma + 1)}{\omega\pi C_p(1+\gamma)^2(\gamma^2 - \gamma + 1)} \leq C_e < 0 \right. \right\}. \tag{3.8}$$

In VE mode, C_e is negative. Therefore, adding C_e to mechanical damping C reduces the total damping for higher vibration amplitudes. It could even form a gross effect of negative damping corresponding to an actuation force, which excites the oscillator from a quiescent state [30].

3.3 Time-sharing Orbit Jumps

In order to facilitate the nonlinear oscillator to reach the HEO for more harvested energy, the main idea is to perturb the oscillator into the basin of attractions for HEOs, regardless of the method used. Therefore, stability analysis and state-space evaluation are necessary to reveal the mechanism of orbit jumps and the influence of the proposed orbit jump solution by the time-sharing operations of BECC.

3.3.1 Autonomous Case

We first analyze the stability of the nonlinear oscillator without external excitation force, which forms an autonomous system with the equation of motion:

$$M\ddot{x} + C\dot{x} + Kx - K_1x + K_3x^3 + K_ex + C_e\dot{x} = 0, \tag{3.9}$$

where the electrically induced C_e and K_e can be determined with (3.6) to (3.8). By writing (3.9) into state-space form, this nonlinear oscillator can be represented as follows:

$$\begin{cases} \dot{x} = y, \\ \dot{y} = -\omega_0^2 x - k_3 x^3 - cy, \end{cases} \tag{3.10}$$

where y represents the velocity of the oscillator. $\omega_0^2 = (K + K_e - K_1)/M$, $k_3 = K_3/M$, $c = (C + C_e)/M$ are the mass M normalized gross effect of linear stiffness, nonlinear cubic stiffness, and the gross effect of linear damping, respectively. Since ω_0^2 is a constant parameter above zero, this nonlinear oscillator is a monostable nonlinear oscillator with a fixed point x_p at the origin. The linearization of the dynamics around the fixed point

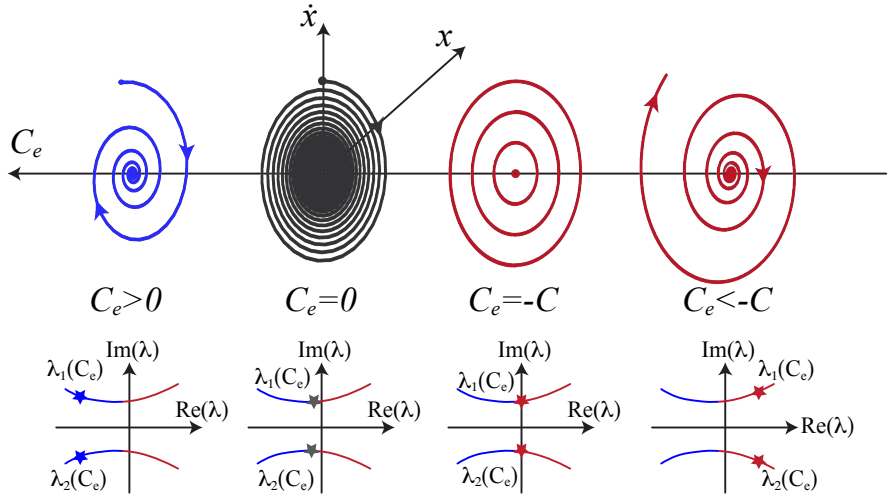

Figure 3.3: Four different phase portraits correspond to different C_e with the eigenvalues depending on C_e.

can be determined by the Jacobian matrix:

$$\boldsymbol{J} = \begin{bmatrix} 0 & 1 \\ -\omega_0^2 - k_3 x^2 & -c \end{bmatrix}. \tag{3.11}$$

By substituting $x = x_p = 0$, we obtain the eigenvalues:

$$\lambda_{1,2}(C_e) = -\frac{c}{2} \pm \frac{\sqrt{c^2 - 4\omega_0^2}}{2}. \tag{3.12}$$

Assuming $4\omega_0^2 > c^2$, the eigenvalues are a pair of complex conjugates. The sign of their real parts is determined by the sign of c. Therefore, the linearized dynamics around the fixed point also depend on the sign of the real part of the eigenvalues. When $c = 0$, the two eigenvalues are purely imaginary, indicating that a two-dimensional center manifold will be determined around the origin. However, different from the nonlinear stiffness K_3 dependent center manifold, which features a Hopf bifurcation with limit cycles on one side of the origin [149]. There is no limit cycle on either side of the bifurcation point when the damping C_e is chosen as a dependent parameter.

Figure 3.3 illustrates four different phase portraits from time-domain integration corresponding to four C_e cases. $C_e = 0$ corresponds to the original nonlinear oscillator without BECC, whose phase portrait is a stable spiral with its original damping C. Under EH mode, the total damping $C + C_e$ becomes larger; therefore, the phase portrait also shows a stable spiral but decays faster to the origin. When $C_e = -C$ for VE mode, the origin becomes a nonlinear center. This is a special case of a degenerate Hopf bifurcation, where the eigenvalues have purely imaginary parts. As C_e further decreases when $C_e < -C$, the real parts of eigenvalues become positive. This corresponds to an unstable spiral such that a self-excited oscillator is formed to achieve higher vibration amplitudes.

3.3.2 Nonautonomous Case

Besides the autonomous stability analysis, we also explore the frequency response of this nonlinear energy harvester under an external periodic driving force around the primary resonance of the nonlinear oscillator. With the assumptions of weak damping, nonlinear reaction force, and weak external force, the governing equation of the nonlinear oscillator with BECC can be written as follows:

$$\ddot{x} + c\dot{x} + \omega_0^2 x + k_3 x^3 = b_f \cos(\omega t), \tag{3.13}$$

where $b_f = B_f/M$ is the mass normalized force amplitude, and ω is the base excitation frequency. Note that an analytical approximation for (3.13) takes the following form:

$$x(t) = a(t)\cos[\omega t + \varphi(t)] + O(\varepsilon), \tag{3.14}$$

where $a(t)$ and $\varphi(t)$ are slowly time-varying real-valued amplitude and phase. This solution can be constructed with asymptotic series through the multiple time scales method [173]. The detailed derivation of the slow flows is documented in Appendix. 3.A. The state space governing equations of them are given as:

$$\begin{aligned} \frac{\mathrm{d}a}{\mathrm{d}t} &= -\frac{ac}{2} - \frac{b_f}{2\omega}\sin\varphi, \\ \frac{\mathrm{d}\varphi}{\mathrm{d}t} &= \frac{\omega_0^2 - \omega^2}{2\omega} + \frac{3k_3a^2}{8\omega} - \frac{b_f}{2\omega a}\cos\varphi. \end{aligned} \tag{3.15}$$

The two derivatives describe the slow flows of the amplitude and phase. Under a steady state, the fixed points or the amplitudes and phase can be obtained by equating the right-hand side to zero as follows:

$$\begin{aligned} \frac{ac}{2} &= -\frac{b_f}{2\omega}\sin\varphi, \\ \frac{a(\omega^2 - \omega_0^2)}{2\omega} - \frac{3k_3a^3}{8\omega} &= -\frac{b_f}{2\omega}\cos\varphi. \end{aligned} \tag{3.16}$$

Squaring and adding the two equations in (3.16) yields the frequency response function of the nonlinear energy harvester:

$$\frac{a}{b_f} = \frac{1}{\sqrt{c^2\omega^2 + \left(\omega^2 - \omega_0^2 - \frac{3}{4}k_3a^2\right)^2}}. \tag{3.17}$$

Alternatively, (3.13) can also be solved by using the harmonic balance method [84]. The expression of the solution has the same form as (3.17) with first-order harmonic assumption. The steady-state displacement amplitude of the nonlinear energy harvester is shown in Figure 3.4. It can be seen that, due to the cubic nonlinear stiffness, the frequency response has a hardening effect with the presence of a hysteresis range. The two stable fixed points from (3.16) and an unstable fixed point give rise to the upper and lower

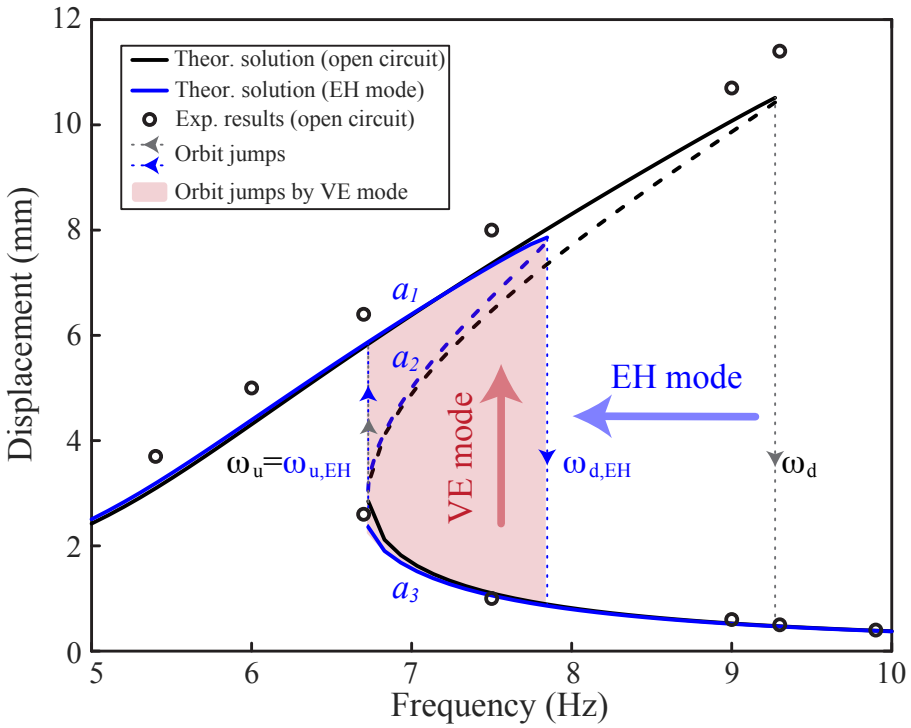

Figure 3.4: Theoretical and experimental frequency response of the nonlinear energy harvester. The black lines represent the open-circuit case. The blue lines represent the energy harvesting case. The red shadow region indicates the hysteresis region where orbit jumps can be realized from LEO to HEO.

branches, which forms the hysteresis range between the two gray dash lines in Figure 3.4.

In order to quantify the influence of electrically induced damping C_e on the hysteresis range of the nonlinear harvester, the two critical frequency ω_u and ω_d for up and down orbit jumps can be determined by imposing the derivative $\mathrm{d}\omega/\mathrm{d}a = 0$ in (3.17). Under the weak damping assumption [174], the two critical frequencies read:

$$\omega_u = \omega_0 \left[1 + \frac{1}{2} \left(\frac{3}{2} \right)^{4/3} \left(\frac{k_3 b_f^2}{\omega_0^6} \right)^{1/3} \right], \tag{3.18}$$

$$\omega_d = \frac{\omega_0}{\sqrt{2}} \left[1 + \left(1 + \frac{3k_3 b_f^2}{\omega_0^4 c^2} \right)^{1/2} \right]^{1/2}. \tag{3.19}$$

It can be seen that ω_u does not depend on the damping coefficient while ω_d does. This dependence on damping leads to the decrease of ω_d from an open-circuit case to an energy harvesting case due to a more significant gross effect of total damping c as shown in Figure 3.4. Therefore, orbit jumps from low-energy orbits to high-energy orbits take effect in the hysteresis range of a nonlinear harvester under EH mode indicated by the red shaded area in Figure 3.4.

When a slowly varying parameter C_e is introduced, the frequency-domain analysis based on the steady-state assumption in (3.16), like harmonic balance, are no longer applicable.

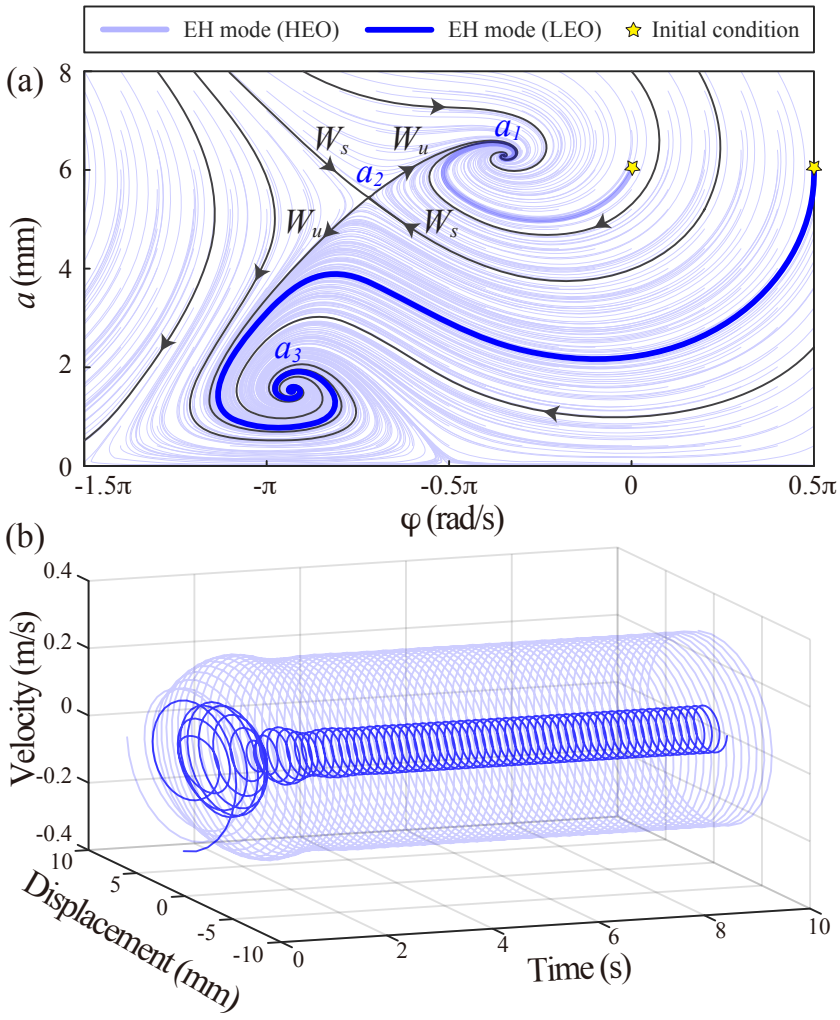

Figure 3.5: Phase portrait and phase evolution under EH mode with base excitation frequency at 7 Hz. (a) (a, φ) phase portrait; (b) Displacement and velocity $(x, \dot{x})$ phase evolution over time.

Thus, in this paper, we utilize the state-space equations in (3.32) to better illustrate the influence of varying electrically induced damping C_e with a periodic harmonic excitation force. The stability of the fixed points and solution branches of the nonlinear oscillator can be determined by the Jacobian of the slow flows in (3.32) as follows:

$$\boldsymbol{J} = \begin{bmatrix} -\frac{c}{2} & a\left(\frac{\omega^2-\omega_0^2}{2\omega} - \frac{3k_3a^2}{8\omega}\right) \\ -\frac{1}{a}\left(\frac{\omega^2-\omega_0^2}{2\omega} - \frac{9k_3a^2}{8\omega}\right) & -\frac{c}{2} \end{bmatrix}. \tag{3.20}$$

The eigenvalues of the Jacobian can be solved as follows:

$$\lambda_{1,2} = -\frac{c}{2} \pm \sqrt{\left(\frac{\sigma_\varepsilon}{2\omega} - \frac{3k_3a^2}{8\omega}\right)\left(\frac{9k_3a^2}{8\omega} - \frac{\sigma_\varepsilon}{2\omega}\right)}, \tag{3.21}$$

where $\sigma_\varepsilon = \omega^2 - \omega_0^2$. For EH mode, the gross effect of damping $c < 0$. The stability of three

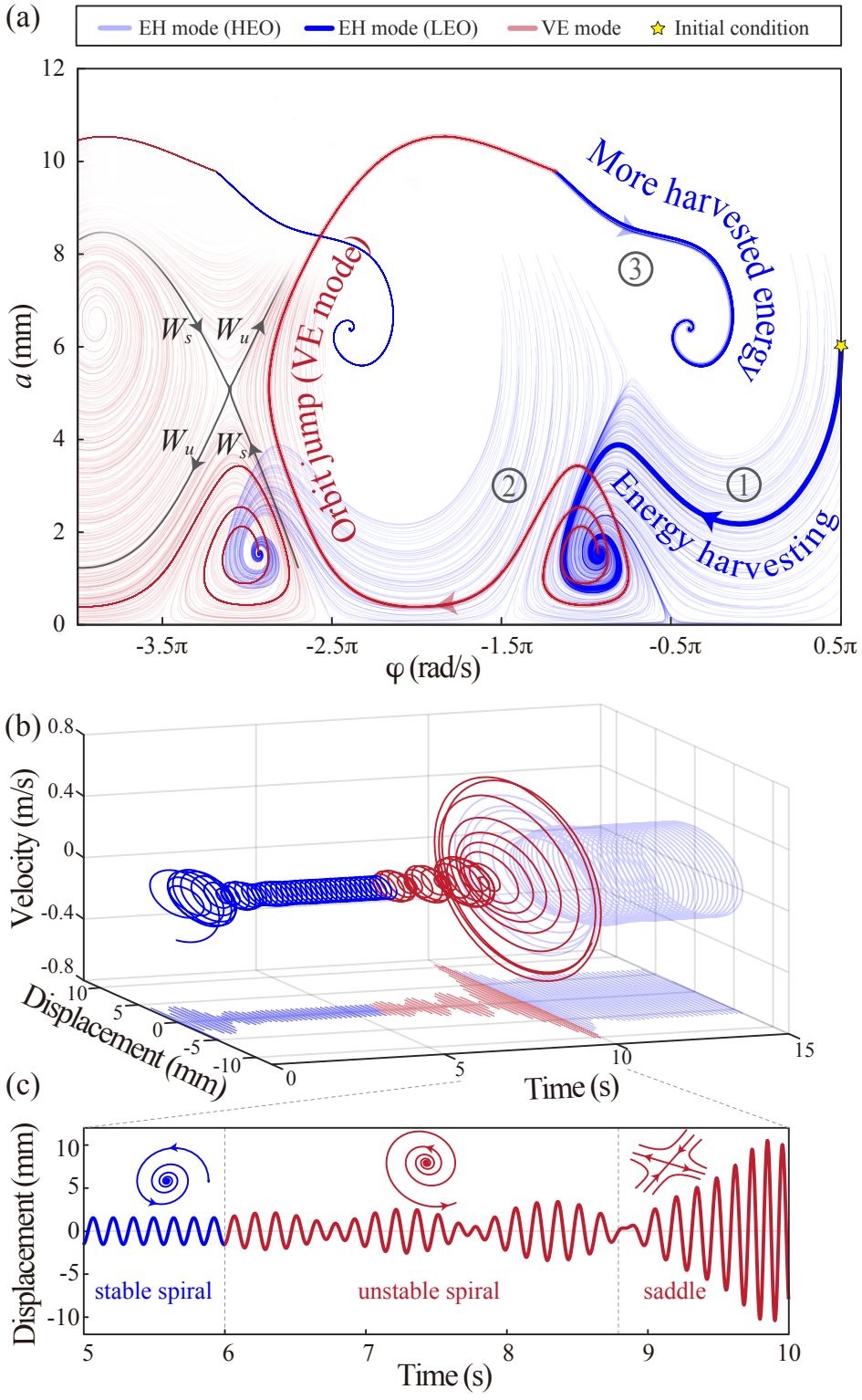

Figure 3.6: Phase portrait and phase evolution of orbit jumps. The system starts from EH mode to VE mode and then to EH mode again under a 7 Hz base excitation. (a) (a, φ) phase portrait with trajectories for orbit jumps; (b) Displacement and velocity $(x, \dot{x})$ phase evolution and its displacement projection over time; (c) The detailed phase evolution of a trail of orbit jump with its stability types.

branches in the hysteresis range indicated with a_1, a_2, and a_3 in Figure 3.4 are determined by their eigenvalues. Taking an example, where $\omega = 2\pi 7$ (rad/s), the two stable fixed points a_1 and a_3 both have a pair of complex conjugate eigenvalues with negative real parts, which create stable spirals. Another unstable fixed point a_2 has a negative and a positive real eigenvalue, which forms a saddle point. As shown in Figure 3.5 (a), this saddle point associates a stable manifold W_s and an unstable manifold W_u, which are tangent to the corresponding eigenvectors. The stable manifold W_s partitions the phase portrait into two regions, which are the basins of attraction of the stable fixed points a_1 and a_3. Different initial conditions attract the trajectories to either a_1 (high-energy orbit) or a_3 (low-energy orbit).

Taking two different initial conditions indicated with yellow stars in Figure 3.5 (a), on both sides of the stable manifold W_s, they finally rest in different energy orbits. As shown with the time evolution of their $(x, \dot{x})$ phase portraits in Figure 3.5 (b), the light blue trajectory for HEO corresponds to the initial condition lies inside the region surrounded by the stable manifold. Therefore, orbit jumps from LEO to HEO equals to shift and tune the (a, φ) phase portrait of the oscillators such that by VE mode of BECC, they can finally be attracted to the high-energy orbit or the a_1 fixed point.

For VE mode, the two stable fixed points a_1 and a_3 in EH mode become unstable if $c < 0$ is satisfied. If we also assume a small absolute value of negative C_e, a_2 will still remain a saddle point. The two unstable spirals and the saddle node are enclosed by red trajectories in Figure 3.6 (a). We first take the initial conditions for LEOs and carry on the orbit jump process. Figure 3.6 (a) shows their phase evolution under different circuit modes. The three steps for orbit jumps labeled with numbers are elaborated as follows:

① The oscillator is first attracted to the fixed point for LEO, and the circuit is initially in EH mode to harvest energy with a positive C_e. The trajectories for this step are stable spirals. All the trajectories attracted to LEO have the same a and φ at steady states. The $(x, \dot{x})$ time evolution for energy harvesting at the LEO is shown with blue curves in Figure 3.6 (b).

② The circuit is switched to VE mode with negative C_e for vibration exciting. The oscillator first leaves the unstable fixed point in the (a, φ) phase portrait in a reverse spiral manner. When trajectories meet the saddle point, they will be first attracted and then repelled by the saddle point into higher displacement amplitudes. The $(x, \dot{x})$ time evolution for vibration exciting is shown with red curves in Figure 3.6 (b).

③ The circuit is switched back to EH mode. The trajectories right now lie in the basin of attraction for the HEO. Therefore, they finally rest in the HEO for more harvested energy. The $(x, \dot{x})$ time evolution in energy harvesting at the HEO is shown with light blue curves in Figure 3.6 (b).

By closely observing the $(x, \dot{x})$ time evolution of orbit jump in Figure 3.6 (c), the displacement envelop depicted by the red curve under the VE mode becomes almost periodic, which is similar to a beat. This is actually due to the phase shift in the (a, φ) phase portrait. At the beginning of vibration exciting, the trajectory slowly leaves the unstable

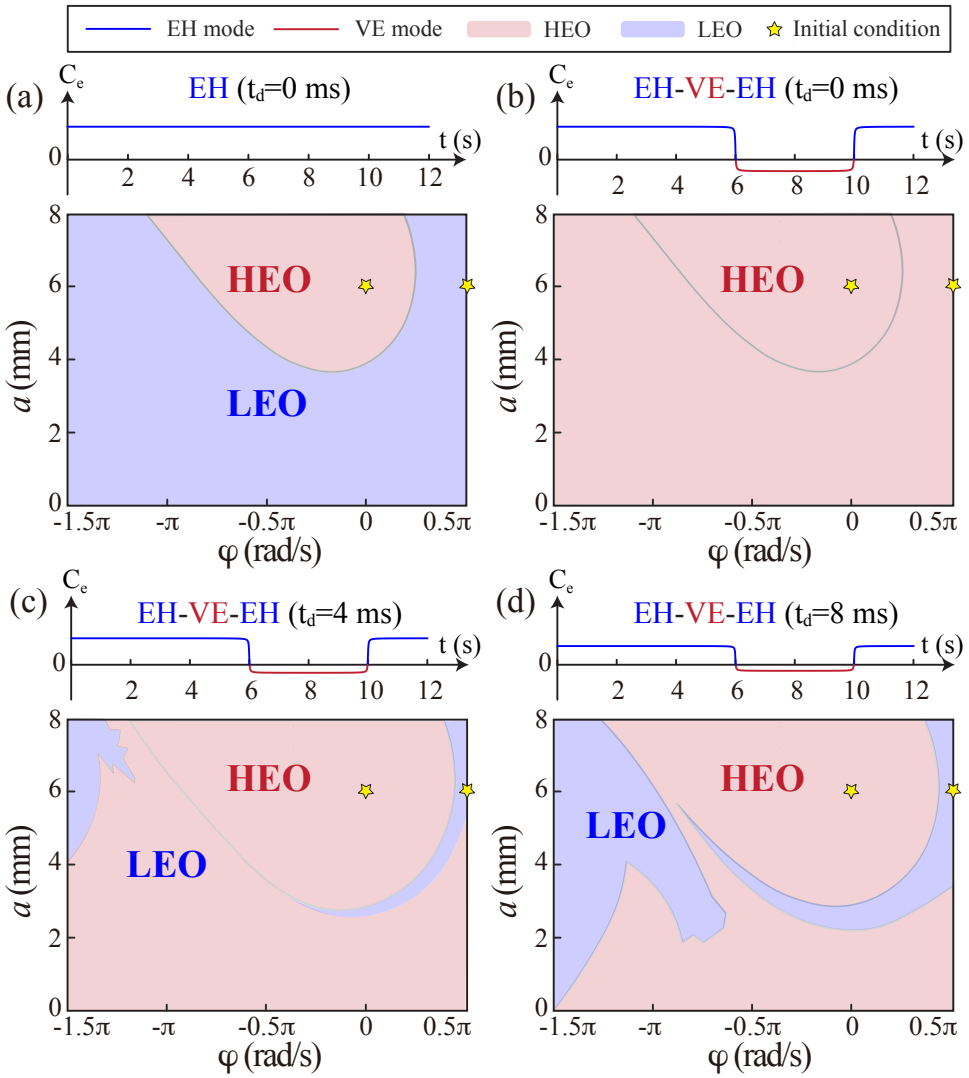

Figure 3.7: The basin of attractions for EH mode and orbit jumps (EH-VE-EH) under different initial conditions and time delays. (a) EH mode with no time delay; (b) Orbit jumps (EH-VE-EH) with no time delay; (c) Orbit jumps (EH-VE-EH) with time delay $t_d = 4$ ms; (d) Orbit jumps (EH-VE-EH) with time delay $t_d = 8$ ms.

fixed point in an unstable spiral manner, during which the displacement amplitude begins to grow. After several cycles, the saddle point attracts and repels the trajectory with the stable and unstable manifolds. During this period, there exist a few cycles of increase and decrease of displacement amplitude, which forms the beating waveform. However, the envelope of the displacement always has an increasing trend due to the negative damping effect. After repelled by the saddle node, the displacement amplitude of the oscillator is amplified and lies in the basin of attraction for the HEO. Therefore, switching the circuit back to EH mode allows the trajectory to be easily attracted to another stable fixed point.

Figure 3.7 shows the evolution of C_e with respect to time and the basin of attractions with different initial conditions. For the EH mode of BECC, as shown in Figure 3.7 (a), C_e maintains a constant positive value which corresponds to a certain load condition for energy harvesting. For the transition from EH to VE mode, C_e turns from a positive to a

negative value starting from 6s to 10s. A smooth transition is applied to avoid undesired numerical instability in the simulations. It can be seen from Figure 3.7 (a) that, for EH mode, the basin of attractions for HEO is surrounded by the stable manifold W_s. While with the phase manipulation by VE mode, the basin of attractions for HEO is extended to all initial conditions in Figure 3.7 (b). The above discussions of the basin of attractions are based on the ideal model that the system does not have time delays. However, in real applications, the laser vibrometer and microcontroller, which form a feedback control loop, may introduce small time delays. The time delay may affect the behavior of a nonlinear energy harvester and its orbit jump. Thus, it is necessary to investigate the effect of time delay in the energy harvesting system. A delay time t_d is therefore introduced to the piezoelectric voltage v_p in (3.3) as follows:

$$v_p^d(t) = \begin{cases} \dfrac{1}{C_p}\displaystyle\int_{\frac{\beta}{\omega}}^{t} i_h \mathrm{d}t - V_M, & \beta \le \omega t < \pi + \beta; \\ V_M - \dfrac{1}{C_p}\displaystyle\int_{\frac{\pi+\beta}{\omega}}^{t} i_h \mathrm{d}t, & \pi + \beta \le \omega t < 2\pi + \beta, \end{cases} \tag{3.22}$$

where $\beta = \omega t_d$ represents a delay phase satisfying $0 < \beta < \pi/2$. Following the same procedures mentioned in Subsection 3.2.2. The equivalent impedance of BECC with a delay time reads:

$$\begin{aligned} Z_e^d(j\omega, \beta) = \frac{4}{\pi\omega C_p}\Big[\cos\beta\left(\cos\beta - \tilde{V}_M\right) \\ + j\left(\sin\beta - \sin\beta\cos\beta - \frac{\pi}{4}\right)\Big]. \end{aligned} \tag{3.23}$$

With the presence of the time delay, the absolute value of the real part of Z_e^d becomes smaller compared with that in (3.5). Therefore, the absolute value of the electrically induced damping C_e also becomes smaller. It not only reduces the gross effect of damping c and harvested power but also decreases the effect of vibration exciting in VE mode. Take a bias voltage $v_b = 2V_{oc}$ as an example. The basin of attractions corresponding to different delay times are illustrated in Figure 3.7 (b) to (d). It can be seen that some initial conditions achieved HEO from LEO with no time delay turn back to LEO eventually in Figure 3.7 (c). This phenomenon is more prominent in Figure 3.7 (d) when $t_d = 8$ ms. Therefore, a larger bias voltage is needed to increase the electrically induced damping and achieve full-hysteresis-range orbit jumps under the same delay time.

3.4 Experiment

In Figure 3.4, the frequency response function of the nonlinear harvester has a hysteresis region between 6.7 Hz and 7.8 Hz. This wide span makes the nonlinear system surpass the linear system in terms of bandwidth. However, there is a premise for making the broadband effect. Because of the dual roots within this hysteresis region, one in LEO and the other in HEO, orbit jump capability is necessary to ensure a high power output. The BECC provides a flexible control to manipulate the energy flow between the mechanical

Table 3.1: System parameters

Harvester geometry:			
Cantilever (mm^3)	90×10×1	Material	Copper
Magnet (mm^3)	10×10×10	Material	Neodymium
Piezoelectric patch (mm^3)	56×7×0.2	Material	PZT
Center-to-center distance of dipole magnets (mm):	32.3		
Mechanical parameters:			
M (g)	8.9	C (Ns/m)	0.011
K (N/m)	52.6	K_1 (N/m)	41.46
K_2 (kN/m^3)	226.7	B_f (mN)	8.9
Electrical parameters:			
α_e (mN/V)	0.127	γ	−0.38
C_p (nF)	35.31	L (mH)	47
r (Ω)	45.2	C_b (μF)	47
R_p (kΩ)	870	MOSFET	ZVN(P)4424

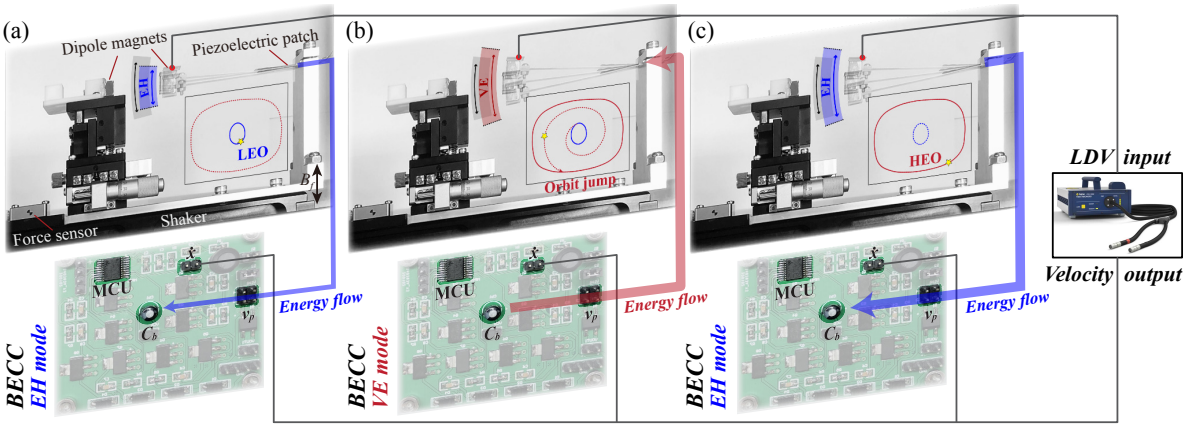

Figure 3.8: Experimental setup and the orbit jump setup. The blue and red shadow lines indicate the energy flows for energy harvesting and vibration exciting. (a) Energy harvesting at LEO with low output power; (b) Orbit jump with vibration exciting mode; (c) Energy harvesting at HEO with high output power.

and electrical ends. With the help of the vibration exciting mode provided by BECC, it is possible to realize the orbit jump using the same switched-mode energy harvesting circuit. This section validates this self-contained time-sharing orbit jump and energy harvesting solution.

3.4.1 Setup

The experimental setup is illustrated in Figure 3.8. A personal computer (PC) controls the base excitation of the energy harvester through a shaker system (APS420, SPEKTRA). A constant base excitation inertial force $B_f = 8.9$ mN is applied to the clamped end of the cantilevered harvester under a constant acceleration magnitude of 1 m/s^2. A laser Doppler vibrometer (OFV-552/5000, Polytec) monitors the tip displacement and velocity

of the oscillator. It sends the information to the PC and a microcontroller (MSP430G2553, Texas Instrument) as an interrupt signal for synchronizing the BECC switch controls. The piezoelectric patch is connected with BECC following a bias/storage capacitor C_b of 47 μF for both energy harvesting and vibration exciting functions. An oscilloscope (HDO6104A, Teledyne) tracks the operation waveform of this nonlinear energy harvesting system. The detailed geometric, mechanical, and electrical parameters of this monostable energy harvester are listed in Table 3.1. The orbit jump setup is also explained in Figure 3.8. As the system is entrained on LEO, as shown in Figure 3.8 (a), the energy harvester collects energy from the vibration source and stores the energy in the bias/storage capacitor at a low rate. As the bias voltage in capacitor C_b reaches 30 V, The BECC is switched to vibration exciting mode. The stored energy is now boosted back into the mechanical structure to amplify the mechanical vibration, as illustrated in Figure 3.8 (b). When the oscillator gradually reaches HEO, BECC is switched back to energy harvesting mode. As a result, the system stabilizes on HEO and realizes higher power output, as shown in Figure 3.8 (c).

3.4.2 Results

With the setup and proposed working mechanism, orbit jumps at different base excitation frequencies are carried out experimentally. One of the experimental trials is shown in Figure 3.9. The magnitude and frequency of the sinusoidal base excitation are 1 m/s^2 and 7 Hz, respectively. The frequency falls in the hysteresis region of the nonlinear oscillator. The red curves note that BECC is under the vibration exciting mode, while the blue curves represent the energy harvesting mode. Two vertical gray planes indicate the mode-transition instants. As we can see from the figure, in the first segment, the system stays at LEO to collect energy at a low rate. At 1.6 s, the vibration exciting mode of BECC is turned on by the microcontroller on the PCB board of BECC. The vibration-exciting actions send energy back from the bias/storage capacitor C_b to the oscillator to provoke large oscillations. Accordingly, the oscillator vibration amplitude grows gradually and jumps over HEO by the saddle node. Afterward, the BECC is switched back to the energy harvesting mode. The system remains on HEO and harnesses energy at a larger power. During the vibration exciting process, the system experiences the oscillation patterns mentioned above in Figure 3.6, as the projected displacement trajectory shows. The gradual increase of displacement amplitude due to the unstable spiral and the saddle node together accounts for the success of orbit jumps. A video clip (Orbitjump.mp4) recording the orbit jumps of the energy harvester is attached with the paper.

In one of our previous conference papers [175], it has been shown that the VE mode of BECC can realize orbit jumps by utilizing the energy stored in the bias/storage capacitor. Here we take a detailed evaluation of energy consumption and recovery. As mentioned above, the piezoelectric voltage is captured and shown in Figure 3.10 for an orbit jump trial. The peak voltage for the EH mode has been amplified several times after the orbit jump. During vibration exciting, the exciting voltage gradually decreases with voltage drop on the bias/storage capacitor. The enlarged views show the nonlinear oscillator's detailed voltage and velocity waveform for VE and EH modes, respectively. The out-of-

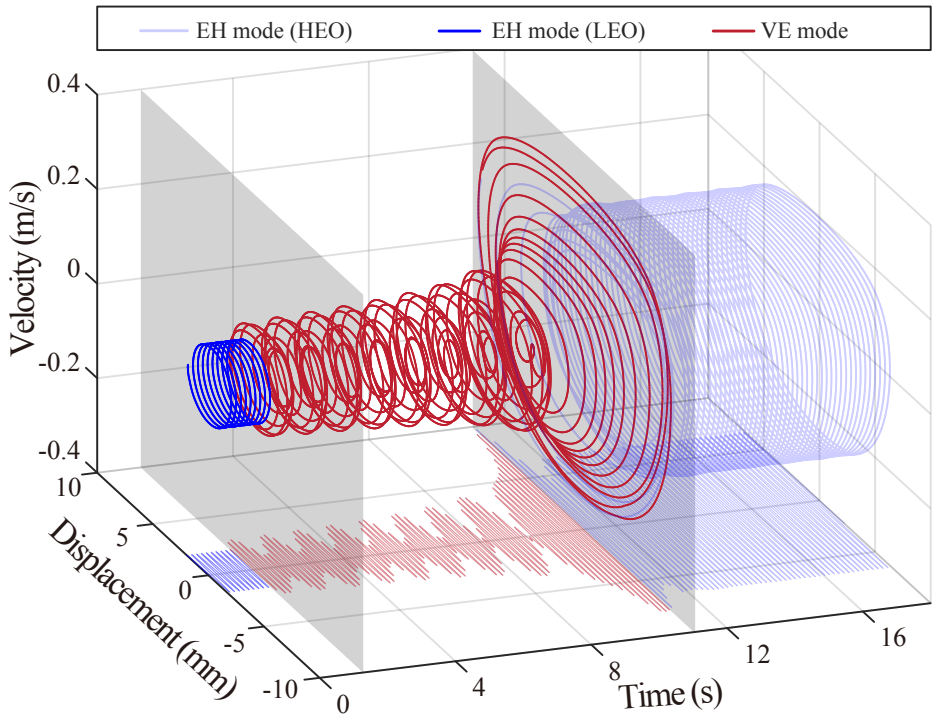

Figure 3.9: A trial of experimental orbit jump in a monostable nonlinear energy harvester with BECC. The curves represent the displacement and velocity $(x, \dot{x})$ phase evolution over time. The orbit-jump segment under VE mode is illustrated in red within two vertical gray planes, which indicate the mode transitions.

phase and the in-phase relationships between piezoelectric voltage and velocity correspond to the energy flow from the electrical to the mechanical domain and reverse directions, respectively, in the nonlinear harvesting system. The energy flow directions agree with the voltage drop and rise across C_b under different operation modes.

The energy gain and loss of the bias/storage capacitor C_b are studied to evaluate the energy consumption of orbit jumps. In the whole orbit-jumping process, the energy is consumed in the microcontroller for switching control, vibration excitation, and also in dissipation in parasitic resistance. Neglecting the minor expenditure in the microcontroller [23], the energy consumption for the orbit jump can be calculated as follows:

$$E_{VE} = \frac{1}{2} C_b \left(V_{bf}^2 - V_{af}^2 \right) \approx 11.2 \text{ mJ}, \tag{3.24}$$

where V_{bf}, V_{af} represent the voltage before and after the exciting action on C_b. V_{bf} is pre-charged to 29 V in this case, and V_{af} is measured to be 19.1 V. Given that $C_b = 47$ μF, the circuit consumes about 1.09 mW average power for the vibration exciting propose during the orbit jump process. It should be noted that the energy consumed from C_b will be partially dissipated by the equivalent series resistance of the inductive branch in the bias-flip actions. Thus, the net injected energy from electrical to mechanical domain is smaller than that is extracted from the storage capacitor C_b. By considering the exciting efficiency of the VE mode of BECC [172], the actual average power for

vibration exciting is around 0.16 mW. The detailed electrical performance, energy flow analysis, and efficiency under different operation modes were documented in [30, 172]. After orbit jumps, the energy consumed will be charged back with a higher harvested power on HEO. In the absence of a load, the average charging rate of the bias/storage capacitor is regarded as the power output. Before the orbit jumps, the harvested power is 0.011 mW. On HEO, after orbit jumps, the harvested power has been boosted for 9.1 times to 0.1 mW. Under this rate, the consumed energy by the vibration exciting action will be recovered in about 2 minutes. A detailed charging curve as shown in Figure 3.11 also indicates a large slope and harvested power after orbit jump (by hand) around 10 s. Considering the size of the transducer, there is room further to optimize the system power output and recovery time. The independence of external devices and the compact dual functions of high-capability energy harvesting and vibration excitation demonstrate the advantages of the proposed self-contained solution for time-sharing energy harvesting and orbit jumps. Besides the base excitation at 7 Hz, multiple experimental trials are performed under different base excitation frequencies in the hysteresis region. Successful orbit jumps are observed between 6.7 Hz to 7.8 Hz, covering the entire hysteresis band in EH-mode operation. Without utilizing extra mechanical or electrical energy sources for vibration excitation, compared with existing studies in literature [26, 153], the proposed self-contained solution realizes the orbit jumps within the full hysteresis range under EH-mode.

3.5 Discussions

In this paper, a monostable nonlinear system is conducted by tuning the distance between the dipole magnets, which expands the bandwidth and increases the output power of the harvester. Besides, other nonlinear systems such as bistable, tristable, and multistable types are extensively explored for similar advantages [147]. However, it is a general case where these nonlinear systems may be trapped in one of its multiple potential wells or randomly transited among wells, which reduces the controllability of orbit jumps. Attempts are carried out with a bistable energy harvester to investigate the feasibility of the proposed orbit jump solution regarding preceding systems. By decreasing the distance between the two repelling magnets such that making $K - K_1 < 0$, the original single potential well bifurcates into two. Under certain excitation and initial conditions, the bistable harvester can present complex motions [149].

- The interwell oscillation. In this case, the vibrator overcomes the energy barrier of potential wells and travels between two wells. It is referred to as the HEO vibration.
- The intrawell oscillation. In this case, the system is trapped in one of its potential wells.
- The chaotic motion. The oscillator randomly vibrates without a deterministic path.

In case the system does not vibrate on HEO, the BECC activates the VE mode to carry out an orbit jump.

In the experiments, the chaotic motion is mostly observed. The system firstly vibrates

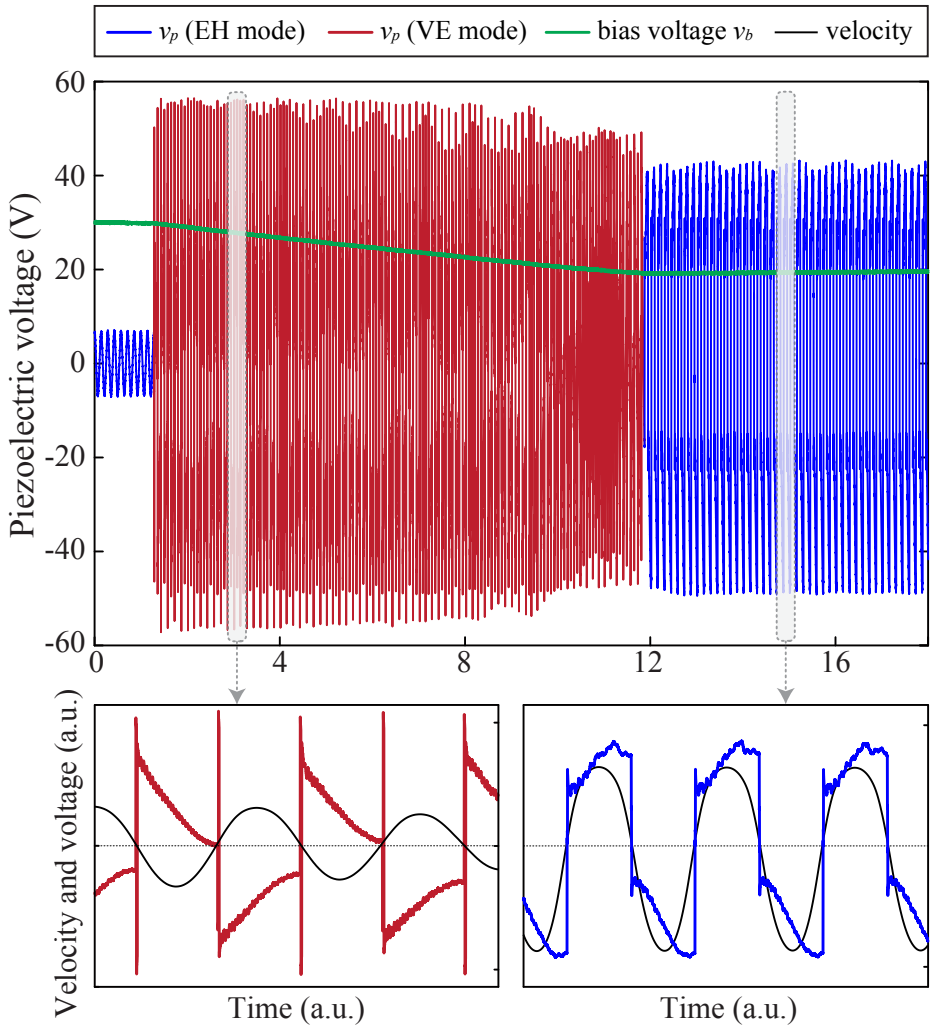

Figure 3.10: Piezoelectric voltage in the experiment, which corresponds to the orbit jump process described in Figure 3.9. The enlarged views show the experimental piezoelectric voltage in VE mode (red) and EH mode (blue), respectively.

chaotically under a sinusoidal base excitation of 5.4 Hz, as shown in Figure 3.12. Then, the oscillator is excited under VE mode for 5.9 s, whose phase portrait is illustrated in red. Afterward, the harvester jumps to HEO, forming the interwell oscillation. Unlike the monostable case, the motion of the bistable oscillator under VE mode does not share the same phase evolution as that in the monostable case, whose phase portrait is shown in Figure 3.9. The first reason is that the intrinsic chaotic motion of a bistable oscillator makes it hard to predict and control the trajectory of a nonlinear oscillator; The second is that the aperiodic motion violates the periodic assumption for calculating the electrical equivalent impedance. Thus the quantitative methods are inappropriate for orbit jumps of bistable energy harvesters with chaotic motions. However, for those bistable energy harvesters whose periodic motions still dominate the dynamics, the methods proposed in this work are still valid. As a result, the VE mode can only realize orbit jumps around ω_u, where the energy barrier is relatively low. The success of orbit jumps is thus considered the consequence of an abrupt voltage stimulus by the vibration exciting of

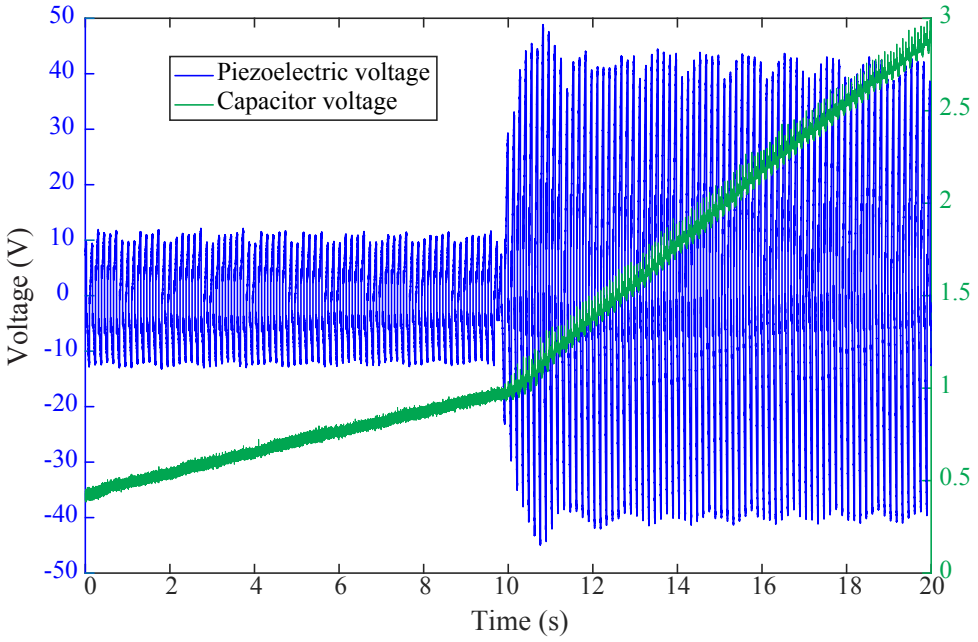

Figure 3.11: Piezoelectric voltage and capacitor voltage under low energy orbit and high energy orbit.

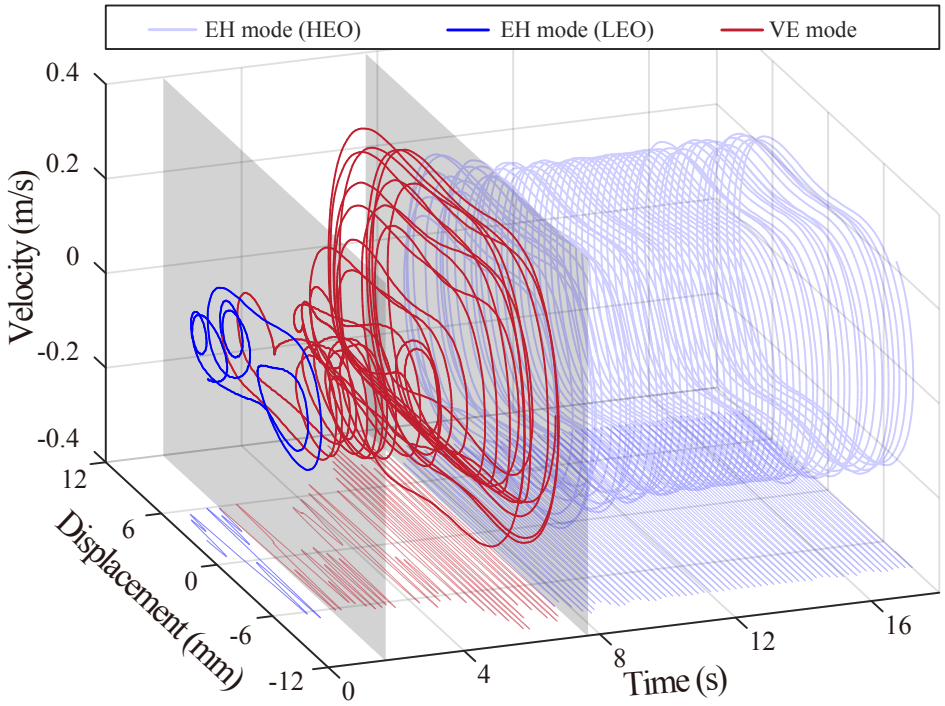

Figure 3.12: A trial of experimental orbit jump in a bistable nonlinear energy harvester with BECC. The curves represent the phase evolution of the displacement and velocity pair $(x, \dot{x})$ over time. The orbit-jump segment under VE mode is illustrated in red within two vertical gray planes, which indicate the mode transitions.

BECC under the low energy barrier cases between LEO and HEO. It is believed that an abrupt high voltage excitation is preferable for orbit jumps of a chaotic system [159]. For other tristable and multistable energy harvesters whose potential barriers are believed to

be minor [147], high-voltage stimuli would be a constructive option. The proposed dual functions of BECC might inspire more efficient energy injection concepts for orbit-jump solutions with nonlinear energy harvesters.

3.6 Conclusion

In summary, this work integrated a nonlinear piezoelectric energy harvesting with the bidirectional energy conversion circuit (BECC) to realize a time-sharing orbit jump and energy harvesting solution. Based on BECC, we first demonstrated the dual functions of energy harvesting and vibration exciting using a BECC without extra energy sources and actuators. Then, the ranges of electrically induced parameters under different operation modes were studied with impedance analysis. Furthermore, the stability analysis, frequency response, and state-space phase evolution of the autonomous and nonautonomous systems were performed to analyze the influence of BECC over the dynamics of a nonlinear oscillator. Particularly, the detailed steps for the time-sharing orbit jump from low-energy orbit to high-energy orbit using BECC were studied. We highlighted the effects of the unstable spiral and saddle node within the nonlinear system. From a practical perspective, the effect of switch time delay on the basin of attractions has also been discussed. Finally, experiments were carried out to validate the feasibility and capability of the proposed orbit jump solution over the entire hysteresis range of the nonlinear energy harvester. The energy evaluation showed that the system's output power yields a ninefold increase in the high-energy orbit. The application in a bistable energy harvesting system also showed the versatility of this solution. This time-sharing orbit jump solution could facilitate the practical applications of nonlinear energy harvesters. It provides an effective method to attain high-capability piezoelectric energy harvesting on high-energy orbits without the need for extra energy sources and actuators.

Acknowledgments

This work was supported by the National Natural Science Foundation of China (Project No. 62271319 and U21B2002) and the Natural Science Foundation of Shanghai (Project No. 21ZR1442300). The support for Mr. Bao Zhao provided by the H2020 FET-proactive project METAVEH under the grant agreement 952039, and the ETH Research, Switzerland Grant (ETH-02 20-1) is also acknowledged.

3.A Appendix

The solution of Eq. 3.14 can be constructed with asymptotic series through the multiple time scales method [173] as:

$$x = x_0(\tau, T) + \varepsilon x_1(\tau, T) + \cdots , \tag{3.25}$$

where the fast and slow time variables are defined as $\tau = t$ and $T = \varepsilon t$. Compared with the harmonic balance or direct time-domain integration methods, the multiple time scales

method can not only solve transient response given fast dynamics in a nonlinear system, but also increases the numerical stability and efficiency by decomposing the system into different time scales and integrating with different time steps [173]. This method particularly fits the nonlinear energy harvester and orbit jump solution proposed in this paper. The time derivatives of (3.25) read:

$$\begin{cases} \frac{\mathrm{d}}{\mathrm{d}t} = \frac{\partial}{\partial \tau} + \varepsilon \frac{\partial}{\partial T} + \cdots = D_0 + \varepsilon D_1 + \cdots, \\ \frac{\mathrm{d}^2}{\mathrm{d}t^2} = D_0^2 + 2\varepsilon D_0 D_1 + \varepsilon^2 D_1^2 + \cdots. \end{cases} \tag{3.26}$$

A frequency detuning parameter σ for the external force is given as follows:

$$\omega_0^2 = \omega^2 + \varepsilon\sigma. \tag{3.27}$$

By substituting (3.25) into (3.13), one can collect the ε^0 and ε^1 items as follows:

$$\begin{cases} D_0^2 x_0 + \omega^2 x_0 = 0, \\ D_0^2 x_1 + \omega^2 x_1 = -\sigma^* x_0 - 2D_0 D_1 x_0 - c^* D_0 x_0 - k_3^* x_0^3 \\ \qquad\qquad + b_f^* \cos(\omega\tau), \end{cases} \tag{3.28}$$

where $\sigma^* = \sigma/\varepsilon$, $c^* = c/\varepsilon$, $k_3^* = k_3/\varepsilon$, and $b_f^* = b_f/\varepsilon$ are the ε-scaled parameters for nonlinear analysis.

The general solution for the first component of (3.25) can be written as follows:

$$x_0 = A(T)e^{j\omega\tau} + \bar{A}(T)e^{-j\omega\tau}, \tag{3.29}$$

where A and $\bar{A}$ represent complex conjugates. By substituting (3.29) into the second equation of (3.28), the result is:

$$D_0^2 x_1 + \omega^2 x_1 = STe^{j\omega\tau} - k_3^* A^3 e^{3j\omega\tau} + cc, \tag{3.30}$$

where ST and cc represent the secular term and the complex conjugate. On setting the source of the secular terms to zero, it gives:

$$2j\omega D_1 A + \sigma^* A + jc^* A\omega + 3k_3^* A^2 \bar{A} - \frac{1}{2} b_f^* = 0. \tag{3.31}$$

By defining the derivative of amplitude $\mathrm{d}A/\mathrm{d}t = \varepsilon D_1 A$ and introducing the polar form of $A = ae^{j\varphi}/2$, (3.31) can be separated into real and imaginary parts for the slow flow of A as follows:

$$\begin{aligned} \frac{\mathrm{d}a}{\mathrm{d}t} &= -\frac{ac}{2} - \frac{b_f}{2\omega}\sin\varphi, \\ \frac{\mathrm{d}\varphi}{\mathrm{d}t} &= \frac{\omega_0^2 - \omega^2}{2\omega} + \frac{3k_3 a^2}{8\omega} - \frac{b_f}{2\omega a}\cos\varphi. \end{aligned} \tag{3.32}$$

Chapter 4

Nonlinear Metamaterial for Elastic Wave Control

Paper Details

The following chapter was published on February 15, 2024, as:
"**Zhao, B.**, Thomsen, H.R., Pu, X., Fang, S., Lai, Z., Van Damme, B., Bergamini, A., Chatzi, E. and Colombi, A., 2024. A nonlinear damped metamaterial: Wideband attenuation with nonlinear bandgap and modal dissipation. *Mechanical Systems and Signal Processing*, 208, p.111079."
DOI: https://doi.org/10.1016/j.ymssp.2023.111079 - Under a Creative Commons license.
This is a post-print version of the article, which differs from the published version only in terms of layout, formatting, and minor amendments which have been implemented in the text to adapt the original paper to the format of the thesis and improve readability.

Author and Co-authors Contributions

The author of this thesis conceived the design of the nonlinear damped metamaterial, developed the theoretical models, and performed the experimental analyses. Dr. X. Pu helped on the part of nonlinear dispersion analysis. Dr. H.R. Thomsen, Prof. Dr. S. Fang, Prof. Dr. Z. Lai, Dr. A. Bergamini, and Dr. B. Van Damme supported the experiments. Prof. Dr. E. N. Chatzi and Dr. A. Colombi provided overall supervision and guidance.

Key Findings

- A nonlinear metamaterial attenuates vibration beyond the bandgap range of the linear counterparts.
- Nonlinear dispersion and frequency response by homogenization and harmonic balance methods.

- Nonlinear damping effect enables efficient modal frequency dissipation.
- Experiments validate the broadening of bandgap and modal frequency dissipation.

General comments and link to the next chapter

By showing the design of the nonlinear damped metamaterial and its effectiveness in **broader bandgap and modal dissipation ability** and **shock wave attenuation**, this chapter completes the third objective (see Section 1.4) of the thesis on the base of nonlinear dynamics of single oscillators studied in Chapter 3. Moreover, this work proposes the numerical harmonic balance method with mode superpositions to solve the nonlinear frequency response for finite beam-based nonlinear metamaterial systems, which offers theoretical tools to solve nonlinear metamaterials with generic nonlinearities.

Abstract

In this paper, we incorporate the effect of nonlinear damping with the concept of locally resonant metamaterials to enable vibration attenuation beyond the conventional bandgap range. The proposed design combines a linear host cantilever beam and periodically distributed inertia amplifiers as nonlinear local resonators. The geometric nonlinearity induced by the inertia amplifiers causes an amplitude-dependent nonlinear damping effect. Through the implementation of both modal superposition and numerical harmonic methods with Alternating Frequency Time and numerical continuation techniques, the finite nonlinear metamaterial is accurately modeled. The resulting nonlinear frequency response reveals the bandgap is both amplitude-dependent and broadened. Furthermore, the nonlinear interaction between the local resonators and the mode shapes of the host beam is discussed, which leads to efficient modal frequency dissipation ability. The theoretical results are validated experimentally. By embedding the nonlinear damping effect into locally resonant metamaterials, wideband and shock wave attenuation of the proposed metamaterial is achieved, which opens new possibilities for versatile metamaterials beyond the conventional bandgap ranges of their linear counterparts.

4.1 Introduction

Mechanical vibrations are commonly encountered when dealing with civil infrastructures, industrial environments, vehicles, and more in general engineering applications. Their detrimental effects often lead to structural and operational failures and harm to human bodies. Therefore, vibration attenuation has received enormous attention from both research and industries. The commonly used vibration control methods include damping enhancement, stiffness tuning, and vibration mitigation by auxiliary attachments. These can be grouped into passive, semi-passive, and active methods [176]. Because of their easy application, passive and semi-passive methods are particularly suitable for vibration mitigation of the host structures without complex control systems. These methods can be distinguished based on the nature of their dynamic properties as follows:

1. Single linear attachment, e.g., tuned mass damper [177] and piezoelectric shunting [50];
2. Single nonlinear attachment, e.g., nonlinear energy sinks [49] and nonlinear damping [178];
3. Multiple linear attachments, e.g., multiple tuned mass dampers [51], and linear locally resonant metamaterials [5];
4. Multiple nonlinear attachments, e.g., nonlinear metamaterials [179].

When it comes to vibration suppression for the host structure, either the energy is efficiently transferred to the auxiliary attachments or the energy is prevented from propagating through the host structure, thus yielding a low transmissibility on the receiver side. Conventionally, attachments could be mechanical resonators [177, 180] or piezoelectric transducers with electrical shunting circuits [50, 145]. They can either transfer and dissipate the energy from the host structure or shift the resonance of the host structure

by additional stiffness and mass to avoid resonances.

However, due to their inherently linear nature, their effective bandwidth is narrow. In contrast, nonlinear attachments can interact with linear host structures in a broadband fashion. In certain conditions, this nonlinear interaction leads to a unidirectional energy flow from the linear structure to the nonlinear attachments. In the context of nonlinear energy sinks [61], this is referred to as nonlinear energy transfer. In addition, the nonlinear reaction forces induced by nonlinear stiffness [84, 181], damping [178], or vibro-impact [68] essentially couple the separated modes of the linear host structure and result in energy transfer, redistribution, and efficient dissipation among different structural modes [182].

When moving from single attachments to multiple attachments, the challenge lies in how to design and optimize multiple attachments or resonators to effectively attenuate the vibration of the host structure, which normally has multiple vibration modes. From a modal analysis point of view, attenuation at modal frequencies forms the guideline for designing different tuned mass dampers [51]. From a wave propagation perspective, vibration modes are attributed to reflections from the domain boundaries. Therefore, to effectively suppress vibration modes, the propagation of the traveling wave from one end of the host structure to the other must be prohibited for certain frequency ranges. This is synonymous with the design of bandgaps in locally resonant metamaterials [5]. Through the proper tuning of mechanical parameters, the propagating wave can be gradually trapped [71, 183], redirected [77, 78, 75], or absorbed [54, 184] with periodically distributed local resonators attached on the host structure, resulting in zero group velocities and low transmissions.

The recent endeavors to introduce nonlinearities through multiple nonlinear attachments have combined the advantages of locally resonant metamaterials and nonlinear dynamics. This has stimulated the emergence of novel concepts in the context of structural dynamics, such as harmonic generations [48], chaotic bands [185], and broadband vibration attenuation [47, 186]. However, owing to the challenges of relatively high degrees of freedom in metamaterials and complex dynamics from nonlinear attachments, theoretical and experimental realizations in this area have been incomplete until recent years. From a theoretical perspective, the high number of degrees of freedom, different nonlinear forms, and intensities of nonlinearities pose difficulties to reach an accurate solution. Compared to the numerical integration method, conventional analytical low-order methods such as harmonic balance methods [185, 48, 47, 187] and perturbation methods [64, 63] fail to converge when the nonlinearities presented are strong, even without accounting branch bifurcations due to stability issues [188]. In addition, these analytical methods, which work for close-form polynomial nonlinearities such as cubic stiffness [185, 47] and quadratic damping [187], are often insufficient for more general nonlinearities such as non-smooth nonlinear damping studied in this paper and piece-wise nonlinear forces. Theoretical advances are further complicated because standard Bloch-Floquet theory is limited in its usability. This popular method cannot reveal the modal interactions of multiple nonlinear attachments in a finite metamaterial, or frequency coupling related to broadband excitation. From an experimental perspective, nonlinear metamaterials need to be designed, fabricated, and tested from the resonator level to the metamaterial level to confirm the proposed nonlinear effect in practical manners, which requires repeatable

and slow sampling with the increase deviation of the nonlinearity of the system from its linear state [185, 48, 47, 186]. In addition, the amplitude-dependent response and the nonlinear coupling in nonlinear metamaterials also open new possibilities that need to be studied for vibration attenuation or energy exchange beyond the frequency range of the linear bandgap [185, 48]. From an ideology perspective, the effects of general nonlinearities in conventional low degree of freedom systems such as nonlinear vibration absorbers [49] have been well studied and documented. Their practical applications and accurate modeling methods in nonlinear metamaterials [48, 186], rather than conceptual verification of the known effects, are of great importance toward broader studies and engineering applications.

Based on our previous published conference paper [189], we present modeling methods for Euler-Bernoulli beam-based nonlinear metamaterials with general local nonlinearities and investigate a novel nonlinear damped metamaterial for wideband vibration attenuation and modal dissipation with a practical design of the nonlinear local resonators. With the goal of designing and solving real nonlinear metamaterial systems, we establish all the analyses on practical experimental parameters. We utilize a dispersion analysis and a modal analysis method with a numerical harmonic balance method to solve the amplitude-dependent response of this nonlinear metamaterial. Through the Alternating Frequency Time (AFT) and numerical continuation techniques, we can handle more general nonlinearities with the possibility of harmonic generations for weak to strong nonlinear scenarios. In addition, the nonlinear modal coupling is discussed to demonstrate the nonlinear interaction between the local resonators and the mode shapes of the host beam, which leads to efficient modal energy dissipation ability beyond the study of the conventional bandgaps. Based on the theoretical analysis, a nonlinear metamaterial is designed to incorporate the geometric nonlinear damping effect induced by the inertia amplifiers. The nonlinear frequency response of a single nonlinear resonator and the transmissibility of the nonlinear metamaterial are measured experimentally. The theoretical and experimental results not only validate the methods for solving the amplitude-dependent responses of the proposed nonlinear metamaterial but also give insights into the mechanisms for wideband attenuation combining nonlinear bandgap and modal frequency dissipation, which opens new possibilities for versatile metamaterials surpassing the limit of their linear bandgap ranges.

4.2 Theoretical Analysis

The proposed nonlinear metamaterial is shown in Figure 4.2, which illustrates a semi-infinite case in the x-direction of the nonlinear metamaterial consisting of a host beam and inertia amplifiers as nonlinear local resonators. Before analyzing the nonlinear metamaterial, we first revisit the nonlinear dynamics of the rotational inertia amplifier proposed by Van Damme et al. [190]. As shown in Figure 4.1, the inertia amplifier consists of two identical disks with mass m_0 on the top and bottom and four beams as connections that are tilted with angle θ. The tilted beams lead to a coupled translation-rotation motion of the top disk and simultaneously deliver a longitudinal spring stiffness k_0. The rotational spring stiffness is considered to be small compared to the longitudinal spring stiffness,

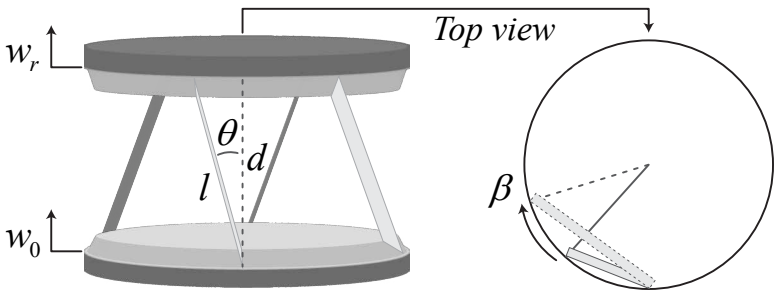

Figure 4.1: The schematic and top view of a rotational inertia amplifier.

which can be ensured by sufficiently thin connector points.

The nonlinearity is induced by the coupling of the translational motion of the bottom and the rotational motion of the top disk. The relative displacement of the top disk with respect to the bottom disk is denoted as w_r. And the rotation angle of the top disk is denoted as β. In Figure 4.1, the top view shows the projected deformation of a connected beam, while the chord length in the top view of Figure 4.1 changes from $\sqrt{l^2-d^2}$ to $\sqrt{l^2-(d-w_r)^2}$. For small w_r, the top disk's rotation angle β is defined as:

$$\beta = \frac{\sqrt{l^2-(d-w_r)^2}-\sqrt{l^2-d^2}}{R} \tag{4.1}$$

where R is the radius of the disk. The angular velocity can be written as:

$$\dot{\beta} = \frac{\dot{w}_r}{R}\frac{d-w_r}{\sqrt{l^2-(d-w_r)^2}}. \tag{4.2}$$

where $l = d/\cos\theta$. The kinetic energy of the top disk can be defined as $T = m_0|\dot{w}_r|^2/2 + I_0|\dot{\beta}|^2/2$, where $I_0 = m_0R^2/2$ represents the moment of inertia of the rotating disk. Its potential energy is $V = k_0w_r^2/2$. Using the Lagrangian $\mathscr{L} = T - V$, its equation of motion can be formulated as:

$$\begin{aligned} F = -m\ddot{w}_0 &= \frac{d}{dt}\left(\frac{\partial \mathscr{L}}{\partial \dot{w}_r}\right) - \frac{\partial \mathscr{L}}{\partial w_r} \\ &= m\ddot{w}_r + c|\dot{w}_r|\dot{w}_r + kw_r, \end{aligned} \tag{4.3}$$

where $F = -m\ddot{w}_0$ is the harmonic base excitation force applied on the bottom disk with the displacement and displacement amplitude denoted as w_0 and W_0, respectively. By substituting Eq. 4.2 into Eq. 4.3, the equivalent mass m, damping c, and stiffness k can

be determined as:

$$\begin{aligned} m &= m_0 + \frac{m_0}{2}\left(1 + \frac{(1-\varepsilon)^2}{A}\right) \\ c &= \frac{m_0}{2d}\left(\frac{1-\varepsilon}{A} + \frac{(1-\varepsilon)^3}{A^2}\right) \\ k &= k_0 \\ A &= \frac{1}{\cos^2\theta} - (1-\varepsilon)^2, \end{aligned} \tag{4.4}$$

where $\varepsilon = w_r/d$ represents the strain along the translational direction. Under small strain ε condition, the Taylor series of the velocity $\dot{\beta}$ reads:

$$\dot{\beta}(\varepsilon) = \frac{\dot{w}_r}{R}\left[\frac{1}{\tan\theta} + \frac{\varepsilon}{\tan\theta\sin^2\theta} + \frac{3}{2}\frac{\varepsilon^2}{\tan^3\theta\sin^2\theta}\right]. \tag{4.5}$$

Due to the nonlinear geometric constraint between displacement and rotation angle, $\dot{\beta}(\varepsilon)$ not only linearly depends on $\dot{w}_r$ with the 0-th order term, the second, third, and high order terms with respect to ε also play important roles under sufficiently small θ cases. However, by assuming the strain ε no more than 2.5%, we can calculate the smallest $\theta = 30°$ that makes the second, third, and higher order terms 10 times smaller than the 0-th order coefficient in Eq. 4.5.

In this case, the 0-th order term with respect to ε of Eq. 4.5, together with the small strain ε condition, can be used to simplify the equivalent parameters in Eq. 4.4:

$$m = m_0 + \frac{m_0}{2\sin^2\theta}, \quad c = \frac{m_0}{2d}\frac{\cos^2\theta}{\sin^4\theta}, \quad k = k_0, \tag{4.6}$$

where k is the spring constant depending on the connections between two disks. From the expression of m, the dynamically added mass due to the top disk is $m_0/2\sin^2\theta$ with the amplification factor $\alpha = 1/\sin^2\theta$. A nonlinear damping effect emerges from the expression of c due to the geometric nonlinear coupling between $\dot{w}_r$ and $\dot{\beta}$. This nonlinear damping force $c|\dot{w}_r|\dot{w}_r$, also known as the drag force [191], has an absolute form with respect to the velocity, which can be cataloged into non-smooth nonlinearities. This enables the amplitude-dependent frequency response and amplitude-dependent bandgaps in nonlinear metamaterials [63].

By assuming a fundamental harmonic solution for $w_r = W_r\sin(wt)$ with W_r representing the displacement amplitude, we can determine a nonlinear correspondence to the linear viscous damping coefficient, an equivalent damping coefficient $c_{eq} = c|\dot{w}_r|$ that increases with the base excitation force. By treating the absolute value with sign function, Eq. 4.3 can be written as:

$$m\ddot{w}_r + c\cdot\mathrm{sign}(\dot{w}_r)\dot{w}_r^2 + kw_r = -m\ddot{w}_0, \tag{4.7}$$

where $\mathrm{sign}(\dot{w}_r)$ is an even square wave with its leading harmonic $4\cos(\omega t)/\pi$. Substituting

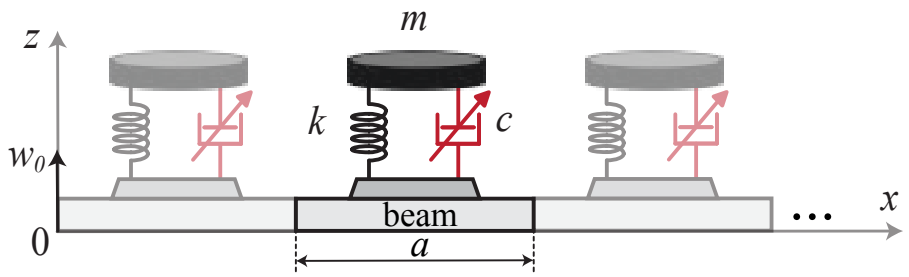

Figure 4.2: A semi-infinite schematic of the nonlinear metamaterial with lattice constant a. The incident wave w_0 in z direction is applied at the origin $x = 0$.

the solutions into Eq. 4.7, and balancing the first order harmonic, yields:

$$\left(\left(k - m\omega^2\right)^2 + \left(3c\omega W_r/\pi \cdot \omega\right)^2\right) W_r^2 = \left(\omega^2 m W_0\right)^2, \tag{4.8}$$

Observing the above equation, the equivalent nonlinear damping reads:

$$c_{eq} = 3c\omega W_r/\pi, \tag{4.9}$$

where W_r is given as:

$$W_r = \frac{\omega^2 m W_0}{\sqrt{(k - m\omega^2)^2 + 9c^2\omega^4 W_r^2/\pi^2}}. \tag{4.10}$$

It can be seen that c_{eq} is a function of frequency ω and the base excitation amplitude W_0. To illustrate the nonlinear effects of the described nonlinear resonator in the proposed locally resonant metamaterial, we use the practical parameters in Table 4.1 for the analyses in the following subsections. The frequency ranges presented in the following figures are normalized with respect to the linear resonant frequency of the inertia amplifiers at 210.7 Hz.

4.2.1 Nonlinear Dispersion Relationship

The dispersion relationship provides a general and fundamental description of the wave propagation characteristics of metamaterials. Unlike linear metamaterials, nonlinear metamaterials give rise to amplitude-dependent dispersion relationships [192, 34], which leads to a better understanding of how the nonlinearity could enable rich dynamics in metamaterials.

We herein discuss the dispersion relationship for flexural waves traveling in the proposed nonlinear metamaterial, where the nonlinearity stems from the resonator's amplitude-dependent damping. This mechanism is much less investigated than amplitude-dependent stiffness changes. As shown in Figure 4.2, the lattice constant of j-th unit cell is a. The linear density of the host beam is $\rho_0 = \rho bh$, where ρ, b, and h represent the density, width, and height of the host beam, respectively. The bottom disk with mass m_0 of the inertia amplifier is fixed on the beam. It is coupled with an equivalent mass m by a linear spring k

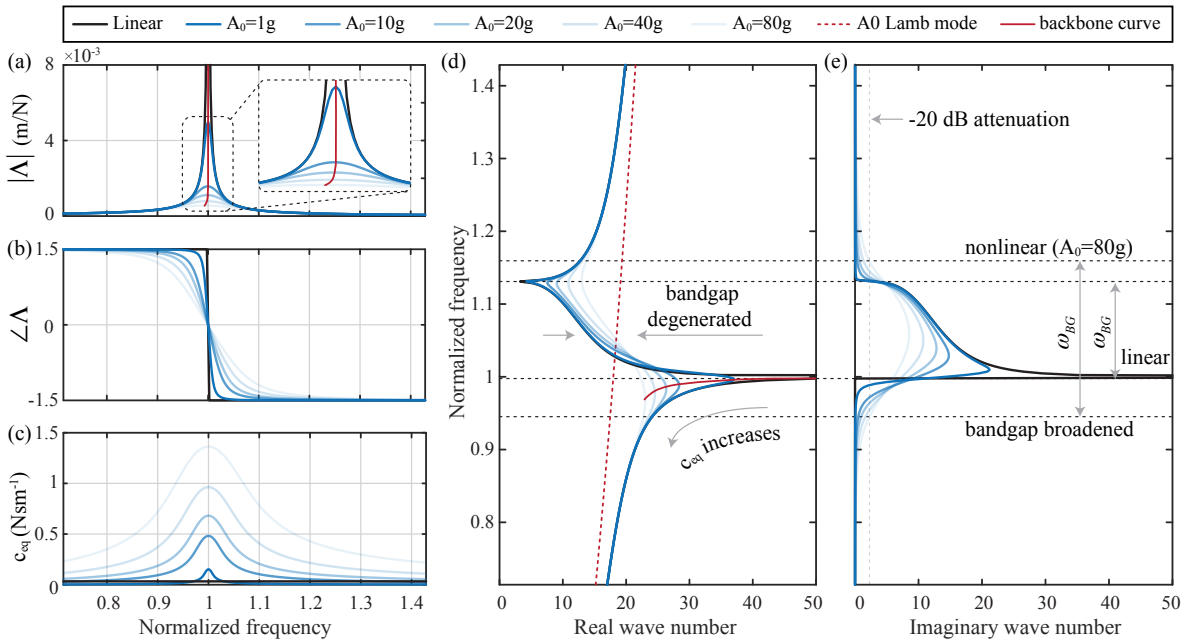

Figure 4.3: The frequency response function, equivalent damping, and dispersion curves under different acceleration amplitudes. (a) and (b): The amplitude and phase of the frequency response function of a local resonator. The enlarged view in (a) shows the shift of the resonant frequency indicated with a red backbone curve; (c) The equivalent damping of a local resonator; (d) and (e): The real and imaginary wave number of the nonlinear metamaterial.

and a nonlinear damper c. An incident wave $w_0 = W_0 \sin(\omega t + \varphi)$ in z direction is applied at the boundary $x = 0$ of the beam, where W_0 is the amplitude of the incident wave. Rather than using a complex-valued frequency and real-valued wavenumber [62], we adopt a real-valued frequency and allow for complex-valued wavenumbers, which is suitable for forced harmonic cases [193, 194] and gives insight in the attenuation of propagating waves [195, 137].

With reference to the parameters from Table 4.1, we can obtain the dispersion curve of the A0 Lamb mode of the host beam by Euler-Bernoulli beam theory as shown with the red dash line in Figure 4.3 (d). The flexural wavelength of the host beam is inversely proportional to the wave number with 2π, which is approximately 35 cm at the linear resonant frequency of the inertia amplifiers. Since the lattice constant is sufficiently smaller than the wavelength under low-frequency vibrations around this frequency range, the wave profile between two adjacent unit cells can be approximated by a smooth function by neglecting the near-field scattering around the inertia amplifiers. Thus, we can utilize the averaging technique from the homogenization method [34] and transform the concentrated reaction force of the local resonator to a uniformly distributed force $f(x,t)$ applied evenly with lattice constant a. The governing equations of the nonlinear metamaterial are given as:

$$\begin{aligned} &D_0 \frac{\partial^4 w\,(x,t)}{\partial x^4} + \rho_0 \frac{\partial^2 w\,(x,t)}{\partial t^2} = -f(x,t) \\ &m(\ddot{w}_r + \ddot{w}) = -k w_r - c|\dot{w}_r|\dot{w}_r \\ &m_0 \ddot{w} + m(\ddot{w}_r + \ddot{w}) = a f(x,t) \end{aligned} \quad , \tag{4.11}$$

where $D_0 = EI$ is the flexural rigidity of the host beam. w is the transverse displacement at beam position x. And w_r is the relative displacement of the local resonator at the same beam position. By adopting the effective medium theory [196], Eq. 4.11 can be transferred into:

$$\begin{cases} D_0 \dfrac{\partial^4 w}{\partial x^4} + (\rho_0 + \dfrac{m_0 + m}{a}) \dfrac{\partial^2 w}{\partial t^2} + \dfrac{m}{a} \dfrac{\partial^2 w_r}{\partial t^2} = 0 \\ m \dfrac{\partial^2}{\partial t^2}(w_r + w) + k w_r + c|\dot{w}_r|\dot{w}_r = 0 \end{cases} . \tag{4.12}$$

By neglecting the higher harmonic generations, we can replace the nonlinear damping force $c|\dot{w}_r|\dot{w}_r$ with an equivalent damping force $c_{eq}\dot{w}_r$ and only consider the fundamental harmonic traveling wave $w = We^{\mathrm{i}(\omega t - kx)}$. The dispersion relationship for the metamaterial beam can be derived from Eq. 4.12 as:

$$k(\omega) = \left[\left(\rho_0 + \frac{m_0}{a} + \frac{k + \mathrm{i}c_{eq}\omega}{a(\omega_r^2 - \omega^2 + \mathrm{i}c_{eq}\omega/m)} \right) \frac{\omega^2}{D_0} \right]^{\frac{1}{4}} , \tag{4.13}$$

where ω_r is the linear resonant frequency of the inertia amplifier. Therefore, the effective mass density for the proposed metamaterial beam reads:

$$\rho_e = \frac{1}{a} \left(\rho_0 a + m_0 + \frac{k + \mathrm{i}c_{eq}\omega}{\omega_r^2 - \omega^2 + \mathrm{i}c_{eq}\omega/m} \right) . \tag{4.14}$$

If $c_{eq} = 0$, the effective mass density and the dispersion for a metamaterial beam recover to its classical linear and undamped case [55]; if $c_{eq} =$ constant, then it represents a linear damped case [193]; if $c_{eq}(\omega, W_0)$ is a function of frequency ω and excitation amplitude W_0 as shown in Eq. 4.9, then this indicates a nonlinear damping case induced by the inertia amplifiers.

From a practical perspective, we prescribe a certain acceleration amplitude A_0 as excitation. Therefore, the equivalent damping c_{eq} is frequency and acceleration dependent. By solving Eq. 4.8, an equivalent local resonator with *Frequency Response Function* Λ can be achieved, together with Eq. 4.13. The results are shown in Figure 4.3 under different acceleration amplitudes. The effect of the increasing damping can clearly be seen by a reduction of the resonator's amplitude and a shift to lower eigenfrequencies (Figure 4.3 (a)), as well as the decrease of the phase slope (Figure 4.3 (b)).

By prescribing a sufficiently small A_0, the results of a linear metamaterial beam can be recovered as black curves in Figure 4.3. With the increase of A_0, the resonant frequency slightly shifts to a lower frequency due to the increase of equivalent damping c_{eq} as shown by the backbone curve in Figure 4.3 (a). In Figure 4.3 (c), the equivalent damping (c_{eq}) reaches the maximum at the linear resonant frequency ω_r.

For undamped linear metamaterials, ρ_e is real-valued. The bandgap is formed when $\rho_e < 0$, and hence the wave number $k(\omega)$ is complex-valued. This convenient criterion gives the classical bandgap range [55]. However, when it comes to damped metamaterials, ρ_e and $k(\omega)$ are always complex-valued, making the bandgap definition unpractical. In this paper, we define the bandgap range as the frequency range in which the transmissibility of

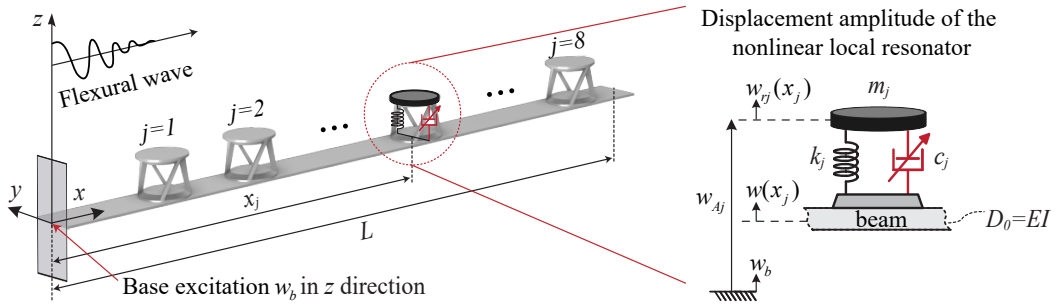

Figure 4.4: The model of the nonlinear metamaterial with finite length and clamped-free boundary condition. The enlarged view shows the displacement components for the absolute transverse displacement amplitude w_{Aj} of the nonlinear local resonator at x_j along the host beam.

a traveling wave along a unit length is reduced by more than -20 dB, which is commonly used as a threshold for vibration attenuation. Therefore, with the assumption of the fundamental harmonic traveling wave, the bandgap range ω_{BG} reads:

$$\left\{\omega_{BG} \in \mathbb{R} \mid 20 \log_{10} e^{-|\operatorname{Im}(k(\omega))|} < -20\right\}. \tag{4.15}$$

The dispersion curves for the proposed nonlinear metamaterial are shown in Figure 4.3 (d) and (e). With the increase of A_0, the real and imaginary parts of $k(\omega)$ become smoother than in the linear case. This is caused by the gradual increase of the damping effect from the local resonators, as shown in Figure 4.3 (c). For the real part of $k(\omega)$ in Figure 4.3 (d), the real wave number becomes smaller with the increase of A_0, which bends its in-phase branches from an infinite value to a finite value and thus leads to less attenuation. This degeneration of the dispersion curve also gives rise to the partial wave number bandgap beyond which the wave propagation is forbidden [197, 194]. The spatial decay of the traveling wave can be observed from the imaginary part of $k(\omega)$ in Figure 4.3 (e). An increase of A_0 not only reduces the resonant frequencies of local resonators for lower beginning frequencies of bandgaps but broadens their bandwidth, which consequentially broadens the bandgap range of the nonlinear metamaterial. Due to the nonlinear damping, the nonlinear bandgap range is broader than its corresponding linear case. It should be noted that this broadening effect comes with a slight bandgap degeneration. Further increase of A_0 could reversely reduce the bandgap range if a certain attenuation level is desired.

4.2.2 Nonlinear Frequency Response

Unlike the nonlinear dispersion relationship mentioned above, the infinite long beam assumption practically does not hold due to boundary reflections under low-frequency vibrations. Modal frequencies of the entire structure induced by boundary conditions interact with the nonlinear local resonators. Therefore, in this part, we discuss the frequency response of the proposed nonlinear metamaterial with a finite length by modal analysis and consider the higher harmonics through the harmonic balance method.

As shown in Figure 4.4, we consider a clamped-free cantilever beam with length $L = 0.6$

m and in total $S = 8$ inertia amplifiers periodically distributed along the beam from $x_1 = 0.14$ m to $x_9 = 0.56$ m. In this paper, we focus on the out-of-plane flexural wave propagation rather than the in-plane wave propagation of the host beam. In order to suppress the undesired in-plane modes, the inertia amplifiers are designed with four beams as connections to the bottom disk attached on the host beam to symmetrically distribute the reaction forces. However, mode conversion could happen at the crossings of dispersion curves when asymmetry or chirality are involved with three beams as connections [198]. The detailed parameters of the cantilever beam are listed in Table. 4.1. The absolute transverse displacement, $w_{Aj}(t)$, of the j-th nonlinear resonator at x_j along the host beam is defined as:

$$w_{Aj}(t) = w_b(t) + w(x_j, t) + w_{rj}(t), \tag{4.16}$$

where $w_b(t)$ is the base excitation displacement at the clamp side and $w_{rj}(t)$ is the relative displacement of j-the nonlinear resonator. The equation of motion of each nonlinear local resonator can be formulated as follows:

$$m_j\left(\frac{\partial^2 w}{\partial t^2} + \ddot{w}_b + \ddot{w}_{rj}\right) + c_j|\dot{w}_{rj}|\dot{w}_{rj} + k_j w_{rj} = 0, \tag{4.17}$$

where m_j, c_j and k_j are determined by Eq. 4.6. By adding the reaction forces of each nonlinear resonator onto the host beam, the governing equation of the host beam can be expressed as:

$$\begin{aligned} &D_0\frac{\partial^4 w}{\partial x^4} + \rho_0\frac{\partial^2 w}{\partial t^2} = -\rho_0\ddot{w}_b + \\ &\sum_{j=1}^{S}\left(k_j w_{rj} + c_j|\dot{w}_{rj}|\dot{w}_{rj}\right)\delta\left(x - x_j\right), \end{aligned} \tag{4.18}$$

where δ represents the Dirac function. We here modify $\rho_0 = \rho bh + m_0/a$ to take into account the inertia force of the bottom disks. The nonlinear metamaterial is then represented by Eq. 4.17 and Eq. 4.18.

Assume the total mass of local resonators is much smaller than the mass of the host beam and linear vibration modes dominate the response of the system so that the nonlinearities induced by the nonlinear damping effect can be treated as perturbations to the underlying linear Euler-Bernoulli equation of host beam [199, 47]. Compared with the conventional finite element method (FEM), the modal superposition method takes advantage of reduced order modeling, effectively reducing the problem's dimension [200]. Thus, the approximated solution of the displacement of the host beam is found by combining the harmonic balance and modal superposition methods, defined as:

$$w(x, t) = \sum_{i=1}^{N}\eta_i(t)\phi_i(x), \tag{4.19}$$

$$\eta_i(t) = \sum_{h=-H}^{H}\hat{\eta}_i(h)e^{\mathrm{i}h\omega t}, \tag{4.20}$$

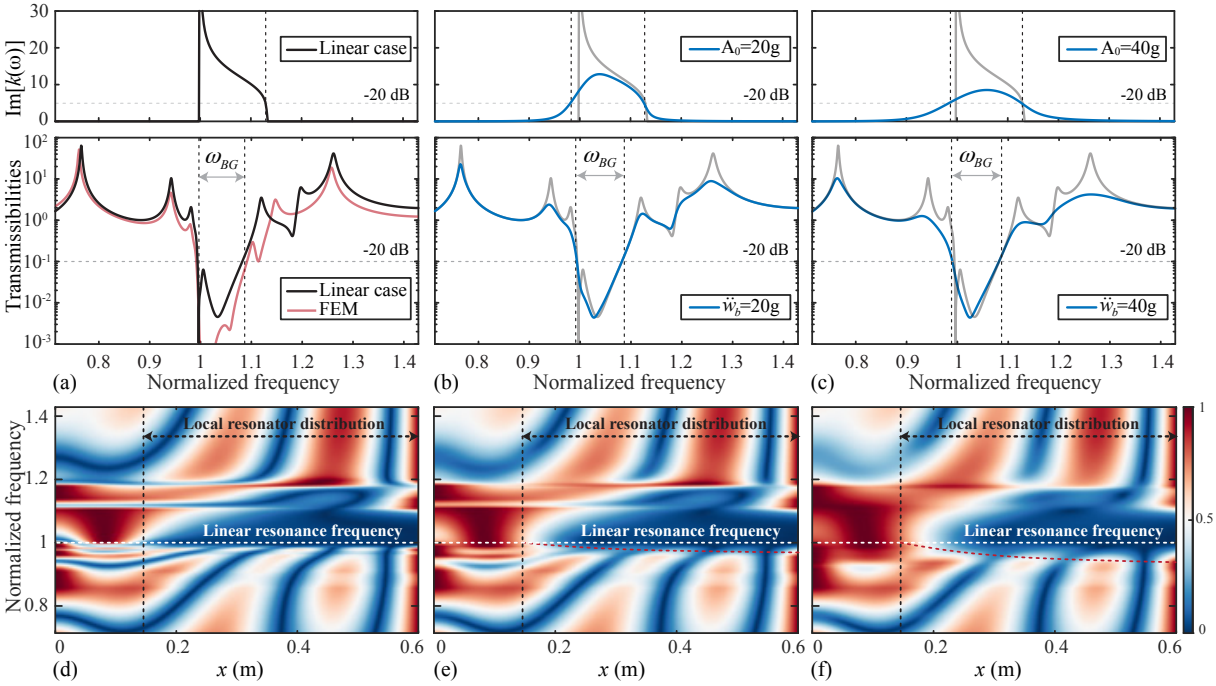

Figure 4.5: The tip transmissibilities and spatial frequency analyses of the nonlinear metamaterial. (a)-(c): Tip transmissibilities for linear, $\ddot{w}_b = 20$g nonlinear, and $\ddot{w}_b = 40$g nonlinear cases; (d)-(f): Spatial frequency analyses demonstrate the normalized displacement amplitude along the host beam for linear, $\ddot{w}_b = 20$g nonlinear, and $\ddot{w}_b = 40$g nonlinear cases.

where N and H are the number of modes and harmonics order considered. $\phi_i(x)$ is the i-th order mode shape of the host beam with its natural frequency ω_i. The modal weight $\eta_i(t)$ is expanded as Fourier series for higher harmonic generations due to the nonlinear reaction forces in the system, where $\hat{\square}$ represents the complex Fourier coefficient.

By applying the boundary conditions of the clamped-free host beam, substituting the ansatz of the solutions, and applying orthogonality [55, 47] (detailed in Appendix 4.A), the second-order differential equations Eq. 4.17 and Eq. 4.18 can be written into matrix form with the dimension of $N + S$ as:

$$\mathbf{M\ddot{u}} + \mathbf{Ku} + \mathbf{F_{nl}}(\dot{\mathbf{u}}) = \mathbf{F_{ex}}(\mathbf{t}), \tag{4.21}$$

where $\mathbf{u} = \left[\ \eta_1\eta_2\cdots\eta_N w_{r1}w_{r2}\cdots w_{rS}\ \right]^\intercal$ describes the modal weights and relative displacements of the nonlinear local resonators.

For the linear part of Eq. 4.21, the detailed form of the mass matrix $\mathbf{M}$ and the linear stiffness matrix $\mathbf{K}$ are given as:

$$\mathbf{M} = \begin{bmatrix} \mathbf{M}_{11} & \mathbf{M}_{12} \\ \mathbf{M}_{21} & \mathbf{M}_{22} \end{bmatrix}, \quad \mathbf{K} = \begin{bmatrix} \mathbf{K}_{11} & \mathbf{0} \\ \mathbf{0} & \mathbf{K}_{22} \end{bmatrix}, \tag{4.22}$$

where $\mathbf{M}_{11}$ is a $N \times N$ matrix with the entries: $m_{mn} = \delta_{mn} + \sum_{j=1}^{S} m_j\phi_m(x_j)\phi_n(x_j)$; $\mathbf{M}_{12}$ is a $N \times S$ matrix with the entries: $m_{mq} = m_q\phi_m(x_q)$; $\mathbf{M}_{21}$ is a $S \times N$ matrix with the

entries: $m_{pn} = m_p \phi_n(x_p)$; $\mathbf{M}_{22}$ is a $S \times S$ matrix with the entries: $m_{pq} = \delta_{pq} m_p$; $\mathbf{K}_{11}$ is a $N \times N$ diagonal matrix with the entries: $k_{mn} = \delta_{mn} \omega_m^2$; $\mathbf{K}_{22}$ is a $S \times S$ diagonal matrix with the entries: $k_{pq} = \delta_{pq} k_{rp}$; The applied external force $\mathbf{F_{ex}}$ with $N + S$ items can be expanded as:

$$\begin{aligned} \mathbf{F_{ex}} = [&q_1 \cdots q_i \cdots q_N \\ &- m_1 \ddot{w}_b \cdots - m_j \ddot{w}_b \cdots - m_S \ddot{w}_b]^\intercal, \end{aligned} \tag{4.23}$$

where q_i is the modal force defined in Appendix 4.A.

For the nonlinear part, the nonlinear force $\mathbf{F_{nl}}(\dot{u})$ can be expressed as:

$$\mathbf{F_{nl}}(\dot{u}) = \mathbf{C_N} |\dot{\mathbf{u}}| \dot{\mathbf{u}}, \quad \mathbf{C_N} = \begin{bmatrix} \mathbf{0} & \mathbf{0} \\ \mathbf{0} & \mathbf{C}_{22} \end{bmatrix}, \tag{4.24}$$

where $\mathbf{C_N}$ represents the nonlinear damping coefficient matrix. $\mathbf{C}_{22}$ is a $S \times S$ diagonal matrix with the entries: $C_{pq} = \delta_{pq} c_{rp}$.

By treating the relative displacements of the nonlinear resonators also as Fourier series and substituting the ansatz of $\mathbf{u}(t)$: $\mathbf{u}(\hat{\mathbf{u}}, t)$ into Eq. 4.21, we can form the residual function $\hat{\mathbf{r}}(\hat{\mathbf{u}}, \omega)$ by using the harmonic balance method up to the truncation order H:

$$\begin{aligned} \hat{\mathbf{r}}(\hat{\mathbf{u}}, \omega) = &\left(\nabla^2 \otimes \omega^2 \mathbf{M} + \nabla^0 \otimes \mathbf{K} \right) \hat{\mathbf{u}} \\ &+ \hat{\mathbf{F}}_{\mathrm{nl}}(\hat{\mathbf{u}}, \omega) - \hat{\mathbf{F}}_{\mathrm{ex}}(\omega) = \mathbf{0}, \end{aligned} \tag{4.25}$$

where $\nabla = \mathrm{diag}[-\mathrm{i}H, \ldots, \mathrm{i}H]$ is a diagonal matrix of dimension $2H + 1$. Eq. 4.25 shows that the linear internal and external forces are decoupled for different harmonic indices k except for the nonlinear forces $\hat{\mathbf{F}}_{\mathrm{nl}}$. With M, K, and $\hat{\mathbf{F}}_{\mathrm{ex}}$ given, the linear parts of Eq. 4.25 can be easily solved, which represents the conventional linear metamaterials setup [55]. The primary challenge is to determine the Fourier coefficients of the nonlinear forces.

Since $\mathbf{F_{nl}}$ is a $\mathcal{C}^1$ continuous nonlinear function without a high degree of smoothness, conventionally, it requires tedious expansions of closed-form expression up to high truncation orders in the frequency domain for convergence. While in the time domain, the nonlinear forces are easy to calculate with the available state histories of the system. By taking the advantages of the two domains, Alternating Frequency–Time (AFT) [201] resolves the Fourier coefficients of the nonlinear force by performing Fourier transforms in the frequency domain with the nonlinear forces evaluated in the time domain as:

$$\hat{\mathbf{F}}_{\mathrm{nl}} \approx \hat{\mathbf{F}}_{\mathrm{nl}}^{\mathrm{AFT}} = \mathscr{F} \left[\mathbf{F}_{\mathrm{nl}} \left(\mathscr{F}^{-1} \left[\omega \nabla \hat{\mathbf{u}} \right] \right) \right], \tag{4.26}$$

where $\mathscr{F}$ denotes the discrete Fourier transform. By taking sufficient sampling points, the inverse Fourier transform $\mathscr{F}^{-1}[\omega \nabla \hat{\mathbf{u}}]$ gives the generalized velocities in the time domain, which are used to generate the nonlinear forces at the sampling instants. Finally, the discrete Fourier transform approximates the Fourier coefficients for the nonlinear force.

Based on the work by Krack and Gross [202], the nonlinear frequency response of the proposed nonlinear metamaterial within the frequency range $[\omega_s, \omega_e]$ can be solved by balancing the residual function Eq. 4.25 with unknown Fourier coefficients through a nu-

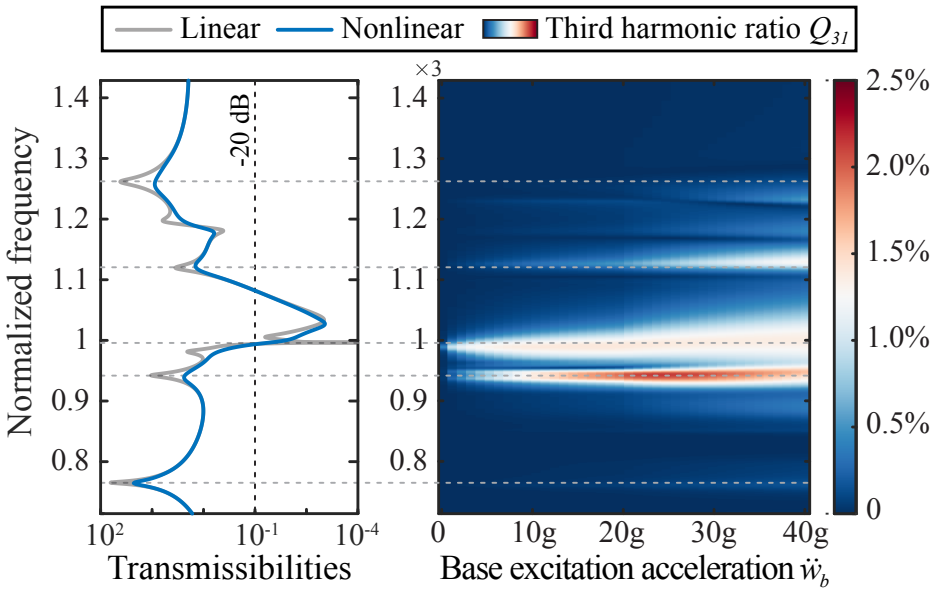

Figure 4.6: Third harmonic generation ratio Q_{31} between the displacement amplitude of the third harmonic at the free tip of the host beam and that of the first order harmonic. The gray dashed lines correspond to the third harmonic generation at modal frequencies.

merical Newton method. Compared with the direct time domain integration method, the harmonic balance method has an outstanding convergence rate due to the prior periodic ansatz of solutions. In addition, the harmonic balance method does not have the transient evolution of the time domain integration. Thus, it does not need a criterion for periodic behavior that stands for the steady state. Nevertheless, Eq. 4.21 can still be solved by the time-domain Runge-Kutta method as a reference with the state-space form:

$$\dot{\mathbf{z}} = \mathbf{B}\mathbf{z} + \mathbf{C}|\dot{\mathbf{z}}|\dot{\mathbf{z}} + \mathbf{D}, \tag{4.27}$$

where

$$\begin{aligned} \mathbf{z} &= \begin{bmatrix} \mathbf{u} \\ \dot{\mathbf{u}} \end{bmatrix}, & \mathbf{B} &= \begin{bmatrix} \mathbf{0} & \mathbf{I} \\ -\mathbf{M}^{-1}\mathbf{K} & \mathbf{0} \end{bmatrix}, \\ \mathbf{C} &= \begin{bmatrix} \mathbf{0} & \mathbf{0} \\ \mathbf{0} & -\mathbf{M}^{-1}\mathbf{C}_\mathbf{N} \end{bmatrix}, & \mathbf{D} &= \begin{bmatrix} \mathbf{0} \\ \mathbf{M}^{-1}\mathbf{F}_\mathbf{ex} \end{bmatrix}. \end{aligned} \tag{4.28}$$

It should be noted that the positions of local resonators could influence the condition number [203] of matrix $\mathbf{M}$ in Eq. 4.22, which measures how sensitive the computed Newton step is with respect to errors in the iteration of the unknown Fourier coefficients in Eq. 4.25. If the local resonators are placed close to the nodes of mode shapes, which increases the condition number, convergence failures could happen in both harmonic balance and time-domain integration. Therefore, we use the linear solutions at the beginning frequency ω_s as the scaling matrix σ:

$$\sigma = \mathrm{diag}\left(\left|\left(-\omega_s^2\mathbf{M} + \mathbf{K}\right)^{-1}\mathbf{F}_\mathbf{ex}\right|\right). \tag{4.29}$$

σ is also known as the Jacobi preconditioner [203], the scaled unknowns are $\sigma^{-1}\mathbf{u}$ with the similar order of magnitude, which reduces the condition number of the iteration problem and increases the convergence.

An isotropic damping ratio 0.005 is used for the host beam and local resonators to avoid numerical instability. The results of tip transmissibilities of the nonlinear metamaterial are shown in Figure 4.5. The linear case is realized by prescribing a small base excitation acceleration $\ddot{w}_b$. The finite element method [204] utilizes one-dimensional two-node Euler-Bernoulli beam elements. The element mass and stiffness matrices are modified to introduce the relative displacement w_{rj} of the local resonators, thus enabling the inertia and reaction forces at the nodes of the resonators' positions. In Figure 4.5(a), the transmissibility from the modal superposition method agrees with that from the FEM method, which means the modal superposition method proposed in Eq. 4.19 is sufficient. For the nonlinear case, the transmissibilities under different base excitations are solved by the harmonic balance method with harmonic order $H = 11$. Since the modal weight η_i not only contains the fundamental harmonic, the third and higher harmonic generations may occur. Thus, we take an example of the third harmonic generation at the free tip of the host beam. The ratio between the displacement amplitude of the third harmonic and that of the first-order harmonic is given as Q_{31}:

$$Q_{31} = \left| \frac{\sum_{i=1}^{N} \hat{\eta}_i\,(3)\,\phi_i\,(L)}{\sum_{i=1}^{N} \hat{\eta}_i\,(1)\,\phi_i\,(L)} \right|. \tag{4.30}$$

By varying the base excitation acceleration $\ddot{w}_b \in (0, 40g]$, the third harmonic generation ratio Q_{31} is illustrated in Figure 4.6. Besides the third harmonic generation at the linear resonant frequency ω_r, the third harmonics also appear at the modal frequencies of the nonlinear metamaterial due to the coupling with nonlinear local resonators. This phenomenon points to the modal energy transfer from low to high frequency, which has been proven useful for modal response attenuation [61]. With the increase of the base excitation, the ratio of the third harmonic becomes larger. However, the strongest third harmonic ratio is no more than 2.5% under $\ddot{w}_b = 40g$, which means the linear vibration modes still dominate the dynamics of the host beam. In Figure 4.5, we only show the results of the fundamental harmonic induced bandgap since the generated harmonics are much higher than the region of interest near the linear resonant frequency ω_r.

Similar to the dispersion analysis in Section 4.2.1, the bandgap in Figure 4.5 (a) to (c) is gradually broadened due to the increase of nonlinear damping with the increase of excitation level. To maintain consistency, we modify the definition of the attenuation range of the bandgap with the actual length L rather than the unit length of the host beam in Eq. 4.15. Regarding the bandgap range defined by -20 dB attenuation, the lower bound gradually shifts to a lower frequency and agrees with the range of the dispersion analysis. For the bandgap's upper bound, there's a deviation between the result from frequency responses and that from dispersion analysis. This deviation is mainly caused by the number of the local resonators [55] and the boundary conditions of the host beam. When the nonlinearity is weak, the solutions of both methods will converge by adding unit cells [189]. However, when nonlinearity is relatively strong, the interactions among

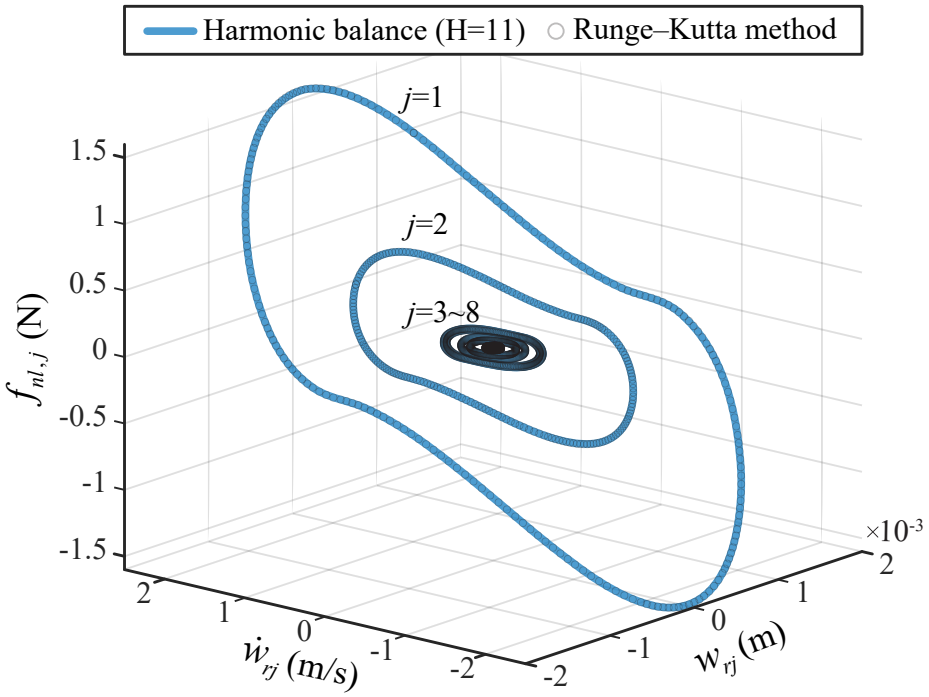

Figure 4.7: Limit cycles of local resonators with their nonlinear forces at the linear resonant frequency ω_r.

nonlinear resonators themselves and with mode shapes of the host beam can not be neglected, which emphasizes the importance of frequency response analysis of a finite beam model. The spatial frequency analysis in Figure 4.5 (d) to (f) shows the overall dynamic response of the metamaterial beam. It can be seen that the attenuation range starts from the first local resonator at position $x = 0.14$m. As nonlinear damping increases, the bandgap becomes less marked [205].

Besides the bandgap, the harmonic balance method also yields the limit cycles of nonlinear local resonators at the fundamental resonant frequency ω_r under base excitation $\ddot{w}_b = 20$g, shown in Figure 4.7. The results from the harmonic balance method synthesized from $H = 11$ harmonic orders show good agreement with time domain integrations. From the 1^{st} to 8^{th} local resonator, the relative displacement and velocity amplitude decrease with the attenuation of the traveling flexural wave. With the increase of vibration amplitudes, the limit cycles indicate more nonlinearities due to the amplitude-dependent nonlinear damping forces $\mathbf{F_{nl}}$. Thus, the bandgap broadening effect near the resonant frequency ω_r is mainly due to the nonlinear damping effect of the resonators that are located near the clamped side of the host beam.

4.2.3 Nonlinear Modal Dissipation

It is well-known that locally resonant metamaterials can create a bandgap for vibration mitigation of the host structure due to the spatial evanescent wave propagation starting from the resonance frequency of the local resonators [5]. On the other hand, nonlinear vibration absorbers have also been proven useful considering their broadband vibration

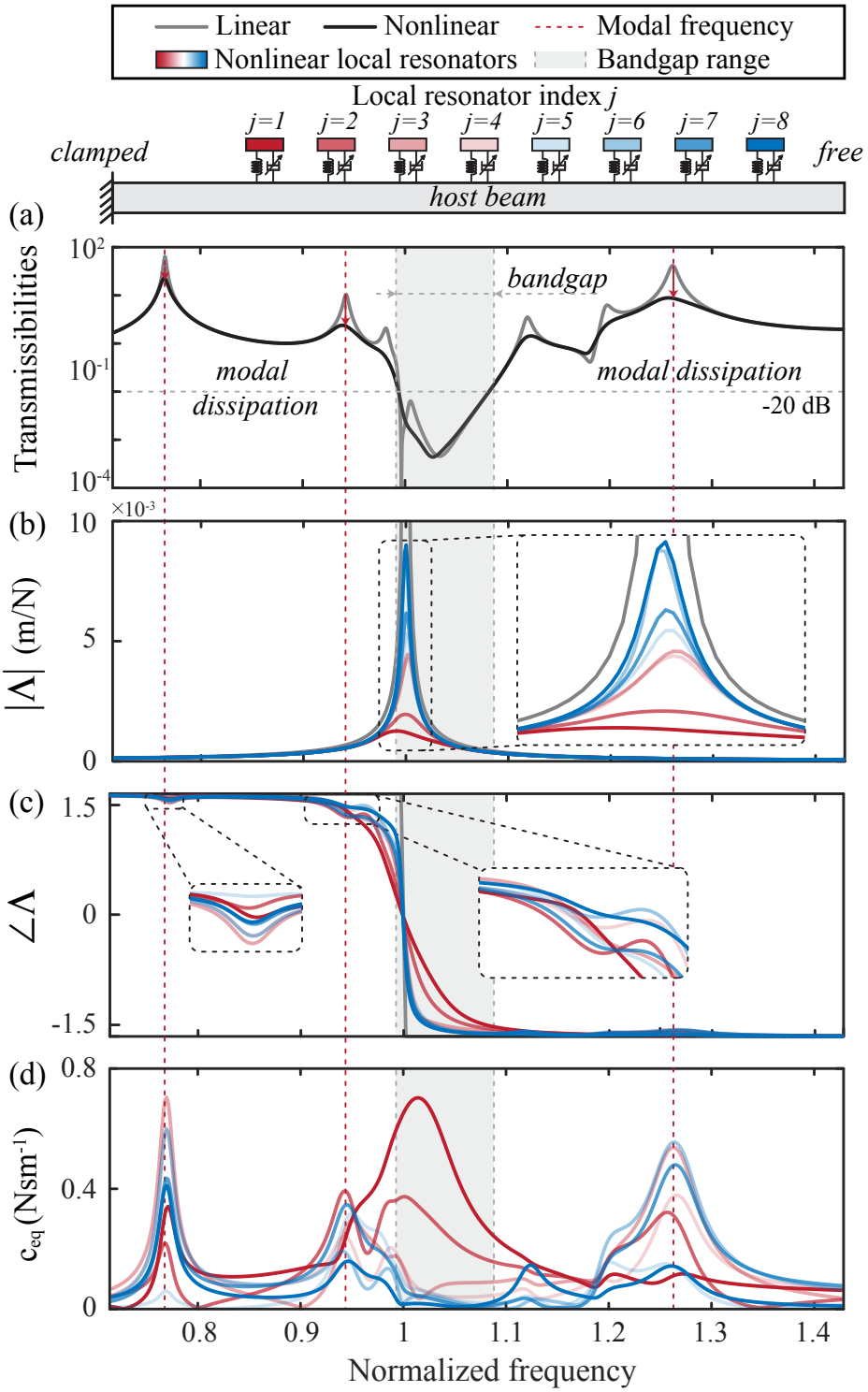

Figure 4.8: Nonlinear modal dissipation in the metamaterial. (a) Vibration attenuation at modal frequencies; (b) and (c): Amplitudes and phases of frequency response functions of local resonators; (d) Equivalent damping of local resonators.

mitigation ranges, which facilitate the redistribution of vibration energy over multiple vibration modes of the host structure and result in an efficient modal dissipative capacity

of the host structure [61]. In this part, we discuss the nonlinear modal dissipation in the proposed nonlinear metamaterial, which leads to the further broadening effect of the vibration attenuation range.

To investigate the nonlinear modal dissipation in the proposed metamaterial, we first look closely at the frequency response of the nonlinear local resonators. With the formulations in Sect. 4.2.2, the fundamental harmonic *Frequency Response Function* Λ_j for each local resonator can be written as:

$$\Lambda_j = \frac{W_{rj}}{\omega^2 m_j \left(W_b + W\right)} = \frac{1}{k_j - \omega^2 m_j + \mathrm{i}\omega c_{eq}}, \tag{4.31}$$

where W_{rj} and W are the fundamental harmonic amplitude of w_{rj} and w. The definition of equivalent damping c_{eq} in Eq. 4.9 can be applied here to demonstrate the effect of nonlinear damping from the local resonators with their fundamental harmonics calculated from the harmonic balance method.

The frequency response of each nonlinear local resonator and their equivalent damping is shown in Figure 4.8 under $\ddot{w}_b = 20\mathrm{g}$. The bandgap formed around the resonant frequency of the local resonators gives the main vibration attenuation range of the nonlinear metamaterial. Within the bandgap range, the frequency responses of the nonlinear local resonators differ from those of the linear resonators, demonstrating the effect of amplitude-dependent nonlinear damping. With the right-going flexural wave, the nonlinear resonators close to the base excitation point present stronger equivalent damping c_{eq} compared with those near the free tip of the host beam. This can be observed by the gradual transitions from the red curves with a larger c_{eq} to the blue curves with a smaller c_{eq} in Figure 4.8 (d). This nonlinear bandgap induced by nonlinear damping forms the first vibration attenuation range of the proposed nonlinear metamaterial due to the spatial decay of wave propagation and is also broadened by the nonlinear damping effect.

Different from the bandgap range where the right propagating wave is eventually attenuated, the influence of reflections, in other words, the modes of the host beam, dominate the dynamical response of the metamaterial beam outside the bandgap range. These modes are not only coupled with each other, but they also interact with nonlinear resonators, which leads to nonlinear modal dissipation in this metamaterial beam. As shown in Figure 4.8 (a), the transmissibilities at the modal frequencies indicated with red dash lines are much lower than its corresponding linear case, which means the mechanical energy is redistributed among different modal frequencies of the host beam and the nonlinear local resonators for efficient modal energy dissipation by different modes and nonlinear damping effect. For a damped linear resonator, the damping effect flattens the slope change of its phase around its resonant frequency, as shown with the gray curve in Figure 4.8 (c). For a nonlinear local resonator attached to a finite-length beam, the equivalent damping c_{eq} is determined by its velocity amplitude and the amplitudes of modal excitations. Therefore, there are multiple slope changes due to the modal frequency excitation from the movement of the host beam. As shown in Figure 4.8 (c), local slope changes of phase curves can be observed corresponding to modal frequencies. The increase of nonlinear damping around modal frequencies can also be observed via c_{eq} in Figure 4.8 (d). In particular,

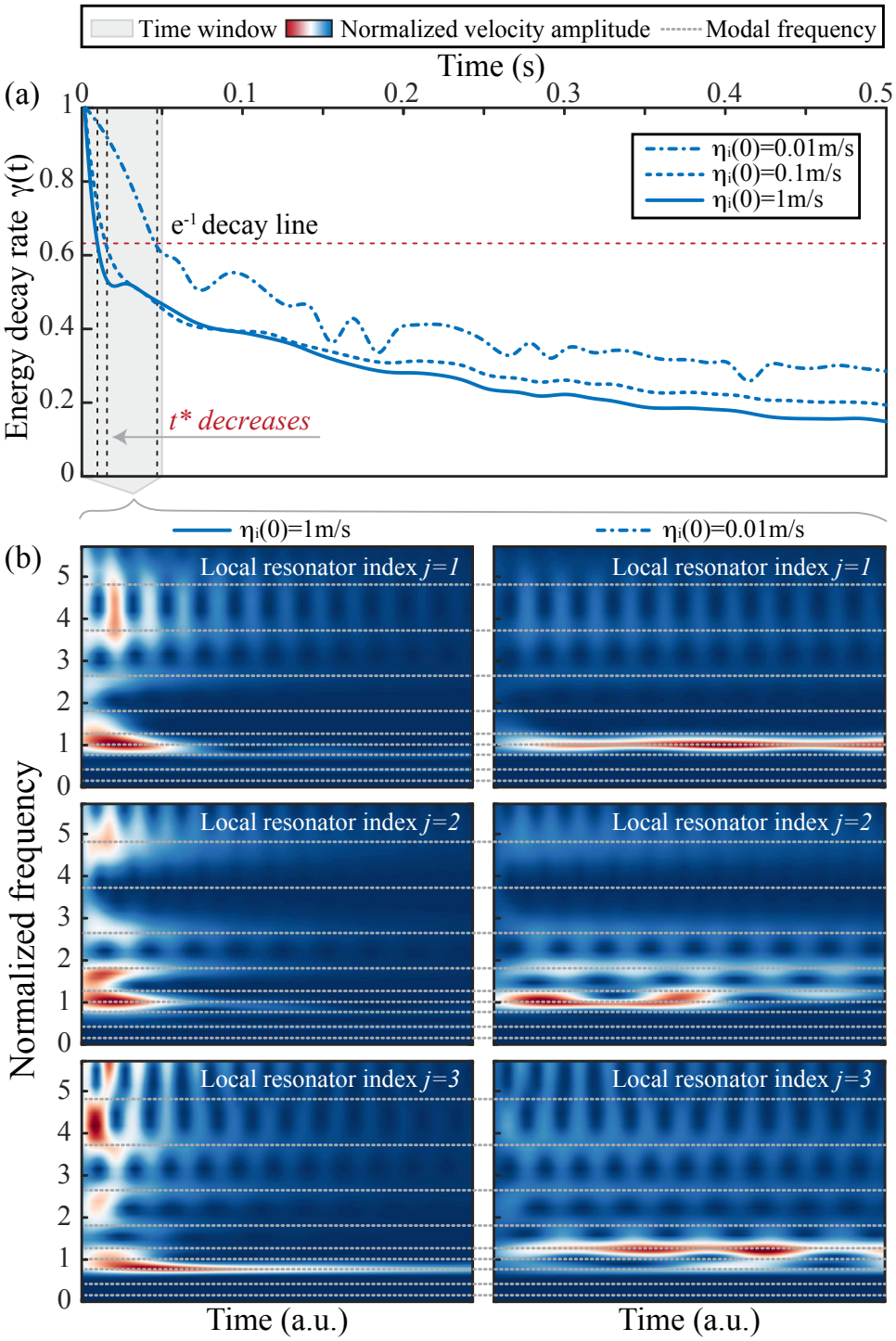

Figure 4.9: The envelope of the energy decay rate and the wavelet transform of the nonlinear metamaterial after initial impact at $t = 0$. (a) The envelope of the energy decay rate $\gamma(t)$ under three different impact velocities; (b) Wavelet transforms of the velocities $\dot{w}_{rj}$ of the first three nonlinear local resonators with the initial impact velocities $\eta_i(0) = 1\text{m/s}$ and $\eta_i(0) = 0.01\text{m/s}$.

those resonators near the middle part and free end of the host beam contribute significantly to vibration attenuation at modal frequencies, which forms a contrast within the bandgap range that only the resonators near the vibration source are more effective. This

nonlinear modal dissipation features a second mechanism besides the nonlinear bandgap and further broadens the range for vibration attenuation at modal frequencies.

In order to validate the efficient modal dissipation capability, we utilize the numerical time-domain integration in Eq. 4.27 with different modal velocities as initial conditions. The total kinetic energy $T(t)$ of the system can be represented with the kinetic energy of the host beam and that of the local resonators as:

$$T(t) = \frac{1}{2}\int_0^L \rho_0 \left(\frac{\partial w}{\partial t}\right)^2 dx + \sum_{j=1}^{S} \frac{1}{2} m_j \dot{w}_{rj}^2. \tag{4.32}$$

The total potential energy of the system $V(t)$ is represented by the strain energy of the host beam and the elastic energy of the local resonators:

$$V(t) = \frac{1}{2}\int_0^L D_0 \left(\frac{\partial^2 w}{\partial x^2}\right)^2 dx + \sum_{j=1}^{S} \frac{1}{2} k_j w_{rj}^2. \tag{4.33}$$

Let $\gamma(t)$ denote the ratio of the instantaneous total energy $T(t)+V(t)$ to the input energy $T(t_0)+V(t_0)$ induced by initial condition:

$$\gamma(t) = \frac{T(t)+V(t)}{T(t_0)+V(t_0)}, \tag{4.34}$$

where $\gamma(t)$ describes how fast the initial energy is dissipated due to the linear and nonlinear damping effect in metamaterials. By following the definition of linear oscillators, we use t^* to denote the time needed for the total energy drops by a factor of e^{-1} of its initial value, which indicates the linear damping coefficient by a time inverse [68].

The results in Figure 4.9 (a) show three initial modal velocities that mimic weak to strong impact conditions of the proposed nonlinear metamaterial. The total energy of the three cases decays at different rates along the time evolution. Under strong impact conditions, the whole nonlinear metamaterial's energy decays faster than in the other two cases, which indicates a stronger modal dissipation ability by the nonlinear damping effect. Due to the local resonators, the modal frequencies of the metamaterial beam are altered. By solving the eigenvalue problem of the underlying linear system in Eq. 4.21, the modal frequencies of the local resonant metamaterial beam are indicated with gray dash lines in Figure 4.9 (b). Compared to the small initial impact case, the wavelet transforms of the strong impact case demonstrate stronger modal coupling with the modal frequencies. This modal coupling not only originates from the nondiagonal characteristic of the mass matrix for the underlying linear system in Eq. 4.22, but the nonlinear reaction forces further facilitate this coupling by mixing the states of the local resonators with the modal coordinates. For the strong impact case, more higher modal frequency components can be observed. This effect can be understood as low-frequency to high-frequency nonlinear energy transfer resulting for faster energy dissipation of the host system [61]. The modal dissipation ability of the proposed nonlinear metamaterial helps the redistribution of

Table 4.1: Parameters in Experiment

Nonlinear Damping induced Metamaterial			
Host Beam			
Size	600×40×12 (mm^3)	Material	Versatile Plastic
Density	980 (Kg/m^3)	E	1.53 (GPa)
Nonlinear Local Resonator			
Material	Versatile Plastic	R	20 (mm)
d	40 (mm)	θ	35°
m_0	3.53 (g)	k_0	15.5 (kN/m)
ω_r	2π×210.7 (rad/s)	$x_j = 140 : 60 : 560$ (mm)	

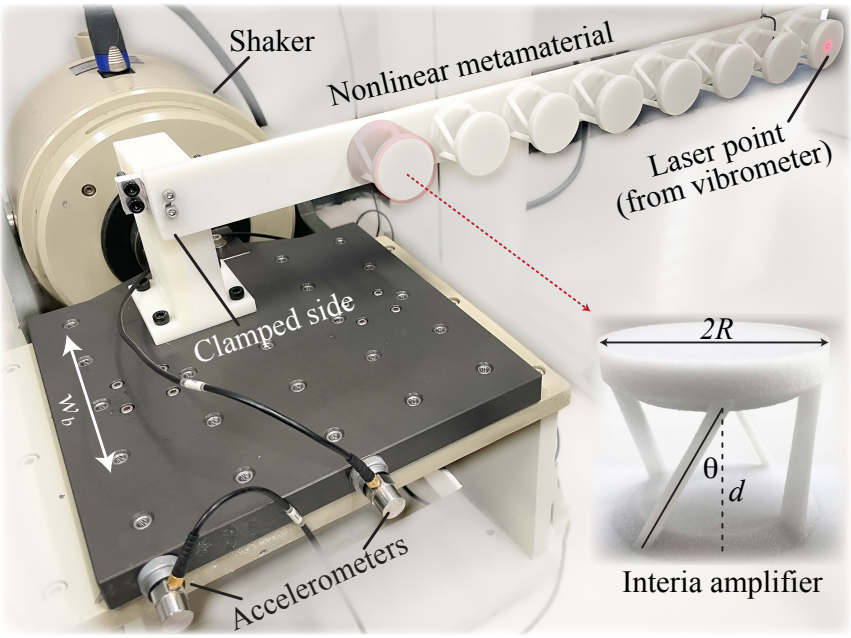

Figure 4.10: Experimental setup.

the energy into nonlinear local resonators and higher vibration modes, which shows the potential application of this nonlinear metamaterial for shock wave attenuation.

4.3 Experiments

The observed theoretical bandgap broadening effect and nonlinear modal dissipation are verified experimentally. We first verify the nonlinear frequency response of the inertia amplifiers as local resonators for the metamaterial. Then, the nonlinear transmissibilities of the metamaterial are recorded under different base excitation conditions.

4.3.1 Setup

Figure 4.10 shows the experimental setup. The nonlinear metamaterial is made of versatile plastic and consists of a 0.6-meter host beam and a series of nonlinear local resonators

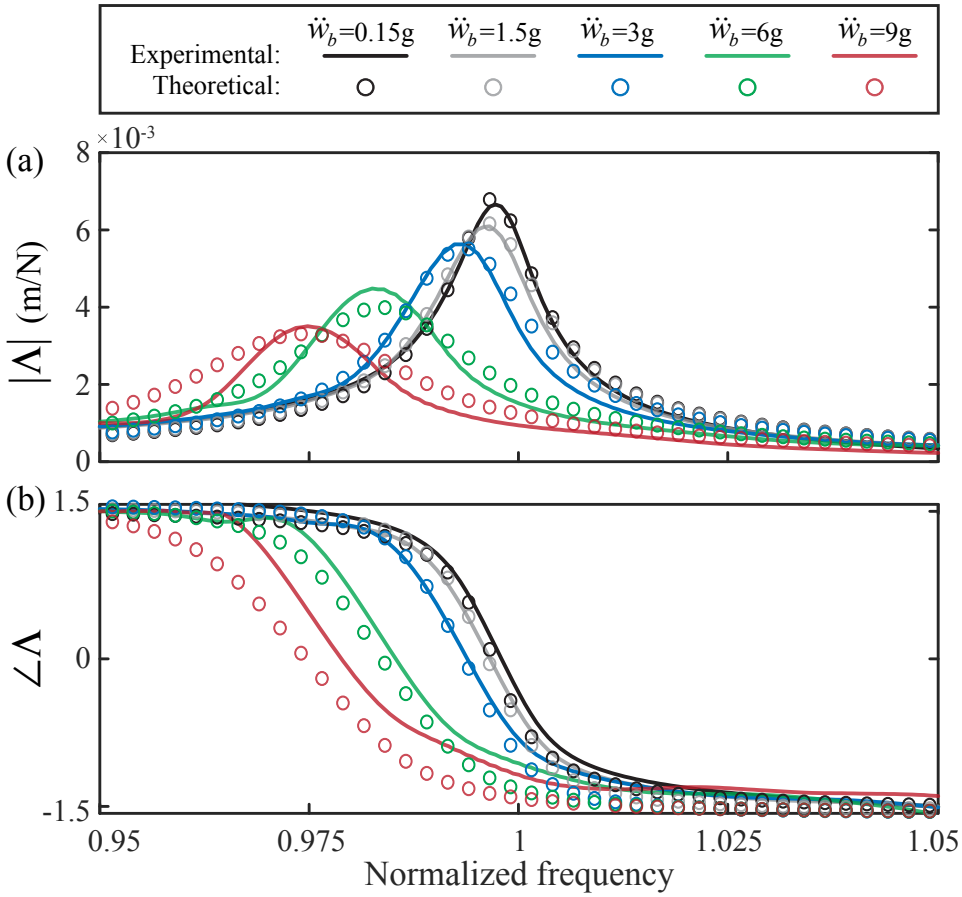

Figure 4.11: Experimental and theoretical frequency response function Λ of an inertia amplifier with $\theta = 35°$ under different base excitation accelerations $\ddot{w}_b$.

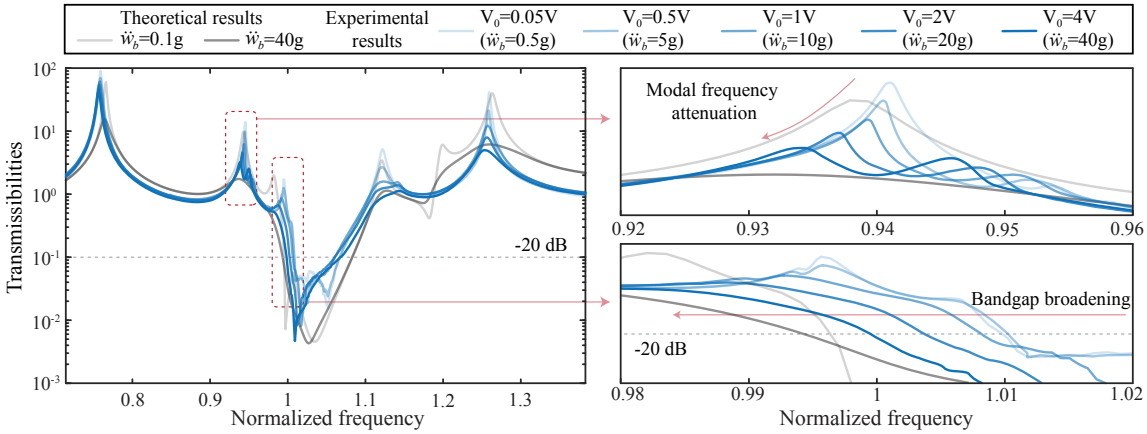

Figure 4.12: Experimental and theoretical transmissibilities of the nonlinear metamaterial under different base excitation voltages V_0 and accelerations $\ddot{w}_b$.

spaced 60 mm apart. The prototype is printed with Selective Laser Sintering 3D printing (EOSINT P760) in one piece. The parameters of the nonlinear metamaterial are shown in Tab. 4.1. To maintain stability during excitation, the nonlinear metamaterial is then hung vertically. One end of the metamaterial is clamped to a shaker (VE-5120) for

base excitation, resulting in a clamped-free boundary condition. A Polytec laser Doppler vibrometer (LDV) is used to record the out-of-plane velocity field at any point along the structure, such as the clamped and free end of the host beam. The data is acquired in the time domain through repeated acquisitions.

4.3.2 Experimental Results

Before the experiments on the nonlinear metamaterial shown in Figure 4.10, we first validate the nonlinear damping effect of an individual inertia amplifier. As shown in the enlarged view in Figure 4.10, we chose a tilted angle of 35°. The 3D-printed inertia amplifier is fixed to the shaker. In order to observe the nonlinear damping effect, a slow sweep signal with a rate of 0.1 Hz/s ranging from 180 Hz to 230 Hz is applied to the base of the nonlinear local resonator at a constant excitation force. Time domain velocity responses at different points on the top disk and excitation base of the resonator are recorded with the LDV.

The resonator's experimental and theoretical nonlinear frequency response is illustrated in Figure 4.11 with different base accelerations from 0.15 g to 9 g. The theoretical results are obtained using Eq. 4.3 by the harmonic balance method mentioned in Section 4.2.2, which show good agreement with experimental results. It can be seen that the resonant frequency of the resonator slightly shifts to a lower frequency with the increase of excitation force, which indicates an increase of the nonlinear damping effect studied previously, and a stiffness reduction that has also been observed in [190]. Therefore, we employed a cubic fitting of the stiffness versus the displacement amplitude W_r of the resonator, which returns the linear stiffness k_0 when W_r is small. A linear damping ratio $\zeta_0 = 0.005$ is also applied here. The nonlinear damping effect becomes prominent under large base accelerations, reducing the amplitude of its frequency response function and broadening its bandwidth. This amplitude-dependent nonlinear damping can also be observed from the phase angle of the frequency response Figure 4.11 (b). The slope of the phase transition around resonances is smaller under large excitation, which qualifies the theoretical model discussed in Section 4.2.1.

Once the nonlinear damping effect on the single resonator level has been identified, the transmissibilities of the nonlinear metamaterial, combining the base beam and sequential resonators, are shown in Figure 4.12. We excite the platform where the clamped side of the host beam is mounted at constant excitation force (controlled by the excitation voltage V_0 of the amplifier). As in the previous experiment, sweep signals slowly varying from 100 Hz to 350 Hz at 0.1 Hz/s are applied.

Due to the influence of modal responses on the excitation base, the experimental transmissibility of the host beam is calculated as the tip velocity of the host beam normalized by the input acceleration. It is further nondimensionalized with the excitation frequency. The theoretical transmissibility takes the same form as explained in Section 4.2.2. We use two theoretical cases ($\ddot{w}_b = 0.1$ g and $\ddot{w}_b = 40$ g) to indicate the effective range of the nonlinear metamaterial and compare these with the experimental results. It can be seen that the general trend and bandgap range of the experimental and theoretical results agree, which validates the analyses in Section 4.2.

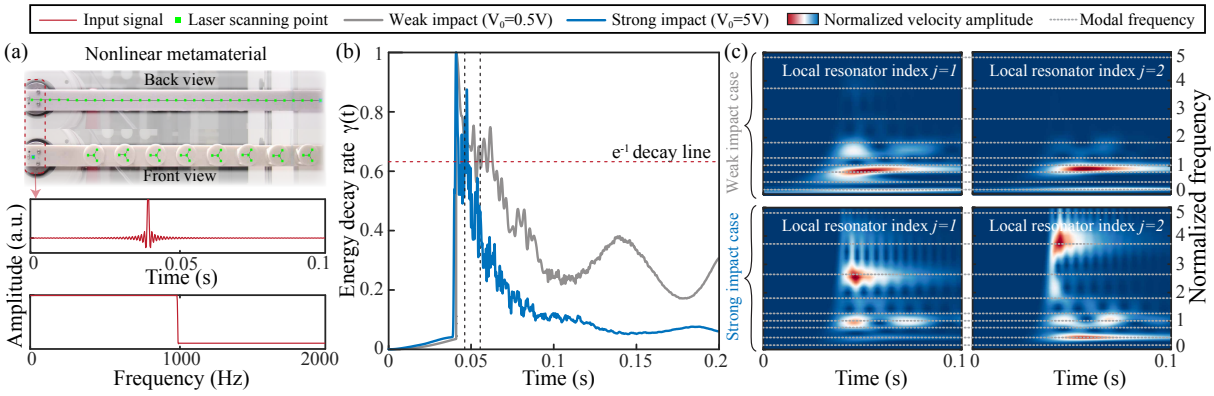

Figure 4.13: Experimental shock wave attenuation of the nonlinear metamaterial under different impact voltages V_0. (a) Experimental setup of the nonlinear metamaterial with the laser scanning points and the profile of the input impact signal; (b) Experimental energy decay rates of the nonlinear metamaterial under different impact intensities; (c) Experimental wavelet transforms of the velocities $\dot{w}_{rj}$ of the first two nonlinear local resonators for the two different impact cases.

By closely checking the enlarged views enclosed in red dashed squares, we can observe the bandgap broadening effect and the nonlinear energy transfer at modal frequencies. Under large excitation levels, the bandgap is broadened not only due to the nonlinear damping effect, but also the shifting of the stiffness of nonlinear local resonators. It should be noted that the bandgap degenerating effect is not obvious since the selected θ in the experiments is not small. Furthermore, the modal frequency peak around normalized frequency 0.9 gradually splits into two smaller peaks with the increase of the excitation level, highlighting the effect of the nonlinear damping.

To further demonstrate the nonlinear modal coupling and dissipation ability of the nonlinear metamaterial beyond its bandgap range, experimental impacts have been applied at the clamped side of the nonlinear metamaterial. The experimental setup is shown in Figure 4.13 (a), multiple laser scanning points are defined at the front and back sides of the nonlinear metamaterial to measure the velocity responses of the nonlinear local resonators and the host beam under different impact intensities. For each measurement of the out-of-plane velocity, a repeatable raised cosine pulse signal, with a bandwidth for modal frequencies lower than 1000 Hz, is excited by the shaker at the clamped side of the nonlinear metamaterial. The scanning points distributed along the host beam are spaced 20 mm apart.

The time evolution of the energy decay rates $\gamma(t)$ under different impact intensities are calculated with Eq. 4.32 to Eq. 4.34, in which the displacement and its derivative versus beam length are acquired by numerical integration of the velocity response and finite difference method, respectively. In Figure 4.13 (b), a stronger impact not only leads to faster energy dissipation of the system but also suggests energy redistribution to high frequency modes of the nonlinear metamaterial, which agrees with the modal dissipation ability studied in Section 4.2.3. By closely checking the wavelet transforms of the first two nonlinear local resonators in Figure 4.13 (c), there exist more frequency components correspond to higher modal frequencies for the strong impact case, which indicates the modal coupling ability of the nonlinear metamaterial for efficient energy redistribution of

the host beam for shock wave and impact attenuation.

4.4 Conclusion

This paper presents a practical, tunable nonlinear resonator based on the nonlinear damping effect induced by rotational inertia amplifiers. This resonator is used to create a nonlinear metamaterial for broadband vibration attenuation, combining a broader bandgap and general modal vibration dissipation within the host structure. Revisiting the nonlinear damping effect mechanism, we establish the nonlinear dispersion relationships for a semi-infinite nonlinear metamaterial case. More importantly, with respect to practical applications, the nonlinear frequency response of a finite structure is studied with modal analysis and Alternating Frequency Time (AFT) multiple harmonic balance methods for general nonlinearities in nonlinear metamaterials. The theoretical results reveal that the bandgap is broadened with the increase of excitation level. Especially, the nonlinear interactions between the local resonators and the mode shapes of the host beam lead to efficient modal frequency dissipation ability in the proposed metamaterial. Finally, experiments were carried out with both the single nonlinear resonator level and the full metamaterial system. The experimental results validate both the nonlinear bandgap and modal dissipation as mechanisms for broadband and shock wave attenuation. By incorporating the effect of nonlinearity with the concept of conventional locally resonant metamaterials, our findings enable new possibilities for vibration attenuation beyond the conventional linear bandgap range.

Acknowledgments

The authors acknowledge support from the ETH Research Grant (ETH-02 20-1), the H2020 FET-proactive project METAVEH under the grant agreement 952039, and the SNSF R'Equip grant 206021_205418.

4.A Appendix

The mass-normalized shape function of the host beam with clamped-free boundary condition can be shown as:

$$\begin{aligned}\phi_i(x) = \frac{1}{\sqrt{\rho_0 L}} \Bigg[&\cos\left(\frac{\lambda_i x}{L}\right) - \cosh\left(\frac{\lambda_i x}{L}\right) \\ &+ \left(\frac{\sin\lambda_i - \sinh\lambda_i}{\cos\lambda_i + \cosh\lambda_i}\right)\left(\sin\left(\frac{\lambda_i x}{L}\right) - \sinh\left(\frac{\lambda_i x}{L}\right)\right)\Bigg], \\ i = 1, 2, \ldots, N\end{aligned} \tag{4.35}$$

where λ_i is the positive eigenvalue of the characteristic equation read as:

$$\cos\lambda_i \cosh\lambda_i + 1 = 0. \tag{4.36}$$

By substituting Eq. 4.19 into Eq. 4.18, applying the orthogonality conditions with $\phi_s(x)$, and integrating over the span of the host beam, Eq. 4.18 is transformed into:

$$\begin{aligned} &\ddot{\eta}_i + \omega_i^2 \eta_i - \sum_{j=1}^{S} \left(k_j w_{rj} + c_j |\dot{w}_{rj}| \dot{w}_{rj}\right) \phi_i(x_j) \\ &= -\rho_0 \ddot{w}_b \int_{x=0}^{x=L} \phi_i(x) dx, \end{aligned} \tag{4.37}$$

where ω_i is the natural frequency of the i-th mode of the host beam. Follow the same procedure to substitute Eq. 4.19 into Eq. 4.17, it gives:

$$\begin{aligned} &m_j \left(\sum_{i=1}^{N} \ddot{\eta}_i \phi_i(x_j) + \ddot{w}_{rj} \right) + c_j |\dot{w}_{rj}| \dot{w}_{rj} \\ &+ k_j w_{rj} = -m_j \ddot{w}_b. \end{aligned} \tag{4.38}$$

The nonlinear reaction forces induced by the local resonators that are applied on the host beam can be represented by Eq. 4.38. Therefore, Eq. 4.37 can be rewrite as:

$$\begin{aligned} &\ddot{\eta}_i + \omega_i^2 \eta_i + \sum_{j=1}^{S} m_j \phi_i\left(x_j\right) \sum_{i=1}^{N} \ddot{\eta}_i \phi_i\left(x_j\right) \\ &+ \sum_{j=1}^{S} m_j \ddot{w}_{rj} \phi_i\left(x_j\right) = q_i, \quad r = 1, 2, \ldots, N \end{aligned} \tag{4.39}$$

where

$$q_i = -\ddot{w}_b \left(\int_{x=0}^{x=L} \rho_0 \phi_i(x) \mathrm{d}x + \sum_{j=1}^{S} m_j \phi_i\left(x_j\right) \right). \tag{4.40}$$

By combining Eq. 4.38 and Eq. 4.39, the matrix form equations of the nonlinear metamaterial can be achieved.

Chapter 5

Conclusions and Perspectives

The following concluding chapter provides a summary of the main findings achieved in this thesis and of the research questions and challenges addressed. Moreover, it offers insights into possible future developments of the presented research.

5.1 Conclusions

The research conducted in this dissertation aims to extend the applications of mechanical systems to guide wave and energy for low-frequency vibrations relevant to the elastic domain, first by revealing the mechanisms to guide elastic waves with locally resonant metamaterials or nonlinear dynamics and then by disclosing the potential of energy conversion in these systems for energy harvesting and dynamics control.

The thesis begins with an overarching theoretical introduction to wave propagation in elastic bodies and locally resonant metamaterials, electromechanical coupled piezoelectric systems, and their integration to form multifunctional metamaterials. Emphasizing elastic wave propagation and equivalent impedance analysis, electromechanical coupling in mechanical systems is investigated for its effects on the dispersion relationship governing elastic wave transmission through periodic media. The theoretical framework concludes by describing the potential functions of electromechanical coupled or nonlinear mechanical systems, leading to the next section, the state of the art. Here, a comprehensive review of groundbreaking mechanical systems for elastic wave attenuation, guiding, energy harvesting, signal sensing, active control, and actuating through different mechanisms is presented while highlighting the main challenges to be tackled.

The first part of the dissertation (Chapter 2) focuses on piezoelectric energy harvesting with the graded locally resonant metamaterial, which preserves its original bandgap for the attenuation of low-frequency vibrations. To this end, the design combines a beam-based graded metamaterial with the self-powered synchronized electric charge extraction circuit, which converts the alternating piezoelectric voltage into direct current power for IoT devices. The proposed metamaterial-based energy harvesting system seeks to overcome some of the challenges raised in the Introduction for practical applications of locally

resonant metamaterials: (i) the electromechanical codesign is mostly omitted in existing research, (ii) practical AC-DC conversion circuits are needed for harvesting DC power rather than AC voltage.
Conventional metamaterial-based energy harvesting studies mainly consider how to manipulate elastic waves but give little attention to the design targets of the energy harvesting system, which features both bandwidth and maximum harvested power. Due to the nature of conventional metamaterials, those studied applied identical single degree of freedom local resonators or wave lensing, focusing only on particular frequencies, i.e., the beginning frequency of the bandgap. To overcome this, in this part of the thesis, a graded design is investigated to employ its multiple resonances for broadband energy harvesting and wave trapping at different positions. Additionally, rather than a simple bridge rectifier or resistor, this study takes advantage of power electronics, which utilizes synchronized switching and buck-boost topology to decouple the energy flow from the piezoelectric clamped capacitor to the load of the circuit. This not only enables higher energy harvesting efficiency compared with bridge rectifiers but also leads to load independence, meaning the output power remains the same under different load conditions for various IoT device tasks. Further to these general considerations, several detailed conclusions can be drawn:

- The graded locally resonant metamaterial experiences a 20 dB transmission from 50 Hz to 300 Hz and an energy harvesting range from 50 Hz to 150 Hz, which broadens the energy harvesting range compared to its non-graded counterpart. This is achieved by gradually increasing the beam length of local resonators, forming a smooth impedance transition for elastic wave propagation to be trapped and amplified at the desired position and frequency.
- Under 0.1 N harmonic excitation at 90 Hz, the harvested power is up to 0.6 mW across all load conditions. Compared with the conventional cantilever beam-based energy harvesting solution, the harvested power of this work yields a four-fold increase. The gross effect of the harvested power from multiple local resonators is over 1 mW, which is already usable to power IoT devices.
- The equivalent impedance method employed in this work offers possibilities to transform the electrical components into their mechanical analogies, allowing the electromechanical coupling effect and the electrical harvested power to be calculated theoretically.

Based on the size and bandgap frequency range of the graded metamaterial, the primary applications are placed in the domains of vibration attenuation and energy harvesting for rotational machines operating at low frequencies, such as motors, generators, turbines, and pumps. By appropriately scaling the metamaterial system, different energy harvesting frequency ranges can also be achieved. These rotational machines typically operate with vibration accelerations ranging from 0.1 g to 5 g, providing a feasible input force for the graded metamaterial-based energy harvesting system to achieve milliwatt-level output power. This power level is sufficient to power microcontrollers with Bluetooth functions, which have low power consumption in sleep modes (around microwatts) and milliwatt-level consumption in active modes [206].

Despite the promising perspectives of the graded metamaterial-based energy harvesting system, the *limitations* of the study presented must be considered. The outcomes of this work are based on the linearization of the piezoelectric interface circuits, which generally work for weakly coupled electromechanical systems. However, the nonlinearities from MOSFET switching and diodes should be considered, as they form a nonlinear metamaterial system and could enable more novel wave and energy control mechanisms. The studies of nonlinear dynamics in electromechanical coupled systems and nonlinear metamaterial systems are further discussed in Chapter 3 and 4.

In the second part of the thesis (Chapters 3), the focus shifts to utilizing the harvested energy from mechanical systems. Thanks to the bidirectional energy conversion channels provided by the piezoelectric coupling transducers, it is possible to control dynamics without the need for external energy sources. Conventional piezoelectric actuation requires an external signal generator and power amplifier, typically realized through inverter designs. However, in this work, we present an energy-harvesting and vibration-actuating solution with a single piece of piezoelectric interface circuit developed by the author of the thesis previously. Its application in nonlinear energy harvesting systems addresses two major challenges: (i) the need for external devices to control dynamics or wave propagation and (ii) the integration and control of dynamics in nonlinear systems.

The outcomes of the first part of this dissertation prove that electromechanical coupling can introduce electrically induced damping and stiffness in the mechanical domain. This insight inspires dynamic control in nonlinear energy harvesting systems, where tuning electrical damping and stiffness can adjust the steady state represented by the fixed points to a certain degree. For example, negative damping or driven force from the actuation of the piezoelectric interface circuit can shift the stable states in nonlinear systems, offering an advantage for piezoelectric energy harvesting where high amplitude states are preferred. Using the multiple time scale method, we have analyzed the orbit jumps in these systems for autonomous and non-autonomous cases, revealing the mechanism of dynamic control with this bidirectional energy conversion circuit. The theoretical results are validated experimentally in both monostable and bistable systems, demonstrating the effectiveness and compactness of the proposed energy harvesting and dynamic control solution. From this chapter, the following conclusions can be drawn:

- The piezoelectric energy harvesting and vibration actuating functions are realized with the same interface circuit, offering a self-contained orbit jump and dynamic control solution for nonlinear energy harvesters.
- The harvested power yields a nine-fold increase after the orbit jump, quickly compensating for the power consumption of the orbit jump process.
- The multiple time scale and stability analysis demonstrate the orbit jump process, revealing the role of unstable spirals and saddle-node bifurcation with negative electrically induced damping.

The promising findings of this study reveal the complexity of nonlinear dynamics and its novel applications in vibration control. However, a complementary investigation of high-dimensional nonlinear dynamical systems, such as nonlinear metamaterials, is still

needed, given the potential for novel wave propagation and control mechanisms.

Chapter 4 presents a comprehensive study of a nonlinear damped metamaterial, which applies the concept of nonlinear dynamics for vibration control to locally resonant metamaterials. Compared with linear locally resonant metamaterials, nonlinear ones offer amplitude-dependent responses, providing flexibility and the ability to tune wave propagation with different input excitation conditions. This work revisits the geometry nonlinear damping effect from the deformation relationship of the local resonators. Its application to locally resonant metamaterials leads to nonlinear dispersion relationships in the infinite beam cases. To address the nonlinear frequency response in finite nonlinear metamaterial cases, the author has developed a numerical harmonic balance-based model that can handle generic nonlinear reaction forces applied to a linear substrate system with boundary conditions, such as a cantilever Euler-Bernoulli beam studied in this work. In addition to the bandgap of the nonlinear metamaterial, the nonlinear coupling of local resonators and mode shapes is discussed, revealing the vibration attenuation capability beyond the bandgap range. To validate the theoretical findings, experiments are first conducted at the nonlinear local resonator level and then at the whole nonlinear metamaterial system level. The bandgap broadening effects, nonlinear modal dissipation, and shock wave attenuation have been verified experimentally. Overall, the following conclusions can be drawn:

- The locally resonant bandgap has been broadened due to the nonlinear damping effect from the local resonators.
- Besides the bandgap range, the nonlinear effect also induces modal coupling with the mode shapes of the host beam, further facilitating energy redistribution in the substrate beam for stronger modal dissipation.
- The nonlinear effect is amplitude-dependent, making the nonlinear damped metamaterial particularly suitable for dampening impact or shock wave propagation along the host beam, as demonstrated by theoretical and experimental results.
- The proposed numerical harmonic balance-based modeling methods can handle generic forms of nonlinearities and bifurcation issues with hysteresis through numerical continuation techniques, providing a generic approach to solving nonlinear metamaterials in the frequency domain.

The investigations conducted in this chapter reveal an important *limitation*: these theoretical methods are based on harmonic excitation and low-dimensional systems. If nonperiodic excitation or higher dimensions are involved, the current formulation may face challenges in both theoretical formulation and computation time. Therefore, exploring extensions with random processes and high-fidelity parallel computing is necessary for addressing nonlinear wave propagation problems in large-scale models.

5.2 Research Contributions and Outlooks

The present research addresses the field of elastic wave propagation and energy conversion in mechanical systems, where manifold designs and physical phenomena well-established

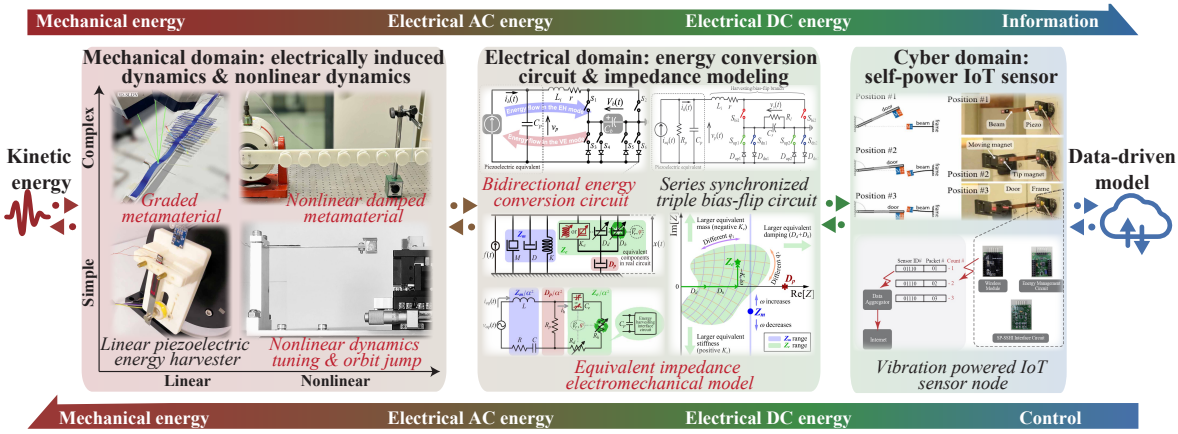

Figure 5.1: Research contribution and research works of the author (The works presented in this dissertation are labeled in red). The mechanical domain: Linear piezoelectric energy harvester [33]; Nonlinear dynamics tuning and orbit jump (Chapter 3) [84, 103]; Graded metamaterials for energy harvesting (Chapter 2) [54]; Nonlinear damped metamaterials for wideband vibration attention (Chapter 4) [67]. The electrical domain: Bidirectional energy conversion circuit (used in Chapter 3) [30]; Series synchronized triple bias-flip circuit [23]; Equivalent impedance electromechanical models (used in Chapter 2) [33, 172]. The cyber domain: Vibration-powered IoT sensor node [207].

in other domains (e.g., electromagnetism, acoustics, or power electronics) have yet to be fully explored. The research contributions and relevant work by the author of this thesis are illustrated in Figure 5.1. Understanding the joint dynamics and effectively managing the relationship between (energy) supply and (information) demand is crucial for guiding waves in mechanical systems and realizing self-powered IoT systems. The following sections outline my rationale, persistence, and interdisciplinary efforts toward achieving this research goal from three main aspects:

The graded metamaterial-based energy harvesting system presented in 2 has demonstrated the potential to power IoT sensor nodes and replace conventional chemical batteries with artificially fabricated metamaterials and piezoelectric interface circuits. This requires coupling of mechanics, dynamics, and electronics principles. In this chapter, the author has demonstrated such a fusion through electrically induced damping and stiffness properties and investigated their impact on wave propagation through these coupled systems. Considering different AC-DC interface circuits, the impedance matching abilities and the joint dynamics of the electromechanical system have been discussed. Based on the understanding of the joint dynamics of piezoelectric energy harvesting systems [33], the author has extended the results into high-degree-of-freedom mechanical metamaterial systems. By incorporating the interface circuit into a graded locally resonant metamaterial, the author studied wave propagation phenomena such as wave-flied amplification and frequency separation in this electromechanical system. Through the codesign of the mechanical domain, the author realized *near-milliwatt DC power output from a single resonator within a local resonant metamaterial* for low-frequency vibrations for the first time [54].

The energy conversion circuit connects the mechanical structures with the electronic device to control the energy flow in the coupled system. Given the flexibility of power electronics and embedded systems, direct and inverse energy flows can be controlled quan-

titatively through charge (energy) manipulations in a two-way coupled electromechanical system. Thus, the source and load can be switched to achieve multifunctions, i.e., energy harvesting and vibration actuating, without external energy input devices. Based on the dynamic models of KEH systems, the author has further made in-depth theoretical studies and practical explorations about multifunctional interface circuit methods, and their applications in nonlinear systems to manipulate energy flows with circuits in Chapter 3. By tuning the phase between voltage (force) and current (velocity) with different MOSFETs switching paths, programmable electrically induced damping and stiffness can be realized. On the one hand, by increasing the positive electrically induced damping, the author has designed a novel interface circuit that can achieve high-capability energy harvesting [23]. Conversely, *negative damping has also been realized intuitively in energy harvesting systems* by the harvested energy [30]. The source's information can also be extrapolated with the system's energy flow based on the energy level and duration. One of the author's previous works also features a transient-motion-powered IoT platform for motion tracking [207].

Parallel with the fundamental concepts, dynamic modeling, performance improvement, and engineering applications of electromechanical coupling systems mentioned above, the author has also studied the nonlinear dynamics for systems with power conditioning circuits or locally resonant nonlinear metamaterials. Based on the dynamic modeling of electromechanical systems, the author has introduced nonlinearity in dynamical systems for broadband energy harvesting owing to the induced hysteresis characteristic. The content presented in Chapter 3 has studied the dynamics of nonlinear energy harvesting systems with power conditioning circuits [84]. Particularly, to maintain a high energy orbit for more harvested energy, the author has provided a new efficient way with a bidirectional energy conversion circuit to control the nonlinear stability of the system with its own harvested energy [103]. Such unprecedented low-powered solutions promote the investigation of electromechanical coupling nonlinear dynamics. Besides the dynamics modeling for nonlinear energy harvesting systems, the author has firstly introduced *the advanced numerical harmonic balance and continuation methods into the research field of nonlinear metamaterials* in Chapter 4, which is regarded as challenging to model due to the need for analytical tools. By developing a customized reduced order modal superposition method with numerical harmonic balance and continuations, the author has verified the nonlinear bandgap and modal dissipation ability theoretically and experimentally [67].

Based on the the research work conducted in this dissertation, the potential outlooks for further investigation are listed as follows:

1: Deep fusion of power electronics with structural dynamics

The application of power electronics in mechanical structures has been introduced previously, for example, in electrical motors. However, most existing research only considers shunting circuits, while the potential of power electronics is not fully released. This first outlook focuses on the possibility of leveraging power electronics to create multifunctional interface circuits for small-scale IoT sensor nodes. These circuits will guide energy flow for efficient energy harvesting, sensing, control, and actuation, serving the purpose of multifunctional electromechanical coupling systems.

2: Complex dynamics modeling for mechanical systems

The circuit solution is only the initial step toward the fusion of power electronics with structural dynamics. This outlook aims to explore novel models for interfacing electromechanical dynamics, especially under complex conditions like nonlinear reaction forces from mechanical structures or interface circuits. The goal is to explore nonlinear wave propagation and control issues toward accurate modeling of frequency or time domain responses of these coupled systems.

3: Applications for Internet of Things

Based on the previous theoretical investigations, self-power electromechanical systems can be realized for monitoring the structural health like buildings, bridges, wind turbines, and generators where ambient vibration is pervasive, which will integrate three core areas: mechanics, electronics, and information technology. These practical applicable systems aim to overcome current limitations in structural health monitoring by combining energy harvesting, which gathers energy from low-frequency mechanical vibrations, with signal processing, which interprets those vibration signals to detect potential structural damages. This direction has significant potential for both academia and industry. By harnessing low-frequency vibrations from the environment, such as those from traffic or machine vibrations, the integrated systems could continuously monitor the health of structures without the need for external power, making it more sustainable.

These considerations represent a natural extension of the study presented in the dissertation. The content and anticipated outcomes of these further research directions aim not only to fulfill the goals mentioned above but also to demonstrate how wave and energy dynamics in mechanical (and electromechanical) systems can lead to the development of self-powered, self-sensing, and self-aware devices with significant scientific and economic value. (1) For the mechanical domain, investigation of complex dynamics in coupled systems will enhance modeling methods and optimal designs beyond the conventional energy conversion context.; (2) For the electrical domain, the potential of power electronics interface circuits can be fully realized for multifunctional applications, including dynamics sensing, mechanical-to-electrical energy conversion, and vice versa, electrical-to-mechanical motion control; (3) For the cyber domain, data-driven models and intelligent IoT applications can be seamlessly integrated for structural health monitoring and decision-making. For broader society, the content and expected results will not only provide sustainable and resilient energy solutions for scientific and industrial applications but also offer potential improvements in daily life and reshape our approach to energy utilization.

List of Figures

List of Tables

Bibliography

[1] K. F. Graff, *Wave Motion in Elastic Solids*. Courier Corporation, 2012.

[2] A. Raghavan, "Guided-wave structural health monitoring," Ph.D. dissertation, 2007.

[3] M. Mitra and S. Gopalakrishnan, "Guided wave based structural health monitoring: A review," *Smart Materials and Structures*, vol. 25, no. 5, p. 053001, 2016.

[4] M. I. Hussein, M. J. Leamy, and M. Ruzzene, "Dynamics of phononic materials and structures: Historical origins, recent progress, and future outlook," *Applied Mechanics Reviews*, vol. 66, no. 4, 2014.

[5] Z. Liu, X. Zhang, Y. Mao, Y. Zhu, Z. Yang, C. T. Chan, and P. Sheng, "Locally resonant sonic materials," *Science*, vol. 289, no. 5485, pp. 1734–1736, 2000.

[6] E. Yablonovitch, "Inhibited spontaneous emission in solid-state physics and electronics," *Physical Review Letters*, vol. 58, no. 20, p. 2059, 1987.

[7] S. John, "Strong localization of photons in certain disordered dielectric superlattices," *Physical Review Letters*, vol. 58, no. 23, p. 2486, 1987.

[8] V. G. Veselago, "The electrodynamics of substances with simultaneously negative values of permittivity and permeability," *Usp. fiz. nauk*, vol. 92, no. 7, pp. 517–526, 1967.

[9] M. S. Kushwaha, P. Halevi, L. Dobrzynski, and B. Djafari-Rouhani, "Acoustic band structure of periodic elastic composites," *Physical Review Letters*, vol. 71, no. 13, p. 2022, 1993.

[10] A. Colombi, P. Roux, and M. Rupin, "Sub-wavelength energy trapping of elastic waves in a metamaterial," *The Journal of the Acoustical Society of America*, vol. 136, no. 2, pp. EL192–EL198, 2014.

[11] H. J. Xiang, Z. F. Shi, S. J. Wang, and Y. L. Mo, "Periodic materials-based vibration attenuation in layered foundations: Experimental validation," *Smart Materials and Structures*, vol. 21, no. 11, 2012.

[12] L. J. Gibson and M. F. Ashby, *Cellular Solids: Structure and Properties*. Cambridge University Press, Cambridge, 1997.

[13] P. Gomez Garcia and J.-P. Fernández-Álvarez, "Floquet-Bloch theory and its application to the dispersion curves of nonperiodic layered systems," *Mathematical Problems in Engineering*, vol. 2015, 2015.

[14] C. Kittel and P. McEuen, *Introduction to Solid State Physics*. Wiley New York, 1976, vol. 8.

[15] N. W. Ashcroft and N. D. Mermin, *Solid State Physics*. Holt-Saunders, 1976.

[16] V. Laude, "Phononic crystals," in *Phononic Crystals*. de Gruyter, 2020.

[17] B. R. Mace and E. Manconi, "Modelling wave propagation in two-dimensional structures using finite element analysis," *Journal of Sound and Vibration*, vol. 318, no. 4-5, pp. 884–902, 2008.

[18] L. Brillouin, *Wave Propagation in Periodic Structures: Electric Filters and Crystal Lattices*. Dover Publications, 1953, vol. 2.

[19] V. Giurgiutiu, *Structural Health Monitoring: with Piezoelectric Wafer Active Sensors*. Elsevier, 2007.

[20] S. H. Simon, *The Oxford Solid State Basics*. Oxford, UK: Oxford University Press, 2013.

[21] J. Liang and W.-H. Liao, "Impedance modeling and analysis for piezoelectric energy harvesting systems," *IEEE/ASME transactions on mechatronics*, vol. 17, no. 6, pp. 1145–1157, 2011.

[22] C. Chen, B. Zhao, and J. Liang, "Revisit of synchronized electric charge extraction (sece) in piezoelectric energy harvesting by using impedance modeling," *Smart Materials and Structures*, vol. 28, no. 10, p. 105053, 2019.

[23] B. Zhao, K. Zhao, X. Wang, J. Liang, and Z. Chen, "Series synchronized triple bias-flip circuit: Maximizing the usage of a single storage capacitor for piezoelectric energy harvesting enhancement," *IEEE Transactions on Power Electronics*, vol. 36, no. 6, pp. 6787–6796, 2020.

[24] "Ieee standard on piezoelectricity," *ANSI/IEEE Std 176-1987*, 1988.

[25] A. Erturk and D. J. Inman, *Piezoelectric energy harvesting*. John Wiley & Sons, 2011.

[26] ——, "Broadband piezoelectric power generation on high-energy orbits of the bistable duffing oscillator with electromechanical coupling," *Journal of Sound and Vibration*, vol. 330, no. 10, pp. 2339–2353, 2011.

[27] D. Guyomar, A. Badel, E. Lefeuvre, and C. Richard, "Toward energy harvesting using active materials and conversion improvement by nonlinear processing," *IEEE Trans. Ultrason. Ferroelectr. Freq. Control*, vol. 52, no. 4, pp. 584–595, 2005.

[28] E. Lefeuvre, A. Badel, C. Richard, and D. Guyomar, "Piezoelectric energy harvesting device optimization by synchronous electric charge extraction," *Journal of intelligent material systems and structures*, vol. 16, no. 10, pp. 865–876, 2005.

[29] J. Liang, "Synchronized bias-flip interface circuits for piezoelectric energy harvesting enhancement: A general model and prospects," *Journal of Intelligent Material Systems and Structures*, vol. 28, no. 3, pp. 339–356, 2017.

[30] B. Zhao, J. Wang, W.-H. Liao, and J. Liang, "A bidirectional energy conversion circuit towards multi-functional piezoelectric energy harvesting and vibration excitation purposes," *IEEE Transactions on Power Electronics*, 2021.

[31] R. W. Erickson and D. Maksimovic, *Fundamentals of power electronics*. Springer Science & Business Media, 2007.

[32] J. Liang and W.-H. Liao, "Energy flow in piezoelectric energy harvesting systems," *Smart Materials and Structures*, vol. 20, no. 1, p. 015005, 2010.

[33] B. Zhao, J. Qiu, and J. Liang, "Circuit solutions toward broadband piezoelectric energy harvesting: An impedance analysis," *IEEE Transactions on Circuits and Systems I: Regular Papers*, pp. 1–12, 2023. [Online]. Available: https://doi.org/10.1109/TCSI.2023.3324618

[34] J. Lou, X. Fang, J. Du, and H. Wu, "Propagation of fundamental and third harmonics along a nonlinear seismic metasurface," *International Journal of Mechanical Sciences*, vol. 221, p. 107189, 2022.

[35] J.-S. Chen, W.-J. Su, Y. Cheng, W.-C. Li, and C.-Y. Lin, "A metamaterial structure capable of wave attenuation and concurrent energy harvesting," *Journal of Intelligent Material Systems and Structures*, vol. 30, no. 20, pp. 2973–2981, 2019.

[36] A. Colombi, V. Ageeva, R. J. Smith, A. Clare, R. Patel, M. Clark, D. Colquitt, P. Roux, S. Guenneau, and R. V. Craster, "Enhanced sensing and conversion of ultrasonic rayleigh waves by elastic metasurfaces," *Scientific Reports*, vol. 7, no. 1, pp. 1–9, 2017.

[37] M. Alshaqaq and A. Erturk, "Graded multifunctional piezoelectric metastructures for wideband vibration attenuation and energy harvesting," *Smart Materials and Structures*, vol. 30, no. 1, p. 015029, 2020.

[38] J. M. De Ponti, A. Colombi, R. Ardito, F. Braghin, A. Corigliano, and R. V. Craster, "Graded elastic metasurface for enhanced energy harvesting," *New Journal of Physics*, vol. 22, no. 1, p. 013013, 2020.

[39] G. Hu, J. Wang, and L. Tang, "A comb-like beam based piezoelectric system for galloping energy harvesting," *Mechanical Systems and Signal Processing*, vol. 150, p. 107301, 2021.

[40] G. Hu, L. Tang, J. Liang, C. Lan, and R. Das, "Acoustic-elastic metamaterials and phononic crystals for energy harvesting: A review," *Smart Materials and Structures*, 2021.

[41] J. B. Pendry, A. J. Holden, D. J. Robbins, and W. Stewart, "Magnetism from conductors and enhanced nonlinear phenomena," *IEEE Transactions on Microwave Theory and Techniques*, vol. 47, no. 11, pp. 2075–2084, 1999.

[42] F. Rahimi, R. Aghayari, and B. Samali, "Application of tuned mass dampers for structural vibration control: A state-of-the-art review," *Civil Engineering Journal*, pp. 1622–1651, 2020.

[43] F. Naeim, *The Seismic Design Handbook*. Springer Science & Business Media, 1989.

[44] F. Meseguer, M. Holgado, D. Caballero, N. Benaches, J. Sanchez-Dehesa, C. López, and J. Llinares, "Rayleigh-wave attenuation by a semi-infinite two-dimensional elastic-band-gap crystal," *Physical Review B*, vol. 59, no. 19, p. 12169, 1999.

[45] C. Sugino, M. Ruzzene, and A. Erturk, "Digitally programmable resonant elastic metamaterials," *Physical Review Applied*, vol. 13, no. 6, p. 061001, 2020.

[46] ——, "Merging mechanical and electromechanical bandgaps in locally resonant metamaterials and metastructures," *Journal of the Mechanics and Physics of Solids*, vol. 116, pp. 323–333, 2018.

[47] Y. Xia, M. Ruzzene, and A. Erturk, "Bistable attachments for wideband nonlinear vibration attenuation in a metamaterial beam," *Nonlinear Dynamics*, vol. 102, no. 3, pp. 1285–1296, 2020.

[48] X. Fang, P. Sheng, J. Wen, W. Chen, and L. Cheng, "A nonlinear metamaterial plate for suppressing vibration and sound radiation," *International Journal of Mechanical Sciences*, vol. 228, p. 107473, 2022.

[49] A. F. Vakakis, "Inducing passive nonlinear energy sinks in vibrating systems," *J. Vib. Acoust.*, vol. 123, no. 3, pp. 324–332, 2001.

[50] H. A. Sodano, D. J. Inman, and G. Park, "A review of power harvesting from vibration using piezoelectric materials," *Shock and Vibration Digest*, vol. 36, no. 3, pp. 197–206, 2004.

[51] L. Zuo and S. A. Nayfeh, "Optimization of the individual stiffness and damping parameters in multiple-tuned-mass-damper systems," *J. Vib. Acoust.*, vol. 127, no. 1, pp. 77–83, 2005.

[52] B. Banerjee, *An introduction to metamaterials and waves in composites*. Crc Press, 2011.

[53] Z. Chen, Y. Xia, J. He, Y. Xiong, and G. Wang, "Elastic-electro-mechanical modeling and analysis of piezoelectric metamaterial plate with a self-powered synchronized charge extraction circuit for vibration energy harvesting," *Mechanical Systems and Signal Processing*, vol. 143, p. 106824, 2020.

[54] B. Zhao, H. R. Thomsen, J. M. De Ponti, E. Riva, B. Van Damme, A. Bergamini, E. Chatzi, and A. Colombi, "A graded metamaterial for broadband and high-capability piezoelectric energy harvesting," *Energy Conversion and Management*, vol. 269, p. 116056, 2022.

[55] C. Sugino, S. Leadenham, M. Ruzzene, and A. Erturk, "On the mechanism of bandgap formation in locally resonant finite elastic metamaterials," *Journal of Applied Physics*, vol. 120, no. 13, p. 134501, 2016.

[56] S. El-Borgi, R. Fernandes, P. Rajendran, R. Yazbeck, J. Boyd, and D. Lagoudas, "Multiple bandgap formation in a locally resonant linear metamaterial beam: Theory and experiments," *Journal of Sound and Vibration*, vol. 488, p. 115647, 2020.

[57] Y. Xiao, J. Wen, and X. Wen, "Longitudinal wave band gaps in metamaterial-based elastic rods containing multi-degree-of-freedom resonators," *New Journal of Physics*, vol. 14, no. 3, p. 033042, 2012.

[58] H. Poincaré, *Sur le problème des trois corps et les équations de la dynamique.* Mémoire couronné du prix de SM le Roi Oscar II, 1889.

[59] G. Duffing, *Erzwungene Schwingungen bei veränderlicher Eigenfrequenz und ihre technische Bedeutung.* Vieweg, 1918, no. 41-42.

[60] B. Van Der Pol, "Vii. forced oscillations in a circuit with non-linear resistance.(reception with reactive triode)," *The London, Edinburgh, and Dublin Philosophical Magazine and Journal of Science*, vol. 3, no. 13, pp. 65–80, 1927.

[61] A. F. Vakakis, O. V. Gendelman, L. A. Bergman, D. M. McFarland, G. Kerschen, and Y. S. Lee, *Nonlinear targeted energy transfer in mechanical and structural systems.* Springer Science & Business Media, 2008, vol. 156.

[62] M. I. Hussein, "Theory of damped bloch waves in elastic media," *Physical Review B*, vol. 80, no. 21, p. 212301, 2009.

[63] M. H. Bae and J. H. Oh, "Amplitude-induced bandgap: New type of bandgap for nonlinear elastic metamaterials," *Journal of the Mechanics and Physics of Solids*, vol. 139, p. 103930, 2020.

[64] ——, "Nonlinear elastic metamaterial for tunable bandgap at quasi-static frequency," *Mechanical Systems and Signal Processing*, vol. 170, p. 108832, 2022.

[65] K. Bertoldi, P. M. Reis, S. Willshaw, and T. Mullin, "Negative Poisson's ratio behavior induced by an elastic instability," *Advanced Materials*, vol. 22, no. 3, pp. 361–366, 2010.

[66] Y. Shen and W. Lacarbonara, "Nonlinear dispersion properties of metamaterial beams hosting nonlinear resonators and stop band optimization," *Mechanical Systems and Signal Processing*, vol. 187, p. 109920, 2023.

[67] B. Zhao, H. R. Thomsen, X. Pu, S. Fang, Z. Lai, B. Van Damme, A. Bergamini, E. Chatzi, and A. Colombi, "A nonlinear damped metamaterial: Wideband attenuation with nonlinear bandgap and modal dissipation," *Mechanical Systems and Signal Processing*, vol. 208, p. 111079, 2024.

[68] M. Gzal, A. F. Vakakis, L. A. Bergman, and O. V. Gendelman, "Extreme intermodal energy transfers through vibro-impacts for highly effective and rapid blast mitigation," *Communications in Nonlinear Science and Numerical Simulation*, vol. 103, p. 106012, 2021.

[69] W. Wu, P. Liu, and Z. Kang, "A novel mechanical metamaterial with simultaneous stretching-and compression-expanding property," *Materials & Design*, vol. 208, p. 109930, 2021.

[70] R. Craster and S. Guenneau, *Acoustic Metamaterials: Negative Refraction, Imaging, Lensing and Cloaking*. London: Springer, 2012.

[71] A. Colombi, D. Colquitt, P. Roux, S. Guenneau, and R. V. Craster, "A seismic metamaterial: The resonant metawedge," *Scientific reports*, vol. 6, no. 1, p. 27717, 2016.

[72] K. L. Tsakmakidis, A. D. Boardman, and O. Hess, "'trapped rainbow'storage of light in metamaterials," *Nature*, vol. 450, no. 7168, pp. 397–401, 2007.

[73] J. Zhu, Y. Chen, X. Zhu, F. J. Garcia-Vidal, X. Yin, W. Zhang, and X. Zhang, "Acoustic rainbow trapping," *Scientific reports*, vol. 3, no. 1, pp. 1–6, 2013.

[74] R. Zaccherini, A. Colombi, A. Palermo, V. K. Dertimanis, A. Marzani, H. R. Thomsen, B. Stojadinovic, and E. N. Chatzi, "Locally resonant metasurfaces for shear waves in granular media," *Physical Review Applied*, vol. 13, no. 3, p. 034055, 2020.

[75] H. R. Thomsen, B. Zhao, and A. Colombi, "Boundless metamaterial experimentation: Physical realization of a unidirectional virtual periodic boundary condition," *Phys. Rev. Appl.*, vol. 19, p. 064019, Jun 2023.

[76] J. M. De Ponti, A. Colombi, E. Riva, R. Ardito, F. Braghin, A. Corigliano, and R. V. Craster, "Experimental investigation of amplification, via a mechanical delay-line, in a rainbow-based metamaterial for energy harvesting," *Applied Physics Letters*, vol. 117, no. 14, p. 143902, 2020.

[77] X. Pu, A. Palermo, and A. Marzani, "Topological edge states of quasiperiodic elastic metasurfaces," *Mechanical Systems and Signal Processing*, vol. 181, p. 109478, 2022.

[78] J. M. De Ponti, L. Iorio, G. J. Chaplain, A. Corigliano, R. V. Craster, and R. Ardito, "Tailored topological edge waves via chiral hierarchical metamaterials," *Physical Review Applied*, vol. 19, no. 3, p. 034079, 2023.

[79] C. Dorn and D. M. Kochmann, "Conformally graded metamaterials for elastic wave guidance," *Extreme Mechanics Letters*, vol. 65, p. 102091, 2023.

[80] D. Shechtman, I. Blech, D. Gratias, and J. W. Cahn, "Metallic phase with long-range orientational order and no translational symmetry," *Physical review letters*, vol. 53, no. 20, p. 1951, 1984.

[81] H. Nassar, H. Chen, A. Norris, and G. Huang, "Quantization of band tilting in modulated phononic crystals," *Physical Review B*, vol. 97, no. 1, p. 014305, 2018.

[82] M. Coppolaro, G. Castaldi, and V. Galdi, "Aperiodic order induced enhancement of weak nonlocality in multilayered dielectric metamaterials," *Physical Review B*, vol. 98, no. 19, p. 195128, 2018.

[83] H. H. Sheinfux, Y. Lumer, G. Ankonina, A. Z. Genack, G. Bartal, and M. Segev, "Observation of anderson localization in disordered nanophotonic structures," *Science*, vol. 356, no. 6341, pp. 953–956, 2017.

[84] B. Zhao, J. Wang, J. Liang, and W.-H. Liao, "A dual-effect solution for broadband piezoelectric energy harvesting," *Applied physics letters*, vol. 116, no. 6, p. 063901, 2020.

[85] J. M. De Ponti, A. Colombi, R. Ardito, F. Braghin, A. Corigliano, and R. V. Craster, "Graded elastic metasurface for enhanced energy harvesting," *New Journal of Physics*, vol. 22, no. 1, p. 013013, 2020.

[86] M. Hwang and A. F. Arrieta, "Input-independent energy harvesting in bistable lattices from transition waves," *Scientific reports*, vol. 8, no. 1, pp. 1–9, 2018.

[87] G. J. Chaplain, J. M. De Ponti, G. Aguzzi, A. Colombi, and R. V. Craster, "Topological rainbow trapping for elastic energy harvesting in graded su-schrieffer-heeger systems," *Physical Review Applied*, vol. 14, no. 5, p. 054035, 2020.

[88] C. B. Williams and R. B. Yates, "Analysis of a micro-electric generator for microsystems," *Sens. Actuators, A*, vol. 52, no. 1, pp. 8 – 11, 1996.

[89] L. Tang, Y. Yang, and C. K. Soh, "Toward broadband vibration-based energy harvesting," *Journal of intelligent material systems and structures*, vol. 21, no. 18, pp. 1867–1897, 2010.

[90] M. Rosso, A. Corigliano, and R. Ardito, "Numerical and experimental evaluation of the magnetic interaction for frequency up-conversion in piezoelectric vibration energy harvesters," *Meccanica*, vol. 57, no. 5, pp. 1139–1154, 2022.

[91] M. Hwang and A. F. Arrieta, "Extreme frequency conversion from soliton resonant interactions," *Physical Review Letters*, vol. 126, no. 7, p. 073902, 2021.

[92] O. R. Bilal, A. Foehr, and C. Daraio, "Bistable metamaterial for switching and cascading elastic vibrations," *Proceedings of the National Academy of Sciences*, vol. 114, no. 18, pp. 4603–4606, 2017.

[93] T. Chen, M. Pauly, and P. M. Reis, "A reprogrammable mechanical metamaterial with stable memory," *Nature*, vol. 589, no. 7842, pp. 386–390, 2021.

[94] H. V. Poor, *An introduction to signal detection and estimation*. Springer Science & Business Media, 2013.

[95] L. Gao, L. Teng, H. Wang, Y. Liu, M. Fu, and J. Liang, "A self-sensing synchronous switch circuit for bidirectional piezoelectric energy conversion," *IEEE Transactions on Industrial Electronics*, 2023.

[96] S. A. Cummer, J. Christensen, and A. Alù, "Controlling sound with acoustic metamaterials," *Nature Reviews Materials*, vol. 1, no. 3, pp. 1–13, 2016.

[97] H. Nassar, B. Yousefzadeh, R. Fleury, M. Ruzzene, A. Alù, C. Daraio, A. N. Norris, G. Huang, and M. R. Haberman, "Nonreciprocity in acoustic and elastic materials," *Nature Reviews Materials*, vol. 5, no. 9, pp. 667–685, 2020.

[98] Y. Wang, B. Yousefzadeh, H. Chen, H. Nassar, G. Huang, and C. Daraio, "Observation of nonreciprocal wave propagation in a dynamic phononic lattice," *Physical review letters*, vol. 121, no. 19, p. 194301, 2018.

[99] Y. Chen, X. Li, C. Scheibner, V. Vitelli, and G. Huang, "Realization of active metamaterials with odd micropolar elasticity," *Nature communications*, vol. 12, no. 1, p. 5935, 2021.

[100] L. Yu, L. Tang, L. Xiong, and T. Yang, "Capture of high energy orbit of duffing oscillator with time-varying parameters," *Chaos: An Interdisciplinary Journal of Nonlinear Science*, vol. 30, no. 2, p. 023106, 2020.

[101] N. Nadkarni, A. F. Arrieta, C. Chong, D. M. Kochmann, and C. Daraio, "Unidirectional transition waves in bistable lattices," *Physical review letters*, vol. 116, no. 24, p. 244501, 2016.

[102] M. Brandenbourger, C. Scheibner, J. Veenstra, V. Vitelli, and C. Coulais, "Limit cycles turn active matter into robots," *arXiv preprint arXiv:2108.08837*, 2021.

[103] B. Zhao, J. Wang, G. Hu, A. Colombi, W.-H. Liao, and J. Liang, "Time-sharing orbit jump and energy harvesting in nonlinear piezoelectric energy harvesters using a synchronous switch circuit," *arXiv preprint arXiv:2305.06016*, 2023.

[104] S. Sharma, R. Kiran, P. Azad, and R. Vaish, "A review of piezoelectric energy harvesting tiles: Available designs and future perspective," *Energy Conversion and Management*, vol. 254, p. 115272, 2022.

[105] J. Huang, X. Li, Y. Wang, and H. Lei, "The effect of energy patents on china's carbon emissions: Evidence from the stirpat model," *Technological Forecasting and Social Change*, vol. 173, p. 121110, 2021.

[106] J. Huang, S. Xiang, P. Wu, and X. Chen, "How to control china's energy consumption through technological progress: A spatial heterogeneous investigation," *Energy*, vol. 238, p. 121965, 2022.

[107] N. Elvin and A. Erturk, *Advances in energy harvesting methods*. Springer Science & Business Media, 2013.

[108] H. Jaffe, "Piezoelectric ceramics," *Journal of the American Ceramic Society*, vol. 41, no. 11, pp. 494–498, 1958.

[109] T. Ng and W. Liao, "Sensitivity analysis and energy harvesting for a self-powered piezoelectric sensor," *Journal of Intelligent Material Systems and Structures*, vol. 16, no. 10, pp. 785–797, 2005.

[110] F. Cottone, L. Gammaitoni, H. Vocca, M. Ferrari, and V. Ferrari, "Piezoelectric buckled beams for random vibration energy harvesting," *Smart materials and structures*, vol. 21, no. 3, p. 035021, 2012.

[111] L. Wang, T. Tan, Z. Yan, D. Li, B. Zhang, and Z. Yan, "Integration of tapered beam and four direct-current circuits for enhanced energy harvesting from transverse galloping," *IEEE/ASME Transactions on Mechatronics*, vol. 24, no. 5, pp. 2248–2260, 2019.

[112] Y. Cha and H. You, "Parameter study on piezoelectric length to harvesting power in torsional loads," *IEEE/ASME Transactions on Mechatronics*, vol. 24, no. 3, pp. 1220–1227, 2019.

[113] Y. Shu, I. Lien, and W. Wu, "An improved analysis of the sshi interface in piezoelectric energy harvesting," *Smart Materials and Structures*, vol. 16, no. 6, p. 2253, 2007.

[114] L. Zhu, R. Chen, and X. Liu, "Theoretical analyses of the electronic breaker switching method for nonlinear energy harvesting interfaces," *Journal of Intelligent Material Systems and Structures*, vol. 23, no. 4, pp. 441–451, 2012.

[115] Y. Liao and J. Liang, "Maximum power, optimal load, and impedance analysis of piezoelectric vibration energy harvesters," *Smart Materials and Structures*, vol. 27, no. 7, p. 075053, 2018.

[116] L. Xie, S. Cai, G. Huang, L. Huang, J. Li, and X. Li, "On energy harvesting from a vehicle damper," *IEEE/ASME Transactions on Mechatronics*, vol. 25, no. 1, pp. 108–117, 2019.

[117] P. S. Tadesse Y, Zhang S, "Multimodal energy harvesting system: Piezoelectric and electromagnetic," *Journal of Intelligent Material Systems and Structures*, vol. 20, no. 5, pp. 625–632, 2009.

[118] I. D. Erturk A, Renno JM, "Modeling of piezoelectric energy harvesting from an l-shaped beam-mass structure with an application to uavs," *Journal of Intelligent Material Systems and Structures*, vol. 20, no. 5, pp. 529–544, 2009.

[119] W. Cai and R. L. Harne, "Investigations on energy harvesting systems incorporating mechanical and electrical nonlinearities to charge reusable batteries," *Energy Conversion and Management*, vol. 252, p. 115045, 2022.

[120] Z. Wang, T. Li, Y. Du, Z. Yan, and T. Tan, "Nonlinear broadband piezoelectric vibration energy harvesting enhanced by inter-well modulation," *Energy Conversion and Management*, vol. 246, p. 114661, 2021.

[121] F. Qian, M. R. Hajj, and L. Zuo, "Bio-inspired bi-stable piezoelectric harvester for broadband vibration energy harvesting," *Energy Conversion and Management*, vol. 222, p. 113174, 2020.

[122] F. Cottone, H. Vocca, and L. Gammaitoni, "Nonlinear energy harvesting," *Phys. Rev. Lett.*, vol. 102, p. 080601, Feb 2009.

[123] E. Lefeuvre, A. Badel, A. Brenes, S. Seok, M. Woytasik, and C. Yoo, "Analysis of piezoelectric energy harvesting system with tunable sece interface," *Smart Materials and Structures*, vol. 26, no. 3, p. 035065, 2017.

[124] J. M. De Ponti, *Graded Elastic Metamaterials for Energy Harvesting.* Springer Nature, 2021.

[125] J. Wang, S. Sun, G. Hu, Y. Yang, L. Tang, P. Li, and G. Zhang, "Exploring the potential benefits of using metasurface for galloping energy harvesting," *Energy Conversion and Management*, vol. 243, p. 114414, 2021.

[126] M. M. Sigalas and E. N. Economou, "Elastic and acoustic wave band structure," *Journal of sound and vibration*, vol. 158, no. 2, pp. 377–382, 1992.

[127] R. V. Craster and S. Guenneau, *Acoustic metamaterials: Negative refraction, imaging, lensing and cloaking.* Springer Science & Business Media, 2012, vol. 166.

[128] C. Sugino and A. Erturk, "Analysis of multifunctional piezoelectric metastructures for low-frequency bandgap formation and energy harvesting," *Journal of Physics D: Applied Physics*, vol. 51, no. 21, p. 215103, 2018.

[129] Y. Li, E. Baker, T. Reissman, C. Sun, and W. K. Liu, "Design of mechanical metamaterials for simultaneous vibration isolation and energy harvesting," *Applied Physics Letters*, vol. 111, no. 25, p. 251903, 2017.

[130] J. M. De Ponti, L. Iorio, E. Riva, F. Braghin, A. Corigliano, and R. Ardito, "Enhanced energy harvesting of flexural waves in elastic beams by bending mode of graded resonators," *Frontiers in Materials*, vol. 8, 2021.

[131] N. Jiménez, O. Umnova, and J.-P. Groby, *Acoustic Waves in Periodic Structures, Metamaterials, and Porous Media: From Fundamentals to Industrial Applications.* Springer Nature, 2021, vol. 143.

[132] J. Wang, B. Zhao, W.-H. Liao, and J. Liang, "New insight into piezoelectric energy harvesting with mechanical and electrical nonlinearities," *Smart Materials and Structures*, vol. 29, no. 4, p. 04LT01, 2020.

[133] E. Lefeuvre, A. Badel, C. Richard, L. Petit, and D. Guyomar, "A comparison between several vibration-powered piezoelectric generators for standalone systems," *Sensors and Actuators A: Physical*, vol. 126, no. 2, pp. 405–416, 2006.

[134] B. Sahu and G. A. Rincón-Mora, "A low voltage, dynamic, noninverting, synchronous buck-boost converter for portable applications," *IEEE Transactions on power electronics*, vol. 19, no. 2, pp. 443–452, 2004.

[135] G. Hu, L. Tang, J. Liang, and R. Das, "Modelling of a cantilevered energy harvester with partial piezoelectric coverage and shunted to practical interface circuits," *Journal of Intelligent Material Systems and Structures*, vol. 30, no. 13, pp. 1896–1912, 2019.

[136] B. Van Damme, K. Van Den Abeele, Y. Li, and O. B. Matar, "Time reversed acoustics techniques for elastic imaging in reverberant and nonreverberant media: An experimental study of the chaotic cavity transducer concept," *Journal of Applied Physics*, vol. 109, no. 10, p. 104910, 2011.

[137] B. Van Damme and A. Zemp, "Measuring dispersion curves for bending waves in beams: a comparison of spatial fourier transform and inhomogeneous wave correlation," *Acta Acustica united with Acustica*, vol. 104, no. 2, pp. 228–234, 2018.

[138] A. E. Miroshnichenko, S. Flach, and Y. S. Kivshar, "Fano resonances in nanoscale structures," *Rev. Mod. Phys.*, vol. 82, pp. 2257–2298, 2010.

[139] Z. Yang, A. Erturk, and J. Zu, "On the efficiency of piezoelectric energy harvesters," *Extreme Mechanics Letters*, vol. 15, pp. 26–37, 2017.

[140] G.-F. Fan, L.-Z. Zhang, M. Yu, W.-C. Hong, and S.-Q. Dong, "Applications of random forest in multivariable response surface for short-term load forecasting," *International Journal of Electrical Power & Energy Systems*, vol. 139, p. 108073, 2022.

[141] A. Al-Fuqaha, M. Guizani, M. Mohammadi, M. Aledhari, and M. Ayyash, "Internet of things: A survey on enabling technologies, protocols, and applications," *IEEE communications surveys & tutorials*, vol. 17, no. 4, pp. 2347–2376, 2015.

[142] F. K. Shaikh and S. Zeadally, "Energy harvesting in wireless sensor networks: A comprehensive review," *Renewable and Sustainable Energy Reviews*, vol. 55, pp. 1041–1054, 2016.

[143] M. Prauzek, J. Konecny, M. Borova, K. Janosova, J. Hlavica, and P. Musilek, "Energy harvesting sources, storage devices and system topologies for environmental wireless sensor networks: A review," *Sensors*, vol. 18, no. 8, p. 2446, 2018.

[144] C. Wei and X. Jing, "A comprehensive review on vibration energy harvesting: Modelling and realization," *Renewable and Sustainable Energy Reviews*, vol. 74, pp. 1–18, 2017.

[145] B. Zhao, J. Qiu, and J. Liang, "Circuit solutions toward broadband piezoelectric energy harvesting: An impedance analysis," *IEEE Transactions on Circuits and Systems I: Regular Papers*, 2023.

[146] X. Wang, C. Chen, N. Wang, H. San, Y. Yu, E. Halvorsen, and X. Chen, "A frequency and bandwidth tunable piezoelectric vibration energy harvester using multiple nonlinear techniques," *Applied energy*, vol. 190, pp. 368–375, 2017.

[147] S. Fang, S. Zhou, D. Yurchenko, T. Yang, and W.-H. Liao, "Multistability phenomenon in signal processing, energy harvesting, composite structures, and metamaterials: A review," *Mechanical Systems and Signal Processing*, vol. 166, p. 108419, 2022.

[148] H.-X. Zou, L.-C. Zhao, Q.-H. Gao, L. Zuo, F.-R. Liu, T. Tan, K.-X. Wei, and W.-M. Zhang, "Mechanical modulations for enhancing energy harvesting: Principles, methods and applications," *Applied Energy*, vol. 255, p. 113871, 2019.

[149] J. Guckenheimer and P. Holmes, *Nonlinear oscillations, dynamical systems, and bifurcations of vector fields*. Springer Science & Business Media, 2013, vol. 42.

[150] G. Sebald, H. Kuwano, D. Guyomar, and B. Ducharne, "Experimental duffing oscillator for broadband piezoelectric energy harvesting," *Smart materials and structures*, vol. 20, no. 10, p. 102001, 2011.

[151] A. Masuda and A. Senda, "A vibration energy harvester using a nonlinear oscillator with self-excitation capability," in *Active and Passive Smart Structures and Integrated Systems 2011*, vol. 7977. SPIE, 2011, pp. 306–314.

[152] C. Lan, L. Tang, and W. Qin, "Obtaining high-energy responses of nonlinear piezoelectric energy harvester by voltage impulse perturbations," *The European Physical Journal Applied Physics*, vol. 79, no. 2, p. 20902, 2017.

[153] N. Kitamura and A. Masuda, "Efficiency and effectiveness of stabilization control of high-energy orbit for wideband piezoelectric vibration energy harvesting," in *Active and Passive Smart Structures and Integrated Systems XII*, vol. 10595. SPIE, 2018, p. 1059503.

[154] J. Wang and W.-H. Liao, "Attaining the high-energy orbit of nonlinear energy harvesters by load perturbation," *Energy Conversion and Management*, vol. 192, pp. 30–36, 2019.

[155] L. Yan, M. Lallart, and A. Karami, "Low-cost orbit jump in nonlinear energy harvesters through energy-efficient stiffness modulation," *Sensors and Actuators A: Physical*, vol. 285, pp. 676–684, 2019.

[156] T. Huguet, M. Lallart, and A. Badel, "Orbit jump in bistable energy harvesters through buckling level modification," *Mechanical Systems and Signal Processing*, vol. 128, pp. 202–215, 2019.

[157] Y. Huang, W. Liu, Y. Yuan, and Z. Zhang, "High-energy orbit attainment of a nonlinear beam generator by adjusting the buckling level," *Sensors and Actuators A: Physical*, vol. 312, p. 112164, 2020.

[158] S. Zhou, J. Cao, D. J. Inman, S. Liu, W. Wang, and J. Lin, "Impact-induced high-energy orbits of nonlinear energy harvesters," *Applied Physics Letters*, vol. 106, no. 9, p. 093901, 2015.

[159] D. Mallick, A. Amann, and S. Roy, "Surfing the high energy output branch of nonlinear energy harvesters," *Physical Review Letters*, vol. 117, no. 19, p. 197701, 2016.

[160] H. Fu and E. M. Yeatman, "Broadband rotational energy harvesting using bistable mechanism and frequency up-conversion," in *2017 IEEE 30th International Conference on Micro Electro Mechanical Systems (MEMS)*. IEEE, 2017, pp. 853–856.

[161] J. P. Udani and A. F. Arrieta, "Sustaining high-energy orbits of bi-stable energy harvesters by attractor selection," *Applied Physics Letters*, vol. 111, no. 21, p. 213901, 2017.

[162] A. Haji Hosseinloo, J.-J. Slotine, and K. Turitsyn, "Robust and adaptive control of coexisting attractors in nonlinear vibratory energy harvesters," *Journal of Vibration and Control*, vol. 24, no. 12, pp. 2532–2541, 2018.

[163] Y. Zhang, C. Ding, J. Wang, and J. Cao, "High-energy orbit sliding mode control for nonlinear energy harvesting," *Nonlinear Dynamics*, vol. 105, no. 1, pp. 191–211, 2021.

[164] G. K. Ottman, H. F. Hofmann, A. C. Bhatt, and G. A. Lesieutre, "Adaptive piezoelectric energy harvesting circuit for wireless remote power supply," *IEEE Transactions on Power Electronics*, vol. 17, no. 5, pp. 669–676, 2002.

[165] I. Lien, Y. Shu, W. Wu, S. Shiu, and H. Lin, "Revisit of series-sshi with comparisons to other interfacing circuits in piezoelectric energy harvesting," *Smart Materials and Structures*, vol. 19, no. 12, p. 125009, 2010.

[166] Y. Chen, F. Qian, F. Scarpa, L. Zuo, and X. Zhuang, "Harnessing multi-layered soil to design seismic metamaterials with ultralow frequency band gaps," *Materials & Design*, vol. 175, p. 107813, 2019.

[167] M. Lallart, L. Garbuio, L. Petit, C. Richard, and D. Guyomar, "Double synchronized switch harvesting (dssh): A new energy harvesting scheme for efficient energy extraction," *IEEE Transactions on Ultrasonics, Ferroelectrics, and Frequency Control*, vol. 55, no. 10, pp. 2119–2130, 2008.

[168] J. Liang, Y. Zhao, and K. Zhao, "Synchronized triple bias-flip interface circuit for piezoelectric energy harvesting enhancement," *IEEE Transactions on Power Electronics*, vol. 34, no. 1, pp. 275–286, 2018.

[169] Q. Dai and R. L. Harne, "Investigation of direct current power delivery from nonlinear vibration energy harvesters under combined harmonic and stochastic excitations," *Journal of Intelligent Material Systems and Structures*, vol. 29, no. 4, pp. 514–529, 2018.

[170] C. Lan, L. Tang, and R. L. Harne, "Comparative methods to assess harmonic response of nonlinear piezoelectric energy harvesters interfaced with ac and dc circuits," *Journal of Sound and Vibration*, vol. 421, pp. 61–78, 2018.

[171] Z. Lai, J. Xu, S. Fang, Z. Qiao, S. Wang, C. Wang, Z. Huang, and S. Zhou, "Energy harvesting from a hybrid piezo-dielectric vibration energy harvester with a self-priming circuit," *Energy*, vol. 273, p. 127205, 2023.

[172] B. Zhao, S. Liu, W.-H. Liao, and J. Liang, "On the positive and negative damping effect of piezoelectric structure using switched-mode bidirectional energy conversion circuit," *Smart Materials and Structures*, vol. 32, no. 1, p. 01LT01, 2022.

[173] J. K. Kevorkian and J. D. Cole, *Multiple scale and singular perturbation methods*. Springer Science & Business Media, 2012, vol. 114.

[174] M. Brennan, I. Kovacic, A. Carrella, and T. Waters, "On the jump-up and jump-down frequencies of the duffing oscillator," *Journal of Sound and Vibration*, vol. 318, no. 4-5, pp. 1250–1261, 2008.

[175] J. Wang, B. Zhao, J. Liang, and W.-H. Liao, "Orbit jumps of monostable energy harvesters by a bidirectional energy conversion circuit," in *International Design Engineering Technical Conferences and Computers and Information in Engineering Conference*, vol. 59285. American Society of Mechanical Engineers, 2019, p. V008T10A016.

[176] A. Preumont, *Vibration control of active structures: an introduction*. Springer, 2018, vol. 246.

[177] J. Ormondroyd, "Theory of the dynamic vibration absorber," *Transaction of the ASME*, vol. 50, pp. 9–22, 1928.

[178] Y. Starosvetsky and O. Gendelman, "Vibration absorption in systems with a nonlinear energy sink: nonlinear damping," *Journal of Sound and Vibration*, vol. 324, no. 3-5, pp. 916–939, 2009.

[179] A. Casalotti, S. El-Borgi, and W. Lacarbonara, "Metamaterial beam with embedded nonlinear vibration absorbers," *International Journal of Non-Linear Mechanics*, vol. 98, pp. 32–42, 2018.

[180] M. Gutierrez Soto and H. Adeli, "Tuned mass dampers," *Archives of Computational Methods in Engineering*, vol. 20, pp. 419–431, 2013.

[181] B. Zhao, J. Wang, G. Hu, A. Colombi, W.-H. Liao, and J. Liang, "Time-sharing orbit jump and energy harvesting in nonlinear piezoelectric energy harvesters using a synchronous switch circuit," *Mechanical Systems and Signal Processing*, vol. 200, p. 110601, 2023.

[182] M. Gzal, B. Fang, A. Vakakis, L. Bergman, and O. Gendelman, "Rapid non-resonant intermodal targeted energy transfer (imtet) caused by vibro-impact nonlinearity," *Nonlinear Dynamics*, vol. 101, pp. 2087–2106, 2020.

[183] B. Davies, G. J. Chaplain, T. A. Starkey, and R. V. Craster, "Graded quasiperiodic metamaterials perform fractal rainbow trapping," *Phys. Rev. Lett.*, vol. 131, p. 177001, Oct 2023.

[184] L. Rosafalco, J. M. De Ponti, L. Iorio, R. Ardito, and A. Corigliano, "Optimised graded metamaterials for mechanical energy confinement and amplification via reinforcement learning," *European Journal of Mechanics-A/Solids*, vol. 99, p. 104947, 2023.

[185] X. Fang, J. Wen, B. Bonello, J. Yin, and D. Yu, "Ultra-low and ultra-broad-band nonlinear acoustic metamaterials," *Nature communications*, vol. 8, no. 1, p. 1288, 2017.

[186] K. A. Chondrogiannis, A. Colombi, V. Dertimanis, and E. Chatzi, "Computational verification and experimental validation of the vibration-attenuation properties of a geometrically nonlinear metamaterial design," *Physical Review Applied*, vol. 17, no. 5, p. 054023, 2022.

[187] Q. Xu, J. Wang, Y. Lv, H. Yao, and B. Wen, "Vibration characteristics of linear and nonlinear dissipative elastic metamaterials rotor with geometrical nonlinearity," *International Journal of Non-Linear Mechanics*, vol. 157, p. 104543, 2023.

[188] R. Seydel, *Practical bifurcation and stability analysis*. Springer Science & Business Media, 2009, vol. 5.

[189] B. Zhao, H. Thomsen, X. Pu, B. V. Damme, A. Bergamini, E. Chatzi, and A. Colombi, "A nonlinear metamaterial induced by nonlinear damping effect with inertia amplifiers," in *10th ECCOMAS Thematic Conference on Smart Structures and Materials*. Dept. of Mechanical Engineering & Aeronautics University of Patras, 2023.

[190] B. Van Damme, G. Hannema, L. Sales Souza, B. Weisse, D. Tallarico, and A. Bergamini, "Inherent non-linear damping in resonators with inertia amplification," *Applied Physics Letters*, vol. 119, no. 6, p. 061901, 2021.

[191] K. Worden and G. R. Tomlinson, "Nonlinearity in experimental modal analysis," *Philosophical Transactions of the Royal Society of London. Series A: Mathematical, Physical and Engineering Sciences*, vol. 359, no. 1778, pp. 113–130, 2001.

[192] S. Sepehri, M. M. Mashhadi, and M. M. S. Fakhrabadi, "Wave propagation in nonlinear monoatomic chains with linear and quadratic damping," *Nonlinear Dynamics*, vol. 108, no. 1, pp. 457–478, 2022.

[193] A. Palermo, B. Yousefzadeh, C. Daraio, and A. Marzani, "Rayleigh wave propagation in nonlinear metasurfaces," *Journal of Sound and Vibration*, vol. 520, p. 116599, 2022.

[194] M. I. Hussein and M. J. Frazier, "Band structure of phononic crystals with general damping," *Journal of Applied Physics*, vol. 108, no. 9, p. 093506, 2010.

[195] L. Van Belle, C. Claeys, E. Deckers, and W. Desmet, "On the impact of damping on the dispersion curves of a locally resonant metamaterial: Modelling and experimental validation," *Journal of Sound and Vibration*, vol. 409, pp. 1–23, 2017.

[196] T. C. Choy, *Effective medium theory: principles and applications*. Oxford University Press, 2015, vol. 165.

[197] F. Farzbod and M. J. Leamy, "Analysis of bloch's method in structures with energy dissipation," *Journal of Vibration and Acoustics*, vol. 133, no. 5, 2011.

[198] A. Bergamini, M. Miniaci, T. Delpero, D. Tallarico, B. Van Damme, G. Hannema, I. Leibacher, and A. Zemp, "Tacticity in chiral phononic crystals," *Nature communications*, vol. 10, no. 1, p. 4525, 2019.

[199] S. L. Brunton and J. N. Kutz, *Data-driven science and engineering: Machine learning, dynamical systems, and control*. Cambridge University Press, 2022.

[200] L. Rouleau, J.-F. Deü, and A. Legay, "A comparison of model reduction techniques based on modal projection for structures with frequency-dependent damping," *Mechanical Systems and Signal Processing*, vol. 90, pp. 110–125, 2017.

[201] T. M. Cameron and J. H. Griffin, "An Alternating Frequency/Time Domain Method for Calculating the Steady-State Response of Nonlinear Dynamic Systems," *Journal of Applied Mechanics*, vol. 56, no. 1, pp. 149–154, 03 1989.

[202] M. Krack and J. Gross, *Harmonic balance for nonlinear vibration problems*. Springer, 2019, vol. 1.

[203] G. H. Golub and C. F. Van Loan, *Matrix computations*. JHU press, 2013.

[204] G. Hu, L. Tang, and R. Das, "General framework for modeling multifunctional metamaterial beam based on a derived one-dimensional piezoelectric composite finite element," *Journal of Aerospace Engineering*, vol. 31, no. 6, p. 04018088, 2018.

[205] Y.-F. Wang, Y.-S. Wang, and V. Laude, "Wave propagation in two-dimensional viscoelastic metamaterials," *Physical Review B*, vol. 92, no. 10, p. 104110, 2015.

[206] A. Rayes and S. Salam, "The things in iot: Sensors and actuators," in *Internet of Things From Hype to Reality: The Road to Digitization*. Springer, 2022, pp. 63–82.

[207] X. Li, H. Tang, G. Hu, B. Zhao, and J. Liang, "Vipsn-pluck: A transient-motion-powered motion detector," *IEEE Internet of Things Journal*, 2021.

Nomenclature

Abbreviations

AC	Alternating Current
AFT	Alternating Frequency Time
BECC	Bidirectional Energy Conversion Circuit
DC	Direct Current
DCM	Discontinuous Conduction Mode
EH	Energy Harvesting
ESR	Equivalent Series Resistance
FEM	Finite Element Method
HEO	High Energy Orbit
IoT	Internet of Things
IWC	Inhomogeneous Wave Correlation
LEO	Low Energy Orbit
MOSFET	Metal Oxide Semiconductor Field Effect Transistor
PCB	Printed Circuit Board
PEH	Piezoelectric Energy Harvesting
PV	Phase Variable
PVDF	Polyvinylidene Fluoride
PWM	Pulse Width Modulation
PZT	Piezoelectric Zirconate Titanate
S3BF	Synchronized Tripe Bias Flip
SDOF	Single Degree Of Freedom

SECE	Synchronized Electrical Charge Extraction
SEH	Standard Energy Harvesting
SLDV	Scanning Laser Doppler Vibrometer
SP	Self Powered
SSHI	Synchronized Switching Harvesting on Inductor
VE	Vibration Exciting
VEH	Vibration Energy Harvesting